RESISTIVE TRANSITION
AND PROTECTION
OF LHC SUPERCONDUCTING
CABLES AND MAGNETS

Von der Fakultät für Mathematik, Informatik und Naturwissenschaften
der Rheinisch-Westfälischen Technischen Hochschule Aachen
zur Erlangung des akademischen Grades eines
Doktors der Naturwissenschaften
genehmigte Dissertation

von

Diplom-Physiker Florian Sonnemann
aus Braunschweig

Berichter: Universitätsprofessor Dr. A. Böhm
            Universitätsprofessor Dr. J. Mnich

Tag der mündlichen Prüfung: 7. Mai 2001

Diese Dissertation ist auf den Internetseiten der Hochschulbibliothek online verfügbar.

To my family

Zusammenfassung

Supraleitung und Superfluidität sind makroskopische Quanten-Phänomene, die in der Technologie genutzt werden können. Eine der bedeutendsten Anwendungen der Supraleitung ist die Konstruktion von sehr starken Magneten, die es ermöglichen, in Kreisbeschleunigern Teilchen mit hohen Energien zu leiten. Beim Large Hadron Collider (LHC) am Europäischen Teilchenphysikzentrum (CERN) bei Genf werden supraleitende Magnete aus konventionellen Supraleitern mit supraflüssigem Helium gekühlt, um noch höhere Ablenkfelder zu erreichen.

Das Übergangsverhalten von supraleitenden Kabeln und Magneten in den normalleitenden Zustand (engl. 'Quench') wird durch mechanische, thermodynamische und elektromagnetische Prozesse bestimmt. Aufgrund der hohen gespeicherten magnetischen Energie müssen supraleitende Elemente im Falle eines Quenches vor hohen Spannungen und Temperaturen geschützt werden. Eine präzise Beschreibung der Quenchmechanismen ist daher nötig, um das Verständnis des Übergangsverhalten von Supraleitern zu verbessern und ein verlässliches Schutzsystem zu konzipieren.

Der erste Teil der vorliegenden Arbeit enthält eine Einführung in die Grundlagen des LHC Beschleunigers sowie der heute verfügbaren technischen Supraleiter und deren Kühlung. Nach der Zusammenfassung der vorhandenen analytischen Quenchmodellen folgt die Beschreibung des im Rahmen dieser Arbeit neu entwickelten numerischen Algorithmus zur Quenchsimulation, der sowohl die Erwärmung des Supraleiters und den Kühlvorgang durch Helium, als auch die thermodynamische Ausbreitung sowie den Einfluß von induzierten Wirbelströmen berücksichtigt.

Der zweite Teil der Arbeit umfaßt die Untersuchung der Quenchprozesse in den verschiedenen Kabeln und Magneten des LHC. Die durchgeführten Messungen und deren Analyse sowie die begleitenden Simulationsstudien, welche die Fortschritte und Erweiterung der Quenchmodellierung illustrieren, werden diskutiert. Abschließend wird das Schutzsystem der supraleitenden Elemente des LHC beschrieben, welches mit Hilfe der Ergebnisse dieser Arbeit optimiert wurde. Die Resultate und Auswirkungen der durchgeführten Analysen und Simulationen werden zusammengefaßt.

Summary

Superconductivity and superfluidity are macroscopic quantum-effects that are used in technology. One of the most important applications of superconductivity is the design of strong magnets, which guide particles at very high energies in circular accelerators. In the Large Hadron Collider (LHC), which is being constructed at the European Laboratory for Particle Physics (CERN) close to Geneva, magnets wound with conventional superconductors are cooled with superfluid helium to access even higher magnetic field strengths.

The resistive transition from the superconducting to the normal-conducting state (known as a quench) can be characterised by mechanical, electrodynamic and thermodynamic processes. Due to the high amount of stored magnetic energy, a quench can potentially cause damage in superconducting elements by overheating or excessive voltages. A detailed description of the related mechanisms is needed to understand the quench process better and to design a reliable protection system. This requires analytical and more importantly numerical models, which include the heat generation of the superconductor, cooling by helium, the thermodynamic propagation of the normal-conducting zone, as well as the impact of induced eddy currents. In the framework of this thesis, a new numerical algorithm has been developed.

The improvements and advancements made in the quench modelling are explained in this thesis. It also includes detailed analyses and simulation studies of the quench processes in LHC superconducting cables and magnets. The LHC protection system that has been optimised by the outcome of this thesis is presented. The results and consequences of the performed analyses and simulations are summarised.

List of variables

$\alpha_{ST} = \frac{G}{h^{He}P}$	Stekly paramater	
α	ratio of transverse and longitudinal quench propagation	
A	cross-section	[m^2]
A_{cu}	copper cross-section	[m^2]
A_{sc}	niobium-titanium cross-section	[m^2]
A_h	heater strip cross-section	[m^2]
B	magnetic field	[tesla]
$B_\parallel$	field component parallel to the conductor block	[tesla]
$B_\perp$	field component perpendicular to the conductor block	[tesla]
C_h	heater power supply capacitance	[F]
c	heat capacity (averaged for conductor)	[J/(m$^3\cdot$ K)]
c_h	heater strip heat capacity	[J/(m$^3\cdot$ K)]
c_{iso}	insulation layer heat capacity	[J/(m$^3\cdot$ K)]
d_f	filament diameter	[m]
f	fraction of conductor exposed to helium	
f_h	fraction of heater energy directed into the superconductor	
F_t	heat transfer function for transverse cooling	[W/m]
ϕ	angle of magnetic field and the conductor block	[rad]
g	logical function that determines whether element is covered by heater	
h	height of Rutherford cable	[m]
h^{He}	heat transfer coefficient to helium	[W/m^2]
I	excitation current	[A]
I_{cc}	induced coupling currents (both interfilament and interstrand)	[A]
I_{if}	interfilament coupling current	[A]
I_{is}	interstrand coupling current	[A]
I_h	heater current	[A]
I_h^0	initial heater current	[A]
I_0	initial excitation current	[A]
J_c	critical current density for the conductor	[A/m^2]
j	heat flux	[W/m^3]
k	thermal conductivity	[W/(m·K)]
k_{iso}	thermal conductivity of the insulation layer	[W/(m·K)]
k_{iso}^h	thermal conductivity of the heater insulation layer	[W/(m·K)]
k_{iso}^t	thermal conductivity of the insulation between turns	[W/(m·K)]
l_h	length (longitudinal) of heater strip	[m]
l_h^{Cu}	length of copper plated part per period of the heater strip	[m]
l_h^{Fe}	length of non copper plated part per period of the heater strip	[m]
l_{iso}	thickness of the insulation layer	[m]
L_{pf}	twist pitch length of a filament	[m]
L_{ps}	twist pitch length of a strand	[m]

M	magnetisation loss	[W/m^3]
$N_{s,l}$	number of strands in one layer of the Rutherford cable	
P	effective wetted perimeter of the conductor	[m]
P_{if}	power loss in strands (interfilament)	[W]
P_{is}	power loss in the Rutherford cable (interstrand)	[W]
$P0$	initial heater power dissipation	[W]
$\dot{q}$	heat pulse provoking the natural quench	[W/m]
R	resistance	[Ω]
R_a	contact resistance between adjacent strands in one layer	[Ω]
R_c	inter layer contact resistance	[Ω]
R_h	heater strip resistance	[Ω]
ρ_{cu}	copper resistivity	[Ωm]
ρ_h	heater resistivity (stainless steel dominated)	[Ωm]
RRR	ratio of copper resistivity at 300 K and 10 K	
$r_{cu/sc}$	ratio of copper to niobium-titanium content	
r	radius of the conductor	[m]
T	temperature	[K]
T_{bath}	helium bath temperature	[K]
T_{crit}	critical temperature	[K]
T_{cs}	current sharing temperature	[K]
T_h	heater strip temperature	[K]
T_{iso}	insulation layer temperature (at boundary to helium bath)	[K]
$T_{n.boil}$	temperature at which nucleate boiling starts	[K]
$T_{f.boil}$	temperature at which film boiling helium starts	[K]
t	time	[s]
t_{det}	quench detection time	[s]
$t_{f.boil}$	time interval needed to start film boiling	[s]
τ_h	heater current decay time constant	[s]
τ_{if}	interfilament current build-up time constant	[s]
τ_{is}	interstrand current build-up time constant	[s]
U_h^0	initial heater voltage	[V]
U_{min}	minimum heater voltage to provoke a quench	[V]
V	volume element	[m^3]
w_h	width of heater strip	[m]
w_t	averaged turn width	[m]
x	longitudinal direction along the conductor	[m]
y	transverse direction between layers	[m]
z	transverse direction between turns	[m]

Contents

Introduction

The LHC (Large Hadron Collider) is the next circular accelerator being constructed at CERN that will provide head-on collisions of protons at a centre of mass energy of $14\,$TeV for high energy particle physics research. The LHC will be hosted in the existing $26\,$km long LEP tunnel and will reuse CERN's existing proton accelerators as injectors. In order to reach the required magnet field strengths, superconducting magnets cooled with superfluid helium will be installed. Although other superconducting accelerators have already been successfully working for quite some time (for example the Tevatron at FNAL, USA, or HERA at DESY, Germany), the construction of the LHC involves new challenges, some of them in the field of applied superconductivity and cryogenic engineering.

The magnetic energy stored in superconducting magnets is very high and can potentially cause severe damage when the superconducting state disappears (known as a quench) due to beam losses or cryogenic failures. The possible damages can vary in severity e.g. degrading magnet performance, short circuits, and open circuits due to a burnt superconducting cable. The protection system that deals with the stored magnetic energy therefore plays a key role in ensuring the operational reliability. Depending on the type of superconducting element and the stored energy per circuit, different protection strategies are applied.

This thesis focuses on the advancements in the modelling and understanding of the quench mechanisms applied to the superconducting elements of the LHC and outlines the conclusions for the protection system. The quench process couples electrodynamic and thermodynamic effects that need to be considered for the design of superconducting accelerator magnets and for the protection system. In the framework of this thesis, two main contributions have been achieved. Firstly, I have developed a new numerical quench simulation model that includes both the electrodynamic and thermodynamic processes related to a quench. This program has been used for simulation studies to understand the results of quench experiments better. Secondly, I have performed detailed analyses of quench tests that were carried out on various prototypes of LHC superconducting cables and magnets.

The LHC accelerator and its main challenges are presented in Chapter 1. The chapter explains the complexity of the LHC magnet system and motivates the need for a better understanding of the quench process for the demand of a reliable protection system. The protection strategies are introduced.

An overview of the basic principles of superconductivity and of the available superconductors is given in Chapter 2. The focus is on hard type II superconductors used for winding accelerator magnets, especially on niobium-titanium (NbTi) wires made of many superconducting NbTi filaments that are embedded in a copper matrix for stabilisation. The copper is required to avoid overheating after a quench in the normal-conducting state. This is followed by an overview of the temperature dependences of helium properties and the principles of superfluidity. The mechanisms of heat transfer into helium are summarised.

Chapter 3 is devoted to the theory of the quench process. It outlines the important quench parameters required to analyse the quench process in various superconducting elements. The summary of analytical approaches is followed by the discussion of their limitations in describing the quench process of the LHC superconducting elements. The new developed numerical model that includes both electrodynamic and thermodynamic quench processes is explained in the Sections 3.2–3.5. The numerical realisation (Simulation Program for Quench Research, SPQR) is presented.

Chapter 4 introduces the measurement techniques for the experiments performed on prototype magnets and busbars. An overview of the test stations for superconducting elements at CERN is given. The foreseen measurements for the magnets of the series production are outlined.

The subsequent chapters present the outcome of quench experiments, their analyses and simulation studies that I have performed for the various superconducting elements of the LHC. The experiments were carried out in close collaboration with the members of the LHC/ICP and LHC/MTA groups. The quench model explained in Chapter 3 is applied to enhance the understanding of the experimental results and to determine the adequate protection scheme:

- The quench process in busbars that can be described with a one-dimensional model in space is discussed in Chapter 5.

- Chapter 6 outlines the quench process of corrector magnets which includes the quench propagation between turns and layers. During a fast current decay, eddy currents contribute to the quench process due to interfilament coupling currents in the multifilament wires.

- The complexity of the quench process increases for main magnets that are wound with Rutherford cables, which are made of 20–30 twisted wires (also called strands) and formed into a two layer structure. Induced eddy currents during the current decay (the interstrand coupling currents and interfilament coupling currents) have an impact on the quench process. These magnets need to be protected by quench heaters that provoke a quench in a large fraction of the magnet, which leads to a better distribution of the stored energy in the magnet (see Sections 1.5 and 3.5.3). The quench process in the main magnets is analysed in Chapter 7.

An overview of the elements and the layout of the LHC protection system is given in Chapter 8. The consequences of the performed simulation studies and quench analyses are presented and the protection strategies for the various magnets and busbars are summarised.

The main results and conclusions of my quench analyses and simulation studies are outlined.

Chapter 1

The Large Hadron Collider

The Large Hadron Collider will collide two counter-rotating proton beams at an energy of 7 TeV per beam. This energy is seven times higher than the beam energy of any other proton accelerator to date. The reason of the particle physics request high energy is briefly reviewed in Section 1.1. The conceptual design of the LHC has been published in the LHC design report (see Fig. 1.1) [1]. The overall symmetry by eight is due to the existing LEP architecture. The LHC will be subdivided in octants and host four large scale experiments. The LHC can also be filled with lead ions up to 5.5 TeV/nucleon and therefore allow heavy-ion experiments.

1232 main superconducting dipole magnets of 15 m length each and about 600 main quadrupole magnets will be installed in the LHC to guide the beams. In order to achieve the high magnetic field of 8.33 tesla, the magnets need to be cooled with superfluid helium at 1.9 K, which requires large cryogenic installations.

The beams are in proton bunches and the machine is designed to achieve a luminosity exceeding 10^{34} cm^{-2}s^{-1}. The luminosity L is defined as

$$L = N_1 \cdot N_2 / (4\pi \cdot \sigma_x \sigma_y) \cdot n_b \cdot f_{rev} \qquad (1.1)$$

L is the interaction rate of particles per unit cross-section, N_1 are N_2 are the number of particles per bunch for each beam, σ_x and σ_y are the beam sizes in the transverse directions cross-section, n_b the number of bunches, f_{rev} the revolution frequency (ca. 11 kHz for the LHC). The high luminosity will be achieved by filling the LHC with 2808 bunches of 10^{11} particles per bunch which gives a time averaged beam current of 0.56 A. In order to keep the particle trajectories stable, the field quality of the magnets must be very high [2]. This is achieved with a large variety of magnets (see Section 1.2).

As the proton bunches collide every 25 ns in the experimental detectors, their electronics must provide a fast response and readout to avoid integrating over many bunch crossings.

Both beams will be stored at high energy for about 10 hours. The amplitude of the particle oscillations around the central orbit should not increase significantly, because this would dilute the beams and degrade luminosity. A tiny fraction of the beam that diffuses towards the beam pipe wall (and is consequently lost) is sufficient to cause a resistive transition in the superconducting magnets (quench), which will interrupt the machine operation for hours.

The feasibility of the LHC has been studied since 1984 [1], with an R+D program for superconducting dipole magnets and the first design of the machine parameters and lattice. The CERN Council approved the LHC project in 1996 to be built in one stage with 7 TeV beam energy. Strong support for the LHC from outside the CERN Member States was found (Canada, India, Japan, Russia and USA will contribute with manpower and money). The LHC accelerator
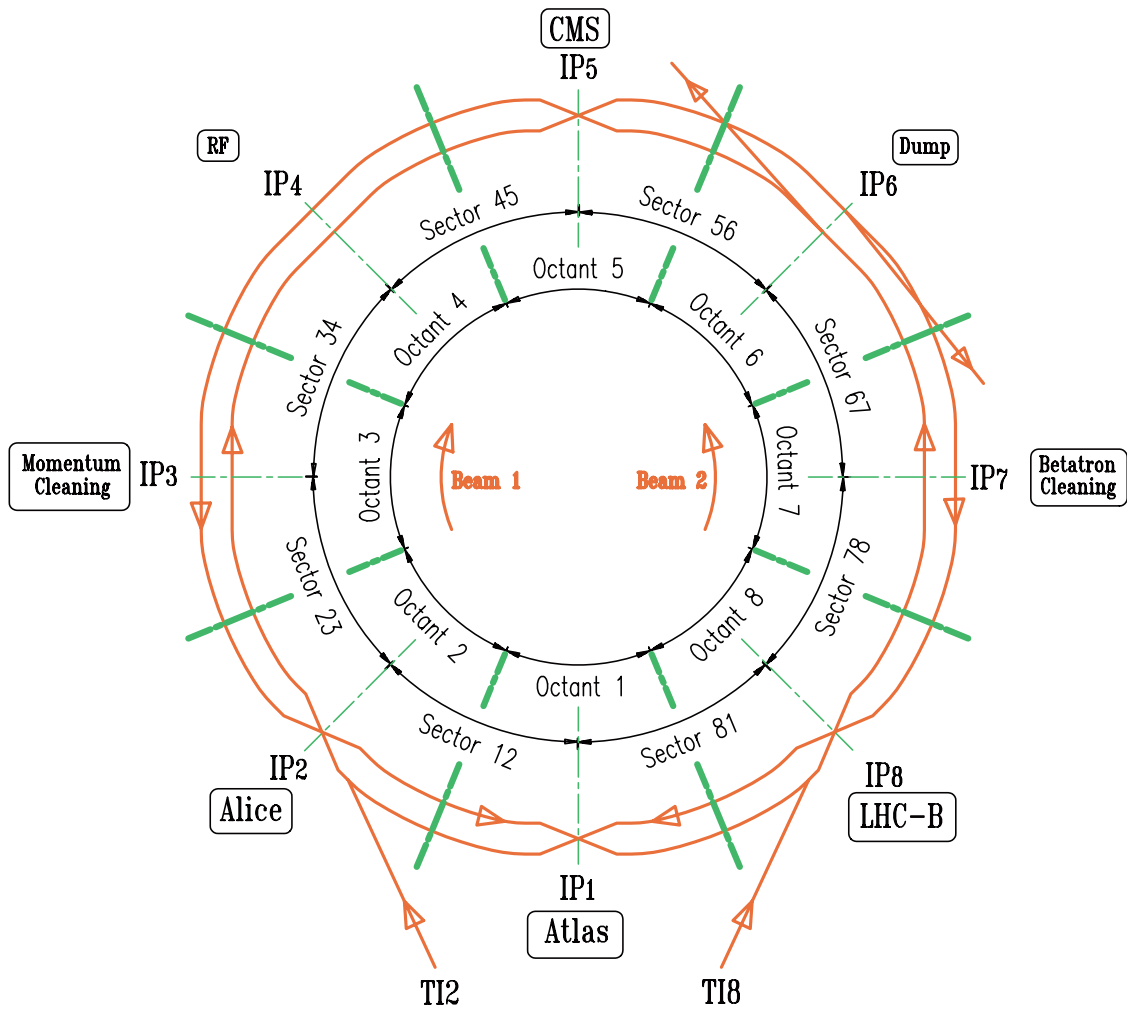
Figure 1.1: *The LHC layout.*

Energy	TeV	7
Injection energy	TeV	0.45
Dipole field	tesla	8.33
Number of dipole magnets		1232
Number of quadrupole magnets		about 600
Number of corrector magnets		about 7000
Luminosity	$cm^{-2}s^{-1}$	10^{34}
Coil aperture	mm	56
Distance between apertures	mm	194
Particles per bunch		10^{11}
Number of bunches		2808

Table 1.1: *LHC parameters [3].*
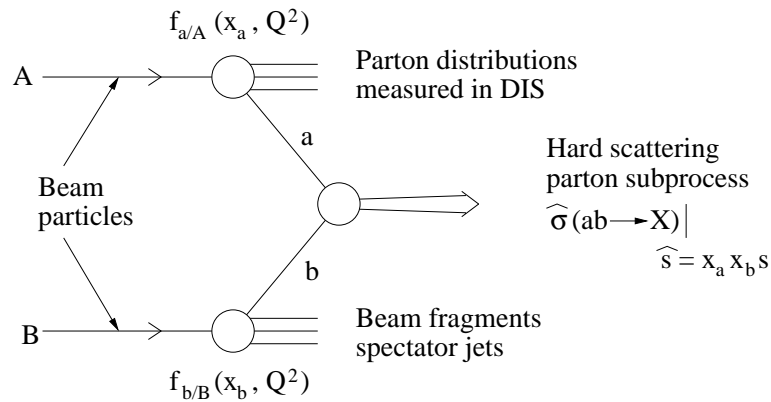
Figure 1.2: *The hard-scattering process between constituents of incoming protons [4].*

construction is in collaboration with laboratories from both Member and Non-Member States and operation shall start in 2006. A summary of the main machine parameters is given in Table 1.1.

1.1 Physics at the LHC

Proton-proton collisions (*pp* collisions) can be subdivided in two classes:

- most interactions due to collisions appear at large distances between incoming protons so that protons interact as a whole with small momentum transfer. This means that particles in final state have small transverse momentum (p_T about 500 MeV) and continue travelling along the beam. These interactions are called minimum-bias events.

- some interactions occur between constituents of incoming protons (hard scattering or 'head on'). These interactions happen at small distances with large momentum transfers that can produce massive particles. Their observed decay products can have large transverse momenta. These events provide more interesting physics. Such an interaction is sketched in Fig. 1.2.

One of the main motivations for the LHC is to find out the origin of particle masses. In the well-established Standard Model, mass is given to particles by the Higgs mechanism. This mechanism includes the existence of the Higgs particle, a boson. If the Higgs boson is not found at other accelerators before the LHC starts operation, the LHC will be able to discover or to exclude a Higgs boson in the range of 110 GeV to 1 TeV.

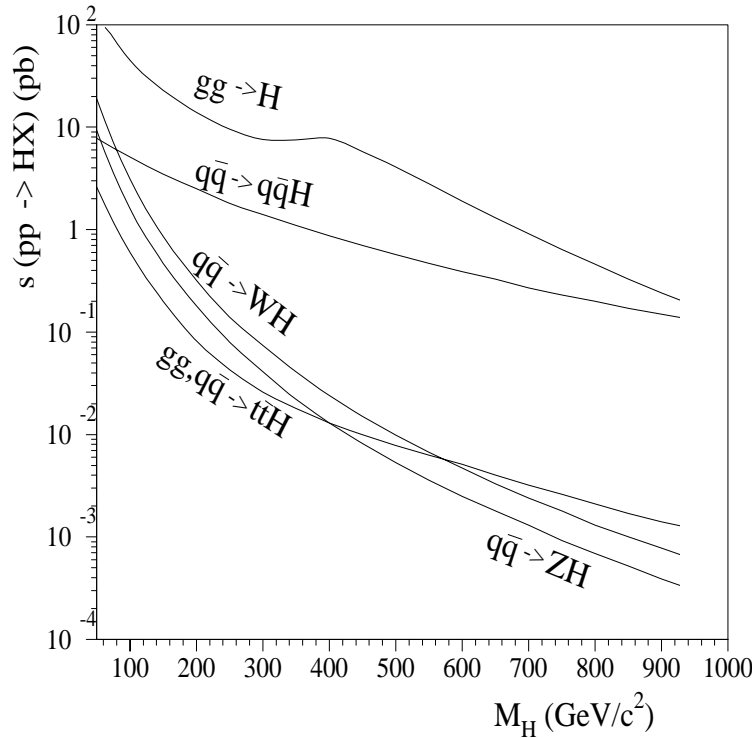The Higgs production cross-section from various processes are shown in Fig. 1.3. The energy

Figure 1.3: *The cross-sections for the Higgs boson production in the LHC as a function of the Higgs mass energy for various Higgs productions [4].*

dependence of various Higgs boson decay channels are shown in Fig. 1.4. Depending on the mass of the Higgs boson, the LHC detectors have to be able to identify the H->$\gamma\gamma$ decay as well as the H->ZZ->*ll ll* (known as 'gold-plated' channel without a large background).

When scaling the energy dependent coupling constants of the electroweak (α_1 and α_2) and strong (α_3) interactions to very high energies, the coupling constants do not unify according to measurement results and the Standard Model. Grand unified theories explain the Standard Model as a low energy approximation. At an energy in the order of 10^{16} GeV, the electromagnetic, weak and strong forces unify. One of these theories is supersymmetry that predicts new particles to be found in the TeV range. The energy scaling of the coupling constants is shown in Fig. 1.5. Supersymmetry relates fermions and bosons by postulating that for each particle p with spin s there exists a SUSY particle $\tilde{p}$ with spin s-1/2 (i.e. q(s=1/2)$\rightarrow$ $\tilde{q}$ (s=0) squarks). The broken supersymmetry at lower energy predicts the existence of at least 5 Higgs bosons (h, H, A, $H^{\pm}$) and in most supersymmetry models also the existence of a stable light supersymmetric particle χ_1^0. The LHC will provide an answer whether supersymmetry particles exist with a mass in the range of 0.1–2 TeV [4].
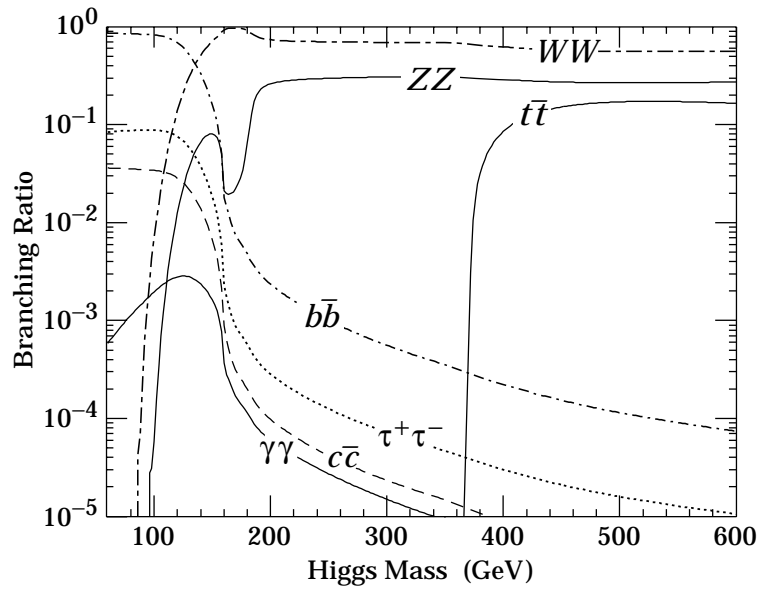
Figure 1.4: *The cross-sections for the Higgs boson decay modes as a function of the Higgs mass [5].*
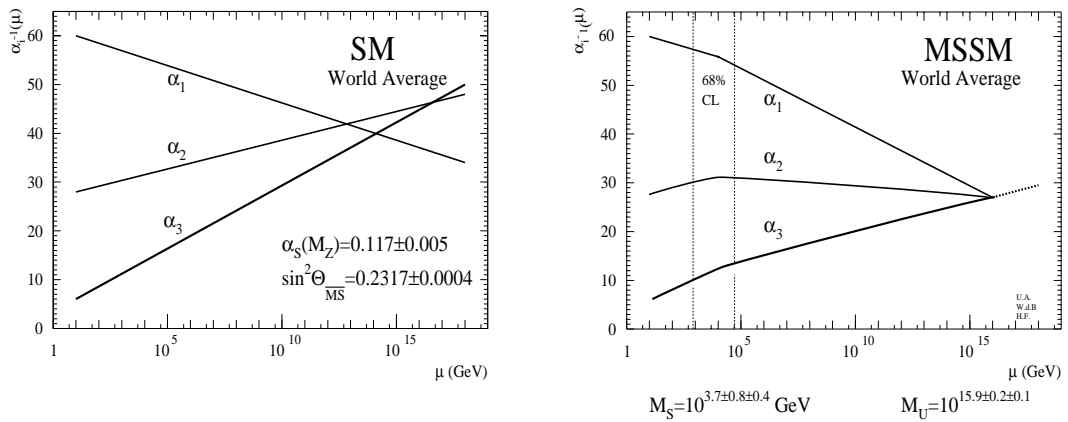

Figure 1.5: *The running coupling constants as function of energy in the Standard Model and the Minimal Supersymmetry Extension of the Standard Model [6].*

Another question that will be addressed by the LHC is whether quarks and leptons are elementary particles as they seem to be today or if they are made up of sub-constituents. The LHC will also allow precise measurements and tests of the Standard Model (i.e. b and top-quark physics) due to the large number of interactions (large statistics).

Four large-scale experiments will perform high energy particle physics research in the LHC. ATLAS and CMS are general purpose experiments located at the interaction points 1 and 5. LHCb covers experiments dedicated to b-quark physics and CP-violation. ALICE is a heavy-ion experiment for quark-gluon plasma studies.

1.2   The Accelerator Layout

The LHC has an 8-fold symmetry with eight arc sections and eight straight sections (see Fig. 1.1). Two counter-rotating proton beams will circulate in separate beam pipes installed in the same magnets ('twin-aperture' magnets, see Fig. 1.6) and cross over at four points with identical path length for each beam. The beams will collide at a small angle in the centre of the four experimental detectors. The other insertions are to be used by systems for the machine operation: beam dump, beam cleaning, RF-cavities (accelerating units), etc. As for all circular accelerators, the arcs consist of a regular cell structure that is repeated many times around the ring.

Dipole magnets are used to deflect the beam whereas quadrupole magnets act as lenses to focus the beam. Different from an optical lens, a magnetic lens focuses in one transverse direction and defocuses in the other transverse direction. In order to obtain a net focusing effect, two quadrupole magnets are needed (similar to the principle of Galileo's telescope). These form the $FODO$-lattice, in which F and D stand for the focusing and defocusing quadrupole. In a circular accelerator the O stands for dipole magnets used to deflect the beam.

Each LHC arc consists of 23 regular cells with six dipole magnets and two quadrupole magnets (see Fig. 1.7). Small dipole magnets are installed to steer the beams. Sextupole, octupole and decapole corrector magnets are located at the ends of the main dipole magnets to correct field errors (see Section 1.3.1). Other quadrupole and sextupole corrector magnets are installed close to the main quadrupole magnets (short straight section) to control beam parameters.

1.3   LHC Magnets

The LHC magnet system contains about 9000 magnets. In order to understand why such a large number and variety of magnets is required, a brief introduction of field calculations [7] and beam dynamics [3] is given; and the various elements of the magnet system and their powering scheme are described.

1.3.1   Field Calculations

The length of a superconducting dipole for a large accelerator (about 10–15 m) is much larger than its aperture (inner diameter of 56 mm) and the current conductors run parallel to the beam over the longest part of the magnet. Although the dipole magnets are bent to follow the beam orbit, the deviation of a straight line is only a few millimetres. The magnetic field can be calculated by analytical functions in a two-dimensional approach, if saturation effects of the iron yoke are disregarded. The situation changes at the coil ends which require the use of numerical methods for the field calculation.
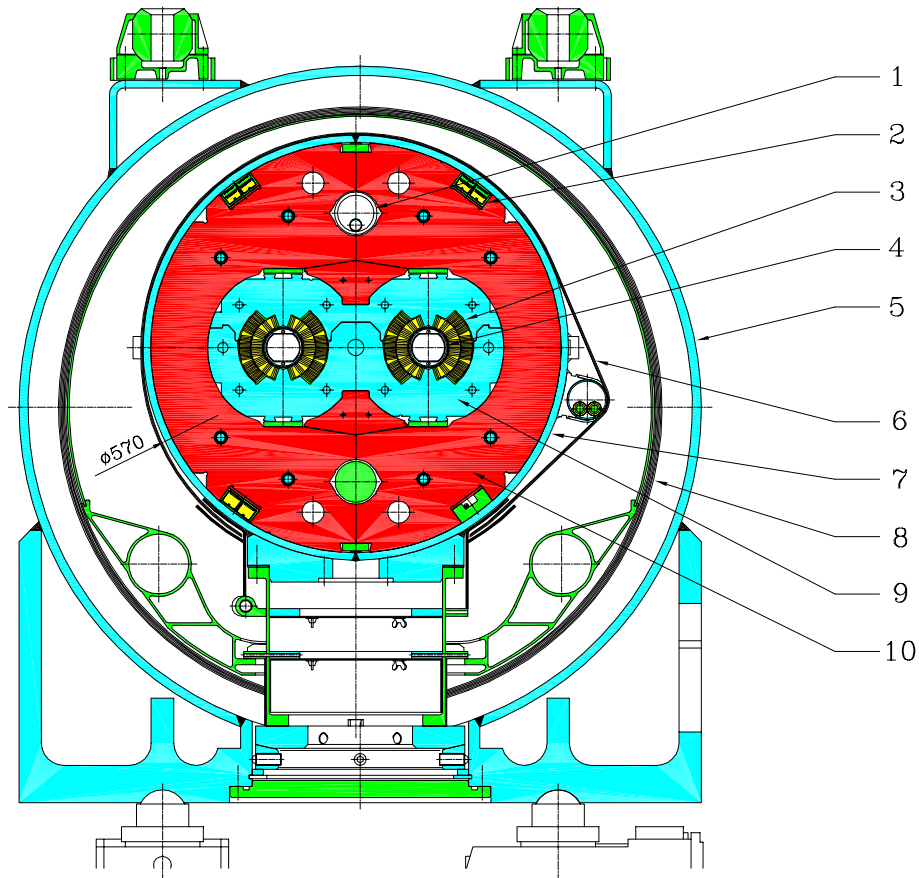
Figure 1.6: *The cross-section of the twin-aperture LHC dipole magnet: 1 = heat exchanger pipe, 2 = superconducting busbars, 3 = superconducting coils, 4 = beam screen, 5 = vacuum vessel, 6 = radiation screen, 7 = shrinking cylinder (He II vessel), 8 = thermal shield (55 to 75 K), 9 = non-magnetic collars, 10 = iron yoke (cold mass at 1.9 K).*
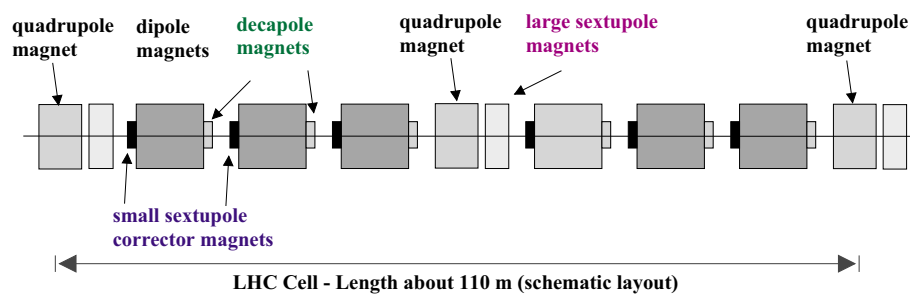

Figure 1.7: *Schematic layout of one LHC cell with dipole, quadrupole and corrector magnets [3].*

In a region free of any currents and magnetised materials, the magnetic field fulfils $\vec{\nabla} \cdot \vec{B} = 0$ and $\vec{\nabla} \times \vec{B} = 0$. This implies that $\vec{B}$ can be expressed in two ways

$$\vec{B} = \vec{\nabla} \times \vec{A}, \qquad \vec{B} = -\vec{\nabla} V \tag{1.2}$$

In case of a two-dimensional problem the vector potential has only z components and the B_x and B_y components can be computed with

$$B_x = -\frac{\partial V}{\partial x} = \frac{\partial A_z}{\partial y}, \qquad B_y = -\frac{\partial V}{\partial y} = -\frac{\partial A_y}{\partial x} \tag{1.3}$$

The complex potential function

$$\tilde{A}(x, y) = A_z(x, y) + iV(x, y) \tag{1.4}$$

is an analytical function of the complex variable $\xi = x + iy$ that can be expanded in a power series at the origin since Eq. 1.3 corresponds to the Cauchy-Riemann conditions which the real and imaginary part of an analytic function have to obey [8]

$$\tilde{A}(x, y) = \sum_{n=0}^{\infty} c_n (x + iy)^n \tag{1.5}$$

Eq. 1.5 converges in the largest circle which contains neither current nor magnetised material. The partial derivatives of Eq. 1.5 yield the multipole expansions for the magnetic field vector.

For two-dimensional magnets it is more convenient to use cylindrical instead of Cartesian coordinates with the z axis being the magnet axis and the two dimensional field given by the coordinates (r, θ).

A line current flowing on the z axis has a purely azimuthal field of the form $B_\theta = \mu_0 I / (2\pi r)$ and the vector potential $A_z(r, \theta) = -\mu_0 I / (2\pi) \ln(r/a)$ with a being an arbitrary length that is cancelled by taking the radial derivative. A current flowing parallel to the z axis with the distance $(r = a, \theta = \phi)$ has the vector potential

$$A_z(r, \theta) = -\frac{\mu_0 I}{2\pi} \ln\left(\frac{R}{a}\right) \tag{1.6}$$

with $R = (a^2 + r^2 - 2ar\cos(\theta - \phi))^{1/2}$ being the distance between the current and the general point $P = (r, \theta)$. For $r < a$ one can write $R^2 = a^2[1 - (r/a)\exp(i(\theta - \phi))][1 - (r/a)\exp(-i(\theta - \phi))]$. Thus, $\ln(R/a)$ can be rewritten as

$$1/2 \ln[1 - (r/a)\exp(i(\theta - \phi))] + 1/2 \ln[1 - (r/a)\exp(-i(\theta - \phi))]$$

Using the Taylor expansion of the logarithm

$$\ln(1 - \xi) = -\sum_{n=1}^{\infty} 1/n \, \xi^n$$

which converges for $|\xi| < 1$, the vector potential and the field components are

$$A_z(r, \theta) = \frac{\mu_0 I}{2\pi} \sum_{n=1}^{\infty} \frac{1}{n} \left(\frac{r}{a}\right)^n \cos[n(\theta - \phi)] \tag{1.7}$$

$$B_\theta(r, \theta) = -\frac{\partial A_z}{\partial r} = -\frac{\mu_0 I}{2\pi a} \sum_{n=1}^{\infty} \frac{1}{n} \left(\frac{r}{a}\right)^{n-1} \cos[n(\theta - \phi)] \tag{1.8}$$

$$B_r(r, \theta) = \frac{1}{r}\frac{\partial A_z}{\partial \theta} = -\frac{\mu_0 I}{2\pi a} \sum_{n=1}^{\infty} \frac{1}{n} \left(\frac{r}{a}\right)^{n-1} \sin[n(\theta - \phi)] \tag{1.9}$$

$$B_z(r, \theta) = 0 \tag{1.10}$$

A single line current produces multipole fields of any order n. A pure multipole field of the order $n=m$ is obtained with the current distribution

$$I(\phi) = I_0 \cos(m\phi) \tag{1.11}$$

The vector potential with the current distribution of Eq. 1.11 is

$$A_z(r, \theta) = \frac{\mu_0 I_0}{2\pi} \sum_{n=1}^{\infty} \frac{1}{n} \left(\frac{r}{a}\right)^2 \int_0^{2\pi} \cos(m\phi)\cos[n(\theta - \phi)]d\phi$$

The integral vanishes unless $n = m$ because of the orthogonality of the trigonometric functions. The field components become

$$B_\theta(r, \theta) = -\frac{\mu_0 I_0}{2a} \left(\frac{r}{a}\right)^{m-1} \cos(m\theta)$$

$$B_r(r, \theta) = -\frac{\mu_0 I_0}{2a} \left(\frac{r}{a}\right)^{m-1} \sin(m\theta) \tag{1.12}$$

The orders $m = 1, 2, 3$ represent dipole, quadrupole and sextupole fields. The fields in Eq. 1.12 are normal multipole fields. Rotating Eq. 1.12 by an angle of $\pi/(2m)$ yields a $\sin(m\phi)$ current distribution and skew multipole fields, e.g. dipole and skew dipole corrector magnets are needed to correct the particle orbit in the horizontal and the vertical plane.

Since current distributions with a $\cos(m\phi)$ dependence are difficult to fabricate with a superconducting cable of constant cross-section, the current distribution is approximated with turns grouped in blocks and positioned in one or several layers (see Fig. 1.8). The quality of such an approximation can be judged from the general multipole expansion

$$B_\theta(r, \theta) = B_{ref} \sum_{n=1}^{\infty} \left(\frac{r}{r_0}\right)^{n-1} [b_n \cos(n\theta) + a_n \sin(n\theta)]$$

$$B_r(r, \theta) = B_{ref} \sum_{n=1}^{\infty} \left(\frac{r}{r_0}\right)^{n-1} [-a_n \cos(n\theta) + b_n \sin(n\theta)] \tag{1.13}$$

Here r_0 is a reference radius and was chosen to be $r_0 = 17$ mm for the LHC field calculations.

Numerical methods are required for the field evaluation in order to take into account the magnetisation of the iron yoke and the coil ends. For the LHC, these calculations are performed with ROXIE [9], which was developed for this purpose at CERN.

1.3.2 Beam Dynamics

When a particle with both zero angle and amplitude travels through a series of perfectly aligned quadrupole magnets without any field errors, the trajectory goes through the centre of each quadrupole magnet. If a magnet is misaligned, the particle is deflected. The magnets in the LHC tunnel will be aligned to about 0.3 mm with respect to a reference line [3]. The resulting deviations of the particle trajectory require corrections with small dipole magnets.
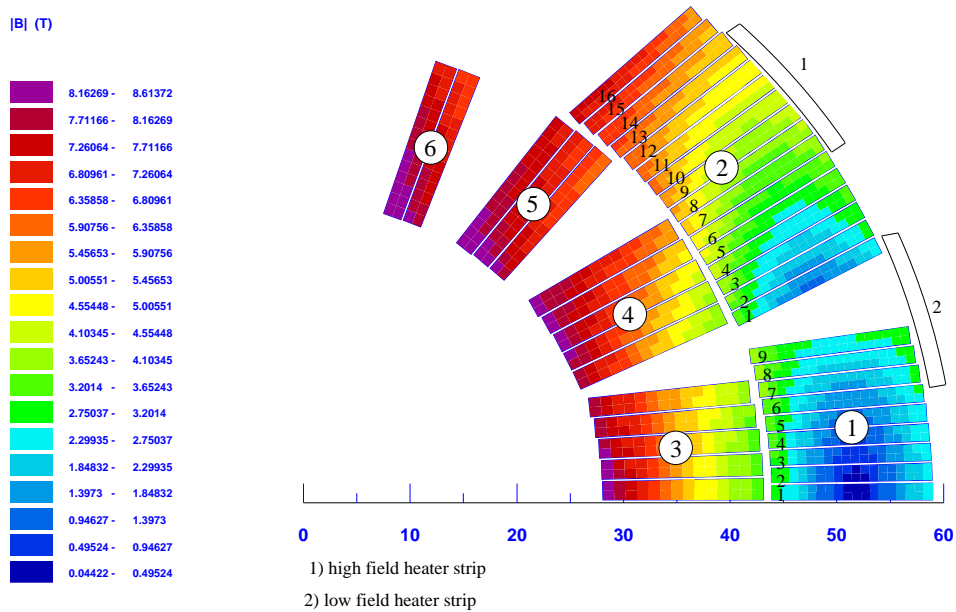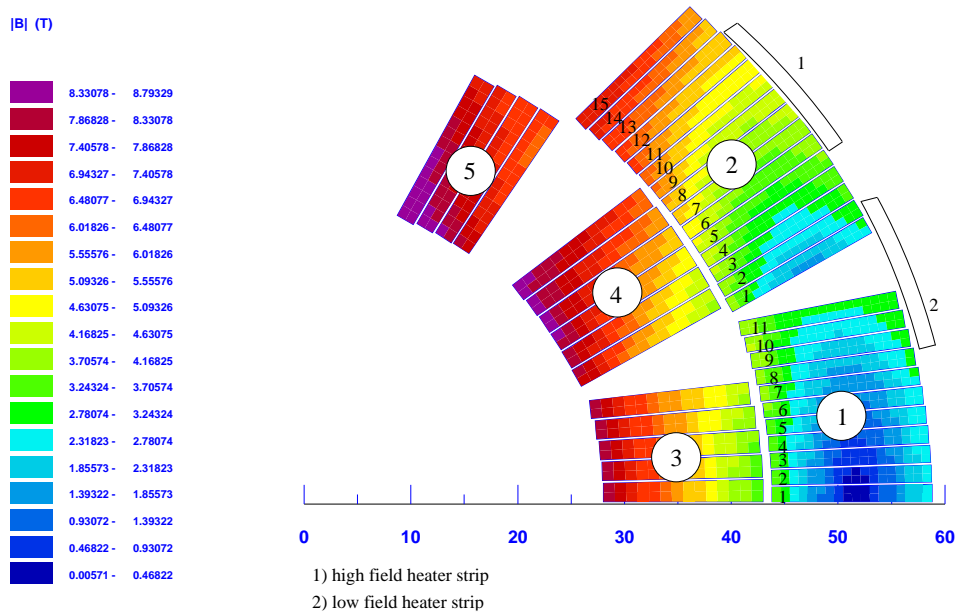
Figure 1.8: *The 2-dimensional cross-section of the LHC dipole: The old five block design (top) and the final six block design (bottom). The blocks are ordered in two layers with one conductor for each layer. The optimisation of the field quality was achieved with the numerical field calculation program ROXIE [9].*

Using a rotating coordinate system, in which the particle travels along s with orthogonal transverse coordinates x and y, the trajectory can be expressed as a harmonic function for each transverse plane, the betatron-function $\beta(s)$. The oscillation of the proton in the vertical plane $y(s)$ is

$$y(s) = const \cdot \sqrt{\beta_y(s)} \cdot \cos(\phi_y(s) - \phi_0) \qquad (1.14)$$

where ϕ is the phase advance of the betatron oscillation. The number of oscillations per turn is called betatron tune (Q_x, Q_y), which is in the order of 60 for the LHC. Particle losses can occur if the condition $l \cdot Q_x + m \cdot Q_y = n$ (l, m, n are integer numbers) is fulfilled as the trajectory becomes unstable. The adjustment of the betatron tune to a level of about 0.001 requires the installation of quadrupole corrector magnets. A skew quadrupole field due to tilted quadrupole magnets or any other imperfections lead to a coupling of the particle oscillations between the two planes. To correct the coupling, skew quadrupole magnets (rotated by 45°) have to be installed in some locations of the LHC lattice.

The beam size is given by $\sigma = \sqrt{\beta\epsilon}$ with β being the amplitude of the betatron-function (see Eq. 1.14) and ϵ being the transverse emittance that corresponds to the phase space covered by the beam. The emittance decreases with increasing energy because of $\epsilon = \epsilon^*\gamma$, $\gamma = E/E_0$ being the energy and ϵ^* being the normalised emittance given by the beam parameters at injection from the pre-accelerators. The maximum beam size is 1.2 mm at injection energy of 450 GeV and 0.3 mm at full energy.

The relative energy spread of the LHC beam is in the order of 10^{-3} at injection and $0.36 \cdot 10^{-3}$ at full energy. The focal length of a quadrupole changes with the energy of the particle. Thus, the energy spread causes a spread of the betatron tune dQ/dE (chromaticity). To limit the betatron tune spread, sextupole magnets are installed close to the main quadrupole magnets (see Fig. 1.7) to correct the chromaticity in both transverse planes. The beam deflection in a dipole magnet changes with the particle energy (dispersion). At the beginning of the arcs, the cells differ from the standard $FODO$-lattice to suppress the dispersion (dispersion suppressor).

The dominating multipole field components in the main bending magnets are the sextupole and decapole field components ($b_3 \approx -11 \cdot 10^{-4}$, $b_5 \approx 1.2 \cdot 10^{-4}$ at injection field level). The multipole field components are compensated with small sextupole, octupole and decapole corrector magnets that are installed at the ends of the main dipole magnets (see Fig. 1.7).

In presence of multipole field components the particle trajectory is no longer a pure betatron oscillation. If the non-linearity exceeds a certain value and the initial particle amplitude is non-zero, the amplitude increases with time and the particle is lost. Particles are tracked through the magnet lattice for 100 s (corresponds to about 10^6 turns) with powerful computers to determine the stability of the particle motion. The initial amplitude for which the trajectory becomes unstable is the dynamic aperture. It is expressed as the ratio of the initial amplitude to the beam size σ and is about 10.

1.3.3 LHC Magnet System

Main Magnets

The LHC main magnets are the dipole magnets to deflect the beam and the quadrupole magnets in the arcs and in the insertions to focus the beam. These magnets are wound with Rutherford type (multistrand) cables (see Section 2.4) insulated with polyimide films.

The subdivision of the LHC into octants reduces the stored magnetic energy per dipole circuit. 154 main dipole magnets are powered in series in each octant. The parameters of the LHC main dipole magnet (MB) are summarised in Table 1.2 for the magnet and in Table 1.3 for the superconducting cables. The energy stored in one dipole magnet is about $7 \cdot 10^6$ J and about $1.1 \cdot 10^9$ J in the circuit.

Magnetic length	14.3 m	Total length	15180 mm
Operating temperature	1.9 K	Stored energy (both apertures)	$7.1 \cdot 10^6$ J
Current at injection (0.45 TeV)	739 A	J_{NbTi} inner layer 7 TeV	1200 A/mm^2
Bending radius	2803.928 m	J_{NbTi} outer layer 7 TeV	1732 A/mm^2
Number of beams per magnet	2	Coil inner diameter	56 mm
Nominal current	11796 A	Coil outer diameter	120.5 mm
Bending angle per magnet	5.1000 mrad	Coil length (incl. end pieces)	14567 mm
Peak field in coil	8.76 T	Number of blocks and layers	6 and 2
Field at injection	0.535 T	Number of turns inner layer	2×15
Field at 7 TeV	8.33 T	Number of turns outer layer	2×26
Inductance per magnet	0.108 H	Cable length for inner layer	433 m
Mass of cold mass	23.8 t	Cable length for outer layer	751 m

Table 1.2: *The main parameters of the LHC dipole magnets.*

The main quadrupole magnets for the LHC are the twin aperture arc quadrupoles (MQ) and insertion quadrupoles (MQM family and the MQY magnets). Some of their parameters are listed in Table 1.4. The arc quadrupole magnets are powered in series of 47 and 51 magnets. The quadrupole magnets in the insertion are powered individually or in series of two.

Corrector Magnets

The corrector magnets of the LHC are small with respect to the main magnets. They are wound with single strand cables and the coils are fully impregnated with epoxy, which reduces the cooling by helium.

In order to achieve the field quality, small sextupole (MCS), octupole (MCO) and decapole (MCD) magnets (spool piece corrector magnets) are installed at the ends of the main dipole magnets to correct multipole field errors. Every aperture of each dipole magnet is equipped with a sextupole corrector coil, whereas only every second dipole magnet will be equipped with octupole and decapole correctors.

The sextupole magnets (MS, MSS) correct the chromaticity and the quadrupole magnets (MQT, MQS, MQTL) compensate coupling between the transverse planes and adjust the betatron tune (see Section 1.3.2). Lattice octupole magnets will be installed to adjust other beam parameters.

About 1000 small dipole magnets (MCB in the arcs and MCBC, MCBR, MCBX, MCBY in the insertions) will be installed to correct the particle trajectory in both transverse planes (see Section 1.3.2), the closed-orbit corrector magnets.

LHC Experimental Insertions

A schematic layout of the insertions for the high luminosity experiments ATLAS and CMS is shown in Fig. 1.9 [3]. At the collision point the two beams with dimensions of about 16 μm are crossing at an angle of about 300 μrad in order to avoid parasitic beam crossings (collisions of

Dipole Cable Inner Layer	
Number of strands	28
Cable width	15.1 mm
Cable mid thickness at 50 MPa	1.9 mm
Keystone angle	1.25^o
Transposition pitch	115 mm
Critical current, 1.9K, 10T	>13750 A
1st insulating Polyimide Layer thickness	0.05 mm
2nd insulation LCI Layer thickness	0.068 mm
Cross section (Cu)	15.33 mm^2
Strand diameter	1.065 mm
Copper to superconductor ratio	>1.6
Filament diameter	7 μm
Number of filaments in strand	8900
Twist pitch of filament after cabling	15 mm
Critical current, 1.9K, 10T	>515 A

Dipole Cable Outer Layer	
Number of strands	36
Cable width	15.1 mm
Cable mid thickness at 50 MPa	1.48 mm
Keystone angle	0.9^o
Transposition pitch	105 mm
Critical current, 1.9K, 9T	>12960 A
1st insulating Polyimide Layer thickness	0.05 mm
2nd insulation LCI Layer thickness	0.068 mm
Cross section (Cu)	12.56 mm^2
Strand diameter	0.825 mm
Copper to superconductor ratio	>1.9
Filament diameter	6 μm
Number of filaments in strand	6520
Twist pitch of filament after cabling	18 mm
Critical current, 1.9K, 9T	>380 A

Table 1.3: *The conductors for the LHC dipole magnet.*

MQM: Quadrupole (3.4 m)
for insertion regions

MQ: Lattice quadrupole in the arc		MQM	
		Nominal gradient	200 T/m
		Nominal current	5390 A
Magnetic length	3.10 m	Magnetic length	3.4 m
Peak field in coil	6.86 T	Peak field in coil	6.3 T
Gradient at injection	14.3 T/m	Aperture separation	194 mm
Nominal gradient	223 T/m	Overall length	3.6 m
Geometrical aperture	56 mm	Overall outer diameter	452 mm
Inductance per magnet	0.0112 H	Coil length	3.55 m
Stored energy (both channels)	$0.784 \cdot 10^6$ J	Coil outer diameter	92.2 mm
Max rating current	13000 A	Number of turns per coil	36
Current density 7 TeV (NbTi)	1789 A/mm^2	Number of coils per aperture	4
Nominal current	11870 A	Stored energy per aperture	219.3 kJ
Current at injection (0.45 TeV)	763 A	Inductance per aperture	15.1 mH
Coil inner diameter	56 mm	Ultimate current	5820 A
Coil outer diameter	118.6 mm	Cable width	8.8 mm
Coil length (incl. end pieces)	3184 mm	Mid thickness	0.84 mm
Number of coil layers	2	Keystone angle	0.91^o
Number of turns per coil (pole)	24	Copper to superconductor ratio	1.75
Cable length per pole	160 m	RRR	80
Total cable length	1280 m	Number of strands	36
Conductor as outer layer MB		Strand diameter	0.48 mm
		Filament diameter	6 μm
		Twist pitch of cable	66 mm
		Critical current density (5T, 4.2 K)	2800 A/mm^2

Table 1.4: *Some parameters for the MQ magnets (left) and the MQM magnets (right).*

neighbouring bunches). An inner triplet of superconducting quadrupole magnets with an aperture of 70 mm is installed at a distance of about 20 m from the collision point. The superconducting quadrupoles must accommodate separated beams at injection, provide high field gradients (up to 250 T/m) and low multipole errors for colliding beams, and sustain considerable heat loads from secondary particles generated in both high luminosity experiments. The collaborations from Japan and the USA will provide the inner triplet quadrupole magnets together with their cryostats. For the high luminosity insertions (with ATLAS and CMS) normal-conducting magnets are used to further separate the beams. For the insertions with ALICE and LHCb superconducting separation dipoles and matching sections share the available space with the injection equipment. When the distance between the beams increases to about 190 mm, a superconducting dipole magnet guides the beams into the separate vacuum chambers of the outer superconducting quadrupole triplet.
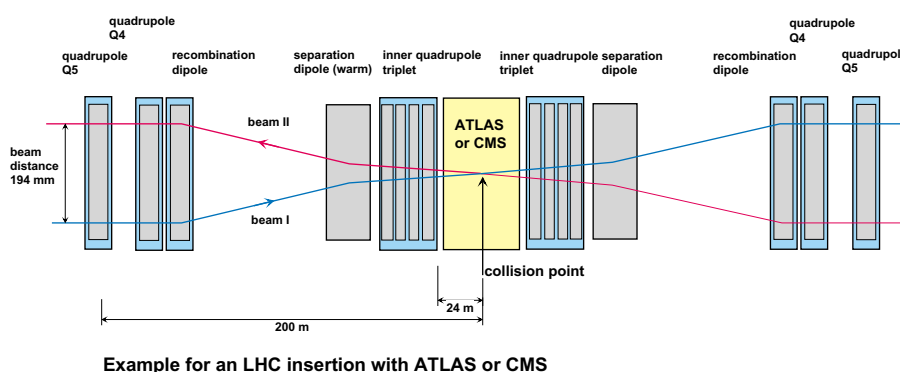

Example for an LHC insertion with ATLAS or CMS

Figure 1.9: *Schematic layout of an insertion for a high luminosity experiment [3].*

1.4   Other Systems

Insertions for Accelerator Operations

Four insertions are used for accelerator operation and machine safety:

Dump insertion: since the energy stored in the proton beam is large (350 MJ), a beam dumping system is required to safely remove the beam from the collider at the end of a physics run, or in case of an equipment failure (for example a quench in a superconducting magnet). Fast kicker magnets deflect the beams into an iron septum magnet, which bends the beam into a 750 m long transport line to an external zone. The beam dimensions increase to reduce the energy density, which allows sending the beam into a dump block made of graphite surrounded with heavier materials.

Two cleaning insertions: proton losses at injection, during the energy ramp and steady losses during collisions might be concentrated near an aperture limitation of the ring. Due to the high intensity of the LHC beams, quenches could be induced by beam losses. A two-stage collimation system to capture such particles will be installed in one of the insertions (betatron cleaning insertion). Since the background radiation is very large in this region, warm magnets are used to increase the beam distance from the standard 190 mm to 224 mm, and to generate the required optical function for collimator installation. A second straight section will be equipped with collimators in order to collect particles with unacceptable energy deviations.

RF insertion: a pair of superconducting dipole magnets increases the separation between the beams to 420 mm. To capture the bunches at injection and to accelerate the beam, a radio-frequency system with superconducting cavities will be installed for each beam. In order to allow for the installation of another experiment, the RF system is placed at a suitable distance from the crossing point.

Cryostats and Cryogenics

Each LHC half cell has a cold mass of about 85 t cooled by approximately 850 litres of superfluid helium. The total cooling power is provided by eight cryoplants located at the four even points of the machine. Each of the refrigeration units provides a cooling power of 2400 W at 1.8 K and is coupled to a 4.5 K refrigerator [10]. The machine cryostats are fed from the cryogenic distribution line (QRL) that runs parallel to the machine cryostats.

The magnets of the arcs and the dispersion suppressors of one octant are housed in a common cryostat of diameter 914 mm, which is about 3 km long with a cold mass of more than 5000 t. The cooldown of the cold mass takes around 24 days.

When a magnet quenches, the generated heat is transferred in the helium bath and increases the helium pressure. The LHC cryostats are equipped with quench relief valves to release the pressure and to recover the helium by a high volume vacuum-insulated recovery line.

The arc cryostat is divided into sectors. Every second short straight section (with the main quadrupole magnet and lattice corrector magnets) is flanked by a cryogenic service module that houses service piping for quench discharge into the helium recovery line and for cooling by pressurised superfluid helium. Various shorter cryostats are located for the magnets in the long insertions (40 cryostats for the entire machine).

Vacuum Systems

Several types of vacuum enclosures are required for the LHC: the insulation vacuum in the cryostat to reduce heat conduction and convection and the beam vacuum to reduce the number of collisions of the beams with gas molecules.

Insulation vacuum systems are used for the magnet cryostat and the cryogenic distribution line. They reduce the heat transfer from the environment at room temperature to the cold parts due to conduction and convection. The working conditions are at a pressure of 10^{-4}–10^{-6} Pa in the temperature operating range of 1.9–293 K.

The vacuum chamber is placed in the bore of the magnet at an operating temperature of 1.9 K. The high intensity proton beam at 7 TeV will emit a power of 0.206 W/m and a photon flux of $9.44 \cdot 10^{16}$ photons $m^{-1} s^{-1}$. This phonton flux and the resistive wall power loss lead to an unacceptable high heat load. In order to reduce the heat load, the vacuum chamber is absorbed on a beam screen that operates in the range of 5–20 K cooled with forced supercritical helium flow. The beam screen is inserted in the magnet cold bore and provides a beam vacuum of 10^{-11} Pa.

1.5   Electrical Engineering Aspects

Risks of Quenches

The superconductivity disappears when the temperature, the applied magnetic field or the current density exceeds material dependent critical values (e.g. 2.3 K at nominal field of 8.33 T in the

dipole magnets).

> **The resistive transition from the superconducting to the normal-conducting state is called a quench (see Chapters 2, 3).**

> **When a quench occurs, the stored magnetic energy can potentially cause severe damage due to excessive voltages and overheating. The consequences can be magnet degradation, a short circuit due to a melted insulation layer or even an open circuit, which occurs when the conductor burns out.**

The quench mechanisms must be studied to design a reliable protection system for the superconducting elements (see Chapter 8). Depending on the type of superconducting elements and on the circuit parameters, the current decays in the range of 0.1–1000 s after the appearance of a quench.

Protection Strategies

The protection of superconducting cables and magnets depends on a reliable quench detection (see Fig. 1.10).
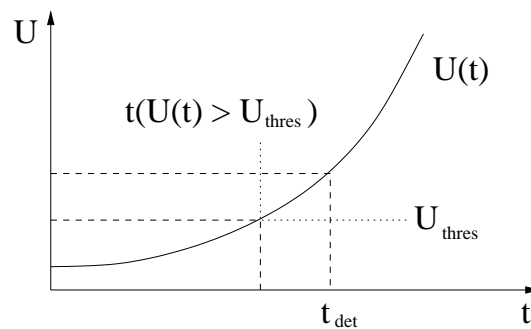

Figure 1.10: *The quench detection principle.*

> **A quench is detected, when the resistive voltage exceeds a predefined threshold for a given time interval (quench validation time Δt_{det}). The quench detection time t_{det} is the time inteval between the end of the quench validation and the start of the quench appearance.**

The quench validation is needed to differ between induced voltage spikes or noise and real quenches. The various quench detection principles are explained in the Sections 5.4 and 8.1.1.

Corrector magnets are designed such that they can withstand the energy deposition of their stored magnetic energy. This magnets are wound with insulated single strand cables made of many superconducting filaments that are embedded in a copper matrix for stabilisation. In these magnets, the normal conducting zone spreads out fast enough to distribute the stored energy in a large fraction of the superconducting structure, which avoids overheating.

> **When several magnets are connected in series, a quenching magnet can be protected by installing a resistor or a diode parallel to each magnet (see Fig. 1.11). The increasing resistance in the magnet causes the current to bypass the quenching magnet and the magnet has only to absorb its own stored energy. A dump resistor can be switched in series with the magnets after quench detection so that the stored energy of the circuit is dissipated into the dump resistor.**

The main magnets are wound with multistrand cables (Rutherford cables). As helium is in direct contact with the individual strands, these cables are more efficiently cooled with helium. The stored magnetic energy in the main magnets is much higher than in corrector magnets. The stronger cooling reduces the natural quench propagation velocity and the stored magnetic energy is distributed over a region of the magnet which is too small to avoid overheating.

Quench heaters are installed along the main magnet coils (see Figs. 1.8 and 1.11). In case of a quench, the heater circuit is fired with a current pulse by a capacitor discharge to provoke a second quench in a large fraction of the magnet. The stored energy spreads out over a larger fraction of the magnet which reduces the temperature at the quench origin (hot spot).

Main magnets connected in series with a string of magnets are additionally protected with diodes that are mounted parallel to the diode. Similar to the protection with parallel resistors for corrector magnets, the current bypasses the quenching magnet when the turn-on voltage of the parallel diode (6–8 V at 1.9 K) is reached.
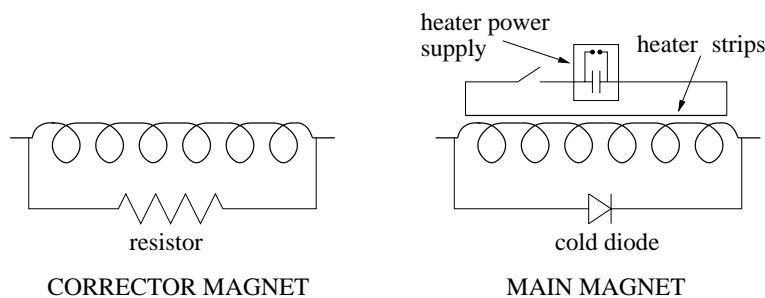
Figure 1.11: *Schematic view of the protection principle with a parallel resistor for corrector magnets and a parallel diode for main magnets connected in series with a string of magnets.*

Various Types of Quenches

The superconducting cables are exposed to a variety of disturbances which may heat the coil locally beyond the critical temperature, i.e. wire motion during excitation of the magnet, cracking of the epoxy insulation or beam losses. Different types of mechanisms can cause a quench in superconducting cables and magnets:

- *training quenches*
  In order to avoid movements of a winding that can cause a quench, the magnet coils are prestressed with collars at ambient temperature such that a stress remains at cold and the windings cannot move. Otherwise the Lorentz force that is built up while increasing the current (current ramp) causes a few turns to move towards a more stable position, which can provoke a quench. If the prestress is too high, the critical current is reduced because of the impact of the critical parameters of the superconductor on the applied strain [8, 11]. In some places the cable can still move depending on the quality of the coil winding. When the current is increased in the magnet a movement appears at a position with little mechanical stability. The mechanism is known as a training quench. During the next magnet excitation a quench can start at another location. After several excitations the quench current reaches a plateau. The number of quenches needed to reach this plateau and the difference between the reached quench current and the critical current is a measure for the quality of the magnet.

- *beam induced quenches*
  In an accelerator, quenches in superconducting magnets can occur because of beam losses which would lead to an energy deposition in the superconductor high enough to exceed the critical temperature.

- *heater provoked quenches*
  Quenches can also be provoked by the protection system when quench heaters are installed. A failure in the detection system could lead to unwanted firing of the heaters.

- *cryogenic failure*
  If the cryogenic system fails, the temperature increases which can provoke quenches.

Busbars

The superconducting magnets are connected in series with highly copper stabilised superconducting cables (busbars). The ratio of the copper fraction to the superconductor content is usually greater than 10 to reduce the probability of a quench originating in the busbars. The copper stabilisation is possible for busbars as more space is available than in magnet coils. It is required to avoid overheating after a quench as the busbars are only protected by dump resistors for energy extraction and not by parallel elements as for magnets. For the LHC superconducting circuits, several types of busbars are foreseen:

- *main busbars*
  For the main dipole magnets and the arc quadrupoles, the busbars will carry a current up to 13 kA. These busbar are made with the superconducting cable used to wind the outer layer of the dipole magnets and the arc quadrupoles. The cable is soldered in a copper housing (see Fig. 1.12). The copper stabilisation for the dipole circuits is in the order of $250\,\mathrm{mm}^2$ and for the quadrupole circuits in the order of $160\,\mathrm{mm}^2$.
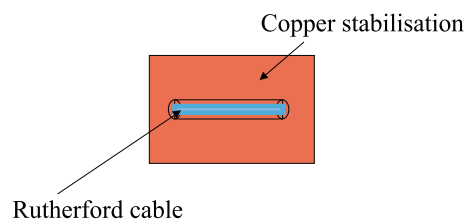

Figure 1.12: *Schematic diagram of the busbar cross-section for the LHC main dipole and arc quadrupole magnets.*

- *insertion quadrupole busbars*
  For the 6 kA insertion quadrupoles (MQM family and MQY magnets) a special busbar has been developed. It contains copper stabilised superconducting strands twisted together with pure copper strands for additional stabilisation (copper to superconductor ratio is higher than 10).

- *corrector busbars*
  For the 600 A corrector magnets (multipole correctors and lattice correctors) two types of busbar cables will be installed in the cryostat. The busbar cable is a strand with a large copper content for stabilisation of about $2\,\mathrm{mm}^2$.

Chapter 2

Superconductors and Cooling

Superconductivity is used in many applications and a large variety of superconductors have been developed. While the theoretical understanding of classical superconductors is very advanced, attempts are being made to increase the critical current density and their stability. A major subject in today's material science research is the development of new applications, e.g. for high temperature superconductors. Liquid helium is the only adequate cooling medium that retains superconductivity of hard superconductors in accelerator magnets at present. To reach the desired magnetic field strength in the LHC magnets made of niobium-titanium (NbTi) requires a temperature lower than the liquefaction temperature of helium, therefore superfluid helium will be used for more efficient cooling.

After a short historical overview, the main characteristics and the range of existing superconductors are summarised, which ends with the presentation of the material properties of hard type 2 superconductors such as niobium-titanium. The theoretical descriptions of type I and II superconductors, namely the London equations, the Ginzburg-Landau and the BCS theory, are briefly outlined. The mechanical stability of superconductors and the realisation of hard superconductors for use in magnets are described, followed by an introduction to the quench process. The temperature dependences of helium material properties and the main features of superfluidity are presented. Finally, the different cooling mechanisms and the limitations of heat transfer into helium are summarised.

2.1   Historical Overview

In 1908 Kamerlingh Onnes succeeded in liquefying helium [12]. While investigating the conductivity of metals at low temperatures, he discovered superconductivity in 1911 [13]. At the boiling temperature of liquid helium Kammerlingh Onnes found that the resistance of a mercury sample dropped to an unmeasurable value and called this unexpected phenomenon 'superconductivity', which occurs below the critical temperature T_c. Superconductivity was encountered in many metals but not in good normal-conducting materials such as copper, which becomes superconducting only at very high pressures.

Meissner and Ochsenfeld discovered in 1933 that a superconductor expels a weak magnetic field below T_c while strong fields can break down superconductivity [14]. This effect was not explainable by means of Maxwell equations and was found to be a quantum phenomenon. H. and F. London developed a phenomenological explanation of the Meissner-Ochsenfeld effect in 1935 [15] which was confirmed by the theoretical description of Bardeen, Cooper and Schrieffer

in 1957, and is called the BCS theory [16]. The BCS theory explains superconductivity as a quantum-mechanical effect on a macroscopic scale and is based on the assumption that the super-current is carried by pairs of electrons of opposite momenta and spins, the Cooper pairs. All pairs occupy a single quantum state, the BCS ground state, whose energy is separated from the single-electron states by an energy gap which can be related to the critical temperature.

Contrary to superconductors made of a pure element like lead or mercury (type I superconductors), superconducting alloys like niobium-titanium form a different class, the type II superconductors. These superconductors have two critical fields and temperatures. The Ginzburg-Landau theory, formed in 1950 [17], provides a phenomenological explanation for the distinction of the two types and can be described as a limiting case of the BCS theory [18].

Josephson investigated quantum-mechanical tunnelling between two superconductors that are separated by a normal conducting material in 1962 [19], which are known as Josephson junctions and allow the measurement of very small magnetic fields.

The development of 'hard superconductors' mainly made of the type II superconductor niobium-titanium allowed the construction of magnets with strong fields (>1 tesla) for applications in research, medicine, particle detectors and accelerators.

In 1986 Bednorz and Müller discovered superconductivity in ceramic copper oxides at much higher temperatures with respect to type I and II superconductors [20]. Some of the high temperature superconductors can operate in liquid nitrogen. Although a large effort has been made in advancing the development of high temperature superconductors, hard type II superconductors remain at present the leading materials for the construction of large superconducting installations.

2.2 Main Characteristics

A detailed overview of the main characteristics of superconductivity can be found in the text books by Buckel [21] and Tilley [22]. A brief introduction is given here based on the lectures and books by Schmüser [7, 8] and Wilson [11, 23].

2.2.1 Meissner-Ochsenfeld Effect and London Equations

When a superconducting cylinder is exposed to an increasing magnetic field from zero to a finite value B, a surface current is induced whose magnetic field cancels the applied field in the interior according to Lenz's law. Since the resistance vanishes in a superconductor, the surface current remains constant when the applied field is kept constant and the superconductor acts as a perfect diamagnetic material below the critical temperature T_c. When the external field rises while the temperature is higher than T_c, eddy currents are induced, which decay quickly because of the resistance, and the applied magnetic field penetrates the interior of the cylinder. If the temperature is decreased below T_c, a surface current is spontaneously created to expel the magnetic field from the interior of the cylinder. This effect is known as the Meissner-Ochsenfeld effect [14]. The transition between normal-conducting and superconducting phases is comparable to different thermodynamic phases. H. and F. London achieved the first theoretical explanation by assuming that the super-current is carried by some conduction electrons in the metal without friction, the 'super-electrons'. Their motion in an electric field is

$$m\frac{\partial \vec{v}}{\partial t} = -e\vec{E} \qquad (2.1)$$

The super-current density is

$$\vec{J}_s = -en_s\vec{v} \tag{2.2}$$

where n_s is the super-electron density. This yields the first London equation

$$\frac{\partial \vec{J}_s}{\partial t} = \frac{n_s e^2}{m}\vec{E} \tag{2.3}$$

Using the induction law of Maxwell's equations $\vec{\nabla} \times \vec{E} = -\partial\vec{B}/\partial t$ results in

$$\frac{\partial}{\partial t}\left(\frac{m}{n_s e^2}\vec{\nabla} \times \vec{J}_s + \vec{B}\right) = 0 \tag{2.4}$$

H. and F. London assumed that the quantity in the brackets vanishes, which gives the second London equation

$$\vec{\nabla} \times \vec{J}_s = -\frac{n_s e^2}{m}\vec{B} \tag{2.5}$$

This equation is only correct for superconductors. Combining the second London equation with the fourth Maxwell equation $\vec{\nabla} \times \vec{B} = \mu_0\vec{J}$ the following equation is achieved for the magnetic field in a superconductor

$$\Delta\vec{B} - \frac{\mu_0 n_s e^2}{m}\vec{B} = 0 \tag{2.6}$$

For a magnetic field parallel to the surface of the superconductor, this changes to

$$\frac{d^2 B_y}{dx^2} - \frac{1}{\lambda_L}B_y = 0 \tag{2.7}$$

with λ_L being the London penetration depth

$$\lambda_L = \sqrt{\frac{m}{\mu_0 n_s e^2}} \tag{2.8}$$

The magnetic field does not stop abruptly at the superconductor surface but penetrates with exponential attenuation into the material. In the BCS theory, the super-electrons have to be replaced by Cooper pairs, which does not have an impact on the London equations as the mass and electric charge double but the density halves.

2.2.2 The Superconducting Phase

The transition from normal-conducting to superconducting below T_c is described with the thermodynamic quantity, the free energy

$$F = U - T \cdot S \tag{2.9}$$

with F being the free energy, U the internal energy and S the entropy. The superconducting state has a lower free energy than the normal states and thus, the transition to the superconducting state implies a gain in energy $\Delta E = F_{normal} - F_{super}$. From the BCS theory point of view the lower entropy of the superconducting states is due to the condensation of a small fraction of valence electrons into Cooper pairs and the pairing and collection into a single quantum state.

The magnetisation of a type I superconductor is $M(B) = -B/\mu_0$. Thus, the potential energy per unit volume ΔV due to the application of a magnetic field to the superconductor is

$$E_{pot} = -\int_0^B M(B')dB' = \frac{B^2}{2\mu_0} \tag{2.10}$$

Applying a magnetic field to a superconductor increases the free energy

$$F_{super}(B) = F_{super}(0) + \frac{B^2}{2\mu_0}\Delta V \tag{2.11}$$

The critical magnetic field is reached when the increase in potential energy is equal to the energy difference between the normal and the superconducting state

$$B_c = (F_{normal} - F_{super}(0))\frac{2\mu_0}{\Delta V} \tag{2.12}$$

2.2.3 Type I and Type II Superconductors

Type I superconductors made of pure metals would not allow the construction of superconducting magnets as the critical magnetic field is very small. Metal alloys and the element niobium are type II superconductors which have two critical fields B_{c1} and B_{c2}. Their magnetisation curve exhibits a more complex dependence on the applied magnetic field (see Fig. 2.1) Below the critical field
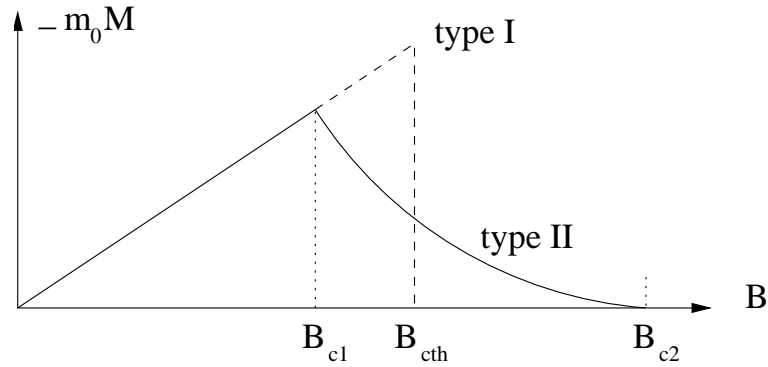

Figure 2.1: *The dependence of the magnetisation of a type II superconductor as function of the applied magnetic field.*

B_{c1}, a type II superconductor is in the Meissner phase with complete exclusion of the field from the interior like a type I superconductor. In between B_{c1} and B_{c2} the substance enters the mixed phase in which part of the magnetic flux penetrates the bulk of the sample. Above B_{c2} the material is normal-conducting.

At a boundary between a normal-conductor and a superconductor, the Cooper pair density does not rise abruptly from zero to its value in the bulk but smoothly over a finite length ξ, the coherence length (see Fig. 2.2). The difference $F_{normal} - F_{super}(0)$ can be interpreted as the Cooper pair condensation energy, which defines the thermodynamic critical field B_{cth} with $B_{cth} = B_c$ for type I superconductors and $B_{c1} < B_{cth} < B_{c2}$ for type II superconductors. Applying B_{cth} per unit area parallel to the surface of a conductor, the field penetrates a depth λ_L which corresponds to an
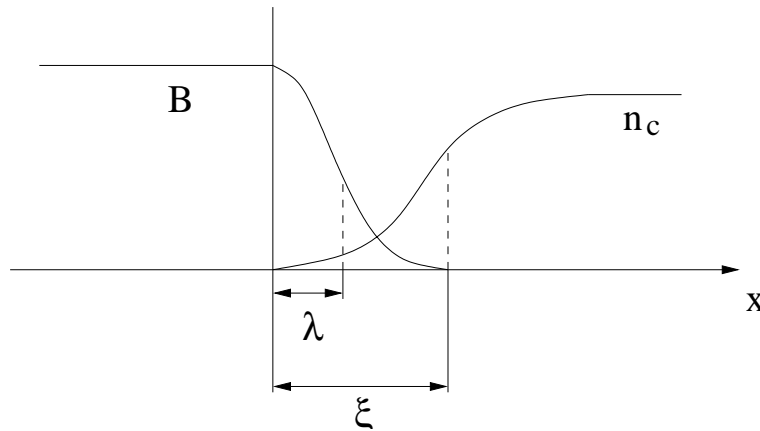
Figure 2.2: *The exponential drop of the magnetic field and the rise of the Cooper-pair density at a boundary between a normal conductor and a superconductor.*

energy gain $\Delta E_{magn} = B_{cth}^2/(2\mu_0) \cdot \lambda_L$. On the other hand the coherence length needed to raise the density of the Cooper pair corresponds to a loss in energy $\Delta E_{cond} = B_{cth}^2/(2\mu_0) \cdot \xi$. A net energy gain is given if $\lambda_L > \xi$. A more refined treatment is given by the Ginzburg-Landau theory [17]. The ratio of the London penetration length and the coherence length is called the Ginzburg-Landau parameter

$$\kappa = \lambda_L/\xi. \tag{2.13}$$

The field penetrates in a type II superconductor in flux tubes that arrange themselves in a triangular pattern. The core of a flux tube is normal-conducting.

The criterion to distinguish for type I or type II superconductivity is then

$$\begin{aligned} \text{type I:} &\quad \kappa < 1/\sqrt{2} \\ \text{type II:} &\quad \kappa \geq 1/\sqrt{2} \end{aligned}$$

The coherence length ξ is proportional to the mean free path of the conduction electrons in the metal and is generally much shorter in alloys than in pure metals. For that reason alloys are always type II conductors. The upper critical field is given by $B_{c2} = \sqrt{2}\kappa B_{cth}$. No simple expressions exists for the lower critical field. In the limiting case $\kappa \gg 1$ it is $B_{c1} = 1/2\kappa \cdot (\ln\kappa + 0.08) \cdot B_{cth}$.

2.2.4   Introduction of the BCS Theory

The main feature of electrical and thermal conduction in metals can be described with the model of the free electron gas that treats electrons as independent and non-interacting particles. They are placed on energy levels computed by solving the Schrödinger equation. The Coulomb attraction of the positive ions in the regular crystal lattice is represented in the Schrödinger equation by a potential well with a flat bottom, the periodic structure is neglected. The filling of the energy levels complies with Pauli's exclusion principle which means there are no more than two electrons of opposite spin per energy level. This principle leads to the application of the Fermi-Dirac statistics for the free electron gas. At the limit $T \to 0\,\mathrm{K}$ all energy levels up to the Fermi energy $E_f = \hbar/2m(3\pi^2 n_0)^{(2/3)}$ are filled (with n_0 being the conduction electron density and m being the electron mass).

One can assume that the origin of Ohmic resistance is due to collisions of free travelling electrons with positive ions. Treating electrons as matter waves and solving the Schrödinger equation shows that no resistance would occur in a perfect lattice at 0 K. Nevertheless the Ohmic resistance is caused by collisions coming from impurities, lattice defects and deviations of the metal ions due to thermal oscillations. The third effect dominates at room temperature giving rise to a resistivity that is roughly proportional to T, whereas the first two effects result in a residual resistivity at low temperature $T < 20\,\mathrm{K}$.

An important parameter for the stabilisation of superconductors with copper is the ratio of the resistivity at room temperature and the residual resistance at low temperature the $Ratio$ of the $Residual$ $Resistivity$ (RRR) value

$$RRR = \frac{\rho(300\,K)}{\rho(10\,K)} \tag{2.14}$$

RRR values for the copper matrix of the LHC cables wound in magnets are about 70–150.

The vanishing resistance in a superconductor can be explained with the help of Cooper pairs. In the case $T \rightarrow 0\,\mathrm{K}$, electrons fill all energy levels up to the Fermi energy E_f with maximum momentum p_f. Cooper pairs are formed by two electrons with opposite spin and momentum $\vec{p} = \hbar\vec{k}$. Cooper showed in 1956 that the electrons form a bound system with an energy less than twice the Fermi energy $E_{pair} < 2E_f$. The attraction force comes from a dynamic lattice polarisation, which was first suggested by Fröhlich and, independently, by Bardeen. The first electron flies through the lattice and attracts the positive ions. The shortest response time of the ions is the highest possible lattice vibration frequency, the Debye frequency ω_D. This lattice deformation attracts the second electron because of the accumulation of positive charges. If the energy of the added electrons is E_1 with $E_f < E_1 < E_f + \hbar\omega_D$ the solution of the Schrödinger equation shows that the energy difference $\delta E = 2E_f - E_{pair}$ is given by

$$\delta E = 2\hbar\omega_D \exp\left(-\frac{2}{V_0 N(E_f)}\right) \tag{2.15}$$

with $N(E_f)$ being the density of single-electron states at the Fermi energy and $V_0 N(E_f) \ll 1$ being the potential of the weak attraction force. The quanta of the lattice vibration are the phonons with maximum energy $\hbar\omega_D \approx 0.01$–$0.02\,\mathrm{eV}$, which indicates that only a small fraction of the electrons in the energy shell $\hbar\omega_D$ around the Fermi energy can be paired. Since the electrons of the Cooper pairs have opposite momentum due to the Pauli exclusion principle, all pairs act as Bosons having the momentum $\vec{P} = 0$ and occupy the same quantum state, the BCS ground state. Unlike other Bosons, Cooper pairs are extended objects and no excited state exists since an excitation is equivalent to breaking them up into single electrons. The BCS ground state can be described by a macroscopic wave function Ψ and the ground state energy that is separated from the energy levels of unpaired electrons by an energy gap Δ

$$\Delta(0\,K) = 2\hbar\omega_D \exp\left(-\frac{1}{V_0 N(E_f)}\right) \tag{2.16}$$

An energy of 2Δ is needed to break up a pair. Eq. 2.16 is a non-perturbative result as the unknown potential V_0 cannot be derived with Taylor series although it is assumed to be weak. The critical temperature T_c is given by the similar expression

$$k_B T_c = 1.14\hbar\omega_D \exp\left(-\frac{1}{V_0 N(E_f)}\right) \tag{2.17}$$

with $k_B = 8.625 \cdot 10^{-5} eV/K$ being the Boltzmann constant. Combining Eq. 2.16 with Eq. 2.17 results in the prediction

$$\Delta(0\,K) = 1.76 k_B T_c \tag{2.18}$$

which is fully accomplished in type I superconductors.

The vanishing resistance of the superconductor can be explained with the energy gap. Applying an electric field $\vec{E}_0$ for δt results in a momentum increase for both electrons of a Cooper pair and the resulting momentum becomes $\vec{P} = \hbar\vec{K} = -2e\vec{E}_0\delta t$. This coherent motion is associated with a super-current density $\vec{J}_s = -n_c\frac{e\hbar}{m}\vec{K}$, with n_c being the Cooper-pair density. The wave function simply changes by a phase factor so that all equations of the BCS theory remain valid. The increased momentum results in an energy increase $\delta E_{pair} \approx p_f P/m$ of the Cooper pairs. As mentioned above the resistivity is due to scattering processes of the single conduction electrons. Cooper pairs do not scatter as long as the energy increase given by the applied field is less than the energy gap $2\Delta - \delta E_{pair} > 0$. This leads to the concept of the critical current density J_c that is given by

$$J_s \ll J_c(T) \approx 2en_c\Delta(T)/p_f \tag{2.19}$$

Coupled to the existence of J_c is the existence of a critical magnetic field. The current flows in a surface layer of thickness λ_L in a type I superconductor. The critical magnetic field $B_c(T)$ is related to the critical current density J_c by

$$B_c(T) = \mu_0\lambda_L J_c(T) \approx \mu_0\lambda_L 2en_c\Delta(T)/p_f \tag{2.20}$$

2.2.5 Quantisation of Magnetic Flux

A type I superconductor can trap the magnetic flux when a magnetic field is applied to the sample at $T > T_c$ before cooling down. The London and the BCS theory predict that the trapped magnetic flux is quantised $\Phi_{mag} = n\Phi_0$ with n being a natural number and

$$\Phi_0 = \frac{\pi\hbar}{e} \tag{2.21}$$

This can be understood in the wave picture of the Cooper pairs. The magnetic flux is given by $\Phi_{mag} = \oint \vec{A} \cdot \vec{ds}$ with $\vec{A}$ being the vector potential. The Cooper-pair wave function can be written as $\Psi = \sqrt{n_c}\exp(i\phi)$. The phase $\phi = \phi(s)$ has to change by multiple 2π when going once around a circular path in the bulk of the superconductor as Ψ is a single-valued function

$$\oint \frac{d\phi}{ds}ds = n \cdot 2\pi \tag{2.22}$$

This means that the circumference is an integer number of the wave lengths. When moving by a distance $\Delta\vec{x}$ the presence of the vector potential adds a phase shift $\Delta\phi = -e/\hbar\vec{A}\Delta\vec{x}$ for an electron, which is known as the Aharonov-Bohm effect after the theoreticians who predicted this phenomenon [24]. As no current is allowed in the bulk of the superconductor, $d\phi/ds \cdot ds = (2e/\hbar) \cdot \vec{A} \cdot \vec{ds}$ for the Cooper pairs. Thus, the magnetic flux enclosed by the circular path is

$$\Phi_{mag} = \oint \vec{A} \cdot \vec{ds} = \frac{\hbar}{2e} \cdot 2\pi \cdot n = n \cdot \Phi_0 \tag{2.23}$$
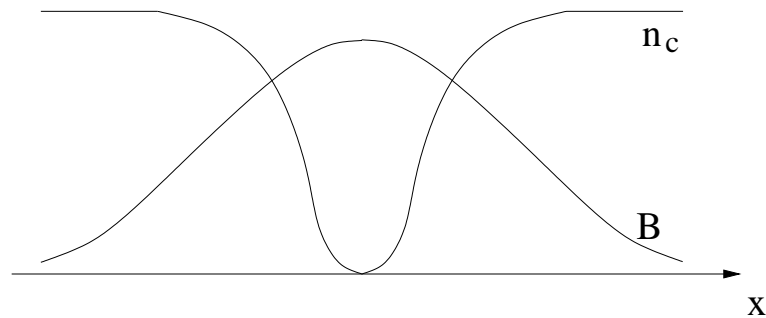
Figure 2.3: *Schematic cross-section of a fluxoid.*

In a type II superconductor the magnetic field penetrates in the form of flux tubes or fluxoids, each containing a single elementary quantum Φ_0. The fluxoids arrange themselves in a triangular pattern to minimise the potential energy related to the mutual repulsion of the flux tubes (see Fig. 2.3). The magnetic field lines are surrounded by a super-current vortex. The Cooper pair density drops to zero at the centre of the vortex, meaning that the core of a flux tube is normal-conducting. Since the area occupied by a fluxoid is roughly given by $\pi \xi^2$ with ξ being the coherence length, the upper critical field B_{c2} can be estimated by the condition that the fluxoids start touching each other $B_{c2} \approx \Phi_0/(2\pi \xi^2)$. Essmann and Träuble [25] experimentally verified the existence of fluxoids in 1967, which were predicted by Abrikosov [26].

2.3 Superconducting Materials

In order to use superconducting cables for the construction of accelerator magnets, the superconductor must be able to carry a large current in the presence of a magnetic field in the range of 5–10 tesla. Type I superconductors are ruled out because their critical field is less than a few tenths of a tesla. Type II superconductors appear appropriate because of their large upper critical field and of high currents being permitted to flow in the bulk material. But these conductors have a problem called flux flow resistance. A current that flows through an ideal type II superconductor, which is exposed to a magnetic field, generates heat since the fluxoids move perpendicular to the current and to the field due to the Lorentz force $\vec{F} = \vec{J} \times \vec{B}$. This is a viscous motion with $\vec{v} \propto \vec{F}$ that leads to the heat generation.

Although the current itself flows without dissipation, the superconductor acts as an Ohmic resistance. The moving field is equivalent to an electric field $\vec{E}_{equiv} = 1/c^2 \vec{B} \times \vec{v}$ and $\vec{E}_{equiv}$ is parallel to $\vec{J}$.

2.3.1 Hard Superconductors

Flux motion has to be inhibited to obtain useful wires for magnet coils. The standard method is to capture them at pinning centres that are defects or impurities in the regular crystal lattice.

The most important pinning centres in niobium-titanium are normal-conducting titanium enrichments that are called 'precipitates' in the α phase [11]. The size of these pinning centres is in the range of the average fluxoid spacing (10 nm range).

Type I or ideal type II conductors have a reversible response to an external magnetic field B_e. They act as a perfect diamagnetic material and their magnetisation M is $M(B_e) = -B_e/\mu_o$ for $0 < B_e < B_c$. A hard superconductor is only reversible if $B_e < B_{c1}$, otherwise magnetic flux enters the sample and is captured at pinning centres. When the field is reduced again these flux tubes remain bound and the specimen keeps a frozen-in magnetisation even for a vanishing external field. One has to invert the field polarity to achieve zero magnetisation M=0. The starting point $B_e = 0$, $M = 0$ can only be reached by warming up the specimen followed by cooling down again. This is similar to the hysteresis in iron but with an opposite sign (see Fig. 2.4). Although pinning
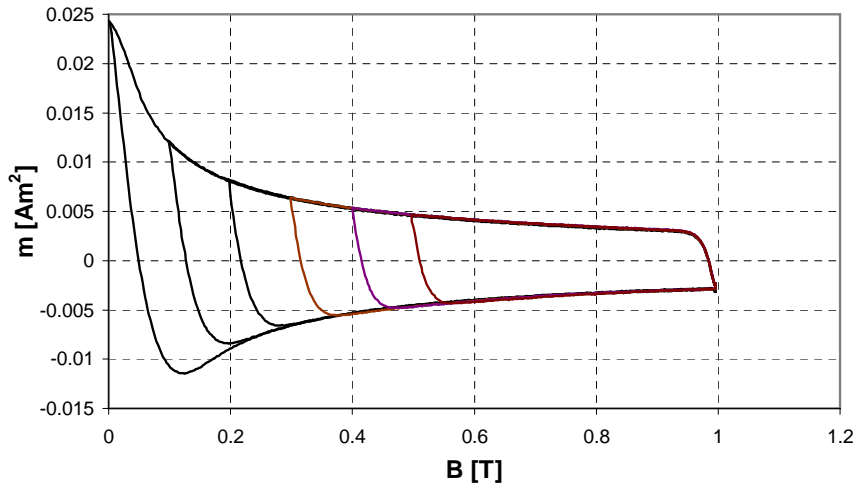
Figure 2.4: *Hysteresis example of a superconducting cable used to wind the inner layer of the LHC dipole magnets [27].*

centres prevent flux flow some flux creep effects remain even at low temperatures such as 4 K. The experimental observation of the flux creep effect showed that the critical current density decays with a logarithmic dependence on the time [28]. The theoretical explanation has been found by Anderson in 1962 [29]. The pinning centres are represented by potential wells of average depth U_0 and width a capturing an average flux $n\Phi_0$. The probability P that a flux leaves a potential well at zero current is $P_0 \propto \exp(-U_0/(k_B T))$. When the superconductor carries a current density J, the potential acquires a slope proportional to the driving force density. This reduces the effective potential well depth to $U = U_0 - \Delta U$ with $\Delta U \approx n\Phi_0 Jal$, l being the length of the flux bundle. The probability increases to $P = P_0 \exp(\Delta U/(k_B T))$. In presence of an external magnetic field B_e the internal field B_{int} is slightly larger by $\mu_0 J_c w$ with w being the conductor thickness. If a bundle of flux is released from its well, it will leave the material thus creating space for some magnetic flux from the bore to migrate into the conductor and refill the well. As a consequence the internal field decreases and with it the critical current density with its time derivative being proportional to the probability P for flux escape. The solution of this differential equation is

$$J_c(t) = J_c(0) - \frac{k_B T}{n\Phi_0 al} \ln t \qquad (2.24)$$

The Critical Surface

Hard superconductors are characterised by a critical current density as a function of applied magnetic field and temperature. The relation of the three quantities is known as the critical surface, which is shown in Fig. 2.5 for the most important conductor used in magnets, niobium-titanium NbTi. Due to flux creep the resistivity of hard superconductors does not completely vanish. The
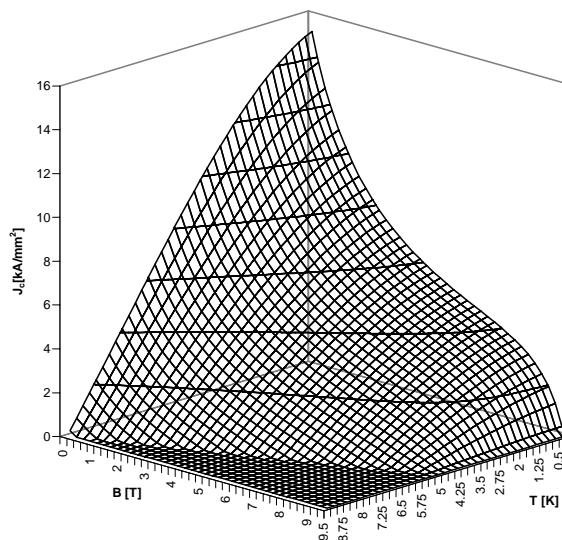

Figure 2.5: *The critical surface for the NbTi superconductor.*

critical current density for a given set of T and B is usually defined by the criterion that the resistivity is $\rho = \rho_c = 10^{-14}\,\Omega\text{m}$. The resistivity at this point is a very steep function of the current density which can be parametrised as

$$\rho(J) = \rho_c \left(\frac{J}{J_c}\right)^n \tag{2.25}$$

The quantity n is a quality index and can be as large as 50.

Critical-state Model

Since the resistivity of a hard superconductor is almost a step function, Bean proposed the critical state model in 1964, in which there are only two states for current flow in a hard superconductor: the current density is either 0 or equal J_c. Fig. 2.6 illustrates the model for an initially unmagnetised slab of superconductor. When the external field parallel to the conductor surface is raised by a small value B_e, a bipolar current of $\pm J_c$ is induced which penetrates to such a depth that the shielding field cancels the applied field in the central region. While increasing the external field both the current and the field penetrate deeper into the conductor until the centre is reached for the penetrating external field B_p. A further increase of the external field leads to a non-vanishing field in the centre of the superconducting sample but reduces J_c, which depends on the external field.

Lowering the external field below B_p, a new bipolar current of opposite polarity is induced which results in the complicated shape sketched in Fig. 2.6c. This model can be used to derive the hysteresis curve required for computing persistent-current field distortions [30].
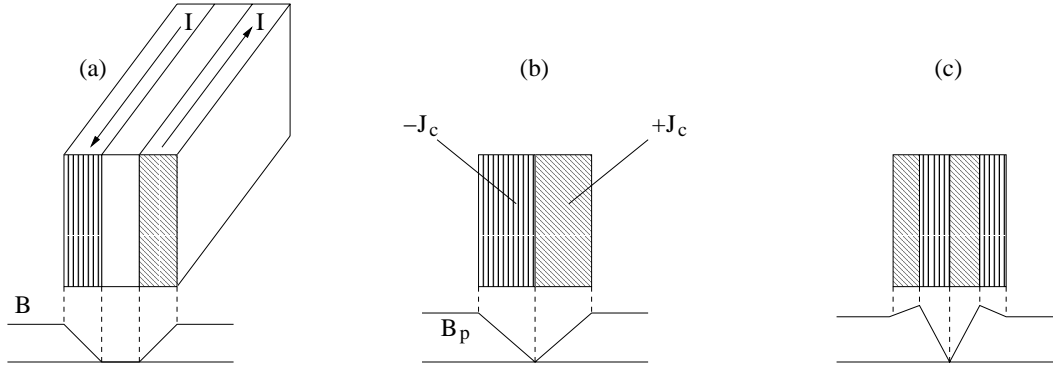
Figure 2.6: *Current and field distribution in a slab of hard superconductor according to the critical-state model with the field being parallel to the surface.*

Flux Jumping

A slab of a superconductor with height h and width $2a$ ($h \gg 2a$) is exposed to a large external magnetic field B_0 which is significantly larger than B_p and parallel to h. Applying the Maxwell equation $\oint \vec{B} \cdot d\vec{s} = \mu_0 I$ leads to

$$B(x) = B_0 - \mu_0 J_c(a - x)h \tag{2.26}$$

Assuming a small heat dissipation ΔQ into the slab, the temperature will rise by ΔT thus reducing the critical current density by ΔJ_c. This increases the field inside the slab resulting in a longitudinal voltage due to induction $U \propto dB/dt$ and heat generation

$$\Delta g = \mu_0 J_c \Delta J_c \frac{a^2}{3}. \tag{2.27}$$

Approximating the change of the critical current density with

$$\Delta J_c = J_c \cdot \Delta T / (T_c - T_0) \tag{2.28}$$

the energy balance $\Delta Q + \Delta g = C\Delta T$ with C being the specific heat gives

$$\Delta Q = \left[C - \frac{\mu_0 J_c^2 a^2}{3(T_c - T_0)} \right] \cdot \Delta T \tag{2.29}$$

An instability is reached for $T \to T_c$ and for $\Delta Q \to 0$. The second condition can appear independently from the temperature as a function of the conductor width $2a$. In that case the slightest disturbance will cause the superconductor to reduce its critical current and expel part of the captured magnetic flux. This process is called flux jumping, which does not necessarily lead to a quench. A recovery is possible because the heat capacity increases with the temperature ($C \propto T^3$). The criterion to prevent flux jumps is to reduce the half thickness of the slab a according to

$$a < \sqrt{\frac{3C \cdot (T_c - T_0)}{\mu_0 J_c^2}} \tag{2.30}$$

This expression is called the adiabatic flux jump stability criterion as cooling effects are neglected. Eq. 2.30 changes for a round superconductor. The expression for the radius is

$$r < \pi/4 \cdot \sqrt{(C \cdot (T_c - T_0))/(\mu_0 J_c^2)} \tag{2.31}$$

In case of a NbTi superconductor applied to a field of 5 tesla, a bath temperature of 4.2 K and $J_c \approx 3 \cdot 10^9 A/m^2$, r_{max} is in the range of 0.1 mm.

In order to prevent flux jumping superconductors that are used to wind magnets are made of multifilament wires (see also Section 2.4).

2.3.2 Superconductors for Accelerators

A large variety of metals and alloys are superconducting at liquid helium temperature but basically only two materials are commercially available for large scale magnet production, niobium-titanium NbTi and niobium-tin Nb_3Sn.

The discovery of high temperature superconductors raised hopes of enabling cooling with liquid nitrogen, however so far usable current densities for magnet production have only been achieved at low temperatures but with a significantly increased critical magnetic field. An overview of the critical current density as a function of the applied magnetic field for various cooling temperatures is given in Fig. 2.7.
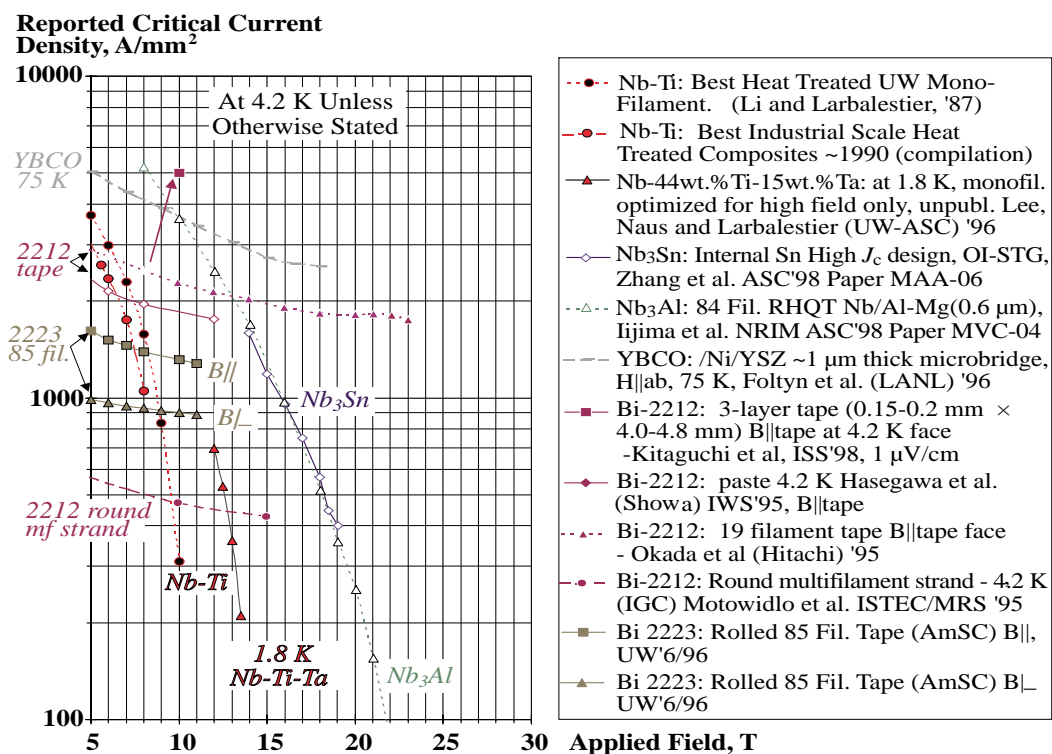
Figure 2.7: *Critical current density as a function of the magnetic field for various superconductors made of metal alloys and high critical temperature superconductors (Larbalestier and Lee 1999 [31]). If not stated otherwise, the cooling temperature is 4.2 K. The various superconductors are introduced in this Section.*

Niobium-Titanium (NbTi)

Niobium and titanium are mutually soluble to form ductile alloys over a wide range of compositions, which may be chosen for optimum critical properties. Because of the

ductility that permits effective and simple fabrication this superconductor is the work horse for magnet production although the upper critical field is only about 8 tesla at 4.2 K for a reasonable current density. Cooling with superfluid helium increases the field level to about 10 tesla. This solution was chosen for the LHC superconducting magnets.

Commercial alloys are almost always designed for optimum critical field rather than for optimum critical temperature, in the range of niobium 46.5–50 weight percent versus titanium [11]. Multifilament wires made of NbTi are fabricated by a wire-drawing process (see Section 2.4).

Niobium-Tin (Nb_3Sn)

Unlike NbTi the other commercially available magnet conductor Nb_3Sn is a brittle intermetallic compound with a crystal structure of type A15 [11]. Because it is so brittle, Nb_3Sn must be formed in situ at its final size before a heat treatment during the course of which the tin reacts with the niobium (the 'wind and react' techniques) [8, 11, 31]. The most popular process to form the conductor is the bronze process in which filaments of Nb are drawn down in a matrix of CuSn, bronze. During the following heat treatment, the tin diffuses through the bronze to produce Nb_3Sn while reacting with niobium.

Another superconductor with crystal lattice of type A15 is Nb_3Al. It reaches even higher magnetic fields than Nb_3Sn. Applications of Nb_3Al are limited since nothing similar to the bronze process exists.

High Temperature Superconductors

The discovery of high T_c superconductors (HTS) in ceramic copper oxides gives an opportunity to construct magnets operating significantly higher than 10 tesla. Some HTS are $YBa_2Cu_3O_{7-x}$ ('YBCO' or 'Y-123' with $T_c \approx 92\,K$), $Bi_2Sr_2Ca_2Cu_3O_x$ ('Bi-2223' $T_c \approx 107\,K$), or $Bi_2Sr_2CaCu_2O_x$ ('Bi-2212' $T_c \approx 90\,K$). Other HTS conductors exist but have not been that widely explored.

For temperatures below 30 K (see Fig. 2.7) these superconductors can carry current densities at a magnetic field strength that are unaccessible with metal alloys such as NbTi or Nb_3Sn. Both YBCO and Bi-2223 superconductor applications are limited to wide tape designs with the tape being made of thin superconducting films. These tapes can carry high current densities but cabling is quite challenging. Multifilament wires of Bi-2223 are being applied to prototype motors, transformers, and for power cables [31].

Bi-2212 appears to have the highest potential since it can be made in round wire form with reasonable high J_c, thus permitting access to the cabling technology of conventional superconductors [31].

At higher temperatures, for instance at the nitrogen liquefaction temperature of 77 K, the use of high temperature superconductors is restricted to low magnetic fields or lower current densities. In the LHC, HTS conductors are applied to current leads that are the feedthroughs for the current from room temperature into the cold mass. The use of high temperature superconductors permits the reduction of the heat load to the cryogenic system with respect to conventional copper current leads [32].

2.4 Stability of Superconductors

When the temperature exceeds the critical temperature, a resistive transition takes place and the superconductor becomes normal conducting. If the cooling is not strong enough to recover the superconducting state, the normal-conducting zone will spread out (start of a quench).

Superconducting cables for magnet coils or power transportation have to be designed to avoid damage in case of a quench or, ultimately, to exclude the possibility of a quench, which is known as cryo-stability. Since superconductors like NbTi have a high resistivity in the normal-conducting state, the superconductors are stabilised with copper. In case of a resistive transition of the superconductor the current redistributes and bypasses the superconductor by flowing through the copper. The copper reduces the heat generation due to the transport current and the stabilisation with copper significantly decreases the probability of a quench. A further stabilisation is obtained by increasing the heat transfer from the conductor into the coolant (see Chapter 3).

Multifilament Wire

In order to avoid flux jumping, multifilament wires (also called strands) of hard superconductors are used for magnets (see Section 2.3.1). These wires operate at currents up to 600 A. The operating current of the LHC multifilament wires is 550 A. A schematic cross-section of a multifilament wire is shown in Fig. 2.8. The filaments are twisted to ensure equal current distribution and to minimise the strength of induced eddy currents due to a changing magnetic field. Eddy currents can have an impact on the achievable field quality and on the quench process (see Section 3.4.2).
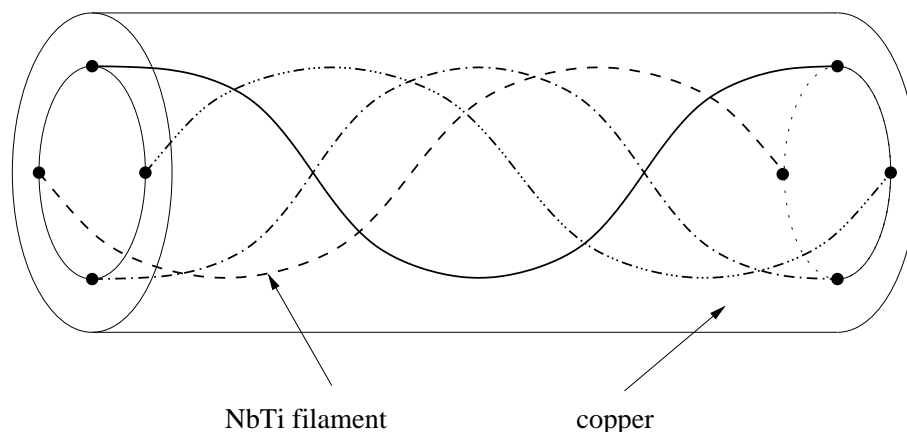

NbTi filament   copper

Figure 2.8: *Schematic cross-section of a multifilament wire (strand). Only four filaments are shown for a better understanding. The shown length is the filament twist pitch L_p^f. For the LHC wires this length is typically about 15–20 mm.*

As the filament diameter must be in the range of some μm to avoid flux jumping, a large number of filaments are embedded in a copper matrix that provides mechanical stability and at the same time serves as an electrical bypass of high conductivity and as a heat sink. The main parameters of the multifilament wire (strand) are the ratio of copper to superconductor $r_{cu/sc}$, the cross-section A or the wire diameter d, the number of filaments N_{fil}, the filament diameter d_{fil}, the filament twist pitch length L_p^f, and the RRR value of the copper stabilisation. For illustration the cross-section of the strand used for the outer layer cable of the LHC dipole magnet is shown in Fig. 2.9 [33].
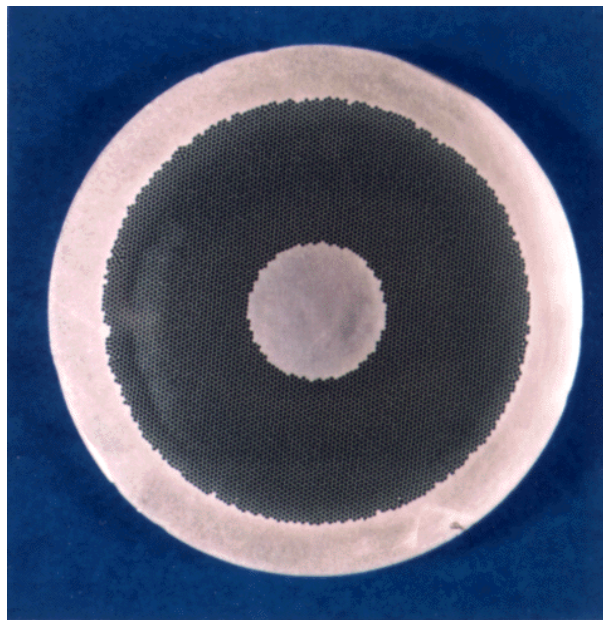
Figure 2.9: *The multifilament wire used for the outer layer of the LHC main dipole magnets, quadrupole magnets and busbars. The parameters are: $d = 0.825\,mm$, $d_{fil} \approx 6\,\mu m$, $RRR > 100$, $1.9 \leq r_{cu/sc} \leq 2.0$, $N_{fil} \approx 6400$.*

Multi-strand Cable

The superconducting cable for the LHC main magnets with nominal field up to 9 tesla at an operating current up to 13 kA are made of 20–40 multifilament wires (strands). As for the filaments of the multifilament wire, the strands in the multistrand cable are twisted. The strand twist pitch L_p^s is typically about 5–12 cm. The strands are compressed into a flat two layer structure with a trapezoidal shape, the Rutherford cable (sketched in Fig. 2.10). The cable is permeable to liquid helium so that the surface of all strands is wetted with the coolant. The insulation of the cable must have a high breakdown voltage, be elastic at room and liquid helium temperature, and radiation hard. The LHC Rutherford cables are insulated by wrapping polyimide films around the cable followed by a heat treatment for the polymerisation.
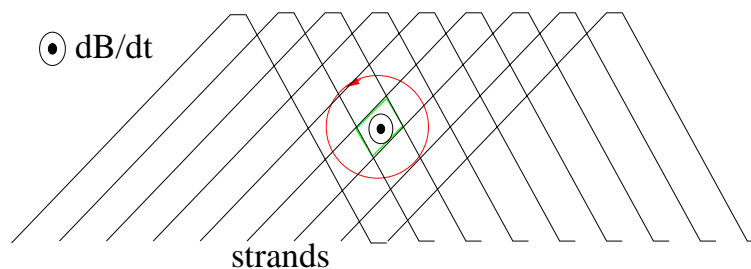
Figure 2.10: *Sketch of a Rutherford cable: strands cross each other and form a two layer structure. Eddy currents are induced that flow through the contact resistances when the applied magnetic field changes (see Section 3.4.2).*

The LHC Rutherford cable used for the outer layer of the main dipole magnets, quadrupole magnets, and the busbars is shown in Fig. 2.11 [33].

Figure 2.11: *The LHC Rutherford cable for the outer layer of the main dipole magnets, quadrupole magnets and busbars: 36 strands, width 15.1 mm, J_c(1.9 K, 9 tesla)$\geq$12900 A, A=19.2442 mm^2, strand twist pitch $L_p^s \approx 10.5$ cm. A short longitudinal section is shown on the left; the trapezoidal cross-section on the right.*

Fabrication

Superconducting cables made of NbTi are fabricated in a multistep process [34]. A cylindrical billet of NbTi is prepared by arc vacuum melting. The alloy NbTi must be produced with high purity and with a variation in titanium contents of less than 1 %. From this high homogeneity material round bars are manufactured with a diameter of about 150 mm and a length of 500 to 750 mm. They are wrapped with a niobium foil of controlled tensile properties and grain size and inserted in a thick-walled can of pure copper (usually $RRR > 100$) with an outer diameter of about 200 mm. The can is closed at the ends by caps that are electron-beam welded. After evacuation the can is compressed and extruded at 600 to 700 °C to a composite of 30–50 mm. A multiple process of drawing and compaction is performed leading to a long bar of hexagonal cross-section with a width of about 3.5 mm. This bar is cut into pieces of 0.5 to 0.75 m length. Several thousand of the carefully cleaned short bars are stacked into another 300 mm diameter thick-walled copper tube around a copper rod centre. The copper lids are electron-beam welded. Compaction, hot extrusion, and a number of drawing steps with heat treatments are repeated to optimise the critical parameters. The last step can be a tinning with final shaping or an anodising if required. The niobium foil is a diffusion barrier that prevents the formation of CuTi during the heat treatment, which is brittle and does not reduce in size during the drawing procedure and might damage the filaments.

Aiming for very thin filaments, a second or even a third multifilamentary billet has to be produced from the hexagonal rods of an intermediate stage. The final wire may contain up to 100 thousand filaments of some μm in diameter. The production aims at a continuous length of several tens of kilometres with reliable reproducibility of the critical current characteristics [8].

The Rutherford cables are produced with machines equipped with the necessary number of wire spools. The wires are guided around a conical mandrel and then rolled to the required trapezoidal cross-section shape by an assembly of rollers, named 'Turk's Heads'. Care must be taken to avoid strand breaks as well as burrs and sharp edges on the cable surface which may puncture the cable insulation and lead to electrical shorts in the coil. In some cases a final shaping process may turn out to be necessary. Within any magnet coil all strands should be of a continuous length without internal welds. Devices have been invented that periodically clamp the cable with a preset compression up to 70 Mpa, and measure the width, the average thickness and the trapezoid angle. A satisfactory cable fabrication is achieved if the degradation of the critical current is less than 2 %. The cabling also reduces the RRR of the copper [8, 11].

A further degradation is due to the winding of the coils. Typically, the Rutherford cable is wound with a tension of 200 N on a mandrel. The baking moulds are stacked from punched steel laminations providing a geometrical accuracy of about 0.02 mm at any cross-section.

After the winding, the coil is cured with a mould that covers the entire length placed on

the top of the coil package and the assembly is moved into a hydraulic press. The heat treatment again increases the RRR value of copper. Typical prestresses are in the order of 80–100 N/mm^2 to balance the thermal contraction during cooldown and to ensure enough tension at low temperature [8, 35].

2.5 Thermodynamic Properties of Helium

In order to cool superconducting materials like NbTi or Nb$_3$Sn liquid helium (or precisely liquid ^{4}He) is used. The phase diagram of helium at low temperatures is shown in Fig 2.12. If not exposed
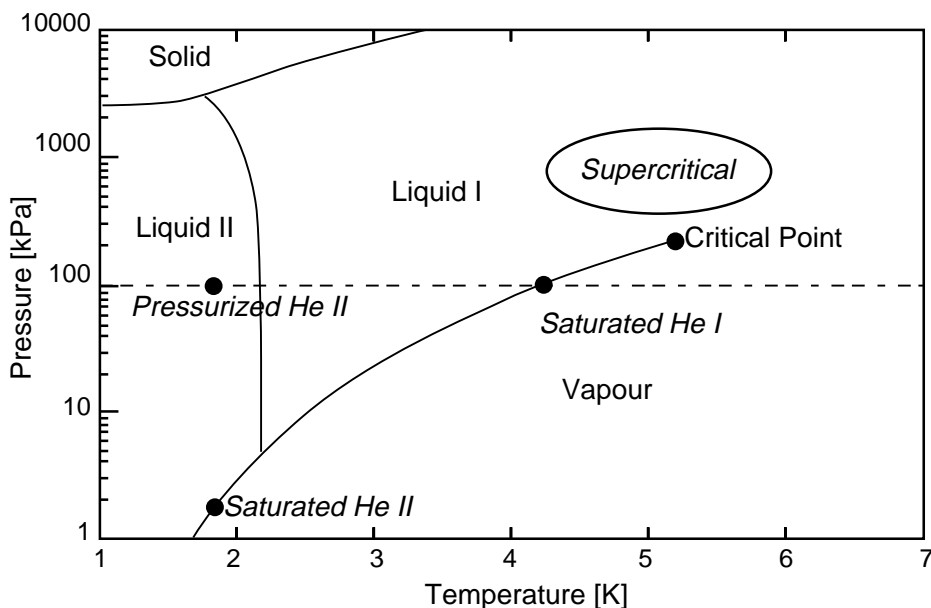
Figure 2.12: *Helium phase diagram [36]. The λ-line separates liquid helium I and liquid helium II.*

to very high pressures (>25 bar) helium does not go through a phase transition into a solid state at low temperatures. Helium has two liquid phases, helium I and and helium II, separated by the λ-line. Helium I is a conventional liquid; helium II is a superfluid. Superfluid means that a fluid can flow without friction in certain circumstances. A brief explanation of superfluidity is outlined in Section 2.6.

An overview of the thermodynamic properties of ^{4}He at low temperatures is shown in Figs. 2.13, 2.14 and 2.15. The sharp peak in the heat capacity phase transition at the λ-line (see Fig. 2.13) indicates a thermodynamic phase transition of a type found in other systems at a temperature similar to the ordering process at the Curie point for a ferromagnetic. The thermal conductivity of helium I is very low. Superfluid helium has a very high conductivity (see Fig. 2.15) with an unconventional behaviour as the heat conduction in superfluid helium obeys a wave equation

$$k\frac{d^2T}{dx^2} = \frac{1}{c^2}\frac{d^2T}{dt^2} \tag{2.32}$$

rather than the usual diffusion equation $kd^2T/dx^2 = cdT/dt$ (see Eq. 3.1), where k is the thermal conductivity and c is the heat capacity. Thus, temperature fluctuations do not diffuse, instead they propagate as a wave (called second sound).
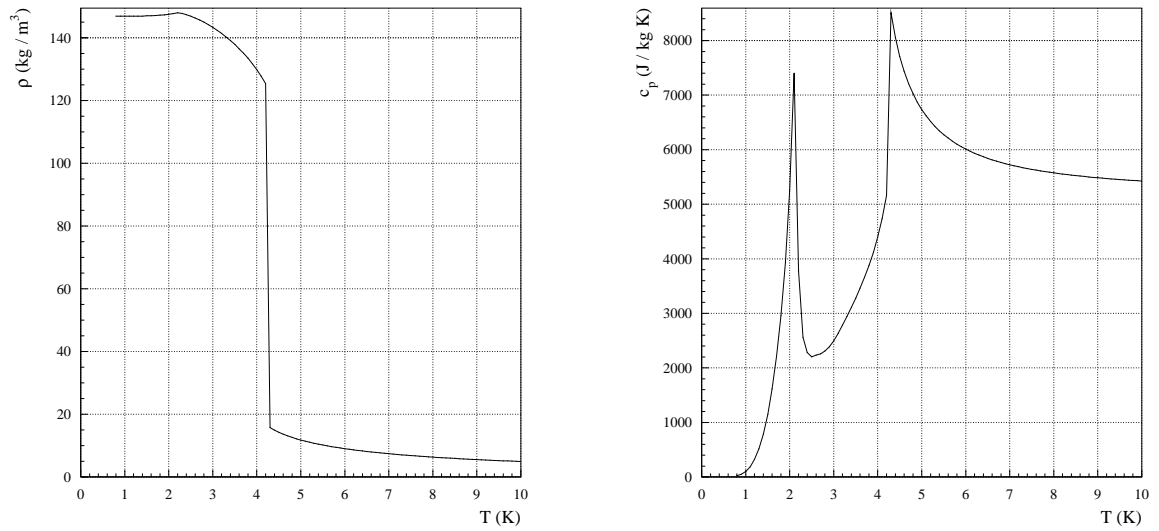
Figure 2.13: *Density (left) and heat capacity (right) of helium versus temperature [37].*
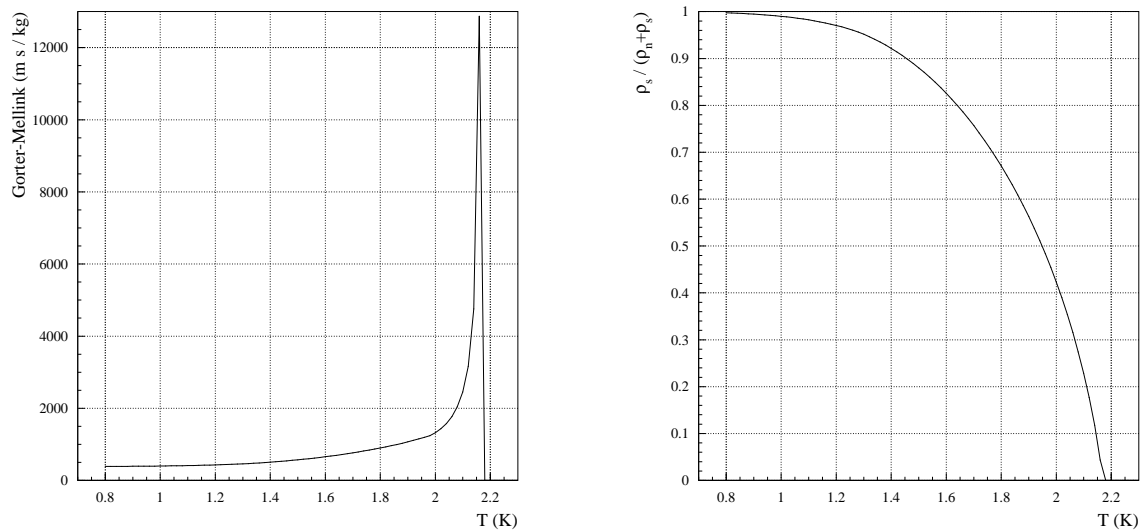

Figure 2.14: *Superfluid helium properties: Gorter parameter (left) and the fraction of the superfluid density (right) as a function of temperature ($\rho_{tot} = \rho_s + \rho_n$).*
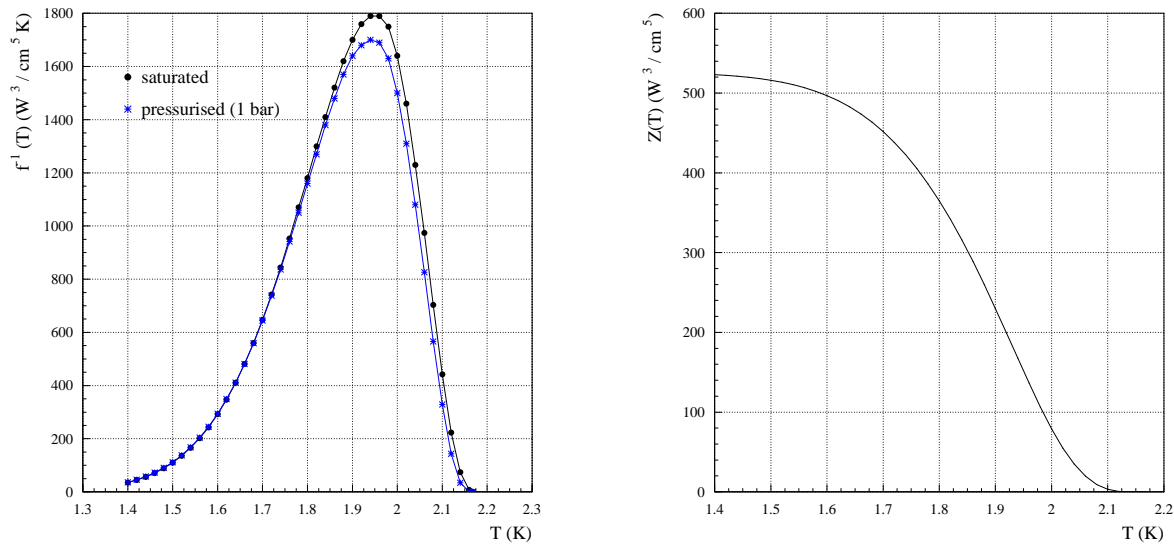
Figure 2.15: *Thermal conductivity of helium (left) and the integrated thermal conductivity of pressurised superfluid helium (right) as a function of temperature.*

2.6   Superfluid Helium

This brief introduction of superfluidity is based on the book of Tilley [22] and the lectures of Vinen [38]. Superfluidity is a macroscopic quantum effect that can be explained in terms of the existence of a Bose condensate. There is a close analogy to superconductivity which relates to frictionless flow of electrons. Known superfluids are for example liquid ^{4}He at a temperature below 2.17 K and liquid ^{3}He at a temperature below about 2 mK. In liquid ^{4}He, the atoms act as bosons whereas in liquid ^{3}He, they combine to form Cooper pairs.

Superfluid helium flows without friction through a very narrow channel, provided that the flow velocity is less than a critical value, which depends on the channel width. This frictionless flow suggests vanishing viscosity, but the damping of a disc, which oscillates at a small amplitude in its own plane in superfluid helium, has been observed.

Bose Condensation

The fact that helium does not even form a solid at $T=0$, except for very high pressures, is an indication of quantum effects. Each atom in the liquid is confined by its neighbours; this confinement leads to a large zero-point energy, which increases with increasing liquid density. The zero point energy therefore tends to keep the atoms apart to an extent that prevents solidification with the attraction force between the helium atoms being quite weak.

The third law of thermodynamics requires that the entropy of the helium must tend towards zero as the temperature reaches zero, even if it remains in its liquid state. Superfluid helium at $T=0$ must therefore be an ordered liquid, which shows that the transition at T_λ is an order-disorder transition. The properties of a hypothetical ideal gas at very low temperatures (hypothetical because all real gases liquefy at a low temperature) depend on the statistics of the particles: ^{4}He atoms are bosons, thus obeying the Bose-Einstein statistics, which allows numerous bosons occupying the same quantum state; whereas the Fermi-Dirac statistics is applied to fermions due to Pauli's exclusion principle.

In an ideal Bose gas, Bose condensation is predicted. Below a certain critical temperature a finite fraction of the bosons occupy the lowest quantum state in the vessel containing the gas, this fraction reaches unity at the limit $T \rightarrow 0$. The ordering takes the form of putting all the particles in the same quantum state.

A form of Bose condensation occurs in liquid helium below the λ-transition which was demonstrated by Penrose and Onsager [39]. The Bose condensation in liquid helium differs with respect to the ideal Boson gas, since the fraction of atoms in the lowest momentum state does not reach unity but only about 0.1 even at $T = 0$.

The Two-fluid Model

A phenomenological description of the observed properties of superfluid helium is the two-fluid model. It assumes that superfluid helium consists of two interpenetrating fluids: a normal component, density ρ_n, and a superfluid component, density ρ_s, behaving like an ideal classical liquid and carrying no entropy. The ratio of $\rho_s/(\rho_n + \rho_s)$ decreases from unity at T=0 to zero at the λ-transition (see Fig. 2.14 right). The Bose condensate fraction cannot be identified with $\rho_s/(\rho_s + \rho_n)$ as it does not exceed 0.1.

The two-fluid model explains the two experimental observations with superfluid helium: the flow through the narrow channel involves only the superfluid component; the oscillating disc is damped by the normal fluid. Two types of wave motion are possible in the system: one in which the two fluids oscillate in phase (first sound) and one in which they oscillate in antiphase (second sound).

Bose Condensation and Superfluidity

When liquid helium contained in a long tube of cross-section A is set into motion with velocity V, the condensate wave function for the superfluid component Ψ takes the form $\Psi = \Psi_0 \exp(ikr)$, with $\hbar k = mV$ (m being the helium mass and r being the position). The helium atoms will interact with the walls in the tube and some atoms will be scattered out of the condensate. This process reduces the amplitude of the condensate wave function, but may not change the phase. The scattering leads to equilibration of the helium with the constraint that the phase of the wave function remains unchanged. This is a case of broken symmetry similar to the situation in a ferromagnetic material in which the overall magnetisation is constrained to point in a certain direction, although the individual atomic magnetic moments are free to point in other directions. The broken symmetry may involve a non-zero mass current density (or momentum density) of the form

$$J_s = \rho_s V \tag{2.33}$$

at low velocities, which describes the superfluid component density ρ_s moving with velocity $v_s = V$. This equilibrium with broken symmetry is metastable and has a finite lifetime as the helium without superflow has a lower energy.

Landau [40] introduced the idea that the lowest excited states of helium can be described in terms of a low-density gas of weakly interacting excitations similar to the excited states of lattice vibrations whose quanta are the phonons. Landau suggested that the lowest excitations in liquid helium are also phonons, but that there are other excitations in liquid helium at a higher energy, called rotons. Phonons and rotons are not clearly distinguishable and form a continuous spectrum. The normal fluid is identified with the gas of excitations. Calculating the distribution function for the excitations when they are in equilibrium with the channel walls allows the evaluation of

the momentum density P_{ext}. Adding P_{ext} to the original momentum density $\rho_n V$ gives the total momentum density

$$P = P_{ext} + \rho_n V > 0 \tag{2.34}$$

for the normal fluid component at low temperatures. The amplitude of ρ_s can be evaluated by comparing Eq. 2.33 and 2.34.

It must be emphasised that ρ_s is only found to be non-zero if the excitation spectrum has the appropriate form. For example the ideal Bose gas is not a superfluid because the excitation spectrum does not have the right form. The existence of phonons at the lowest energies is a sufficient condition. A theoretical explanation of the helium excitation form was provided by Feynman [41].

Quantisation of Superfluid Circulation

The velocity v_s is linked to the phase S as $v_s = \hbar/m \nabla S$. Similar to the quantisation of the magnetic flux (see Section 2.2.5) this leads to a quantisation of superfluid circulation. The circulation in the superfluid component is $\kappa = \oint v_s dr$. The condensate wave function must be single-valued, which leads to the condition

$$\kappa = n\frac{h}{m} \tag{2.35}$$

The quantum h/m is macroscopically large ($\approx 10^{-7}\,\mathrm{m^2/s}$). As for the flux line in a type II superconductor, the circulation in a superfluid leads to free quantised vortex lines that fill the superfluid and change some properties. The excitations of the normal fluid are scattered by the cores of the vortices. Any motion of the superfluid and the normal fluid results in a frictional force between them, a force of mutual friction.

2.7   Cooling with Helium

The heat transfer into helium is generally described by means of the heat transfer coefficient h^{He}, which is a function of the temperature, its time derivative and pressure of the helium as well as the conductor surface and the overall geometry. In general superconducting magnets for accelerators such as the LHC are cooled in a helium bath whereas other applications such as magnets for fusion reactors in a tokamak require cooling with a forced helium flow. Forced flow cooling increases the heat transfer by convection of helium which can transport more heat away but is not practical for the LHC due to technical reasons.

The cooling mechanisms presented in this Section determine the temperature dependence of the heat transfer coefficient that is used in Chapter 3 for the modelling of the quench process in the presence of helium cooling.

Kapitza-like Heat Transfer

The Kapitza resistance opposes heat transfer through the interface of two dissimilar materials and strongly decreases with temperature. It is theoretically explained with phonon radiation. The Kapitza resistance leads to a heat transfer dependence of the type

$$h_K(T) = a_K(T^n - T_b^n) \tag{2.36}$$

with h_K in [W/m²], T_b being the helium bath temperature and T being the temperature at the surface exposed to the helium. Various measurement results for a_K and n for various materials including copper and polyimide films are summarised by P. Bauer (1998) [42].

Cooling with Liquid Helium I

The heat transfer into liquid helium I has been the subject of many experiments and publications. A detailed summary can be found in the text book by van Sciver (1986) [43].

Liquid helium I has a small thermal conductivity and a large specific heat which means that density driven convection dominates the heat transfer and heat conduction plays a minor role. The heat transfer for the natural convection determined with classical hydrodynamics is of the form $h = c_{nc} \cdot (T - T_b)$ with $c_{nc} \approx 500\,\text{W/(K·m}^2)$ being a function of the heating dimension.

Above a critical heat flux $h_c \approx 10\,\text{W/m}^2$, bubbles of helium vapour form at the surface which increases the heat flux as a function of the temperature up to 5–15 kW/m². This regime is known as the nucleate boiling heat transfer. It can be understood by accounting for the latent heat of the helium within the bubble. A departing bubble transports a large amount of energy away and its space is replaced by a new layer of liquid helium that cools the surface. Kutateladze derived a phenomenological correlation in 1952 [44] demonstrating a temperature dependence $h(T) \propto (T - T_b)^{2.5}$, for $h_c < h(T) < h^*$. The maximum nucleate boiling heat transfer depends on the orientation and surface treatment and can be increased when the surface exposed to helium faces upwards.

When the heat flux is further increased beyond $h(T) > h^*$, the nucleate boiling bubbles become larger and detach themselves at a significantly slower rate. They become unstable and coalesce into a continuous vapour film. The heat transfer correlation was derived by Breen and Westwater in 1962 [43]. It can be described as $h(T) = c_{fb} \cdot (T - T_b)$ with $c_{fb} \approx$ 300-1000 W/(Km²). Reducing the heat flux leads to a recovery of the nucleate boiling at approximately $0.35 \cdot h^*$ [43].

In transient cases the heat flux can be significantly increased and is dominated by Kapitza conductance for short times due to the pure conduction in helium I. Burn-out limits are reached when the heat transfer exceeds the limit of nucleate film boiling. Because of the low thermal conductivity the heat penetration depth δ into helium is in the range of a few micrometers for $\Delta t < 10$ ms. Film boiling is triggered when the heat transferred into the heated helium volume exceeds the latent heat of vaporisation λ associated to it. Transient heat transfer to pool boiling helium I has been investigated by Schmidt [45].

Cooling with Liquid Helium II

As mentioned in Section 2.6 the two-fluid model can be used to describe the different characteristics of superfluid helium with normal hydro-dynamics [43]. The heat transfer correlation in the Landau regime (slow motion) is

$$h(T) = \frac{d^2(\rho_n, s_{mn})^2 T}{\beta \eta_n} \mid \vec{\nabla} T \mid \tag{2.37}$$

with d being the helium channel diameter, the normal fluid density ρ_n and its entropy density s_{mn}, β being a geometrical constant in the range of 10–20, and η_n being the viscosity of the normal fluid.

Heat transport equation in turbulent helium II is calculated with 2-flow fluid-dynamics assuming a viscous drag between the normal fluid and the superfluid vortices.

$$| \vec{\nabla} T | = \frac{\beta \eta_n}{d^2 (\rho_n, s_{mn})^2 T} h + \frac{A \rho_n}{\rho_s^3 s_{mn}^4 T^3} h^3 + ... \tag{2.38}$$

The first term is equivalent to the viscous flow in the Landau regime (see Eq. 2.37). The second term describes the mutual friction interaction of the normal fluid with the superfluid and dominates due to its temperature dependence $\propto T^3$. $A(p, T)$ is the experimentally obtained Gorter-Mellink mutual friction parameter (see Fig. 2.14 left). Eq. 2.38 describes the heat transfer for turbulent helium II, the Gorter-Mellink regime.

As the thermal resistance in superfluid helium is small, the heat transfer on the surface cooling to superfluid helium is determined by the interface Kapitza resistance. A high heat flux into a restricted volume of helium can trigger film boiling. The heat diffusion equation for superfluid helium can be written as

$$\frac{dT}{dr} = f(T) h^m \left(\frac{r_0}{r} \right)^m \tag{2.39}$$

with $m=3$ being an empirical fit parameter. The empirical conductivity function f^{-1} is shown in Fig. 2.15 (left). It goes through a maximum at 1.9 K for pressurised helium II (1 bar).

The Gorter-Mellink regime is sustained as long as the helium II in a channel of width $L \equiv r_0$ has not reached the transition temperature T_λ to helium I at any point. The integrated thermal conductivity of helium II is shown in Fig. 2.15 (right). The critical steady state heat flux in helium II, h^{*II}, is obtained by the integrated thermal conductivity and by integrating over the channel length

$$h^{*II} = \left(\frac{2}{r_0} \int\limits_{T_b}^{T_\lambda} f^{-1}(T) dT \right)^{1/3} \tag{2.40}$$

At T_b=1.8 K, r_0=1 mm, h^{*II} is as large as 150 kW/m^2. The critical steady state heat flux can also be derived from Eq. 2.38 for the one-dimensional approximation. When h^{*II} is exceeded, a film of liquid helium I is created which is followed by film boiling.

The transient critical heat flux can be significantly higher than the critical steady state heat flux due to a finite burn-out time that is required to reach the limiting heat flux conditions before film boiling starts. The heat conduction equation for helium II (Eq. 2.32) was solved by Dresner for the transient case assuming constant properties (averaged heat conductivity K and capacity C) which allows the calculation of the burn-out time t^{*II} [46]

$$t^{*II} = 1.438 \cdot K^3 \cdot C (T_\lambda - T_b)^2 \frac{1}{h^4} \tag{2.41}$$

The limiting time is called the second sound limit (see Eq. 2.32). The burn-out time derived for turbulent helium yields the Gorter-Mellink limit.

The burn-out time corresponds to the energy transferred into helium to start film boiling either due to the Gorter-Mellink limit or to the second sound limit. This process is similar to the channel limitation for helium I.

Chapter 3

Quench Theory

A brief introduction of the risks of a quench and the protection strategies was already given in Section 1.5. This Chapter is devoted to the theory of the quench process.

Most existing theories describe a quench as a thermodynamic process with resistive heating, using simplified analytical methods some of which were developed within the research program of superconducting accelerators as the Tevatron or the SSC project. Experimental evidence highlights the limitations in accuracy and usability of these analytical approaches as their application at 1.9K can lead to unphysical results. A complete description of the quench process requires a complex thermodynamic model, which needs to be approximated by numerical methods. The effect of eddy currents also has to be taken into account. These are induced inside the superconductor in the presence of a magnetic field changing with time.

After the review of some analytical quench models and their application to the case of the LHC main dipole magnets and busbars, a theory is explained that treats the quench process as a coupled electrodynamic and thermodynamic phenomenon. This algorithm has been developed in the framework of this thesis. The influence of eddy currents and the importance of adequate modelling of the cooling conditions are stressed and the chosen numerical approach and its robustness are discussed. Two different simulation models are introduced: firstly, the finite difference method, which approximates the heat balance equation and determines the temperature profile in the presence of cooling and heat generation conditions that vary with time; secondly, the piecewise modelling of electric circuits to evaluate the quench propagation, temperatures and voltages in a chain of superconducting magnets. The outcome of the first model gives quench parameters such as the longitudinal and transverse quench propagation velocity, the impact of the cooling on the hot spot temperature, the voltage development after a quench, the influence of the quench back effect, and the quench heater delays. These parameters are required by the second model, which is used to determine adequate protection for a chain of superconducting magnets.

3.1   Classical Quench Theory

The critical surface of NbTi was shown in Fig. 2.5. On this surface any of the three critical parameters (temperature, current density, magnetic field) is a function of the two other variables. When one of these parameters exceeds the critical value, the superconductor becomes normal-conducting. If the cooling power is insufficient to recover the superconducting state, the normal-conducting zone expands. This process is called a quench.

The differential equation that describes the quench process is the heat balance equation. This equation will be covered in detail in the Sections 3.4 and 3.5. Considering a conductor with the current flowing in x direction and a homogeneous temperature across the cross-section A that may be a function of the longitudinal position $A(x)$, the one-dimensional heat balance equation is

$$\frac{d}{dx}\left(k(T(x,t))\frac{dT(x,t)}{dx}\right)A(x) - h^{He}(T(x,t),t)P(x) + G(T(x,t),t)$$
$$= c(T(x,t))A(x)\frac{dT(x,t)}{dt} \tag{3.1}$$

with c being the heat capacity, k being the heat conductivity, h determining the heat transfer into helium, P being the wetted perimeter of the conductor exposed to helium, and G being the internal heat generation.

The term on the right side of Eq. 3.1 is called the thermal impedance. It is given by the heat capacity c as a function of temperature multiplied by the time derivative of the temperature.

The first term on the left side of Eq. 3.1 describes the heat conduction along the conductor with the conductivity k as a function of the temperature.

The term $h^{He}P$ represents the simplest model for cooling by heat transfer into helium (transverse cooling). Various models for the temperature dependence of h^{He} are described in Section 3.5 including a more general cooling model that takes into account the heat transfer through the electrical insulation layer.

A hard superconductor exhibits a gradual transition from vanishing to high resistivity close to J_c (critical current density). When the current I in the composite wire is slowly increased to a value just above the critical current I_c, the superconductor enters the resistive state and transfers part of the current to the copper matrix. As the resistivity of NbTi steeply rises from 0 when I_c is exceeded, one can assume the current I_c is carried by NbTi and $I - I_c$ is carried by the copper. In this current sharing regime both the NbTi filaments and the copper matrix are resistive.

The current sharing occurs as a result of a local temperature increase. If the temperature is raised from T_0 to T_1 the transport current I_0 with the initial condition $I_0 < I_c(T_0)$ may fulfil $I_0 > I_c(T_1)$ as the critical current drops due to the temperature increase. The excess current has to be taken over by the copper matrix.

The current sharing temperature T_{cs} at which the current starts to bypass the superconductor and to flow through the copper can be calculated using a linear dependence of I_c on the temperature

$$I_c(T) \simeq I_c(T_0) \cdot \frac{T_c - T}{T_c - T_0} \tag{3.2}$$

which gives

$$T_{cs}(I) = T_0 + (T_c - T_0) \cdot \left(1 - \frac{I}{I_c(T_0)}\right) \tag{3.3}$$

and always complies the condition $I < I_c(T_0)$.

The current sharing model distinguishes three regimes of the Ohmic heating $G(T(x,t))$: below T_{cs} heat is not generated; above T_c the heat generation is $G(T(x,t)) = \rho_{cu}(T(x,t)) \cdot I^2(t)/A_{cu}$; between T_{cs} and T_c the heat generation increases linearly as $G(T(x,t)) = \rho_{cu}(T(x,t)) \cdot I^2(t)/A_{cu} \cdot (T - T_{cs})/(T_c - T_{cs})$. The resistivity of copper is ρ_{cu} and A_{cu} is the copper cross-section of the composite. As a first approximation [11] one can neglect the current sharing regime and use an abrupt step function that determines whether there is Ohmic heating or not. Disregarding the heat

conduction along the composite conductor and the cooling by helium, one obtains the adiabatic heat balance equation

$$\rho_{cu}(T(x,t)) \cdot \frac{I(t)^2}{A_{cu}(x)} = c(T(x,t)) \cdot A(x)\frac{dT(x,t)}{dt} \tag{3.4}$$

The temperature in Eq. 3.4 can only increase, which is an appropriate first approximation for short timescales (about 100 ms for the LHC dipole magnets) after the start of a quench. For a position x one can rearrange and simplify Eq. 3.4 to

$$\int_{t_0}^{t_1} I(t')^2 dt' = A \cdot A_{cu} \cdot \int_{T_0}^{T} \frac{c(T')}{\rho(T')}dT' \equiv F(T) \tag{3.5}$$

Eq. 3.5 is the definition of the quench load that is frequently used for a first estimate of the hot spot temperature.

It demonstrates that the measurement of the squared current integral over the quench duration (quench load) yields the maximum temperature with adiabatic assumptions (hot spot temperature). This approach neglects heat transfer into helium and heat conduction along the conductor. An example of the temperature evolution as a function of the quench load is shown in Fig. 3.1.
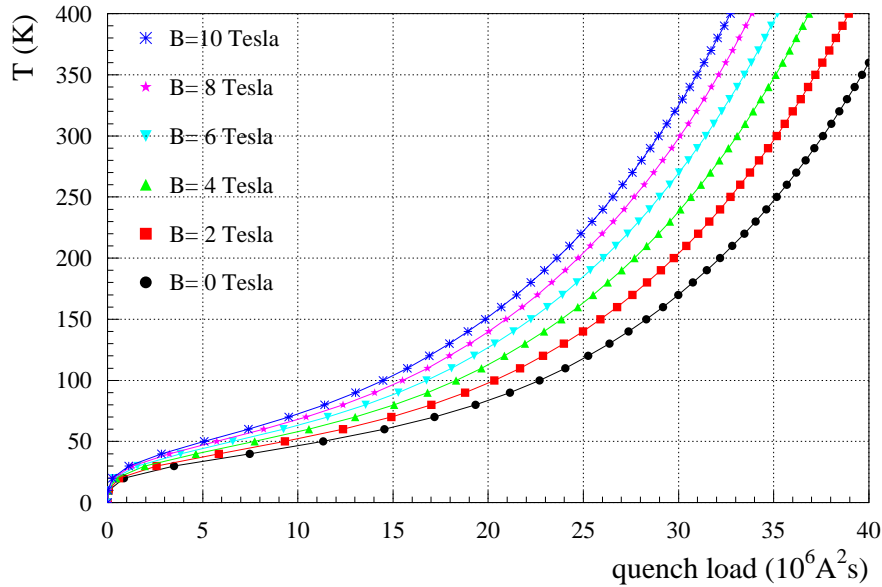
Figure 3.1: *Calculated hot spot temperature as a function of the quench load for the outer cable of the LHC dipole magnet ($RRR = 100$, $r_{cu/sc} = 1.9$, $A_{tot} = 19.2442 \, mm^2$).*

3.1.1 Stability

The stability of a coil is a measure of its ability to recover superconductivity after a resistive transition in a small zone. The heat balance equation (Eq. 3.1) includes two mechanisms that can cause the recovery:

- the cooling due to helium ($h^{He}P$). Heat is transferred into the helium either directly or through an insulation layer, which re-cools the conductor.

- heat conduction along the conductor ($d/dx(kdT/dx)$). Heat is conducted away from the hot spot along the conductor that can also cause the recovery of the superconducting state.

Cooling by Heat Transfer to Helium

In the limiting case that only transverse cooling is present, recovery will take place if the cooling power is stronger than the Ohmic heat generation. The ratio is the Stekly parameter [47]

$$\alpha_{St} = \frac{G(T(x,t),t)}{h^{He}(T(x,t),t)P(x)} \tag{3.6}$$

The simplest approximation of the cooling by helium is $h^{He}P = hP(T-T_b)$, where h is a constant and T_b is the bath temperature. Assuming that the conductor is normal-conducting for the length l at an average temperature $T > T_{cs}$ and $T_{cs} \approx T_b$, the cooling power is then $hP(T - T_b)l$ and the Ohmic heating is $\rho_{cu}I^2/A_{cu}(T - T_b)/T_c - T_b) \cdot l$. Thus, α_{St} becomes

$$\alpha_{St} = \frac{\rho_{cu}I^2}{A_{cu}hP(T_c - T_b)} \tag{3.7}$$

Conductors with $\alpha_{St} < 1$ are cryo-stable as a quench cannot appear as long as the cooling power remains stronger than the heat generation.

Generally, cryo-stable conductors can not be used to wind magnet coils for accelerators as the copper to superconductor ratio has to be much higher than 10, which would require very bulky and expensive coils. For most applications of superconductors in accelerators $\alpha >> 1$ and therefore cryo-stability is not achievable at nominal operating current. However, at lower currents (beginning of the current ramp) the conductor might become cryo-stable.

As the heat generation and cooling conditions are non-linear functions of time and temperature, any stability criterion is time dependent. An approach that takes the temperature dependence into account is the equal-area theorem by Maddock et al. (see Fig. 3.2 for illustration) [48]. The steady state one-dimensional heat balance equation reduces Eq. 3.1 to

$$\frac{d}{dx}k(T(x))\frac{dT(x)}{dx} = h(T(x))\frac{P(x)}{A(x)} - G(x). \tag{3.8}$$

If k is assumed to be independent of T, the normal-conducting zone would not expand and the following equation is valid (definition of the equal-area theorem)

$$\int_{T_0}^{T_1} \left(h(T(x)) - \frac{A(x)}{P(x)}G(T(x)) \right) dT = 0. \tag{3.9}$$

This condition requires that the difference between cooling and heat generation integrated over temperature must be zero. In other words; the heat generation can be larger than the cooling power in a certain temperature interval. This regime needs to be compensated by another temperature interval in which the cooling power is larger than the heat generation. If both regime have the same area (area has the unit of power times temperature per surface [W·K/m^2]), Eq. 3.9 applies and the normal conducting zone neither expands nor collapses. An example of the heat generation and the cooling power as a function of temperature is given in Fig. 3.2.

The usability of this approach is limited since it does not include transient effects nor the temperature dependence of the heat conductivity.
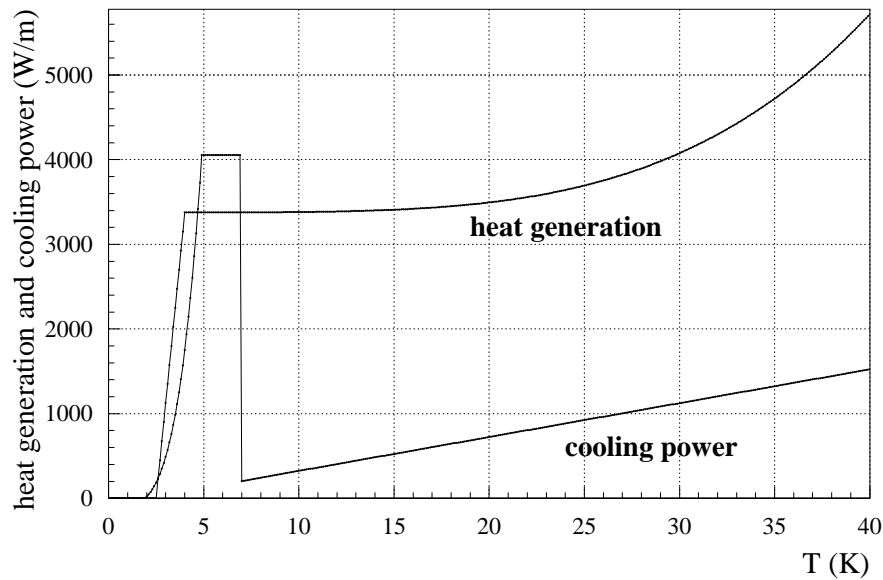
Figure 3.2: *Comparison of the heat generation and transient cooling power as a function of temperature example for the LHC dipole magnet (initial current 11.8 kA, applied magnetic field 2 tesla, RRR=100). The heat generation includes the current sharing model explained in Section 3.1, the cooling mechanisms were explained in Section 2.7. The graph illustrates the equal-area theorem: if the surfaces between the crossing points of the two curves are identical in size, the normal conducting zone neither expands nor collapses. The effective cooling power in the superconducting cable is smaller than shown in the graph because of limited heat transfer through an insulation layer (see Section 3.5.2). The curve of the heat generation is given by Eq. 3.46, that of the cooling power by Eq. 3.84.*

Transient effects play an important role as the heat transfer from the conductor surface into the helium bath changes depending on the state of helium and the pressure increase. Some transient aspects for stability that are based on simple relations between material properties and temperatures have been summarised by Wilson [11]. The models for heat transfer presented in Section 3.5.1 presume either constant pressure (for simulations of quenches in busbars) or an increasing pressure (for simulations of quenches in magnets). Effects of turbulent or forced flow helium are not included.

As the heat generation is much larger than the cooling for cables used in the LHC magnets (not necessarily for busbars), stability has to be studied to determine if a quench can occur in first place. As soon as the current starts to bypass the superconductor and to flow through the copper, a recovery is almost excluded and the evaluation of the hot spot temperature and the required protection are the important issues.

Cooling by Heat Conduction

In some situations cooling by heat transfer to helium does not occur (i.e. very low heat conductivity of the insulation layer). This generally applies for fully epoxy-impregnated coils.

Assuming a normal-conducting zone of length l at T_c the heat generated in this zone can only be removed by heat conduction along the wire in two directions. The normal zone expands if the

heat generated exceeds the heat removed

$$\rho_{cu}I^2/A_cul \geq 2k(T_c - T_b)A/l \tag{3.10}$$

Eq. 3.10 sets the lower limit for the length that a normal zone must have for developing a quench. With $A = A_{cu} + A_{sc}$ and $r_{cu/sc} = A_{cu}/A_{sc}$ the length for the minimum propagating zone (MPZ) for a composite wire with copper stabilisation is [8]

$$l_{MPZ} = \sqrt{\frac{2kA^2(T_c - T_b)}{\rho_{cu}I^2}\frac{r_{cu/sc}}{1 + r_{cu/sc}}} \tag{3.11}$$

Eq. 3.11 disregards the resistivity of NbTi ρ_{sc} above T_c as the resistivity of copper is significantly smaller. Eq. 3.11 demonstrates that an increase in the copper to superconductor ratio increases the minimum propagating zone.

A pure superconducting cable has a heat generation $\rho_{sc}(I^2/A)l = \rho_{sc}J^2 \cdot (Al)$. This gives the definition of the minimum propagation zone for a pure superconductor

$$l_{MPZ}^{sc} = \sqrt{\frac{2k(T_c - T_0)}{\rho_{sc}J^2}} \tag{3.12}$$

A length l_{MPZ}^{sc} of about 1 μm is sufficient to expand the normal conducting zone showing that a pure superconductor cannot be used to wind magnet coils (moreover flux-jumping occurs for wires of more than 50–100 μm diameter). For a composite wire with copper stabilisation, l_{MPZ} increases to a few centimeters (about 1.5 cm at nominal current for the cable in the LHC dipole magnets).

Wilson [11] calculated l_{MPZ} for the three-dimensional quench propagation assuming that the temperature T in the normal-conducting zone is in the range $T_{cs} < T < T_c$ and that the normal-conducting zone remains constant with time

$$l_{MPZ} = \pi\sqrt{\frac{k(T_c - T_b)A^2}{\rho_{cu}I^2}\frac{r_{cu/sc}}{1 + r_{cu/sc}}} \tag{3.13}$$

In reality these two conditions are not valid as the normal-conducting zone varies with time. For that reason Eq. 3.13 can be considered as a condition for an onset of instability. Dresner [46] showed that the conditions leading to a quench and to a quench recovery can be different.

The energy to warm up l_{MQZ} to the critical temperature is called the minimum quench energy (MQE).

$$E_{MQE} = (H(T_c) - H(T_b)) \cdot A \cdot l_{MQZ} \tag{3.14}$$

with H being the enthalpy. Eq. 3.11 and Eq. 3.13 may be used to calculate the minimum quench energy. For accelerator magnets, the calculated minimum quenching energy is in the range of 0.001–0.1 J. The quench energy can be much larger than E_{MQE} because heat transfer into helium has been neglected in Eq. 3.14. For example, the quench energy of a provoked quench by a heater is larger than E_{MQE} as part of the energy is deposited in the insulation layers and in the heater strip itself.

The above considerations always assume a normal-conducting zone at T_c and neglecting the cooling by heat transfer into helium. This means that the normal-conducting zone required to provoke a quench has to be longer than the l_{MPZ} and that the minimum quench energy is larger.

The required normal-conducting length for an expanding quench reduces if the critical temperature is exceeded or if an additional heat source such as a quench heater provides more energy than the minimum quench energy.

3.1.2 Quench Propagation

Calculation of the Quench Propagation Velocity

The limiting cases of the quench propagation velocity v_q are either $I \to 0$ or $I \to I_c$. The quench propagation velocity is zero as a normal-conducting zone cannot expand at a very low transport current (cryo-stability). In the second case the quench propagation approaches the velocity of light when the transport current is the critical current since the entire cable quenches practically at the same time. A very high current pulse can quench a long superconducting cable instantaneously.

At first, the quench propagation velocity is evaluated between the two cases without transverse cooling. For constant metal properties and cross-section along the conductor the heat balance equation (see Eq. 3.1) is

$$k\frac{d^2T}{dx^2} + G(T(x,t)) = c\frac{dT}{dt} \tag{3.15}$$

To find a solution the assumption is made that the warm front moves with a constant velocity v in x-direction along the conductor (see Wilson [11]). Since the expansion takes also place in the opposite direction, the warm zone expands with $2v$. Introducing the moving coordinate at the end position of the normal zone $\xi = x - vt$ Eq. 3.15 can be rewritten as

$$k\frac{d^2T}{d\xi^2} + cv\frac{dT}{d\xi} + g(\xi) = 0 \tag{3.16}$$

Disregarding current sharing, the Ohmic heating $g(\xi)$ is approximated by a step function

$$g(\xi) = \begin{cases} 0 & \text{for } \xi > 0 \\ \rho_{cu}I^2/A_{cu} & \text{for } \xi \leq 0 \end{cases} \tag{3.17}$$

and the temperature at the centre of the warm front is approximated to $T_w = 0.5(T_c + T_b)$ with $T_b < T_c$, T_b being the helium bath temperature. Eq. 3.16 has the solution

$$T(\xi) = \begin{cases} T_c - (T_c - T_w)\exp(a\xi) & \text{for } \xi < 0 \\ T_b + (T_w - T_b)\exp(-b\xi) & \text{for } \xi \geq 0 \end{cases} \tag{3.18}$$

with $T(\xi)$ being well defined at $\xi = 0$. Requiring also the continuity of the heat flux $dT/d\xi$ the unknown constants a, b can be calculated with Eq. 3.16.

This yields the adiabatic longitudinal quench propagation velocity for $T_b < T_c$

$$v \equiv v_{adiab} = \frac{I}{cA}\sqrt{\frac{\rho_{cu}k}{T_c - T_b}} \tag{3.19}$$

The index adiabatic in Eq. 3.19 includes the longitudinal heat conduction which is neglected for the temperature evaluation as a function of the quench load (Eq. 3.5). Neither of the equations include the heat transfer into helium.

The above considerations assumed constant material properties (ρ, k, c). Even if these properties are averaged between T_b and T_c this assumption is an additional error source. The specific heat can be parameterised as a function of temperature $c(T) = aT + bT^3$. The linear term comes from the conduction electrons, the cubic term from lattice vibrations. The coefficients can be calculated with the free-electron-gas model and the Debye theory of lattice specific heat.

Using the Wiedemann-Franz law $L_0 T = \rho k$ with $L_0 = 2.45 \cdot 10^{-8}$ V^{2}K^{-2} the adiabatic quench propagation velocity (Eq. 3.19) is

$$v = \frac{J}{c(T_b)} \left(\frac{L_0 T_b}{T_c - T_b} \right)^{1/2} \cdot \frac{T_c}{T_b} \tag{3.20}$$

Dresner [49] calculated the adiabatic quench propagation velocity including the linear temperature dependence of the specific heat in Eq. 3.16 as

$$v = \frac{J}{c(T_b)} \left(\frac{L_0 T_b}{T_c - T_b} \right)^{1/2} \cdot \left(\frac{2T_b}{T_b + T_c} \right)^{1/2} \tag{3.21}$$

The T^3 dependence of the specific heat was also treated by Dresner [46] in Eq. 3.16, which gives

$$v = v_{adiab} \sqrt{ \frac{4 T_b^5 (T_c - T_b)}{T_c^2 (T_c^4 - T_b^4)} } \tag{3.22}$$

Using the realistic specific heat in Eq. 3.16 modifies the expression for the quench propagation velocity [49]

$$v = \frac{J(L_0 T_c)^{1/2}}{(c(T_c) \int_{T_b}^{T_c} c(T') dT')^{1/2}} \tag{3.23}$$

Dresner also deduced a correction factor which takes into account the effect of current sharing [46]. Eqs. 3.19–3.23 assume $T_b < T_c$.

Effect of Transverse Cooling

Wilson [11] derived an expression for the quench propagation velocity including transverse cooling by heat transfer into helium. Using the same assumptions as above, the heat balance equation with the moving coordinate ξ including transverse cooling $hP(T - T_b)$ is

$$k \frac{d^2 T}{d\xi^2} + cv \frac{dT}{d\xi} - \frac{hP}{A}(T - T_b) + g(\xi) = 0 \tag{3.24}$$

The temperature in the centre of the quenched zone is T_1 with $T_1 > T_c$ which has reached thermal equilibrium $hP(T_1 - T_b) = \rho_{cu} I^2 / A$. With the boundary conditions $T_w(\xi = 0) = 0.5(T_c + T_b)$, $T \to T_1$ as $\xi \to -\infty$, and $T \to T_b$ as $\xi \to \infty$ the solution for Eq. 3.24 is

$$T(\xi) = \begin{cases} T_1 - (T_1 - T_w) \exp(a_c \xi) & \text{for } \xi < 0 \\ T_b + (T_w - T_b) \exp(-b_c \xi) & \text{for } \xi \geq 0 \end{cases} \tag{3.25}$$

where

$$a_c = \frac{1}{2} \cdot \sqrt{(vc/k)^2 + 4hP/kA} - \frac{vc}{2k} \tag{3.26}$$

$$b_c = \frac{1}{2} \cdot \sqrt{(vc/k)^2 + 4hP/kA} + \frac{vc}{2k} \tag{3.27}$$

$$T_1 = T_b + \frac{g(T_c)A}{hP} \tag{3.28}$$

The requirement for the continuity of the heat flow at the interface between the two regions gives

$$-k\frac{dT}{d\xi}\bigg\|_{\xi\to 0,\xi<0} = -k\frac{dT}{d\xi}\bigg\|_{\xi\to 0,\xi>0} + vQ_L \tag{3.29}$$

where vQ_L represents transient effects in boiling heat transfer. Using Eq. 3.24–3.29 Wilson obtains an expression for the quench propagation velocity including transverse cooling

$$\begin{aligned}v &= \sqrt{\frac{khP}{A}}\frac{T_1 - T_b - 2(T_w - T_b)}{\sqrt{Q_L^2 + Q_Lc(T_1 - T_b) + c^2(T_w - T_b)(T_1 - T_w)}}\\&= v_{adiab}\frac{1 - 2y}{\sqrt{yz^2 + z + 1 - y}}\end{aligned} \tag{3.30}$$

The terms y and z are corrections to the adiabatic propagation velocity due to steady-state and transient heat transfer into helium. Wilson defines the steady-state term y

$$y = \frac{T_w - T_b}{T_1 - T_b} = \frac{hP(T_w - T_b)}{Ag(T_c)} = \frac{A_{cu}hP(T_w - T_0)}{I^2\rho_{cu}} \tag{3.31}$$

The transient term z is formulated in terms of latent heat per unit volume Q_L at temperature T_w

$$z = \frac{Q_L}{c(T_w - T_b)} \tag{3.32}$$

The term Q_L can be used to represent the main transient effect in boiling heat transfer, i.e. the energy needed to establish a vapour film on the transition from nucleate boiling to film boiling [11]. This term is used as a fit parameter.

Turck [50] obtained various equations for the propagation velocity including the effect of cooling. He introduced the reduced velocity as a way to determine whether recovery will take place.

Transverse Quench Propagation

As well as travelling along the conductor, the normal-conducting zone spreads sideways in a coil from turn to turn. The transverse quench propagation can either be expressed as the time needed for a quench to propagate into the adjacent turn Δt_t (turn-to-turn-delay) or as a transverse propagation velocity dominated by the heat conductivity of the insulation material k_t. Without cooling by heat transfer into helium, the ratio of the longitudinal and the transverse propagation velocity is

$$\alpha = \frac{v_{transverse}}{v_{longitudinal}} = \left(\frac{k_t}{k}\right)^{1/2} \tag{3.33}$$

If the insulation layer thickness is not negligible with respect to the dimension of the conductor the heat capacity of the insulation has to be included. It follows that

$$\alpha = \frac{c_{avm}}{c_{av}}\left(\frac{k_t}{k}\right)^{1/2} \tag{3.34}$$

where c_{av} is averaged over the total cross-section and c_{avm} is taken over the metallic constituents only. With the insulation layer thickness Δl_t the turn-to-turn-delay Δt_t can be calculated with Eq. 3.34

$$\Delta t_t = \frac{\Delta l_t}{\alpha v} \tag{3.35}$$

where v is the longitudinal quench propagation velocity. In fully impregnated coils like the multipole correctors for the LHC Δt_t is in the range of 2–3 ms.

The expressions for the quench propagation velocity presented above are all linearly dependent on the applied current (apart from the correction terms for the impact of transverse cooling). Consequently, these expressions become obsolete in the limit $I \rightarrow I_c$.

Voltage Development

The voltage as a function of time $V(t)$ across an entire magnet coil is

$$V(t) = I(t)R(t) + L(I)\frac{dI(t)}{dt} - \sum_i M_i \frac{dI}{dt} - U_{PC} \qquad (3.36)$$

where $I(t)$ is the current, $R(t)$ is the resistance, $L(I)$ is the self inductance as a function of current, M_i is the mutual inductance of a neighbouring turn or coil, and U_{PC} is the voltage of the power converter that is negligible for most power converters used for superconducting magnets. The mutual inductances are due to the magnetic flux from neighbouring windings. As a result of the induction law this flux induces a voltage when changing with time. Eq. 3.36 does not include the effect of induction due to adjacent windings powered with different currents, which can be important for busbars. Generally, the inductance of a magnet is a function of the applied current because of saturation effects in the iron yoke. At low currents the field contribution of the yoke is proportional to the applied current. This contribution saturates at about 0.6 tesla in the LHC dipole magnets for currents higher than 6 kA, thus reducing the inductance of the magnet by a few percent. Corrector magnets are operated at a higher margin (smaller ratio of operating current to critical current) and their inductance is nearly independent of the applied current in the entire operating range.

Supposing the inductance is constant with current, the voltage for a quenching zone can be expressed as

$$V_Q(t) = I(t)R(t) + L_Q(t)\frac{dI}{dt} \qquad (3.37)$$

where L_Q is the partial inductance and $R(t)$ is the resistance of the quenching zone. Assuming $U_{PC} \approx 0$ and ignoring the mutual inductance, Eq. 3.36 reduces to

$$-L\frac{dI}{dt} = I(t)R(t) \qquad (3.38)$$

The combination of Eq. 3.37 and 3.38 leads to

$$V_Q(t) = I(t)R(t) \cdot (1 - L_Q(t)/L) \qquad (3.39)$$

During a quench the resistance and the partial inductance of the expanding normal-conducting zone grow. After quench detection the power converter is switched off and the current starts to decay. As a consequence the voltage rises to a peak value and then falls. A schematic diagram of the voltage distribution around the circuit of a quenching superconducting magnet is shown in Fig. 3.3.
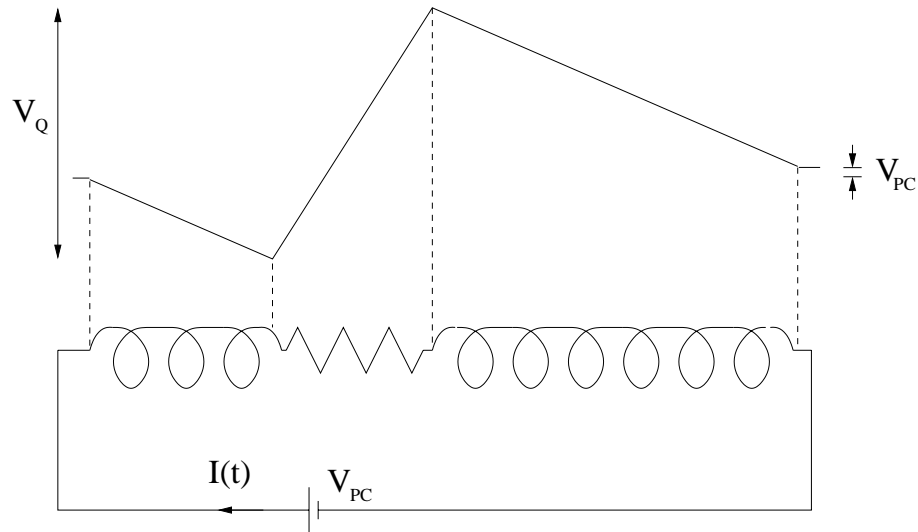
Figure 3.3: *Schematic view of the voltage distribution around the circuit of a quenching superconducting magnet.*

Mutual Inductances

The calculation of the mutual inductances of N voltage signals is necessary to derive the resistive fraction of a voltage signal, which is a sum of an inductive and a resistive part:

$$U_i(t) = U_{tap1} - U_{tap2} = R_i(t)I_i(t) + L_i(I_i(t))\frac{dI_i(t)}{dt} - \sum_{j=1, j\neq i}^{N} M_j(I_j(t))\frac{dI_j(t)}{dt} \qquad (3.40)$$

Measurements showed that within an accuracy of 5% L_i and M_j can be considered as being constant with the excitation current for the LHC dipole magnets. If a higher precision is required, the saturation effects of the iron yoke have to be taken into account.

Resistance Growth and Current Decay

During a quench with an expanding normal-conducting zone the resistance grows for several reasons:

- the expanding normal-conducting zone increases the resistance $R(t) = \rho l(t)/A = \rho v t/A$.

- in a magnet coil the resistance also increases due to the transverse quench propagation that causes neighbouring turns to quench $R(t) = \rho l/A \cdot (1 + \text{int}(t/\Delta t_t))$.

- the resistivity is temperature dependent. Since the temperature in the normal-conducting zone increases, this causes a further resistance growth.

When the power converter is switched off, the current starts to decay due to the resistance in the circuit. If the resistance of the circuit is assumed to be a constant, the current decays as $I(t) = I_0 \exp(-t/\tau)$ with $\tau = L/R$. As the resistance is a function of time, the current decay is

$$I(t) = I_0 \exp\left(\frac{-\int_{t_0}^{t} R(t')dt'}{L}\right) \tag{3.41}$$

The current decay after a quench can be approximated with analytical functions which is presented in Section 3.4. Wilson [11] derived an analytical equation for the resistance growth and the current decay with simplified assumptions. He supposes that the resistivity is a linear function of the temperature and the temperature increases with the square root of time. The current density is constant until the entire stored energy is dissipated and then abruptly falls to zero. These assumptions give the resistance as a function of time

$$R(t) = \frac{4\pi\rho_0\alpha^2 J_0^4 v^3 t^5}{30 A^2 T_b^2} \tag{3.42}$$

The index 0 stands for a value at the quench starting time. In this model the time t_Q needed to dissipate the stored energy is evaluated from

$$\int_0^{t_Q} I(t)^2 R(t)dt = \frac{1}{2}LI_0^2 \tag{3.43}$$

and gives

$$t_Q = \left(\frac{90 L T_b^2 A}{4\pi J_0^4 \rho_0 \alpha^2 v^3}\right)^{1/6} \tag{3.44}$$

Using Eq. 3.42 and 3.43 Wilson calculated the current decay as

$$I(t) = I_0 \exp(-t^6/(2t_Q)^6) \tag{3.45}$$

3.1.3 Case Study: Application of Analytical Models for LHC Dipole Magnets and Busbars

Comparison of Quench Propagation Velocities

Fig. 3.4 shows the application of the various expressions for the quench propagation velocity for the 600 A busbar cable. The difference between the calculated value with and without cooling by heat transfer into helium is understandable, but the scatter between various adiabatic equations demonstrates their limited use. The uncertainty of modelling the heat transfer into helium causes the quench propagation velocity to vary by a factor of more than 20 at a nominal current of 550 A. Tests on various prototype busbar cables resulted a quench propagation velocity at 600 A in the range of 8–10 m/s [51].

The application of the adiabatic quench propagation velocity with averaged specific heat gives 80 m/s at 11.8 kA for the cable used for the outer layer of the LHC dipole magnets. Since the Rutherford cable is exposed to helium (measured helium content in the cable is about 4.5 %) the cooling should be taken into account. Applying Wilson's equation the quench propagation velocity is about 40 m/s (without using the term Q_L as a fit parameter). The measured values are in the range of 15–20 m/s showing that the cooling impact is difficult to predict by analytical equations.
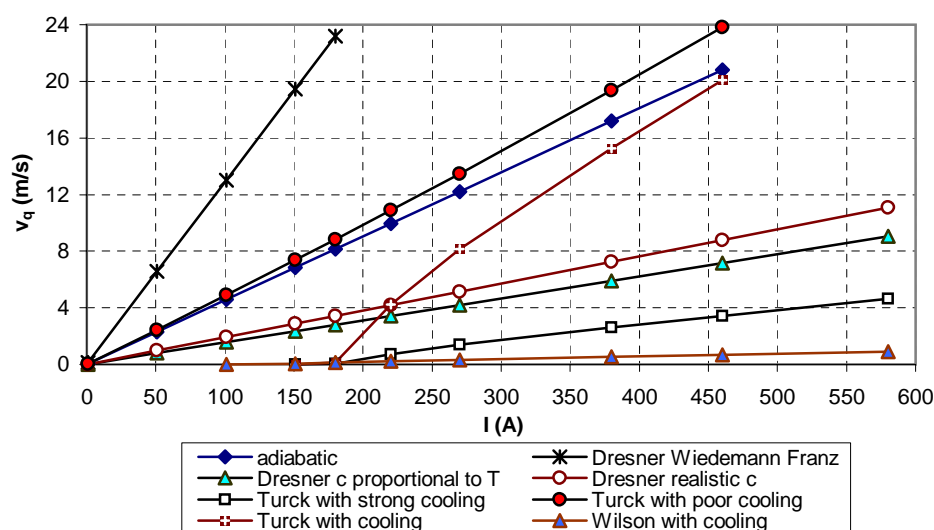
Figure 3.4: *The quench propagation velocity as a function of the applied current calculated with various formulas that were presented in Section 3.1.2. The expressions for the quench propagation velocity were deduced by Wilson [11], Dresner [49], and Turck [50]. The calculations were performed for the auxiliary busbar powering the LHC corrector magnets (A_{tot} =2 mm², $r_{cu/sc}$ =9, RRR =100). A comparison with the measured quench propagation velocity as a function of applied current is given in Fig. 5.10.*

The quench propagation for a prototype main busbar was measured to be about 0.3–0.4 m/s at 12 kA. The adiabatic calculation gives 3 m/s and the formula including strong cooling (Turck's formula [50]) yields 2 m/s.

The corrector magnets are fully impregnated coils. Thus, the adiabatic formula is applied. The quench propagation velocity was measured to be 30–40 m/s at 600 A (same cable) but the adiabatic formula gives 70 m/s.

Although there is the significant mismatch of the quench propagation velocity between measurement and analytical equations, the slope of the quench propagation velocity as a function of current is similar and linear.

Adiabatic Temperature Calculations

Eq. 3.5 is a method of calculating the adiabatic hot spot temperature as a function of the quench load. The mismatch of the calculated quench propagation velocity leads to a prediction of a faster current decay, which reduces the quench load and the expected hot spot temperature. Consequently, one may believe that special protection equipment is not required.

On the contrary, the adiabatic calculation of the hot spot temperature for well cooled magnets can also be too conservative. This might lead to an over-design of the protection system for some superconducting circuits.

When the time required to detect a quench is not included, the calculated quench load and expected hot spot temperature are much smaller. The underestimated quench load can lead, for example, to design a copper stabilisation that is too small for protection.

Limitations of Analytic Approaches

An increased copper stabilisation reduces the quench propagation velocity due to a higher heat capacity and less heat generation (see Eq. 3.19). A slower quench propagation velocity increases the time required to reach the quench detection threshold and because there is less heat generation the current decay is slower, which increases the quench load. As the heat capacity is increased, the larger quench load does not necessarily result in a higher temperature (see Eq. 3.5).

The reduction of the copper stabilisation increases the quench propagation velocity and heat generation, which leads to a reduction of the quench load. As there is less material, a smaller quench load can cause a higher temperature.

In order to find a solution to this problem a reliable model is required to evaluate the quench propagation velocity and the hot spot temperature in presence of longitudinal and transverse cooling.

Analytical solutions of the heat balance equation are not available when the strong non-linear dependence of the material properties is included. The impact of the transverse cooling by heat transfer into helium is not taken into account or is strongly simplified in analytical models (see Section 2.7). Although some analytical approaches have been made that include the current sharing regime [49], the resistivity was taken as a constant and thereby limit the usability of the model. An example of the resistivity as a function of temperature is shown in Fig. 3.5. Up to a temperature of about 20 K the resistivity is a function of the RRR and the magneto-resistance but not of the temperature.
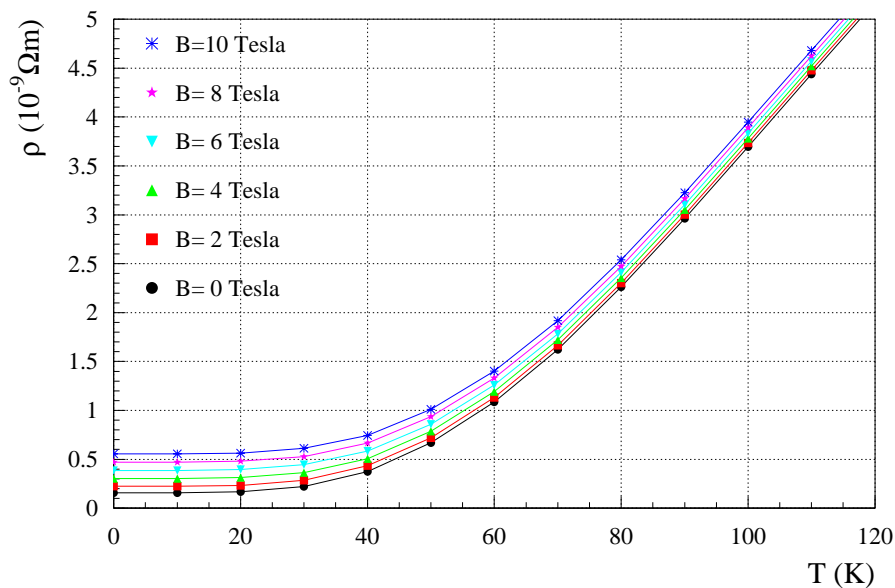
Figure 3.5: *The resistivity as a function of temperature including magneto-resistance: the non-linear dependence at low temperatures because of RRR value and the magneto-resistance demonstrates the limitations of analytical quench models using an averaged value of ρ_{cu}. The resistivity as a function of temperature is calculated for $RRR = 100$.*

The analytic approaches describe a quench in an individual element but do not address a circuit of several superconducting elements connected in series. For a machine as complex as the LHC, the presented examples demonstrate that analytical quench models are inadequate to design the protection system.

3.2 Quench Process Modelling

In order to improve the characterisation of the quench process, numerical methods have to be used to approximate the heat balance equation. Some quench mechanisms are not included in analytical approaches. The resulting simulation model takes the following points into account:

- the non-linear temperature dependence of the material properties, such as the heat conductivity, the resistivity and the heat capacity, has to be included.

- in order to model the heat generation correctly, the current sharing model needs to be implemented.

- a more accurate evaluation of the temperature during a quench requires to model the heat transfer into helium. The temperature dependence has to be taken into account by the cooling model. For insulated conductors, the heat transfer through the insulation layer has to be modelled.

- the magnetic field in magnets is a function of the current. During the current decay, the magnetic field changes and induces eddy currents in the superconducting cable because of the twisted filaments and strands. The magnetisation of a hard superconductor and the heat generation of the eddy currents at contact resistances cause losses that can have an impact on the quench process. This is not covered by any analytical quench model.

- for magnet coils that are protected by quench heaters (see Section 1.5), the simulation model needs to include forced quenching by heat transfer from the heater strip through the insulation layer into the cable.

This list demonstrates that the quench process couples electrodynamic and thermodynamic effects. The following sections present the simulation model that was developed and used for simulation studies for the LHC superconducting magnets and busbars. A suitable coordinate system for the quench simulation is shown in Fig. 3.6.
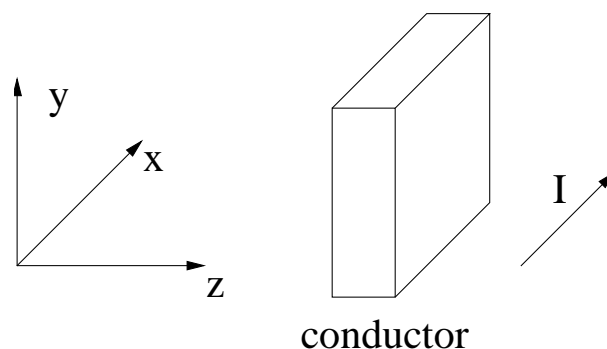
Figure 3.6: *The coordinate system of the simulation model. The current flows parallel to the x-direction.*

3.3   Simulation Programs

Various quench simulation programs have been developed. One of the first numerical codes was named 'QUENCH' (Wilson 1968 [11]). Starting with initial values for the current, length of a normal-conducting zone, and resistance, the quench propagation velocity is calculated with Eq. 3.30 for the local temperature and assumed to be constant for a time interval Δt. The quenched zone during Δt is added and the new resistance is evaluated. The new resistance updates the present current and the propagation velocity recalculated. The process is continued until the current has decayed. The main problem of this first numerical code is that the accuracy of the quench propagation velocity depends on the cooling assumptions. Several modifications of this program exist. Another group of numerical codes approximate the heat balance equation with the finite difference method similar to the numerical approach described further below.

Two quench simulation programs were developed at CERN with the aim of determining the adequate protection of superconducting magnets and busbars. They are presented below.

3.3.1   QUABER - Piecewise Modelling of Electrical Circuits

In order to simulate the voltage and temperature development of a series of magnets the generally applicable simulation package QUABER has been developed (Rodriguez-Mateos et al. [52]), which is based on the professional tool SABER.[1] SABER allows the time transient simulation of any electrical circuit. The QUABER libraries contain the thermodynamic model that defines the resistance development as a function of time for various parts of a magnet. A superconducting magnet is divided into different pieces that are connected according to the electrical powering scheme. This template representing the superconducting circuit is solved time transiently by SABER. Apart from the general magnet geometry (number of turns and layers per coil, magnetic field and length), the QUABER libraries require quench parameters as input data (i.e. the longitudinal quench propagation velocity at the initial current, the time delay for quenching neighbouring turns and layers, and the quench heater delays). The magnetic field map and the conductor parameters are needed to compute the resistivity as a function of temperature, magnetic field and RRR, and the temperature as a function of the quench load.

Reliable QUABER results depend on the input quench parameters that can only be obtained from special experiments or other simulation programs. The uncertainty of the input parameters is the dominating error source of the QUABER outcome. A limitation of the simulation model is due to the adiabatic assumption of the temperature evaluation. The impact of induced eddy currents on the quench process can only be included artificially by forcing a quench at a certain time.

When the input parameters are known from experiments on prototypes or other simulation results, QUABER reliably reproduces the voltage development between turns, coils and magnets. Even if the various input parameters are unknown, QUABER can be used after calibrating the model by fitting the simulated hot spot temperature to reproduce the experimental result. This calibration requires, for example, a change of the quench propagation velocity or the time delay for quenching adjacent turns or layers to reproduce the measured voltages.

On the contrary to other simulation tools, the QUABER approach is able to simulate the protection scheme for a string of superconducting magnets; which means for instance the functionality of parallel resistors and diodes or dump resistors for energy extraction can be tested.

---

[1]Trademark of Analogy Inc.

QUABER was used for the simulation studies presented in this thesis after the required input parameters were determined by experimental results or by other simulation studies with the program SPQR, which is described below. The outcome was used to determine the adequate protection scheme for a series of magnets.

3.3.2 SPQR - Finite Difference Method

The simulation model described below has been developed for this thesis and used to write the finite difference program SPQR[2] (Simulation Program for Quench Research). With respect to existing simulation programs, SPQR includes more quench mechanisms such as the modelling of the transverse cooling by heat transfer through an insulation into helium, forced quenching by heaters, and the impact of dynamic losses by magnetisation and induced eddy currents.

At the program start the material properties are calculated according to the geometry and input parameters (for instance the copper resistivity as a function of RRR and applied magnetic field). The coordinate system was defined in Fig. 3.6 with current flowing in x direction. An initial Gaussian temperature profile is computed to provoke a quench with peak temperature $Tinit$ and sigma xT_decay (also yT_decay and zT_decay for the three-dimensional model). The temperature evaluation depends on the balance of the internal heat generation, the longitudinal heat conductivity, the heat transfer from or into the surrounding environment and the heat capacity of the structure. The start of the current decay can be predefined by the user or determined by parameters of the protection system such as the threshold voltage for quench detection.

The program assumes a homogeneous cross-section of the conductor that can be any mixture of niobium-titanium, copper, and helium (if helium cross-section is not specified, it is assumed to be zero). A helium fraction has to be included for the quench simulation in Rutherford cables where helium is present between the strands. The material properties of copper are calculated depending on the RRR and magnetic field values. According to the proportion of copper, niobium-titanium, and helium, the averaged heat capacity, conductivity and resistivity are determined as a function of temperature and stored in a look-up table. During the program execution, the structure is treated as being homogeneous per discrete element.

The quench detection time (for validating the quench signal, Section 1.5) is t_{det}. If the quench originates in the first element (standard mode), the program evaluates the propagation in one direction only, thus saving computation time. In this case the resistive voltage is doubled to take into account that in reality the quench propagates in two directions along the conductor.

The simulation results are written to ASCII table files for further analysis. The program execution can include various quench mechanisms. The standard setup assumes a symmetric temperature development around the hot spot which means that calculating half of the propagating normal zone is sufficient. However, the user can also choose where the quench starts and force the endpoints to be kept at a constant temperature that allows estimating worst case scenarios.

The quench processes that can be simulated with the different models are summarised in the Tables 3.1 and 3.2 and are explained in the Sections 3.4 and 3.5.

---

[2]The abbreviation SPQR for the program name was chosen as the simulation model has first been presented at a workshop in Frascati [53]. SPQR stands for senatus populusque romanus in Latin – the Senate and the People of Rome.

	1D	1DI	1DH	1DHM	3D	3DC	ED	EDM	P
longitudinal propagation	x	x	x	x	x	x	x	x	x
transverse propagation					x	x			
heater delays			x	x	x	x	x	x	
heater performance			x	x	x	x	x	x	
quench back							x	x	
cooling impact	x	x	x	x	x	x	x	x	x
insulation layer		x	x	x	x	x	x	x	x
matrix model				x		x		x	x
plug calculations									x

Table 3.1: *Overview of the possible combinations of quench processes included in SPQR and their applications. The different quench mechanisms are explained in Sections 3.4 and 3.5.*

1D	one dimension, Joule heating, conduction, direct heat transfer into helium bath, thermal impedance
1DI	as 1D with modelling of the insulation layer with linear approximation
1DH	as 1DI with forced quenching by heaters through an insulation layer
1DM	as 1D with discretised modelling of the insulation layer
1DHM	as 1DM with forced quenching by heaters
3D	as 1DH for three dimensions for main magnets (with Rutherford type cables)
3DC	as 1DH for three dimensions for corrector magnets (fully impregnated coils, helium only at the end elements)
ED	as 1DH with modelling of induced eddy currents
EDM	as 1DHM with modelling of induced eddy currents
P	as 1DM with two different materials of the insulation layer along the conductor

Table 3.2: *Names for the available quench models in SPQR.*

3.4 Electrodynamic Processes

The electrodynamic processes during a quench include the Ohmic heat generation and the dynamic losses due to magnetisation and the induction of eddy currents.

3.4.1 Ohmic Heat Generation

Using a linear approach between the critical current and temperature the temperature dependence of the heat generation rate including current sharing is (see Section 3.1)

$$G(T(x,t),t) = \begin{cases} 0 & \text{if } T(x,t) \leq T_{cs}(t) \\ \rho_{cu}(T(x,t))\frac{I(t)^2}{A_{cu}(x)}\frac{T(x,t)-T_{cs}(t)}{T_c(t)-T_{cs}(t)} & \text{if } T_{cs}(t) < T(x,t) \leq T_c(t) \\ \rho_{cu}(T(x,t))\frac{I(t)^2}{A_{cu}(x)} & \text{if } T(x,t) > T_c(t) \end{cases} \tag{3.46}$$

Current Decay

The current decay inside magnets can be modelled with a Gaussian function [54]. Assuming an exponential decay of the current is appropriate for the quench simulation in a busbar. The current starts to decay when the resistive voltage U_{res} exceeds a detection threshold U_{thres}. Several functions for the current decay can be chosen in SPQR

$$I(t) = \begin{cases} I_0 & \text{if } U_{res}(t) < U_{thres} \\ I_0 \exp\left(-\frac{t-t_{det}}{\tau}\right) & \text{if } U_{res}(t) \geq U_{thres} \wedge \text{mode=exp} \\ I_0 \exp\left(-\frac{(t-t_{det})^2}{\tau^2}\right) & \text{if } U_{res}(t) \geq U_{thres} \wedge \text{mode=gauss} \\ I_0 - k \cdot (t - t_{det}) & \text{if } U_{res}(t) \geq U_{thres} \wedge I(t) > 0 \wedge \text{mode=lin} \\ 0 & \text{else} \end{cases} \tag{3.47}$$

The current decay can also be evaluated using the resistance growth of the normal-conducting zone plus an optional external resistance

$$I(t) = \begin{cases} I_0 & \text{if } U_{res}(t) < U_{thres} \\ I_0 \cdot \exp\left(-\int\limits_{t_{det}}^{t} \frac{R(t')+R_{ex}}{L} dt' \cdot (t - t_{det})\right) & \text{if } U_{res}(t) \geq U_{thres} \wedge \text{mode=R(t)} \end{cases} \tag{3.48}$$

3.4.2 Magnetisation and Eddy Current Losses

An electric field $\vec{E}$ is induced in presence of a magnetic field $\vec{B}$ changing with time due to Maxwell's law

$$\frac{d\vec{B}}{dt} = -\nabla \times \vec{E} \tag{3.49}$$

The electric field is related to a current density in a conductor by Ohm's law

$$\begin{aligned} \vec{J} &= \sigma\vec{E} \\ \sigma &= \frac{1}{\rho} \end{aligned} \tag{3.50}$$

This section explains the effect of dynamic losses (AC losses) due to eddy currents and magnetisation losses that are induced during the decay of the magnetic field after a quench and that limit the current ramp rate. These induced eddy currents can provoke a quench in a large fraction of the magnet, which is referred to as magnetic quench back.

The influence on the field quality has been discussed for example by T. Ogitsu [55]. The numerical model is based on the work of Devred, Morgan, Niessen, Ogitsu, Verweij and others [55, 56, 57, 58] and is here applied to the quench process.

Different types of eddy currents are induced in magnets:

- *eddy currents in copper spacers, collars and yokes*
  The changing magnetic field induces eddy currents not only in the cable but also in the copper spacers (wedges) in between the conductor blocks, the magnet collars and the iron yoke. The collars and the iron yoke are made of laminations to reduce the strength of the induced eddy currents. Copper wedges are installed to separate the different magnet coils in order to approximate the cosine like current distribution that is required to obtain the desired magnetic field (see Section 1.3.1). The eddy currents in the copper spacers cause these parts to behave as secondary inductances that extract energy [59]. For the case of the LHC main magnets, the amount of energy dissipated into the copper wedges was calculated to be less than a few percent of the stored magnetic energy.

- *interfilament coupling currents*
  Each strand is made of many NbTi filaments embedded in a copper matrix. The filaments are twisted over the length L_p^f. The trajectory along the strand (in x direction) of two neighbouring filaments in the projection perpendicular to the applied external magnetic field are two sinusoid curves crossing each other. At the crossing point of the projections, the two filaments have the minimum distances d_{min} (see Fig. 3.7). A changing magnetic field
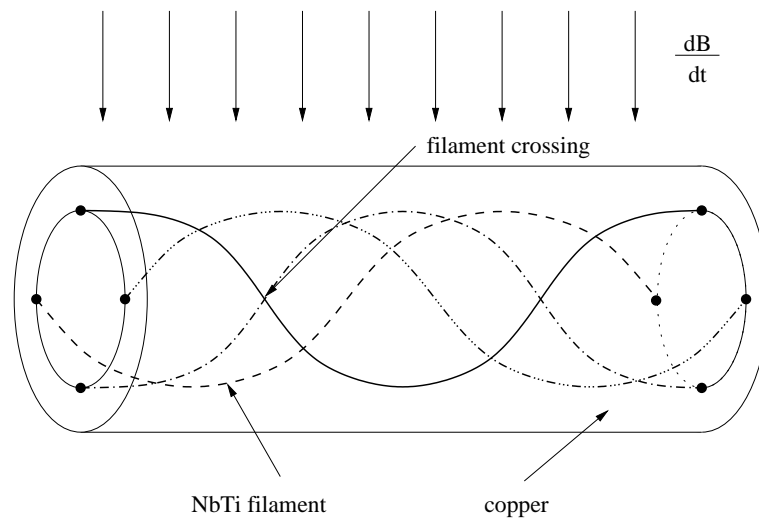
Figure 3.7: *Induced eddy currents between filaments in a strand. The length shown is the filament twist pitch length L_p^f.*

induces a coupling current from one filament to the other. Due to the symmetric structure, the strengths of this interfilament coupling current can be calculated independent from x as a function of the filament diameter d_f, L_p^f and the changing applied magnetic field dB/dt.

- *interstrand coupling currents*
  The superconducting cable used for the LHC main busbars and magnets is a Rutherford type cable consisting of several strands (36 strands in the cable for the outer layer of the

dipole magnets and 28 strands in the cable for the inner layer of the dipole magnets). The cable has a width w and a diameter d. The strands are twisted with the cable pitch L_p^s and cross in both transverse planes, the $x - y$ and the $x - z$ plane, with the corresponding contact resistances R_a and R_c (see Fig. 3.8). The averaged strength of the coupling currents
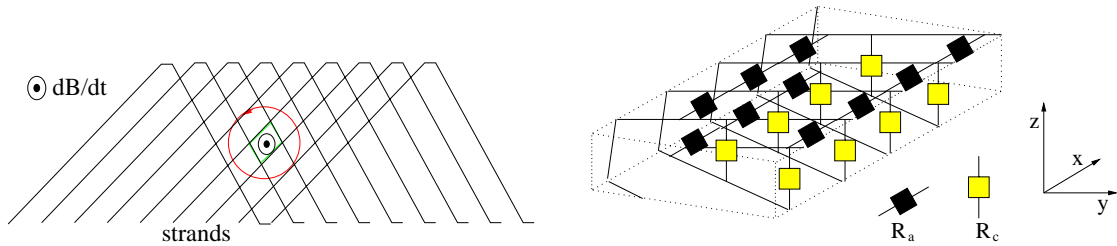
Figure 3.8: *Sketch of a Rutherford cable (see Fig. 2.10) including the interstrand contact resistances R_a (adjacent strand contact resistance) and R_c (inter layer contact resistance).*

is numerically calculated as a function of the applied magnetic field components parallel $B_\parallel$ and perpendicular $B_\perp$ to the broad side of the cable, R_a and R_c, w and L_p^s, and the number of parallel strands N_p and layers of strands N_s (two for Rutherford cables).

If the magnetic field varies across the width of the cable, the interstrand coupling currents can only be numerically evaluated. Interstrand currents can close a loop that is by far larger than the length of one cable pitch when the magnetic field varies along the cable or when the value of the contact resistances R_c and R_a are not constant. In this case the induced eddy currents are known as boundary induced coupling currents that have been predicted and experimentally verified [60, 61].

A quench starts if the interfilament or the interstrand currents added to the transport current exceed the critical current of a filament or a strand. The quench condition is $I(t) > I_c(T(t), B(t), dB/dt(t))$.

A quench can also occur since the temperature increases due to the power of interfilament and interstrand coupling currents. This leads to the quench condition $T(t) > T_c(I(t), B(t), dB/dt(t))$.

Both effects are called magnetic quench back.

In order to calculate the power of the induced coupling currents, their built-up time that is characteristic for the dimensions of the filaments, the strands and the cable has to be considered. Another effect leads to magnetisation losses: A high enough external magnetic fields penetrates the filament and causes a magnetisation that results in a hysteresis and an additional contribution to the power loss while changing the magnetic field strength $d/dt \int M(B)dB$ (see Section 2.3.1).

During the development programme for the LHC, many different types of prototype magnets were tested. The current decay and voltages across parts of the magnet, such as poles or blocks, were recorded during training quenches and quenches were provoked with heaters. Here, observations for two types of magnets are outlined that will be described in more detail in Chapters 6 and 7.

During the test of a sextupole magnet, one pole quenched and the current decayed from 600 A with a time constant in the order of 100 ms [62]. An inductive voltage was observed across the non-quenching poles for about 60 ms, showing that only one pole started to quench. After about 60 ms all other poles quenched. For a magnet with impregnated coils, a quench propagation along the wire to all other coils at the same time is not possible, but this observation can be fully explained by quench back.

In an experiment with a 10 m long prototype dipole magnet, only the heaters installed on the coils in one aperture of the twin aperture magnets were fired [54]. The current in the magnet decayed with a time constant of about 150 ms. The inductive voltage across the coil in a non-quenching aperture would exceed 1 kV. In the experiments it was observed that the voltage did not exceed 100 V, which is explained by a fast quench of the second aperture. A thermo-hydraulic quench propagation is unlikely, since the time constant of quench propagation via warm helium is several seconds [63]. When quench back is included in the simulation the observations can be understood.

Following M.A.Green [64], quench back in superconducting magnets has two causes:

- *thermal quench back*
  Normal regions can be induced by heat transfer from components outside the coil to the superconductor. Thermal quench back is used in superconducting solenoid magnets as an integral part of the magnet quench protection system [65].

- *magnetic quench back*
  Normal regions can be induced by AC losses from eddy currents in the superconductor due to a changing magnetic field. Eddy currents and AC losses have been investigated in order to understand field errors during the current ramp, when eddy currents dominate the field errors in accelerator magnets. Interstrand coupling currents in Rutherford type cables were modelled by means of a discrete network of nodes by Niessen [57] and Verweij [58]. AC losses from interfilament coupling currents have been investigated by Morgan [66]. The impact of interfilament coupling currents for the protection of multicoil magnets has been studied by Takeuchi [67]. In addition, the impact of interstrand coupling currents on the quench process has been analysed for this thesis.

For the LHC main dipole and quadrupole magnets, after firing quench heaters, the excitation current decays with a time constant in the order of some hundred milliseconds, compared to the time for current ramping of about 20 min. The losses from both interfilament and interstrand currents for a fast change of the magnetic field during a quench are some orders of magnitude larger than AC losses during the ramp. Heating power due to interstrand and interfilament coupling currents can quench large fractions of the magnet coils after some ten milliseconds. The superconductor would also quench when the sum of excitation current and induced current exceeds the critical current, but this has not been observed in the LHC magnets [53].

Contact Resistances

The contact resistance of the interfilament coupling currents is determined by the resistance of the copper bulk. The quality of the copper and the geometry of a strand defines its value.

Two types of contact resistances occur in a Rutherford type cable: the interlayer contact resistance R_c and the contact resistance between adjacent strands in the same layer R_a. Due to the fabrication process of copper stabilised NbTi cables, R_c is much smaller than R_a (R_c=10–30 $\mu\Omega$, R_a=50–300 $\mu\Omega$).

Modelling

The formalism presented below for the calculation of the eddy currents was summarised by Vervweij [58]. For an applied magnetic field $B > B_p$ (B_p is the penetration field) the magnetisation loss per unit volume is

$$M = -\frac{2}{3\pi} J_c d_f \frac{dB/dt}{|dB/dt|} \tag{3.51}$$

where $J_c = I_c/A_{NbTi}$ is the critical current density and d_f is the filament diameter. The interfilament currents are given by

$$I_{if}(t) = \frac{dB}{dt} \frac{L_p^{f2} d_f}{4\pi^2 \rho(T(t))} \cdot \left(1 - exp\left(-\frac{t}{\tau_{if}}\right)\right) \tag{3.52}$$

$$\tau_{if} = \frac{\mu_0}{2\rho(T(t))}\left(\frac{L_p^f}{2\pi}\right)^2 \tag{3.53}$$

where τ_{if} is the time constant of the interfilament coupling current (about 5–20 ms for the LHC strands) and L_p^f is the filament twist pitch. Both effects lead to the combined interfilament losses of coupling currents and magnetisation per unit volume V_{if}

$$P/V_{if} = \frac{1}{\rho}\left(\frac{dB}{dt}\right)^2\left(\frac{L_p^f}{2\pi}\right)^2 \cdot \left(1 - \exp\left(-\frac{t}{\tau_{if}}\right)\right)^2$$
$$+ \frac{2}{3\pi} J_c d_f \left|\frac{dB}{dt}\right|\left(1 - \exp\left(-\frac{t}{\tau_{if}}\right)\right) \tag{3.54}$$

The interstrand currents have been computed for a Rutherford cable of the LHC type [58]

$$I_s = \left(0.0415\frac{L_p^s w N_{s,l}}{R_c}\frac{dB}{dt}\cos(\phi) + 0.25\frac{L_p^s h}{R_a N_{s,l}}\frac{dB}{dt}\sin(\phi)\right)\left(1 - \exp\left(-\frac{t}{\tau_{is}}\right)\right) \tag{3.55}$$

$$\tau_{is} = 1.68 \cdot 10^{-8}\frac{L_p^s(N_{s,l}^2 - 4N_{s,l})}{R_c} \tag{3.56}$$

with L_p^s being the strand twist pitch, $N_{s,l}$ the number of strands per layer, w the width and h the height of the strand. Typical values of τ_{is} are about 20–30 ms for the LHC Rutherford cables. The angle ϕ determines the parallel and rectangular components of the magnetic field with respect to the broad side of the cable (a perpendicular field component has $\phi=0$, a parallel field component has $\phi=\pi/2$). The interstrand losses per unit volume V_{is} are given by

$$P/V_{is} = \left(0.170\frac{L_p^s w^2(1 - 1/N_{s,l})}{R_a}(\cos(\phi))^2 + 0.125\frac{L_p^s h^2}{R_a}(\sin(\phi))^2 + \right.$$
$$\left. 8.49 \cdot 10^{-3}\frac{L_p^s w^2(N_{s,l}^2 - N_{s,l})}{R_c}(\cos(\phi))^2\right)$$
$$\left(\frac{dB}{dt}\right)^2\left(1 - \exp\left(-\frac{t}{\tau_{is}}\right)\right)^2 \tag{3.57}$$

For the simulation of the impact of eddy currents, the magnetic field as a function of the current can be expressed as $B(I(t)) = a + bI(t)$ [58] and the time derivative can be easily computed.

3.4.3 Eddy Currents in Copper Spacers

The coupled system of the magnet coil and the induced eddy currents in copper spacers (wedges) can be expressed in two differential functions for the current. The differential equation for the current inside the magnet is

$$R_{mag}(t)I_{mag}(t) + L_{mag}(t)\frac{dI_{mag}(t)}{dt} - M\frac{dI_{cu}(t)}{dt} = 0 \tag{3.58}$$

where I_{mag} is the magnet current and I_{cu} is the current in the copper spacer. The differential equation for the current inside the copper spacer is

$$R_{cu}(t)I_{cu}(t) + L_{cu}(t)\frac{dI_{cu}(t)}{dt} - M\frac{dI_{mag}(t)}{dt} = 0 \tag{3.59}$$

As a first approach the conductor symmetry is simplified according to Fig. 3.9. The copper block
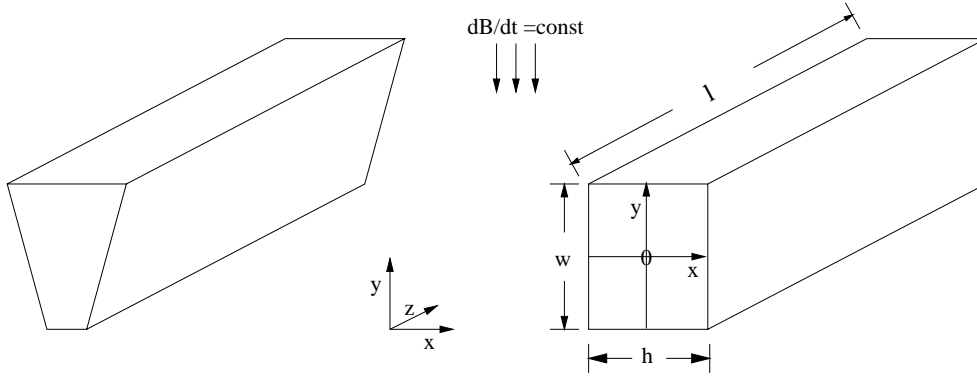
Figure 3.9: *Changed geometry of the copper spacer.*

is taken as a right parallelepipeds with average thickness h and width w. The origin is chosen to be in the middle of the block in the x-y plane. As the dimensions in x and y are small compared to the length of the magnet the eddy current is calculated for the limit $l \rightarrow \infty$. The magnetic field change dB/dt is taken to be constant with time and independent from x, y, z. Using the induction law (Eq. 3.49) and choosing the coordinate system such that $\vec{B} = (0, B, 0)$ yields

$$
\begin{aligned}
\frac{dE_z}{dy} - \frac{dE_y}{dz} &= 0 \\
\frac{dE_x}{dz} - \frac{dE_z}{dx} &= -\frac{dB}{dt} \\
\frac{dE_y}{dx} - \frac{dE_x}{dy} &= 0
\end{aligned}
\tag{3.60}
$$

For $l \gg w$ and $l \gg h$ one can assume that the electric field is not a function of z so that

$$
\begin{aligned}
\frac{dE_x}{dz} &= 0 \\
\frac{dE_y}{dz} &= 0
\end{aligned}
\tag{3.61}
$$

As $\vec{E} \perp \vec{B}$ one obtains

$$E_y \equiv 0 \tag{3.62}$$

and therefore E_x and E_z do not depend on y. Combining Eq. 3.62 and 3.61 with Eq. 3.60 gives

$$\frac{dE_z}{dx} = \frac{dB}{dt} \tag{3.63}$$

The Maxwell equation (Eq. 3.49) can be written in the integral form

$$\int_V \vec{\nabla} \times \vec{E} = \oint \vec{E} dS = -\int_V \frac{d\vec{B}}{dt} \tag{3.64}$$

which for the given symmetry can be reduced to

$$E_z(x) = \int\limits_{-x_{max}}^{x_{max}} \frac{dB}{dt} dx \tag{3.65}$$

With the chosen origin, integrating Eq. 3.65 gives

$$E_z(x) = \frac{dB}{dt} \cdot x \tag{3.66}$$

The current density $\vec{J}$ in a conductor depends on $\vec{E}$ according to Ohm's law

$$\vec{E} = \vec{J} \cdot \rho \tag{3.67}$$

and $\vec{J}$ becomes

$$\vec{J} = (0, 0, J_z) = J_z(x) = \frac{\frac{dB}{dt} x}{\rho} \tag{3.68}$$

The current is $I = \int J dA$ which gives

$$I(x) = \frac{dB}{dt} \cdot \frac{x^2 y_{max}}{2\rho} \cdot \frac{x}{|x|} \tag{3.69}$$

with the condition

$$\oint I dA = 0 \tag{3.70}$$

The total power P is calculated disregarding the effects at the ends of the coil and using z_{max} as the length of the copper wedge

$$P(t) = \int \rho J^2 dV = RI^2 = \left(\frac{dB}{dt}\right)^2 \frac{x_{max}^3 y_{max} z_{max}}{\rho} \tag{3.71}$$

With the volume $V = 2 \cdot x_{max} y_{max} z_{max}$ the power at time t is

$$P(t) = \left(\frac{dB}{dt}\right)^2 \frac{V x_{max}^2}{2\rho} \tag{3.72}$$
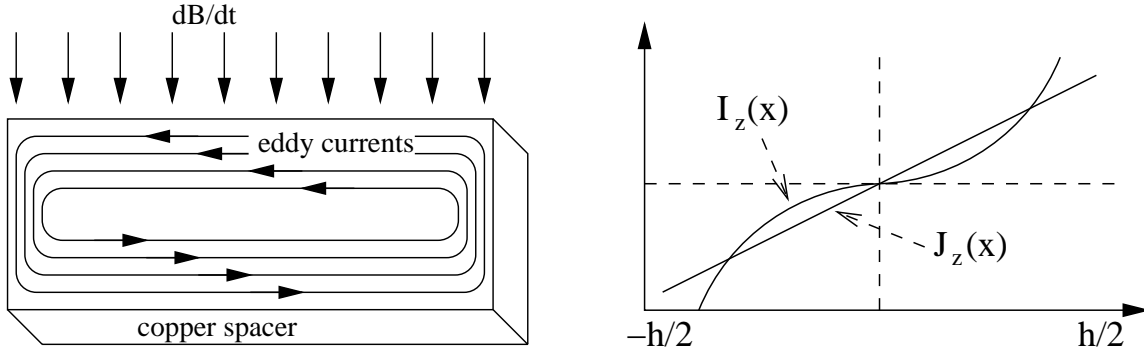
Figure 3.10: *Eddy current distribution and x dependence of I_z and J_z.*

Fig. 3.10 shows the current distribution and the dependence of I_z and J_z on x. An average value of ρ is taken as a constant independent of B and T. The current decay inside the magnet is assumed to be Gaussian like. Using a linear relationship between B and I, the time dependent change of the magnet field is

$$B(t) = a + bI(t) \tag{3.73}$$

$$I(t) = I_0 \exp\left(-\frac{t^2}{\tau^2}\right) \tag{3.74}$$

$$\frac{dI(t)}{dt} = -I_0\frac{t}{\tau^2}\exp\left(-\frac{t^2}{2\tau^2}\right) \tag{3.75}$$

$$\frac{dB}{dt} = -bI_0\frac{2t}{\tau^2}\exp\left(-\frac{t^2}{\tau^2}\right) \tag{3.76}$$

Inserting Eq. 3.76 in Eq. 3.72 gives

$$P(t) = \left(bI_0\frac{2t}{\tau^2}\exp\left(-\frac{t^2}{\tau^2}\right)\right)^2 \frac{Vx_{max}^2}{2\rho} \tag{3.77}$$

The energy dissipated into the copper wedges is

$$E(t) = \int_0^t P(t')dt' \tag{3.78}$$

Combining Eq. 3.77 and Eq. 3.78 yields

$$E(t) = \int_0^t \left(bI_0\frac{2t'}{\tau^2}\exp\left(-\frac{t'^2}{\tau^2}\right)\right)^2 \frac{Vx_{max}^2}{2\rho}dt'$$

$$= \left(\frac{bI_0}{\tau^2}\right)^2 \frac{2Vx_{max}^2}{\rho} \int_0^t t'^2 \exp\left(-\frac{t'^2}{\tau^2}\right)dt' \tag{3.79}$$

The last integral includes the function $\Gamma(x)$, which gives

$$\int_0^\infty x^2 \exp(-a^2x^2)dx = \frac{\sqrt{\pi}}{4a^3} \tag{3.80}$$

for $a > 0$ (Bronstein [68]). With τ being $1/a$, Eq. 3.79 can be calculated for $t \rightarrow \infty$

$$
\begin{aligned}
E_{tot} = \lim_{t \to \infty} E(t) &= \left(\frac{bI_0}{\tau^2}\right)^2 \frac{2V x_{max}^2}{\rho} \frac{\sqrt{\pi}\tau^3}{4} \\
&= (bI_0)^2 \frac{V x_{max}^2}{\rho} \frac{\sqrt{\pi}}{2\tau}
\end{aligned}
\tag{3.81}
$$

Inserting numbers of the LHC dipole magnet in Eq. 3.81, the maximum energy dissipated in the copper wedges is less than 5 % of the stored magnetic energy. This demonstrates the small influence of the energy dissipated into the copper wedges from the protection point of view.

A more realistic approach is possible if the magnet field is known as a function of x and y. The real geometry requires the radial magnet field $B_r \equiv B(x,y)$ instead of B_y. One should note that the temperature dependence of the copper resistivity was neglected in the derivation of Eq. 3.81.

3.5 Thermodynamic Processes

The heat balance equation Eq. 3.1 was introduced in Section 3.1 and the various heat sources were covered in Section 3.4. This section presents the thermodynamic processes during a quench.

3.5.1 Heat Transfer Modelling

The cooling by helium is expressed by the heat transfer coefficient h and the wetted perimeter P, which is $P = f \cdot 2\pi r$ for a circular conductor (r is the radius and f the effective fraction). P corresponds to the surface per unit length of the conductor that is exposed to liquid helium. Since this parameter is unknown it can either be estimated from experience or be modified such that the simulation output reproduces experimental results, i.e. the quench propagation velocity and the hot spot temperature. The heat transfer models available in SPQR assume an infinite helium bath with constant temperature. A possible quench acceleration due to convection of forced helium-flow is not simulated.

The equations for the temperature dependence of the heat transfer coefficient are derived from the helium cooling mechanisms presented in Section 2.7. The cooling conditions can be approximated using different heat transfer model to helium (h_1^{He}–h_4^{He}) as follows

$$
h_1^{He}(T(x,t),t) = \begin{cases} 0 & \text{if } T(x,t) \leq T_b \vee t - t(T > T_{f.boil}) > t_{f.boil} \\ a_1 \cdot (T(x,t)^4 - T_b^4) & \text{if } T(x,t) \leq T_{f.boil} \\ a_2 \cdot (T(x,t) - T_b) & \text{if } T(x,t) > T_{f.boil} \wedge t - t(T > T_{f.boil}) < t_{f.boil} \end{cases}
\tag{3.82}
$$

This model of heat transfer is based on a fourth order Kapitza resistance (constant a_1 and the temperature to the power of four) below the film boiling temperature, and on the linear cooling model for the film boiling region (see Section 2.7)

$$
h_2^{He}(T(x,t),t) = \begin{cases} 0 & \text{if } T(x,t) \leq T_b \vee t - t(T > T_{f.boil}) > t_{f.boil} \\ a_1 \cdot (T(x,t)^4 - T_b^4) & \text{if } T(x,t) \leq T_{f.boil} \\ a_3 & \text{if } T(x,t) > T_{f.boil} \wedge t - t(T > T_{f.boil}) < t_{f.boil} \end{cases}
\tag{3.83}
$$

This heat transfer model is slightly modified such that a constant is used above film boiling temperature instead of a constant times the temperature difference with respect to the bath

$$
h_3^{He}(T(x,t),t) = \begin{cases} 0 & \text{if } T(x,t) \leq T_b \\ a_1 \cdot (T(x,t)^n - T_b^n) & \text{if } T(x,t) \leq T_{n.boil} \\ a_2 & \text{if } T_{f.boil} > T(x,t) > T_{n.boil} \\ a_3 \cdot (T(x,t)^m - T_b^m) & \text{if } T(x,t) > T_{f.boil} \wedge t - t(T > T_{n.boil}) < t_{f.boil} \\ a_4 & \text{if } t - t(T > T_{f.boil}) > t_{f.boil} \end{cases} \tag{3.84}
$$

The modified model allows for fitting the heat transfer model according to the surface treatment and differs between nucleate and film boiling conditions [69, 70]. The heat transfer is kept constant between the starting temperature of nucleate boiling and film boiling. The simplest model for heat transfer to liquid helium is

$$
h_4^{He}(T(x,t),t) = a \cdot (T(x,t) - T_b) \tag{3.85}
$$

The constants for the different models of heat transfer into helium strongly depend on the surface treatment [42, 43]. The model 3 (Eq. 3.84) for the heat transfer requires 9 parameters whereas the model 4 (Eq. 3.85) needs only 2 parameters. Fig. 3.11 shows two models for the heat transfer coefficient as a function of temperature (Eq. 3.85 on the left, Eq. 3.84 on the right).
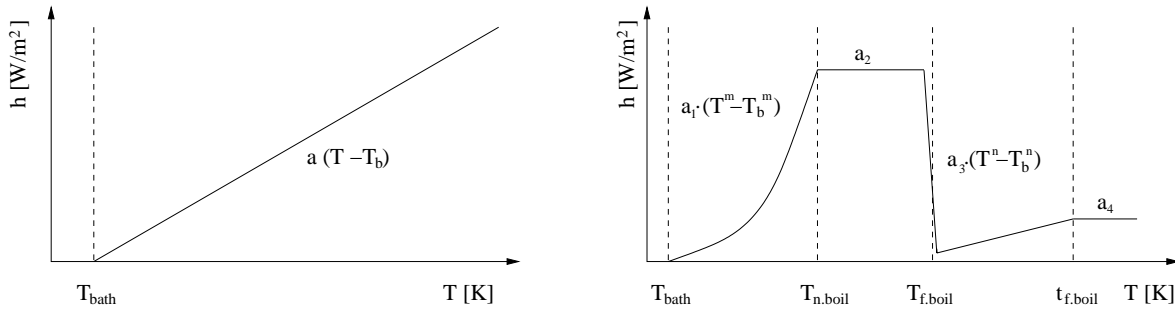
Figure 3.11: *Heat transfer coefficient as a function of temperature according to Eq. 3.85 (left) and Eq. 3.84 (right). The left graph assumes a linear temperature dependence of the heat transfer. The right graph includes several cooling regimes: a fourth order Kapitza resistance; nucleate boiling with constant heat transfer where bubbles transport the heat and are replaced by liquid helium; and film boiling where the conductor is entirely surrounded by vaporous helium.*

3.5.2 Insulation Layer

The low heat conductivity of the insulation material limits the amount of heat that is transported into helium. An adequate modelling of the heat transfer through an insulation layer into helium requires a two-dimensional model if the insulation layer thickness is comparable to the dimensions of the conductor. This approach would require a significant amount of computational time. For this reason a different approach is used. The heat balance equation (Eq. 3.1) can be generalised as

$$
\begin{aligned}
&\frac{d}{dx}(A(x)j_x) + G(T(x,t),t) + F_t(T(x,t), \frac{dT(x,t)}{dt}) \\
&= c(T(x,t))A(x)\frac{dT}{dt}
\end{aligned} \tag{3.86}
$$

where $j_x = k(T) \cdot dT/dx$ and F_t is the transverse heat flux from the surface of the superconducting cable, which is a function of the temperature and its time derivative because of the thermal impedance of the insulation layer. As the longitudinal heat propagation inside the insulation layer is negligible with respect to that in the conductor, the transverse heat flux F_t can be evaluated separately, which allows the reduction of the two-dimensional to two one-dimensional problems.

Steady State

In order to study the steady state solution of Eq. 3.86, the function $F_t(T, 0)$ has to be evaluated. The steady state means that the temperature inside the insulation remains constant with time and changes only as a function of its radial position. The heat balance equation is

$$\oint_P \vec{j}_t(r) \cdot d\vec{r} = const \tag{3.87}$$

where $\vec{j} = k(T) \cdot dT/dr$. When the superconducting cable is radial symmetrical the heat balance equation reduces to

$$r \cdot k_{iso} \cdot \frac{dT}{dr} = R_1 \cdot h^{He}(T_{iso}) \tag{3.88}$$

The index iso stands for the material properties of the insulation layer. Eq. 3.88 can be solved with the numerical integral

$$\int_{T_{cu}}^{T_{iso}} k_{iso}(T)dT = R_1 \cdot h^{He}(T_{iso}) \int_{R_0}^{R_1} \frac{1}{r}dr \tag{3.89}$$

This solution investigates stability temperature points and gives a first estimate of T_{max}. As the quench propagation velocity is related to the propagating front of the temperature profile, in which the temperature varies with time to some thousand K/s, the steady state solution is insufficient to model the entire quench process.

Constant Temperature Gradient Approximation

A linear temperature profile inside the insulation material is assumed (see Fig. 3.12), which is an adequate approach if the thickness of the insulation is small compared to the dimensions of the superconducting cable

$$\frac{d}{dx}\left(k(T(x,t))\frac{dT(x,t)}{dx}A(x)\right) + k_{iso}\left(\frac{T(x,t) + T_{iso}(x,t)}{2}\right)P(x)\frac{T_{iso}(x,t) - T(x,t)}{l_{iso}} +$$
$$\dot{q} + G(T(x,t),t) = c(T(x,t))A(x)\frac{dT(x,t)}{dt} \tag{3.90}$$

The temperature T_{iso} on the surface of the insulation that is exposed to the helium bath is evaluated as follows

$$k_{iso}\left(\frac{T(x,t) + T_{iso}(x,t)}{2}\right)P(x)\frac{T(x,t) - T_{iso}(x,t)}{l_{iso}} - h^{He}(T_{iso}(x,t),t)P(x)$$
$$= c_{iso}(T_{iso}(x,t))A(x)\frac{dT_{iso}(x,t)}{dt} \tag{3.91}$$
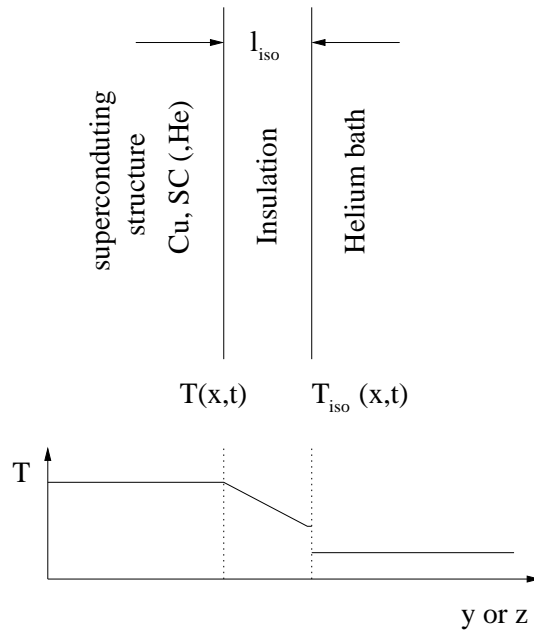
Figure 3.12: *Schematic temperature profile including heat transfer through insulation. The temperature jump at the surface of the insulation layer to the helium bath is due to the modelling principle. The helium bath is assumed to be infinite and permanently at T_b. The heat transfer is then calculated as a function of the surface temperature with the help of the helium heat transfer coefficient h^{He}. Another approach would require to model the temperature as a function of the position inside the helium bath. This would significantly complicate and lengthen the temperature evaluation process, which is not needed as the simulation aims to evaluate the temperature in the conductor. Therefore the introduction of $h^{He}(T(x,t))$ avoids the computation of the temperature in the helium bath.*

Matrix Evaluation of the Heat Flux

A precise evaluation for the transverse cooling by heat transfer requires to discretise the radial heat balance equation and to solve it time transient. When neglecting the longitudinal heat propagation in the insulation layer with respect to that of the superconducting structure, this equation is

$$-\vec{\nabla} \cdot \vec{j}(r, \varphi) = c_{iso} \cdot \frac{dT_{iso}}{dt} \tag{3.92}$$

Assuming radial symmetry Eq. 3.92 changes to

$$-\frac{1}{r} \frac{d}{dr}\left(r \cdot k_{iso} \cdot \frac{dT}{dr}\right) = c_{iso} \cdot \frac{dT_{iso}}{dt} \tag{3.93}$$

The temperature evaluation starts with a homogeneous temperature profile at T_b inside the insulation layer. The temperature of the superconducting wire is increased with a constant rate $\frac{dT}{dt}$ and the heat flux is evaluated for each temperature step. This procedure is repeated for various rates of $\frac{dT}{dt}$ and the results are stored in a two-dimensional matrix file as a function of T and $\frac{dT}{dt}$. The calculated values are linearly interpolated to approximate $F_t(T, \frac{dT}{dt})$ for the simulation of the quench propagation with Eq. 3.86.

3.5.3 Quench Heaters

Quench heaters are installed to protect magnet coils when the natural quench propagation is not fast enough to avoid overheating and excessive voltages (see Section 1.5). They consist of stainless steel strips that are positioned along the magnet between the coil and the collars and are heated by a capacitor bank discharge after quench detection. The heat is transferred through the insulation layer into the coil, which provokes a quench. The process of a forced quench by heaters is sketched in Fig. 3.13.

> **In order to reduce the number of required capacitor banks, heater strips can be partially plated with copper to reduce their resistance. The heaters provoke a quench in the cable only below a non plated part and the natural quench propagation drives the entire conductor into the normal conducting state [54].**

The design of a quench heater strip is shown in Fig. 3.14. Studying the quench process after firing the quench heaters requires modifications to the heat balance equation (Eq. 3.1 or 3.86) to incorporate the heat flux from the heater strip into the conductor.

The temperature in the heater strip is determined by solving the one-dimensional heat balance equation. Heat conduction along the heater strip is disregarded as the heat generation is the same along the heated zone. The heat transfer between heater strip and liquid helium is taken into account by assuming only a fraction f of the heat that is transferred into the superconducting cable. The resistance and temperature increase in the copper-plated parts of the heater strip is neglected as the heat generation inside the superconducting cable becomes larger by several orders of magnitude. Typical initial heater currents are about 60 to 80 A [71].

$$\frac{\rho_h(T_h(t)) \cdot I_h^2(t)}{A_h} - k_{iso}^h \left(\frac{T(x,t) + T_h(t)}{2} \right) \frac{w_h}{l_{iso}^h} \cdot f_h \cdot (T_h(t) - T(x,t)) = c_h(T_h) \cdot A_h \cdot \frac{dT_h(t)}{dt} \quad (3.94)$$

In addition to the terms introduced in Eq. 3.1, Eq. 3.94 contains the heat conduction through the insulation into the superconducting cable. In order to calculate the heat generation in the heater strip, a constant capacitance C_h of the heater power supply is assumed for evaluating the heater current. The initial current is $I_h^0 = U_h^0/R_h(T = T_b)$, where U_h^0 is the loading voltage and $R_h(T = T_b)$ is the heater resistance at helium bath temperature.

The temperature dependent heater strip resistance is evaluated with the new temperature after each timestep and the actual current decay time constant is

$$\tau_{QH}(T(t)) = R_h(T(t))C_h \quad (3.95)$$

The heater resistance is calculated as

$$R_h(T(t)) = \frac{\rho_h(T(t))l_h}{A_h} \frac{l_h^{Fe}}{l_h^{Fe} + l_h^{cu}} \quad (3.96)$$

where l_h is the length, l_h^{Fe} is the length of the non-plated parts, and l_h^{cu} is the length of the plated parts of the heater strip. The heaters are fired when a quench is detected at time t_{det} (see Section 1.5). The detection requires that the resistive voltage exceeds a threshold for a certain time interval. The detection time can be set to zero if a quench is initialised by heaters. This is used to study experimental results of quench heater delay tests.
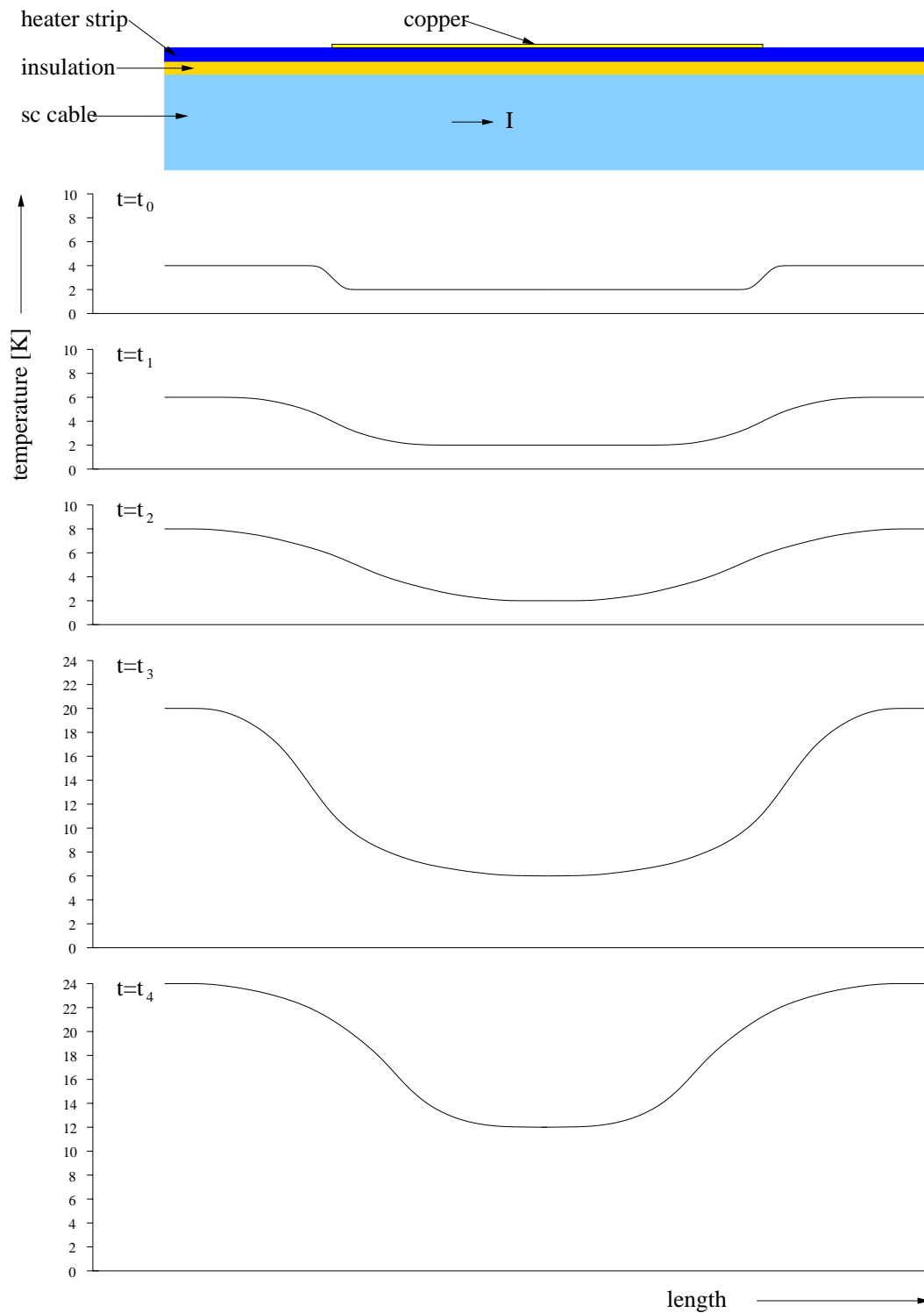
Figure 3.13: *Principle of forced quenching by heaters. At t_0 the heat flux from the heater strip starts to warm up the conductor, which provokes a quench at t_1. The heat generation starts inside the conductor and the heat conductivity leads to a longitudinal propagation of the warm zone into those areas that are below the copper-plated part of the heater strip (t_2, t_3). At t_4 the entire conductor is quenched. The time interval $t_4 - t_1$ depends on the magnet type and the excitation current. At nominal magnet current, this time interval is about 30–50 ms for the LHC dipole magnets.*
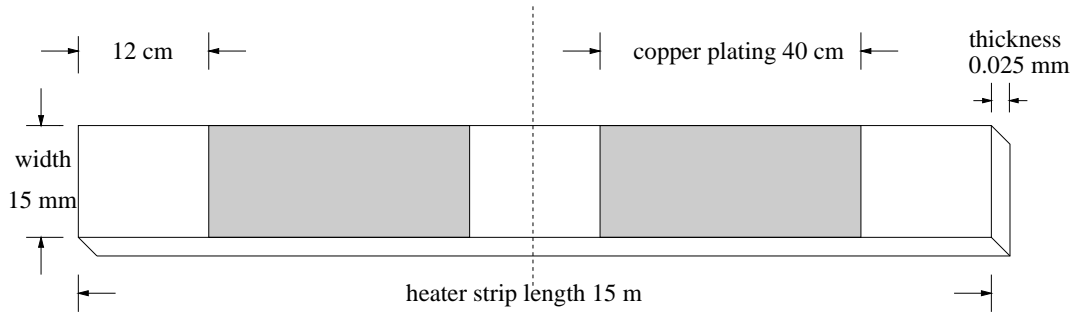
Figure 3.14: *Heater strip design with the copper-plating cycle for the LHC dipole magnets of 12 cm heated part and 40 cm copper-plated part (12-40 heaters).*

The time dependence of the heater current is given by

$$
I_h(t) = \begin{cases} 0 & \text{if } t < t_{det} \\ I_h^0 \cdot \exp(-\int\limits_0^t \frac{C_h dt'}{R_h(T(t'))}) & \text{if } t \geq t_{det} \end{cases}
\tag{3.97}
$$

The heat transfer through the insulation into the superconducting cable is given by the thermal conductivity of the insulation material $k_{iso}^h(T(t))$, the heater strip width w_h which corresponds to the surface per unit length and the insulation layer thickness l_{iso}. As a first approach f_h is equal to 0.5 (half of the generated heat is conducted into the cable the other half towards the collars). If the insulation thickness differs between the coil and the heater strip l_{iso}^h with respect to the thickness between the collars and the heater strip l_{coll}^h, it is more accurate to set

$$
f_h = \frac{l_{iso}^h + l_{coll}^h}{l_{iso}^h}
\tag{3.98}
$$

The heat capacity of the heater strip insulation layer is disregarded, as its volume per unit length is much smaller than that of the superconducting cable.

Alternatively, the temperature evaluation of the heater strip can include the heat transfer from the surface of the heater strip into the magnet collars.

$$
\frac{\rho_h(T_h(t)) \cdot I_h^2(t)}{A_h} - k_{iso}^h \left(\frac{T(x,t) + T_h(t)}{2} \right) \frac{w_h}{l_{iso}^h} \cdot f_h \cdot (T_h(t) - T(x,t))
$$
$$
-k_{iso}^h \left(\frac{T(x,t) + T_b}{2} \right) \frac{w_h}{l_{iron}} \cdot (T_h(t) - T_b) = c_h(T_h) \cdot A_h \cdot \frac{dT_h(t)}{dt}
\tag{3.99}
$$

The added term takes into account the heat transfer through the insulation layer into the magnet collars. For this simple model the length l_{iron} has to be chosen so that the temperature difference $T_h(t) - T_b$ can be used as an approximate approach. The heat balance equation including the impact of quench heaters heaters is

$$
\frac{d}{dx} \left(k(T(x,t)) \frac{dT(x,t)}{dx} \right) A(x) - h^{He}(T(x,t),t)P(x) + \dot{q} + G(T(x,t),t) +
$$
$$
g(x) \cdot k_{iso}^h \left(\frac{T(x,t) + T_h(t)}{2} \right) \frac{l_{width}}{l_{iso}^h} (T_h t - T(x,y,t)) =
$$
$$
c(T(x,t))A(x) \frac{dT(x,t)}{dt}
\tag{3.100}
$$

with l_{width} being the width of the cable (turn) towards the heater strip. The term $\dot{q}$ expresses the initial heat pulse that leads to a quench. The function $g(x)$ determines whether the cable is below a heated part of the quench heater strip or not. Eq. 3.100 and Eq. 3.99 have to be solved iteratively.

Eq. 3.100 changes to Eq. 3.101 when the heat transfer into helium through the insulation layer is modelled

$$\frac{d}{dx}\left(k(T(x,t))\frac{dT(x,t)}{dx}\right)A(x) + g(x)k_{iso}^h\left(\frac{T(x,t)+T_h(t)}{2}\right)\frac{l_{width}}{l_{iso}^h}(T_h(t)-T(x,t)) +$$

$$+\dot{q} + G(T(x,t),t) + k_{iso}\left(\frac{T(x,t)+T_{iso}(x,t)}{2}\right)P(x)\frac{T_{iso}(x,t)-T(x,t)}{l_{iso}} +$$

$$= c(T(x,t))A(x)\frac{dT(x,t)}{dt} \tag{3.101}$$

3.5.4 Two-dimensional Model

The two-dimensional heat balance equation for a superconducting cable includes the heat conduction from the heater through the insulation and heat conduction along the broad side of the superconducting cable. This approach assumes a Rutherford cable with the broad side in y-direction that is discretised and a constant cross-section along the conductor

$$k(T(x,y,t))\left(\frac{d^2T(x,y,t)}{dx^2} + \frac{d^2T(x,y,t)}{dy^2}\right) + \frac{G(T(x,y,t),t)}{A(x,y)} - h^{He}(T(x,y,t),t)\frac{P(x,y)}{A(x,y)} +$$

$$g(x,y)k_{iso}^h\left(\frac{T(x,y,t)+T_h(t)}{2}\right)\frac{w_t}{l_{iso}^h A(x,y)}(T_h t - T(x,y,t)) + \frac{\dot{q}}{A(x,y)} =$$

$$c(T(x,y,t))\frac{dT(x,y,t)}{dt} \tag{3.102}$$

where h_t is the height (layer) in y-direction and w_t is the average width (turn) in z-direction that corresponds to the surface exposed to the heater per unit length. The definitions of the variables used in Eq. 3.102 are the same to those introduced in Eq. 3.1. The function $g(x,y)$ expresses that heat conduction between the cable and the heater strip only occurs on the side of the cable that faces a heated part of the heater strip.

3.5.5 Three-dimensional Model

In order to study the quench propagation from one quenching turn to the next in a Rutherford cable, a three-dimensional model has to be used to solve the heat balance equation. The turn width is used for the discretisation in z-direction.

The turn thickness is averaged (Δz) which corresponds to w_t in the two-dimensional model. The heat transfer between two turns is calculated by heat conduction through the insulation layer, using the thermal conductivity k_{iso}^t and the width h_{iso}^t.

The finite volume element is $dV = dx \cdot dy \cdot dz$ and the finite surface element is $A(x,y) = dy \cdot dz$. The other terms were already included in Eq. 3.102

$$k(T(x,y,z,t))\left(\frac{d^2T(x,y,z,t)}{dx^2} + \frac{d^2T(x,y,z,t)}{dy^2}\right) + \frac{\dot{q}}{A(x,y,z)} + \frac{G(T(x,y,z,t),t)}{A(x,y,z)} +$$

$$\frac{k_{iso}^t(T(x,y,z,t))}{l_{iso}^t}\frac{dT(x,y,z,t)}{dz} - h^{He}(T(x,y,z,t),t)\frac{P(x,y)}{A(x,y,z)} +$$

$$g(x, y, z)k_{iso}^h \left(\frac{T(x, y, z, t) + T_h(t)}{2} \right) \frac{w_t}{l_{iso}^h A(x, y, z)} (T_h(t) - T(x, y, z, t))$$
$$= c(T(x, y, z, t)) \frac{dT(x, y, z, t)}{dt} \tag{3.103}$$

For a corrector magnet, the quench propagation between turns and layers is of general interest. Since both transverse dimensions of the conductor used to wind corrector coils are of similar size, the discretisation in y-direction is used to model the quench propagation between layers

$$k(T(x, y, z, t)) \frac{d^2 T(x, y, z, t)}{dx^2} + \frac{G(T(x, y, z, t), t)}{A(x, y, z)} +$$
$$\frac{k_{iso}^l(T(x, y, z, t))}{l_{iso}^l} \frac{dT(x, y, z, t)}{dy} + \frac{\dot{q}}{A(x, y, z)} +$$
$$\frac{k_{iso}^t(T(x, y, z, t))}{l_{iso}^t} \frac{dT(x, y, z, t)}{dz} - h^{He}(T(x, y, z, t), t) \frac{P(x, y)}{A(x, y, z)} +$$
$$g(x, y, z)k_{iso}^h \left(\frac{T(x, y, z, t) + T_h(t)}{2} \right) \frac{w_t}{l_{iso}^h A(x, y, z)} (T_h(t) - T(x, y, z, t)) +$$
$$= c(T(x, y, z, t)) \frac{dT(x, y, z, t)}{dt} \tag{3.104}$$

3.5.6 Program Execution

The input parameters are stored in a file that is read at the beginning of the SPQR simulation run. Depending on the input parameters, an initial temperature profile is calculated or read from a file.

When the copper cross-section or the cooling conditions are varied along the superconducting structure, the cross-section and the longitudinal position are provided as an input file. The common material parameters are recalculated for the average cross-section. The matrix file is read when the matrix model is used for the heat transfer modelling through the insulation layer.

Some examples of the output of the program are given in Figs. 3.15 to 3.18. Fig. 3.15 shows the temperature evaluation as a function of x in a two-dimensional plot. The time dependence is included with temperature profiles in different colours for various times. Fig. 3.16 shows the same simulation result in a 3-dimensional representation. The examples are obtained with SPQR for the quench propagation study of the main busbars including modelling of the heat transfer through the insulation layer into helium.

An example of the recorded global variables like current, voltage, development of the dissipated energy, resistance and normal-conducting zone is given in Fig. 3.17 (on the left). The fit of the expanding normal-conducting zone versus time derives the quench propagation velocity and is shown on the right.

A simulation result with a collapsing quench is shown in Fig. 3.18. The program also allows the study of the minimum quench energy in the presence of liquid helium by changing the initial temperature profile.

The robustness and the quality of the simulation model used in SPQR is discussed in Appendix A and the performed simulation studies for the different types of busbars and magnets are presented in Chapters 5, 6 and 7. The program execution times become large when discretising a long conductor or coils with many layers and turns. For that reason SPQR is mainly used to compute parameters such as the longitudinal and transverse quench propagation velocity, expected quench heater delays, the quench back starting time, and the hot spot temperature in presence of helium cooling.
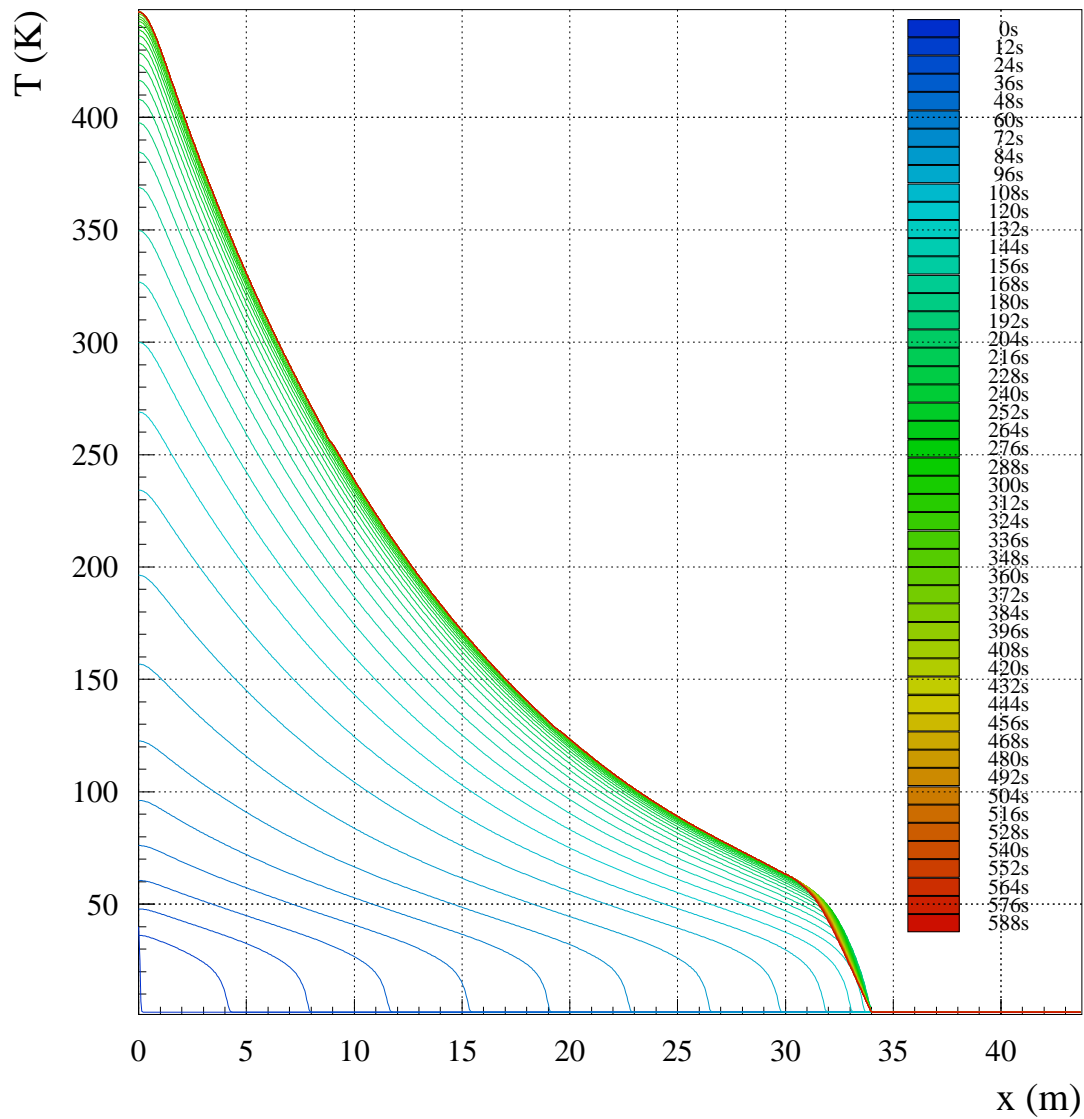
Figure 3.15: *Example of the temperature profile as a function of x and t as a 2D plot. The time interval between two curves is 12 s. The simulation shows the temperature evaluation of the main busbar for the LHC dipole magnets with $I_0=12$ kA and $A_{tot}=303$ mm^2 (see Chapter 5).*
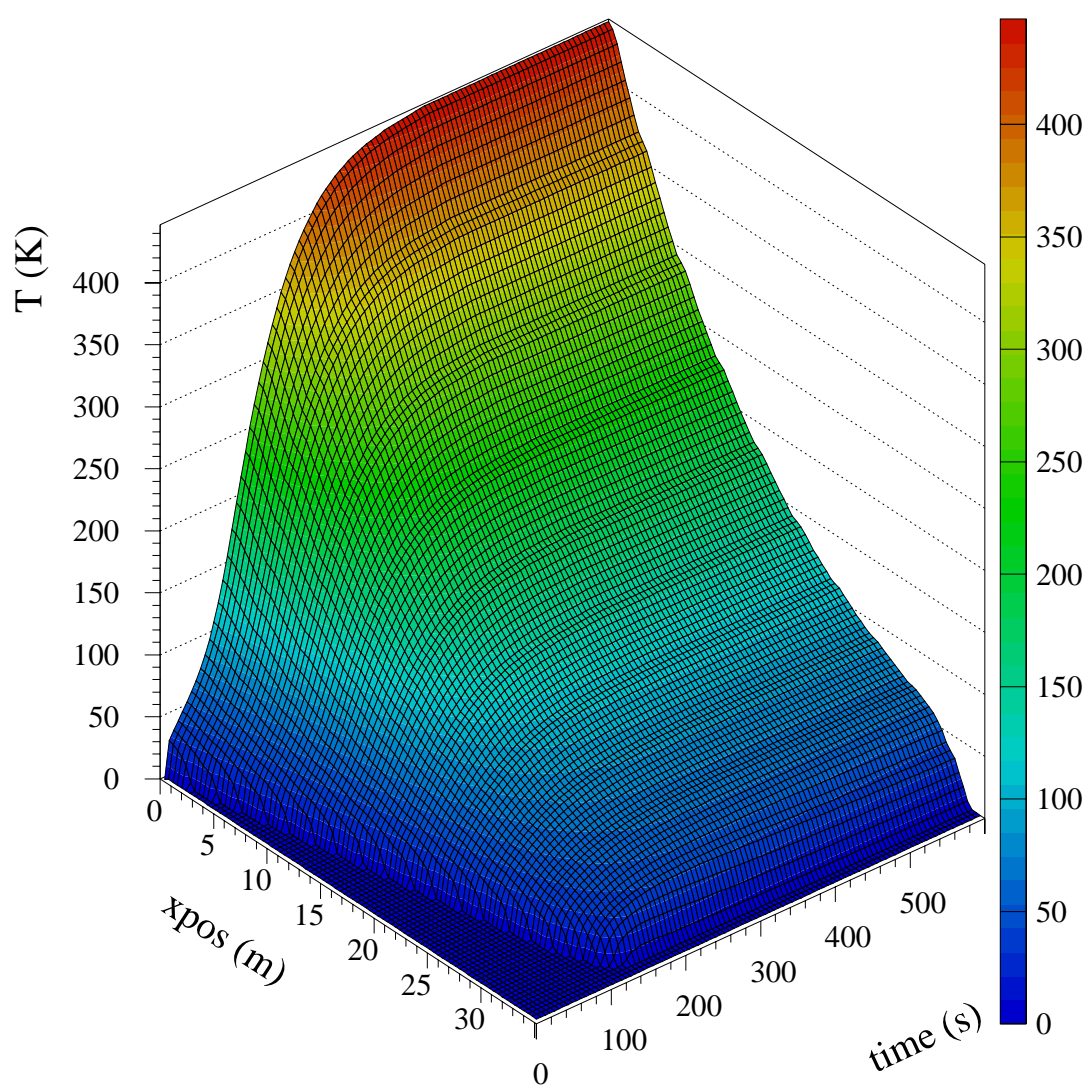
Figure 3.16: *Example of the temperature profile as a function of x and t as a 3D plot. The figure shows the same simulation result as Fig. 3.15.*
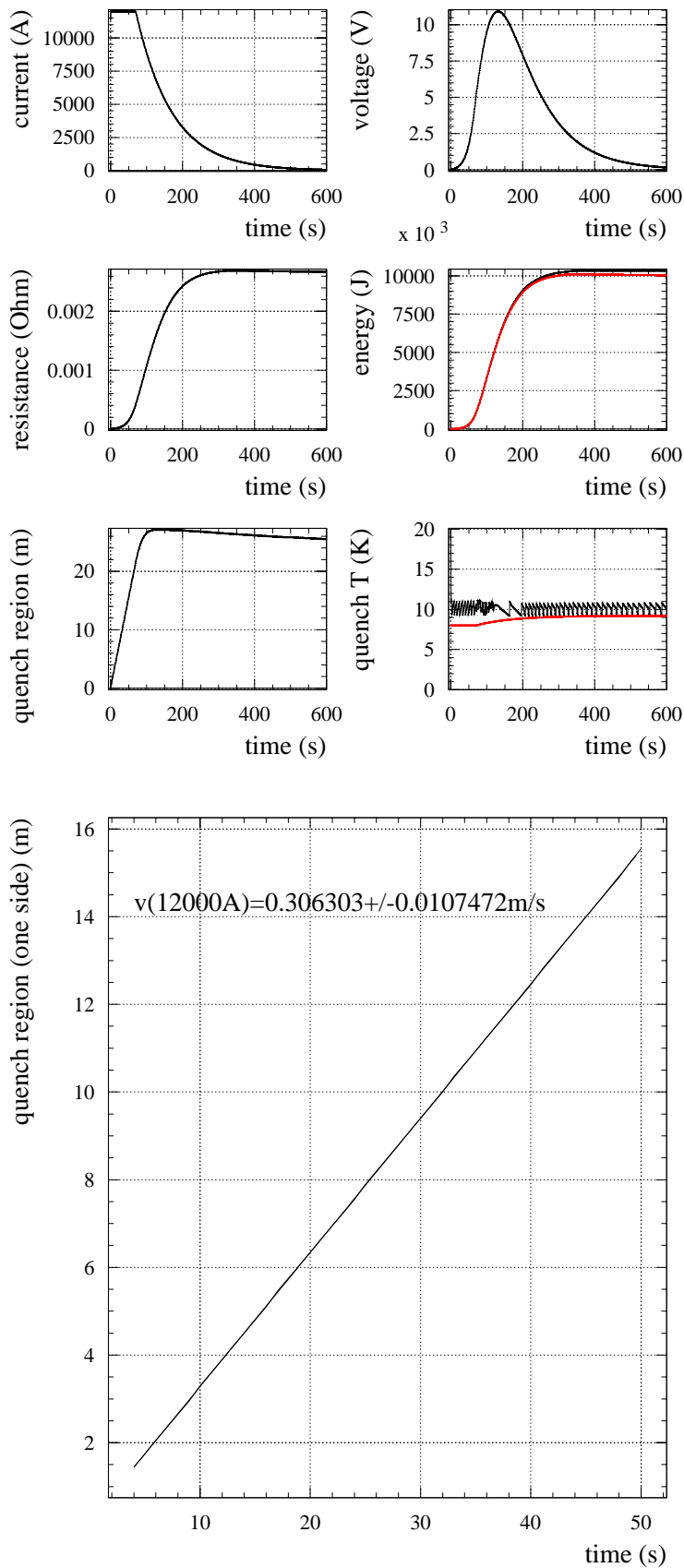
Figure 3.17: *Example of the recorded global variables during the quench propagation (upper graph) and the quench propagation velocity (lower graph) (I_0=12 kA, U_{det}=5 V, A_{tot}=303 mm^2). These plots are used to crosscheck the simulation model with the experimental result.*
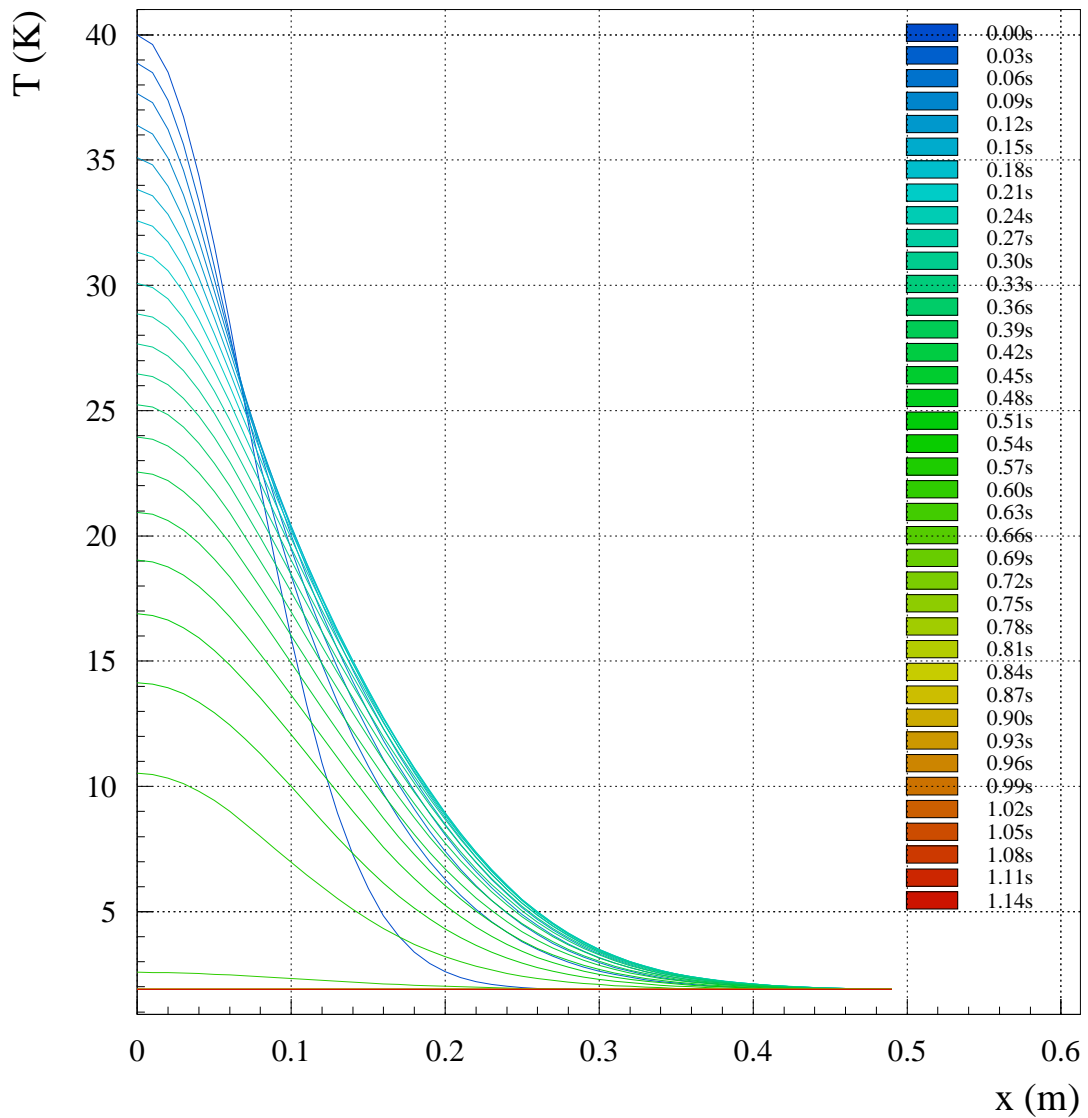
Figure 3.18: *Example of a collapsing quench when the initial energy is not sufficient to provoke a quench (I_0=12 kA, U_{det}=5 V, A_{tot}=303 mm^2). The result is shown in the 2D presentation as described in Fig. 3.15.*

Chapter 4

Measurements and Test Stations

Experiments are performed on prototype elements in various test stations at CERN and at collaborating laboratories in order to study the different quench mechanisms and to calibrate simulation models. This chapter introduces the experimental installations at CERN. The cryogenic and powering systems are briefly outlined and the instrumentation and data acquisition for the powering tests are described. Small prototype magnets are tested in an experimental hall (Block 4) and experiments on long prototype dipole and quadrupole magnets are carried out on test benches in the building SM 18. A prototype full cell is being installed to test various systems under operation conditions. Other test facilities have been built at CERN, e.g. for tests on superconducting cables or cryogenic equipment.

4.1   Measurements on Prototype Magnets and Busbars

Experiments on prototype magnets aim to validate the design by determining their quench performance (training of the magnet and protection) and the field quality (measuring the field harmonics). Busbars and current leads are tested to verify whether they can transport the design current and to evaluate the required protection.

Quench Performance of Magnets

The reached quench current of the magnet with respect to the critical current of the cable determines the overall quality of the magnet winding. It defines the current level at which the magnet can be operated. The current decay allows a first estimation of the hot spot temperature after a quench.

Quench heater tests determine the time between firing the quench heaters and detecting a provoked quench (quench heater delay). The efficiency of the heater system is tested by measuring the quench load as a function of the magnet excitation current. In order to optimise the heater system, the powering parameters (heater strip resistance and initial voltage) are changed. The tests give the minimum heater voltage required to provoke a quench at various magnet operating currents, and the limitations for the heater strip design (copper-plating cycle, insulation layer thickness and position with respect to coil windings).

High voltages that develop between turns in a quenching coil can exceed the breakdown voltage of the insulation layer and potentially cause damage.

Voltage taps are installed in the coil to measure the voltage increase between various poles and turns during a quench. They are made of thin instrumentation wires that are fed into the cryostat and soldered on the superconducting cable at various voltage potentials.

The voltage across two taps is recorded during a quench. When several voltage taps are installed along the same turn in the straight part of a magnet, the difference voltages of adjacent voltage taps allow the precise determination of the longitudinal quench propagation velocity. If an expanding quench reaches the zone between two neighbouring taps, the voltage starts to increase linearly until the entire zone is normal-conducting (see Fig. 4.1). The time interval of the voltage onset between two neighbouring signals (three voltage taps) yields the quench propagation velocity when the distance of the voltage taps is known. Voltage taps are also placed between various turns to
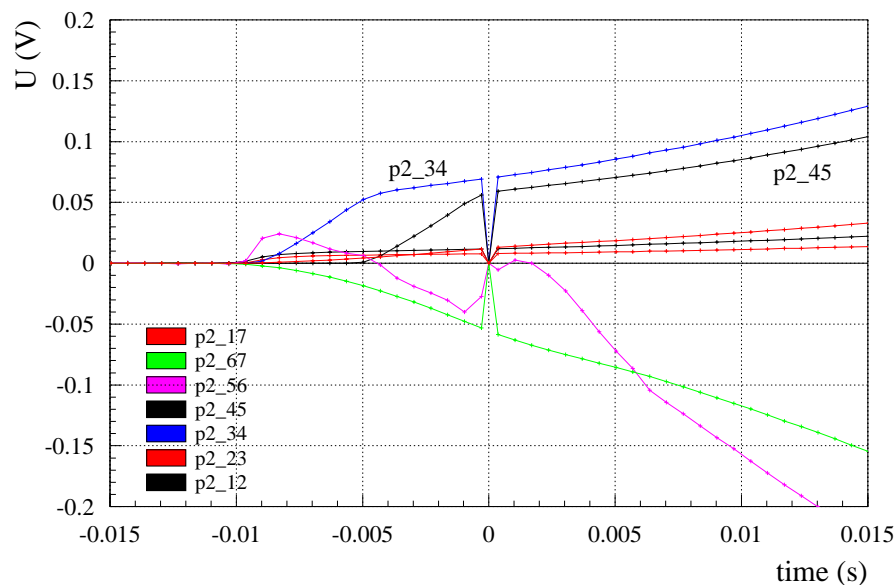
Figure 4.1: *Voltage signals of an instrumented MQT magnet (quench provoked at a current of 550 A) used to determine the longitudinal quench propagation. 4 ms are needed for the quench propagation between the position p2_34 (pole 2, voltage across tap 3 and 4) and p2_45 (pole 2, voltage across tap 4 and 5). The voltage taps 3, 4, and 5 are distributed with equal distance (10 cm) along the inner turn of pole 2. At t=0 the quench is validated (corresponds to t_{det}) and the power converter is switched off which causes a noise signal in the data acquisition.*

evaluate the transverse quench propagation velocity (see Fig. 4.2). Pickup coils (quench antennas) are inserted into the magnet bore during the quench performance measurements. The set of pickup coils covers the length of the magnet dividing it into sections. Several pickup coils are placed in each section. The propagating quench changes the magnetic flux and voltages are induced in the pickup coils, which determines the longitudinal position of the quench origin [72].

In order to perform quench experiments at a given current, prototype magnets and busbars are equipped with small heaters (spot heaters). Spot heaters are fired with a capacitance of about 1 mF applying a voltage range of 10–50 V to provide short current pulses, which results in a maximum energy deposition of up to 1 J. Since more energy is needed to provoke a quench in a busbar, they are equipped with larger spot heaters.
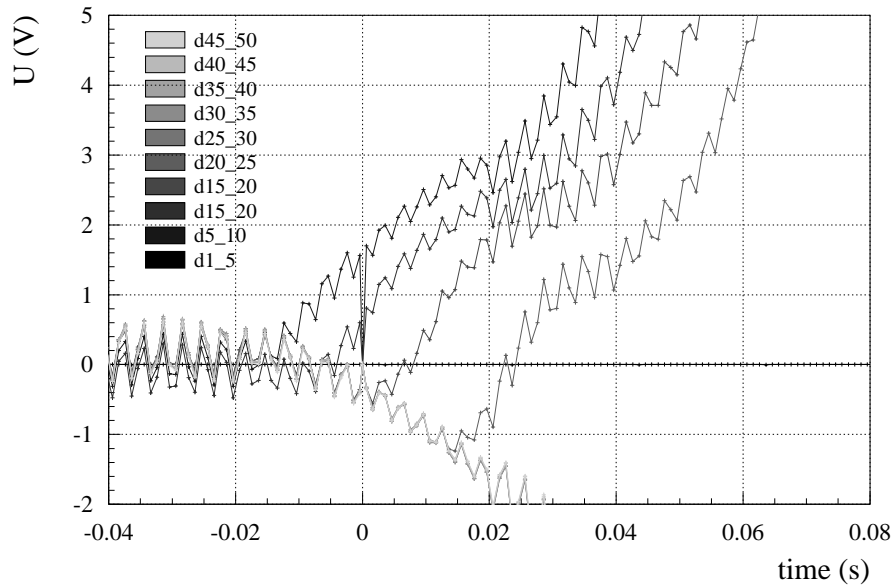
Figure 4.2: *Transverse quench propagation velocity determined with voltage signals on a MCB magnet (closed orbit dipole corrector) with a quench current of 60 A. The time difference between two voltage curves that stop being purely inductive (increasing the negative voltage) yields the transverse quench propagation velocity. The small oscillations in the signals are due to induced noise by the power converter.*

The temperature of the helium bath T_b is permanently recorded for the computation of the critical current $I_c(T_b)$ and the comparison with the reached quench current.

Magnetic Field Measurements

The field harmonics are measured with rotating pickup-coils, Hall sensors and NMR probes [8] and determine the field quality. The required accuracy aims to measure the field harmonics with a relative precision better than 10^{-5}. The comparison of the predicted and measured field quality provides feed-back for the magnet design and manufacturing process.

Dynamic losses (due to magnetisation and induced eddy currents) are measured by the voltage development during special current cycles. The experiments yield the contact resistances and the hysteresis of the superconductor. The results are used to model the impact of dynamic effects on the field quality and on the quench process.

Test Procedure for Magnets

The insulation of the magnet to ground is tested at ambient temperature and after cooldown. The quench heater efficiency is validated at an intermediate operating current. The current level is changed without reaching the quench current to observe the noise in the voltage signals. The prototype magnets are trained (training quenches) until the quench current stabilises. After a quench, the cryogenic system has to cool the magnet down to the operating temperature. Similar tests are carried out on prototype busbars. A dump resistor can be switched in series with the magnet to extract part of the energy, which protects the prototype magnet and reduces the heat load on the cryogenic system. The operating temperature is reached in a shorter time, which reduces

the time interval between two training quenches. After the training of the magnet, the magnet performance is tested without energy extraction. The test program is continued with magnetic field measurements and special protection experiments (e.g. quench heater tests).

The training of the magnet is performed at two temperatures: at 1.8 K and at 4.2 K to test if the cable is intact. The reached quench currents in both temperature regimes determine the gain of cooling at 1.8 K with respect to 4.2 K. Some magnets and busbars also have to be operated in both temperatures at different places in the LHC. The magnet operating current at 4.2 K is smaller than that at 1.9 K.

For the computation of the RRR, the resistivity of the copper fraction is determined using a small current of 0.5–2 A (four point measurement) at a bath temperature of about 10 K. The evaluation is completed with the measurement of the resistivity at ambient temperature to derive the RRR value.

The training of a magnet can be repeated after a thermal cycle to test whether the trained quench current level remains.

4.2 Test Stations

4.2.1 Block 4

Block 4 is an experimental hall for quench performance and magnetic field measurements at 1.8 and 4.2 K. Short models of main dipole and quadrupole magnets of 1 m length and lattice corrector magnets can be tested in two vertical cryostats. The short model dipole program was launched to have a faster experimental feedback of design changes. A third vertical cryostat is available for testing up to three multipole corrector magnets at the same time. Tests on prototype busbars powering the corrector and insertion quadrupole magnets are performed in Block 4 to determine the required copper stabilisation and protection. The design of the 13 kA busbar for the main dipole and quadrupoles magnets in the arc was tested at CEA in Saclay, France.

The magnets are powered by power converters with a maximum current of 20 kA, 2 kA, and bipolar 600 A. Two magnet cryostats can be kept at 1.8 K at the same time. The evaporated helium during a quench is recuperated and recooled. After a quench in a short prototype dipole magnet without energy extraction, the bath temperature exceeds the helium λ-point and recooling to 1.8 K takes about 3–4 hours.

The powering cables are connected with the power converter that is controlled by a workstation. The instrumentation cables from the voltage taps and from the inserted pickup coils are linked to industrial VME A/D converters. A workstation controls the rotating pickup-coils for magnetic measurements. The output signals of the magnetic field measurement equipment are connected to industrial VME integrators. All data is transferred via an MXI field bus to a workstation and stored. The control and data acquisition software is written at CERN and based on LabView[1] and TeamPro[2] applications. The data signals can be recorded with different acquisition frequencies in various time intervals. All data is stored in a binary database so that it can be analysed later (see Fig. 4.3).

---

[1]Trademark of National Instruments

[2]Trademark of Nicolet Instruments

Power Tests   **Magnetic Measurements**
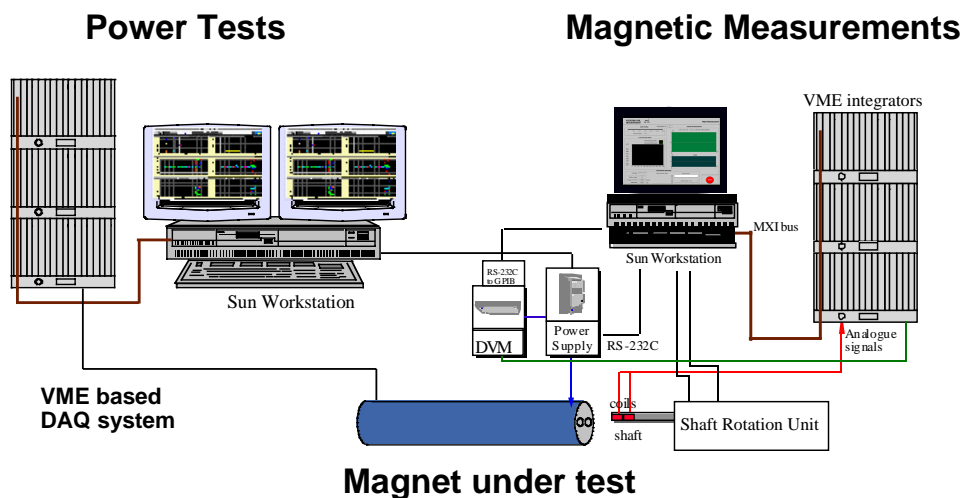
Figure 4.3: *Principle of the data acquisition system for quench performance and magnetic field measurements (courtesy of M. Peryt).*

4.2.2   Magnet Test Benches in SM 18

The 15 m long prototype dipole magnets and the short straight sections (SSS) that contain the arc quadrupole magnets are tested on magnet test benches.

In the test bench, the magnets are mounted in a horizontal cryostat as they will be mounted in the LHC. In the experimental hall, the cryostat is connected to the cooldown and warmup unit (CWU) and the magnet feed box (MFB). The CWU delivers 120 W of refrigeration power at 1.8 K and allows cooling down of a twin aperture dipole magnet in about one day. The magnet feed box supplies the magnet with the required cryogenic fluids and electrical power during the operation. It has a built-in heat exchanger for the last phase of the cooldown from normal-liquid to superfluid helium. The connection units, the supervision and data acquisition systems are the subsystems of the test bench.

All processes are controlled by a local programmable logic controller (PLC) for continuous and sequential process control. An Ethernet plant network links the PLCs and is operated by supervision software on a Unix workstation. Ten PLCs are installed per test bench and about 1500 signals are supervised.

The data acquisition system is based on LabView applications. The software for the automation of the standard magnetic field measurements is similar to the one used in Block 4 (see Fig. 4.3). Different sets of signals are defined that can be recorded regularly or as a snap shot during a quench with different data acquisition frequencies (1–50 kHz).

Two test benches are commissioned and used for testing prototype magnets. The installation of a total of 12 test benches is foreseen for the series measurements of all LHC main dipole and arc quadrupole magnets. All magnet test benches will be hosted in the CERN hall SM 18.

4.2.3   Magnet String

A prototype half cell (three dipole magnets and a quadrupole magnet) was tested in the String I program until the end of 1998. At that time the dipole magnets were 10 m long prototypes.

Experience was gained operating this string of magnets and many components were tested and optimised [73].

A second operation of a string of magnets is planned with a full size prototype cell of the LHC arc (two half cells with three 15 m long dipole magnets and one quadrupole magnet each), the String II project (see Fig. 4.4) [74].

The experimental program covers quench propagation experiments, test of the reliability of magnet protection schemes, performance of the cryogenic system, evaluation of the required vacuum installation, operation scenarios for the LHC, etc.

Examples for the experiments related to magnet protection are the measurement of the quench propagation from one magnet to the next and the longterm operation of the protection equipment. Quench experiments on prototype busbars can also be performed on a longer scale than in a magnet test station.
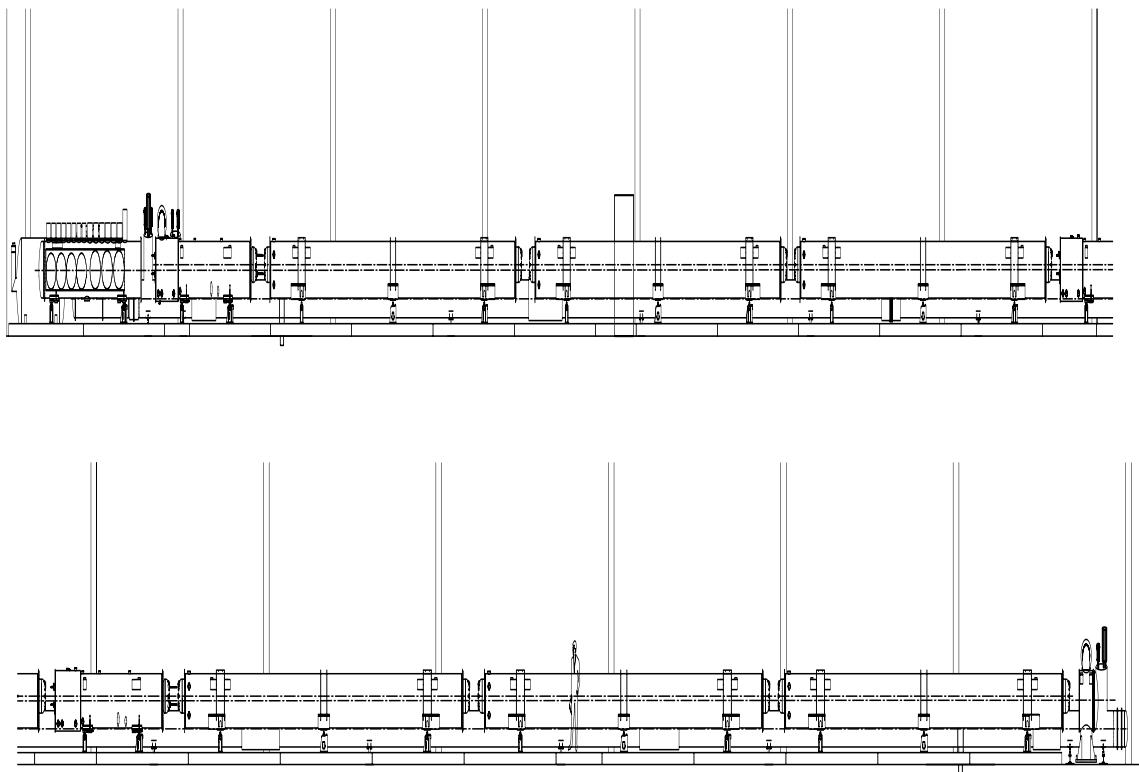
Figure 4.4: *Schematic view of String II showing (from left to the right) the powering feedthroughs, the first quadrupole, three dipole magnets, the second quadrupole and another three dipole magnets.*

4.3   Series Measurements

The field harmonics will be measured for all LHC main magnets on magnet test benches in SM 18. The information will be used for the compensation of the individual multipole field components by sextupole, octopole and decapole spool piece corrector magnets. The results of the magnetic field measurements will be stored in a database, which will provide the information on how to

cycle the machine after a beam abort signal in order to avoid dynamic multipole components due to hysteresis and induced eddy currents (persistent currents [8] and boundary induced coupling currents [58]).

Up to three training quenches and a standard magnetic field measurement program are planned for 90 % of the magnets and an extended test program will be carried out on the other 10 %. Overall 10 % of the magnets are expected not to reach the ultimate current during the first test sequence. For these magnets a second test sequence is foreseen. If the ultimate current cannot be reached after the second test, the magnet will not be installed in the LHC. A magnet can also be rejected for intolerably high multipole components.

The main quadrupole magnets for the insertions (MQM family and MQY magnets) will be tested in Block 4. The single aperture quadrupole magnets of the experimental insertions (MQX) are supplied by Japan and the USA and will be tested in local laboratories.

The series production of the small lattice and closed-orbit correctors will be tested at 4.2 K in industry. Only a few percent will be retested at CERN at 4.2 and at 1.8 K in Block 4.

4.4   Analysis of Quench Data

During the quench experiments the helium bath temperature and the quench is noted and the adiabatic temperature is evaluated with the quench load. The quench origin is determined by analysing the various voltage and quench antenna signals. The quench heater delays are already measured during the tests.

The experimental data is stored in a database for later analyses. The data can be analysed with the data acquisition software or with any other software package using the provided data extraction tools. Quench data from the prototype cell can be extracted using the WWW and stored for example in ASCII tables. The TeamPro package also offers the extraction to ASCII files. Data extraction programs have been implemented that do not need to be run on LabView or TeamPro. One program extracts data from the LabView database (data_extraction by Peryt 1999), the other program extracts data from the TeamPro database (team_convert by Sonnemann 1998). The programs extract a predefined set of variables in a chosen time interval. The output is generally written to ASCII files, which are transferred to a local workstation by FTP.

The quench data has mainly been analysed with PAW[3] and partially with EXCEL[4]. The data extraction program team_convert writes the information either to binary n-tuples readable by PAW or to ASCII tables. The program provides a 50 Hz filter, filtering by moving averages over n points, data smoothing and compressing, taking out initial offsets and the calculation of time derivatives of selected channels. Other parameters such as maximum and minimum values of the channels including the timestep and the quench load value are stored in an information file. The team_convert output includes a macro that can be executed with PAW for the data analysis.

A UNIX command shell can run the programs several times to extract selected channels of various quench experiments. The written macros for EXCEL and PAW lead to an automation of the data analysis that allows the systematic study of any quench parameter (e.g. automatic fit of partial inductances to compute the resistance growth during a quench).

---

[3]CERN software development
[4]Trademark of Microsoft

Chapter 5

Quenches of Busbars and Current Leads

The busbars of the LHC are highly copper stabilised cables that connect all the magnets of a family and attach them to the current leads, which are the feedthroughs from 300 K to the cold part of the circuit. Due to the given geometry, the modelling of the temperature along a single conductor is adequate to study the quench propagation. As busbars are located in areas of low external magnetic field, eddy currents do not affect the current decay. A quench of a busbar is therefore represented by the thermodynamic model including Ohmic heating.

After the introduction of busbars powering the various types of LHC magnets, the quench process is analysed for the different types of superconducting busbars. The results of analytical models, numerical simulations, and experiments on prototype busbars are compared and the calibration of the simulation model is presented. Quenches are simulated, which originate in a geometry where the boundary conditions change such as busbars passing through interconnects and feedthroughs. The outcome of the simulation study in predicting the temperatures after a busbar quench in the LHC and the proposed protection scheme are discussed. For completeness, the protection issues of the high temperature superconducting current leads are summarised.

5.1   Busbars for the LHC

In Section 1.5 the various types of busbars for the LHC were introduced. When a quench originates in a busbar, the copper stabilisation has to be large enough to avoid overheating.

The energy stored in a main dipole circuit with 154 magnets connected in series is about $1.3 \cdot 10^9$ J (inductance of 16.5 H at an operating current of 11.8 kA). This energy corresponds to the kinetic energy of a 100 t plane travelling with 600 km/h. The value of the dump resistor switched in series after quench detection is given by the voltage-to-ground limitation at the mechanical switches of 900 V. The current decay time constant is about 100 s for the LHC dipole magnet circuits. The energy stored per circuit for the arc quadrupoles circuits with 47 and 51 magnets connected in series is about 24 MJ and the current decay time constant is about 50 s.

The quadrupole magnets in the insertions and recombination dipole magnets are powered individually or in pairs. They are operated up to 6 kA and are protected by quench heaters. The busbar does not require a copper stabilisation as strong as for the 13 kA busbars because the maximum energy stored in these circuits is about 3.6 MJ. After quench detection, all heaters are fired and the current decays in less than a second so that an energy extraction resistor is not required.

Two types of 600 A busbar cables have been developed for the LHC to power the multipole spool piece corrector magnets and the corrector magnets in the short straight sections. These circuits store a magnetic energy in the range of 2.5–100 kJ depending on the type of magnet and number of magnets connected in series. Tests have been performed on prototype busbar cables [51, 75]. The comparison of the simulation study with the test results is presented in Section 5.3.

Simulation Model

In order to simulate the quench process in busbars, the one-dimensional approach described in Section 3.2 is adequate.

For the correct computation of the quench propagation velocity, the heat transfer through the insulation layer has to be modelled. Quench simulations in the main busbars are performed with the constant temperature gradient approximation (see Section 3.5.2) since the insulation layer thickness is small with respect to the busbar dimension. On the contrary the simulation of a quench in the 600 A busbar cable requires the discretisation of the insulation layer which is done by using the matrix model in SPQR (see Section 3.5.2) [75].

Numerical Stability

The timestep Δt to be used in order to stabilise the simulation results is about 1 μs for the main busbars and 1–10 ns for the busbar cable. The maximum discretisation in x-direction Δx that can be used to produce consistent results is about 10 cm for the main busbars and 1 cm for the busbar cable.

Doubling Δx reduces the program execution time but leads to wrong results as the assumption of a constant temperature for such a long piece is not applicable. A further reduction of the timestep or Δx with respect to the values given above significantly increases the program execution time and is not required as the simulated temperature profiles differ only by about 10 K. The quench propagation velocity varies by a few percent.

The simulation studies performed for quenching busbars test the robustness of the numerical code. A numerical instability occurs when Δx is chosen to be very small and Δt is relatively large. In this case the evaluation of the temperature with the finite difference method can produce temperature oscillations between neighbouring elements. The heat generation is taken as a constant for the time interval Δt, which leads to a large jump in temperature for a small Δx that just became normal-conducting. During the next iteration, the temperature difference to the adjacent superconducting element increases the heat transfer from the normal-conducting into the superconducting element such that the temperature in the normal-conducting element can become smaller than in the adjacent elements. If Δx is too large, temperature oscillations result because of the intrinsic numerical instability of the explicit method [76].

The implicit approach is numerically stable since the new temperature is iterated by a matrix inversion and adjusts the time discretisation, which excludes temperature oscillations. The program algorithm uses the explicit method as it avoids a matrix inversion and simplifies the implementation of various quench mechanisms. Numerical instability and reliability compromise a fast program execution. The discretisation in space and time therefore have to be varied to ensure a consistent simulation result.

Using the constant temperature gradient approximation for the main busbar, the program execution of a quench with a duration length of 500 s takes about 15 minutes on a WindowsNT[1] workstation with a Pentium II processor[2] operated at 400 Mhz.

The execution was carried out with an initial timestep of 1 μs, applying the timestep control mechanism described in Eq. A.26 with α=0.1 and a maximum timestep of 0.5 ms.

5.2 Main Busbars

The RRR value (Eq. 2.14) of a busbar with a copper block for stabilisation ($\approx$50) is smaller than the RRR of the copper in a Rutherford cable ($\geq$80) because of the cold working during the forming process. Since the main busbar is insulated, the adiabatic formula (Eq. 3.19) was applied to calculate the longitudinal quench propagation velocity which yields v_q=3 m/s (see also Section 3.1.3). The required copper stabilisation was obtained by assuming a fast quench detection and an exponential current decay with a time constant of τ=100 s. This gives a quench load (Eq. 3.5) for a quench starting at 12 kA of

$$\int\limits_{t_0}^{\infty} [I_0 \cdot \exp(-t'/\tau)]^2 dt' = I_0^2 \frac{\tau}{2} = 7.2 \cdot 10^9 \, \text{A}^2\text{s} \qquad (5.1)$$

It should be noted that a typical value of the quench load of a quench in a LHC main dipole magnet at nominal current is about $2.9 \cdot 10^7 \, \text{A}^2$s. The quench load for the main busbar is two orders of magnitude larger since the current decay time constant is about 100 s for the busbar (given by the ratio of the dump resistor and the inductance of 154 dipole magnets) and 0.2–0.3 s in the magnet due the protection with a bypass diode and quench heaters (see Section 1.5). As a bypass element cannot be installed for a busbar that powers magnets connected in series over a length of about 3 km, the busbar is highly stabilised with copper.

The adiabatically calculated temperature would be about 250 K for a copper stabilisation of 250 mm^2 and RRR=50. The copper stabilisation of the prototype busbar was about 310 mm^2. Due to large copper stabilisation the resistive voltage rises much slower with respect to a quench in a magnet and a quench is significantly later detected. If the propagating quench is detected after 40–60 s (measured v_q =0.3–0.4 m/s) the quench load value doubles, thus the hot spot temperature of a busbar with a copper stabilisation of 310 mm^2 exceeds 400 K. The adiabatic temperature calculation can be used as a first approach but is not suited for design optimisation since the quench propagation velocity and the hot spot temperature are not predicted accurately enough.

5.2.1 Quench Propagation

An example of the temperature profile is shown in Fig. 5.1 for the minimum required copper stabilisation. The simulation studies demonstrated that an increasing temperature at the quench origin always leads to an expanding normal-conducting zone for realistic cooling scenarios and $A(x) \equiv A$. Otherwise the temperature decreases and recovery takes place. Due to the long time period of the quench process, the maximum temperature is not affected by the quench initialisation temperature. When the normal conducting zone is neither expanding nor shrinking, the hot spot temperature remains constant until the cooling conditions vary. This situation would increase

---

[1]Trademark of Microsoft Corporation
[2]Trademark of Intel Corporation
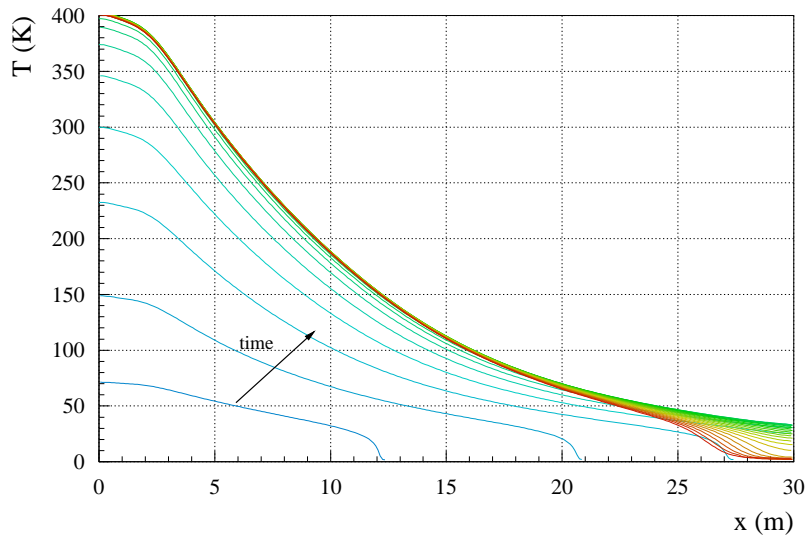
Figure 5.1: *Temperature profile as a function of space and time showing the expanding normal-conducting zone for the main busbar. The parameters for this simulation study are A_{tot}=303 mm^2, U_{thres}=1 V, I_0=12.5 kA, cooling conditions according to model 3. The quench was initiated with T_{init}=20 K, σ_T=0.8 m. The time interval between two adjacent curves in the figure is 25 s.*

the heat load on the cryogenic system. If the cooling power decreases, the temperature starts to increase and the normal conducting zone first expands, then followed by quench detection and current decay. The limits for the copper cross-section of the busbars presented below ensure that no excessive temperatures will be obtained in such a case.

5.2.2 Calibration

The simulation model was calibrated using experimental results of prototype busbar tests [77]. The prototype busbar for the LHC main dipole magnets has a cross-section of A_{cu}=296.5 mm^2 and A_{sc}=6.5 mm^2. The quenches were induced by firing a spot heater immediately followed by a linear current discharge. Several cooling models were used for the simulation. Model 1 and 2 do not include the heat transfer through the insulation layer and require a fit of the effective wetted perimeter to obtain the measured quench propagation velocity. Model 1 uses the heat transfer coefficient modelled as in Eq. 3.85 and model 2 is based on Eq. 3.84. The hot spot temperature of the simulation was then compared with the experimental result for the measured quench load during the tests. The wetted perimeter is not a fit parameter if Eq. 3.84 is used to model the heat transfer into helium and taking into account the heat transfer through the insulation layer (model 3). If a small amount of helium is present in the busbar or in the insulation layer, the helium proportion has to be included for the adjustment of the model (adjusted model 3).

Since the proportion of the copper stabilisation dominates the total cross-section, the adjustment of model 3 is negligible and the simulation model is very robust (see Table 5.1).

5.2.3 Scaling and Detection

Quench experiments have been performed on a 7 m long prototype busbar for the main magnets in Saclay [77]. After provoking a quench with a spot heater the current was ramped down linearly

model	variable	measurement	simulation
model 3	v_q	0.3-0.4 m/s	0.42 m/s
adjusted model 3	v_q	0.3-0.4 m/s	0.36 m/s
	T_{max} at T_b=1.9 K	55 K	60 K
	T_{max} at T_b=4.2 K	76 K	80 K

Table 5.1: *Comparison of simulation and experimental results. The parameters of the cooling model are a_1=180 W/(m²K⁴), a_3=100 W/(m²K), n=4, m=1, $t_{f.boil}$=0.02 s. A helium fraction of 0.5 % of the total cross-section is used for the adjustment.*

with a discharge rate of 125 A/s, which is the maximum discharge rate at the start of the exponential current decay in the LHC machine. The quench load in the LHC machine is about eight times larger than the measured quench load during the prototype tests (see Fig. 5.2) because the time required for quench detection (see Sections 1.5 and 8.1.1), opening the extraction switches, and for the exponential current decay were ignored. For that reason the experimental results have to be scaled and extrapolated to study the situation of a quenching busbar in the LHC machine.
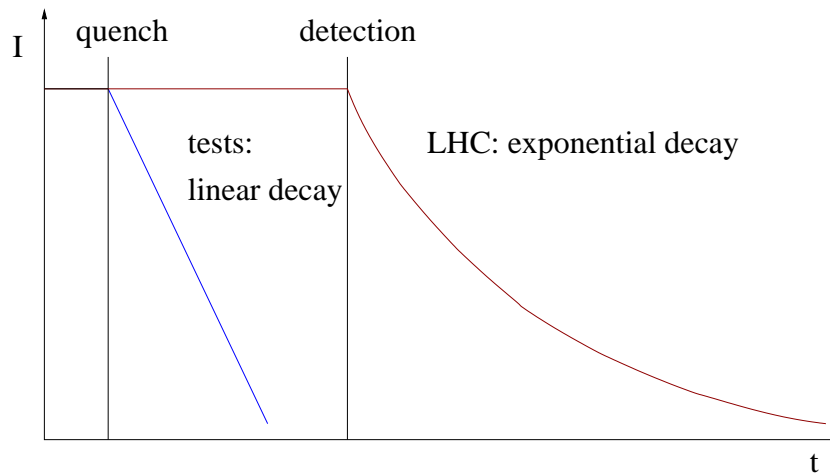
Figure 5.2: *Schematic comparison of the current as a function of time for the tests on the prototype busbars and for a quench originating in a busbar in the LHC machine.*

The detection time for various threshold levels was evaluated as a function of cooling conditions keeping the busbar cross-section constant. A quench validation time interval of 1 s was assumed. As the longterm cooling conditions are not very well known, the hot spot temperature was estimated with the different cooling models. The maximal temperature differences are about 50 K at a 1 V detection level. Table 5.2 shows that a detection level of 1 V limits the hot spot temperature to tolerable values whereas a threshold of 5 V leads to excessive temperatures [78].

5.2.4 Required Copper Stabilisation

Since the forming process of a busbar such as bending it at the ends of a magnet becomes more difficult with an increasing cross-section, one is interested to determine the minimum required copper stabilisation. The simulation study includes the heat transfer through an insulation layer of 200 μm thickness and the complex cooling model (adjusted model 3).

Cooling model	Simulation parameter	P [m]	U_{thres} [V]	v_{quench} [m/s]	T_{max} [K]	T_{ad} [K]	zone [m]	Quench load [A^{2}s]	t_{det} [s]	U_{max} [V]
-	adiabatic		5	1.04	383	-	309	$1.38 \cdot 10^{10}$	45.6	16.9
1	simple model	0.0035	5	0.31	450	480	64	$1.49 \cdot 10^{10}$	86.1	8.5
2	$t_{f.boil} = 20\,ms$	0.0160	5	0.30	688	710	54	$1.69 \cdot 10^{10}$	68.2	11.3
2	$t_{f.boil} = \infty$	0.0069	5	0.30	576	780	55	$1.74 \cdot 10^{10}$	71.9	10.5
-	adiabatic		1	1.10	206	-	272	$1.05 \cdot 10^{10}$	22.6	6.6
1	simple model	0.0035	1	0.31	214	240	46	$1.13 \cdot 10^{10}$	50.0	2.6
2	$t_{f.boil} = 20\,ms$	0.0160	1	0.30	318	325	38	$1.28 \cdot 10^{10}$	40.0	3.7
2	$t_{f.boil} = \infty$	0.0069	1	0.30	261	355	37	$1.33 \cdot 10^{10}$	42.6	3.3
3	$l_{iso}=200\,\mu m$	0.072	1	0.36	297	334	49	$1.29 \cdot 10^{10}$	38.0	3.5

Table 5.2: *Detection times and hot spot temperatures for a main busbar quench in the LHC (A_{tot}=303 mm^2). The wetted perimeter is the fit parameter for model 1 and 2 (no insulation layer; 1 = heat transfer as in Eq. 3.85; 2 = heat transfer as in Eq. 3.84). The cooling model parameters used are given in Table 5.1. T_{ad} is the adiabatic temperature calculated for the given quench load; zone is the expected maximum length of the normal-conducting zone.*

A decrease of the copper cross-section reduces the quench load and the heat capacity of the conductor (less material), increases the heat generation per unit length, and leads to a faster temperature increase. This results in a faster quench propagation and an earlier quench detection. The quench detection time as a function of the copper cross-section is shown in Fig. 5.3. The quench propagation velocity increases with the current and a reduced cross-section (see Fig. 5.4).

The increase of the copper cross-section yields a smaller hot spot temperature, since the heat capacity of the conductor increases and the heat generation decreases. For a detection level of U_{det}=1 V the hot spot temperature was simulated as a function of the copper cross-section and operating current for the busbars of the main dipole and quadrupole magnets. The simulation result of the hot spot temperature as a function of copper cross-section is shown in Fig. 5.5.

The minimum required copper cross-section to avoid temperatures higher than 400 K was simulated to be A_{Cu}^{MB}=240 mm^2 for the dipole magnet busbar and A_{Cu}^{MQ}=160 mm^2 for the quadrupole magnet busbar. The copper cross-section of the quadrupole magnet is smaller because of the shorter current decay time constant. Due to this reduction the quench detection time is only half as long as for the dipole busbar.

Cooling by helium reduces the hot spot temperature with respect to the adiabatically calculated temperature up to 200 K for a given quench load. The hot spot temperature varies by less than 10 % for the different cooling models assuming the same detection time. When the quench detection time is determined for each cooling model, the hot spot temperature varies by about 20 %.

5.2.5 Reduced Copper Stabilisation along Short Stretches

Interconnects are normal-conducting junctions of superconducting cables. The superconducting cables overlap and are connected either by ultrasonic welding or soldering. Typical values of interconnect resistances are about a few $10^{-9}\,\Omega$. A schematic view of the different types of interconnects is shown in Fig. 5.6.

Interconnects appear in magnets between layers and poles that are wound with different cables. The LHC twin aperture dipole has seven interconnects inside the magnet (four poles with two layers) and two interconnects to the busbars.
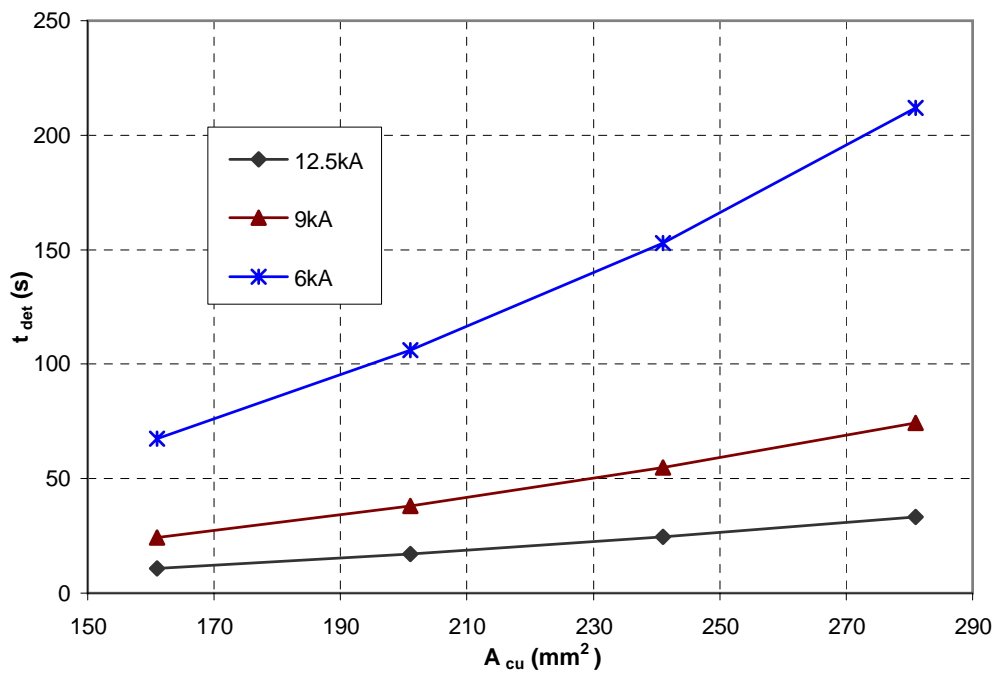
Figure 5.3: *Simulated quench detection time as a function of copper stabilisation for the main dipole busbar at various operating currents.*
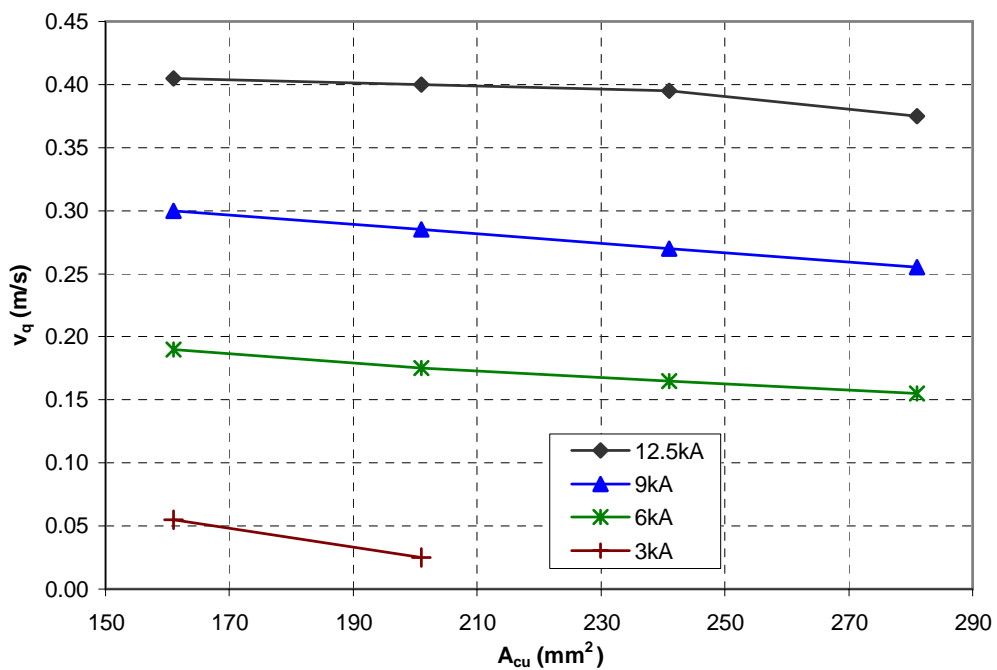
Figure 5.4: *Simulated propagation velocity as a function of copper stabilisation for the main dipole busbar at various operating currents.*
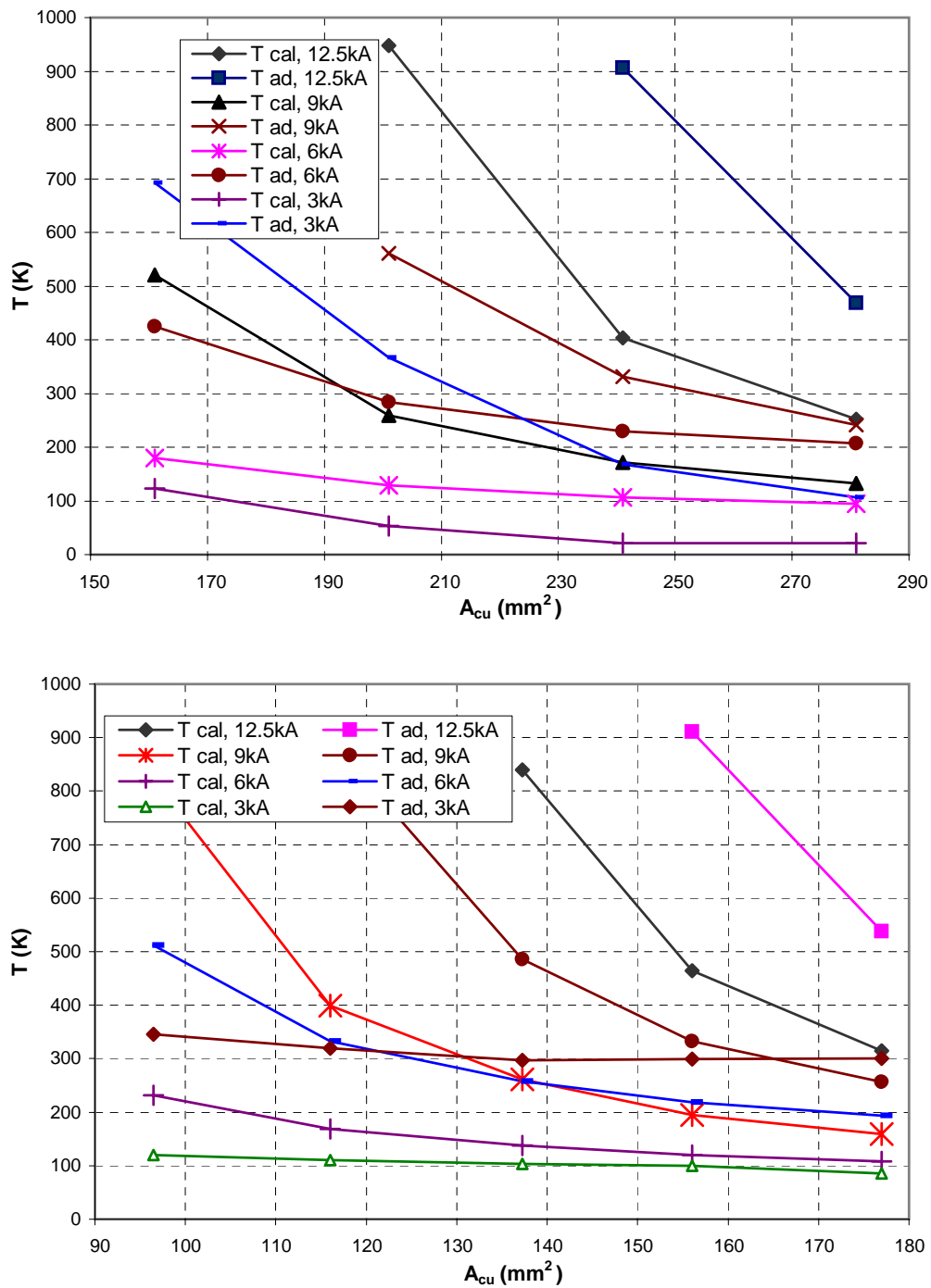
Figure 5.5: *Hot spot temperature as a function of copper cross-section (stabilisation and cable fraction) for the busbars for the main dipole (top) and quadrupole magnets (bottom) at various operating currents. The adiabatically calculated hot spot temperature is presented in addition to the simulated hot spot temperature including cooling by helium for the quench load obtained for the quench simulation.*
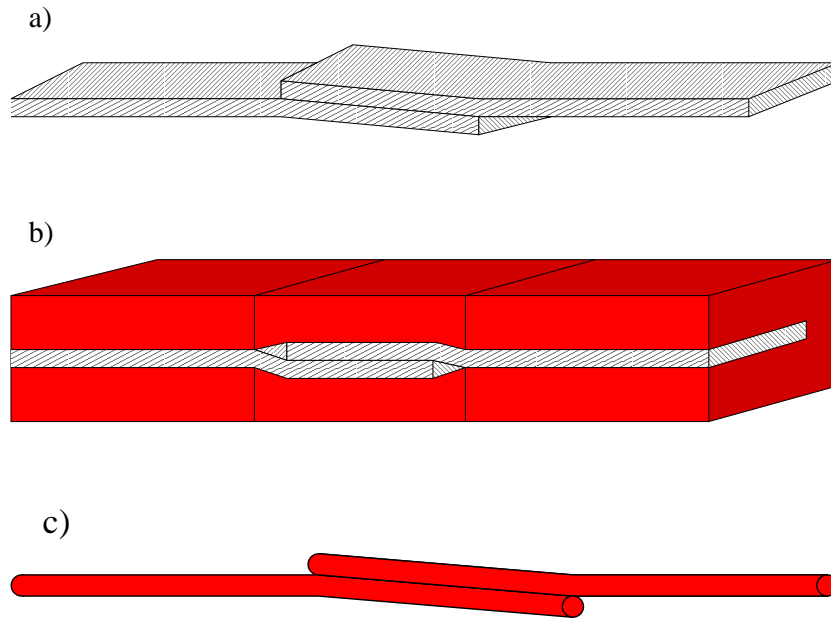
Figure 5.6: *Schematic view of interconnects: a) in magnet windings; b) between main busbars; c) between busbar cables.*

A simulation study was carried out to investigate possible reductions of the copper cross-section of main busbars in interconnects. A simulation result is shown in Fig. 5.7.

In the given example the quench started at x=0 and the copper stabilisation was reduced at six different positions by ΔA_{cu} as follows:

1. ΔA_{cu}=40 mm^2 along 10 cm
2. ΔA_{cu}=80 mm^2 along 10 cm
3. ΔA_{cu}=40 mm^2 along 5 cm
4. ΔA_{cu}=80 mm^2 along 5 cm
5. ΔA_{cu}=40 mm^2 along 20 cm
6. ΔA_{cu}=80 mm^2 along 20 cm

The hot spot temperature in the simulation does not reach excessive temperatures because the quench did not start at a position with smaller copper cross-section. If the quench starts close to or at a position with less copper stabilisation, the simulated temperature becomes unacceptably high (keeping the busbar layout as described) as shown in Figs. 5.8 and 5.9.

The present baseline for the interconnects of the main busbars is to keep the overall cross-section constant, which means a reduction of the copper cross-section by about 20 mm^2. The simulation studies showed that this reduction does not risk excessive temperatures if a quench starts in an interconnect.

5.3   Busbar Cables

String I Tests

Quench experiments were performed in String I with a 100 m long prototype cable installed in a stainless steel tube inside the bore of the dipole magnets. The prototype cable parameters
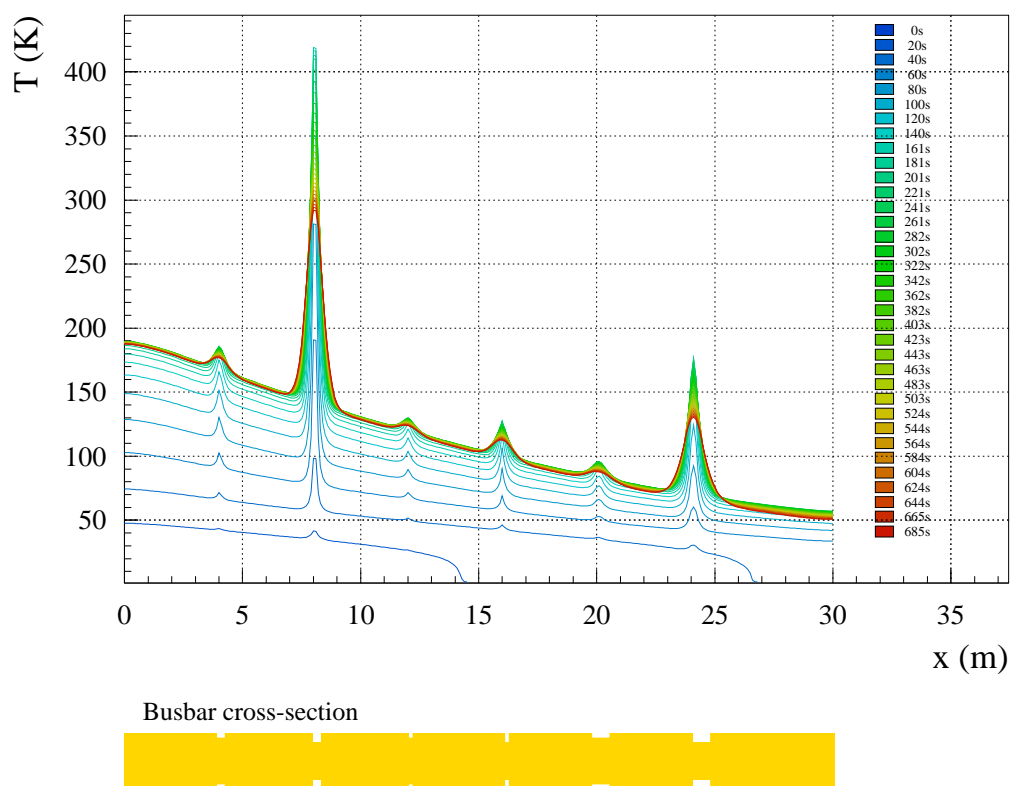
Figure 5.7: *Impact of reduced copper stabilisation along short stretches of a main dipole busbar (simulation for a quench starting at 12 kA, quench detection at 1 V, standard copper stabilisation of 296 mm^2).*
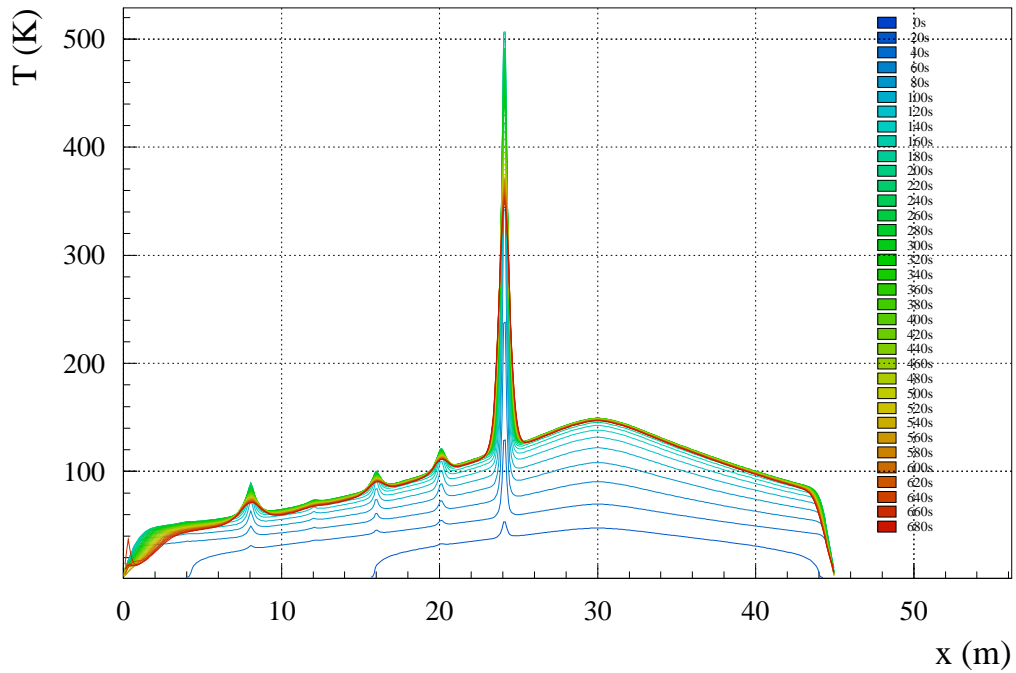
Figure 5.8: *Impact of reduced copper stabilisation along short stretches of a main dipole busbar with the quench starting close to a weak point (the simulation parameters are given in Fig. 5.7).*
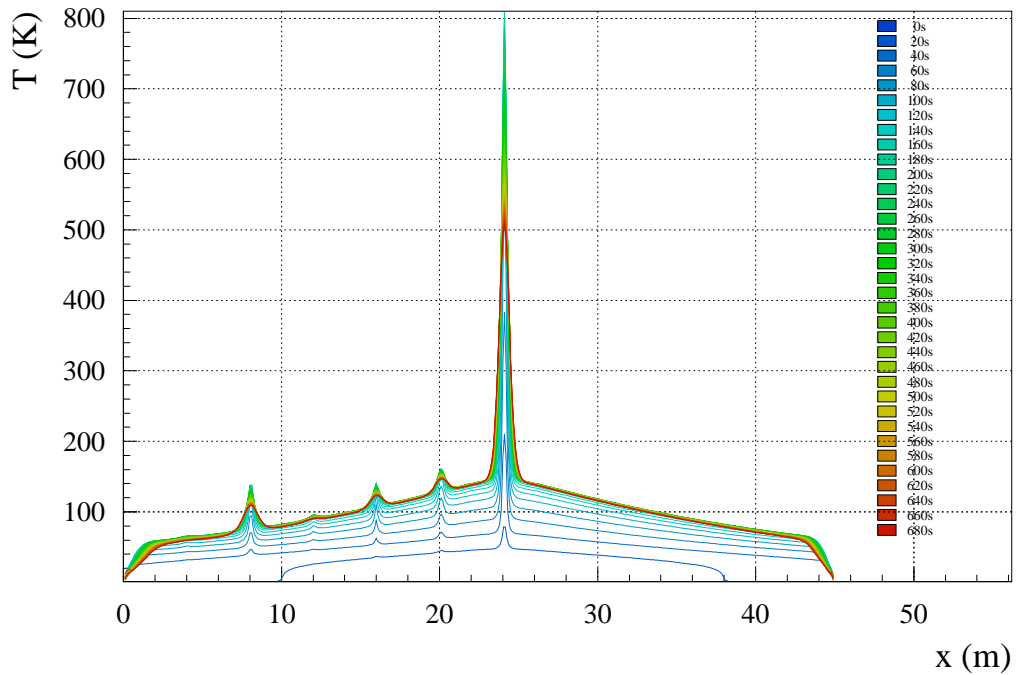
Figure 5.9: *Impact of reduced copper stabilisation along short stretches of a main dipole busbar with the quench starting in a weak point (the simulation parameters are given in Fig. 5.7).*

were $r_{cu/sc} = 9$, made of 18 NbTi filaments, diameter of 1.6 mm ($A_{tot} = 2$ mm^2) and a 200 μm thick insulation layer of polyimide tape. The maximum quench current without applied field was about 1700 A. Since the cable was not fixed, a training in quench current was observed when an external magnetic field was applied. Changing the direction of the current flow, a detraining was observed [51]. No natural quenches occured in the operating range of the cable (up to 600 A). Quenches were provoked with spot heaters and the quench propagation was measured by the resistance growth. Since the copper resistivity remains constant up to about 20 K, the increase of resistance is due to the expanding normal-conducting zone. The evaluation of the quench propagation with this method is restricted to short times after the quench start since the hot spot temperature at the quench origin exceeds 20 K within some 10 ms. This method also requires the correct measurement of the RRR value. The comparison of the measured and simulated quench propagation velocity is shown in Fig. 5.10. The prototype busbar cable was cryo-stable
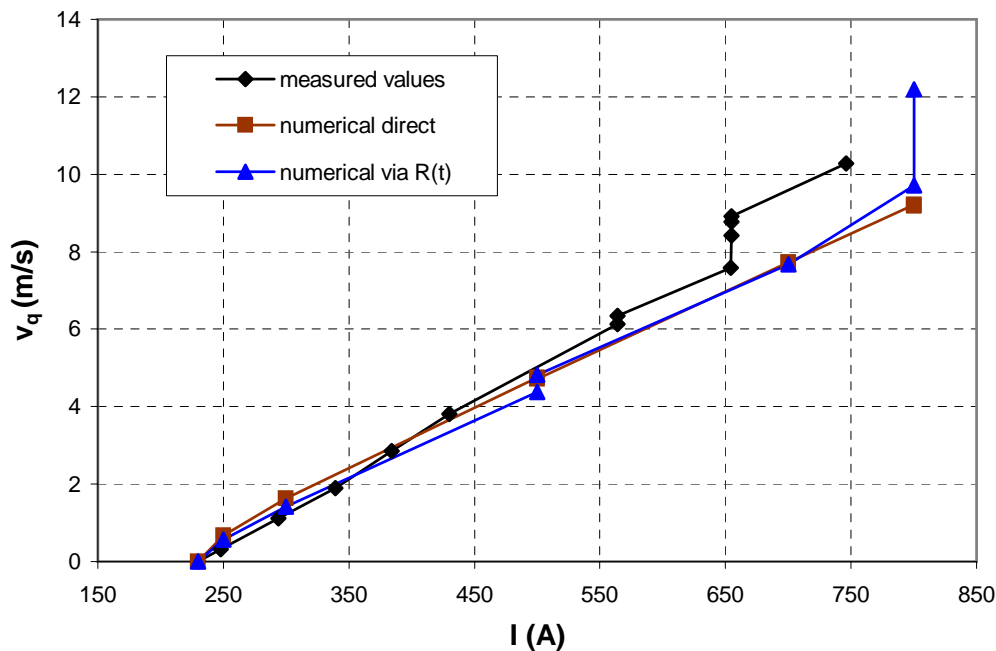
Figure 5.10: *Comparison of simulated and measured quench propagation velocity of the 600 A prototype busbar cable.*

below an excitation current of about 220 A. The simulation study shown in Fig. 5.10 used a simple helium cooling model (Eq. 3.85) including heat transfer through the insulation. Due to the small heat conductivity of the insulation material, the insulation layer thickness determines the cooling efficiency and the simulation outcome for insulated conductors depends less on the model of the heat transfer coefficient h^{He} than conductors without insulation.

Experiments in Block 4

Tests were also performed on a prototype busbar cable installed in the bore of a short prototype dipole magnet in Block 4. The first quench current at 1.8 K appeared at about 1400 A. The installed spot heater could not provoke a quench below 500 A. The measured quench propagation velocity

halved, which could be explained with more efficient cooling and a change of the RRR value. The RRR is affected by many steps in the manufacturing process and can cover a broad range (50–200). As it is difficult to keep the temperature in the cryostat constant in the range of 10–20 K, the RRR measurement can have a large error.

Experiments on another prototype busbar cable performed in Block 4 gave a quench propagation velocity of 6–8 m/s at 600 A. Below a current of 250–300 A the conductor was cryo-stable. Above 400–500 A the quench propagated quickly and a thermal runaway occured at the quench origin with temperatures up to 300 K. In the intermediate quench current region the quench propagated slowly but the temperature at the quench origin remained below 20 K. Simulation studies performed with the matrix model in SPQR (see Section 3.5.2) explain the experimental result [75]. At the propagating front, the heat generation is stronger than the heat flux through the insulation into the helium leading to an expanding normal-conducting zone. At the quench origin, the heat generation and heat flux from the conductor into helium are equal which yields a metastable situation and the temperature remains constant until the entire helium reservoir is warmed up.

Experiments on Feedthroughs

Each LHC cell is a cryogenic unit that allows a warm-up of a cell while the rest of the arc cryostat remains at 1.9 K. The busbars are fed through plugs that separate the helium bath of two adjacent cells. The cooling of the busbars in the plugs is much weaker since a different material (generally epoxy) is used for a thicker insulation layer.

Experiments were carried out to determine protection issues for the plug design. The SPQR quench model has been extended to simulate a quench originating in a plug. Excessive temperatures in the plug can be avoided with short plugs (<4 cm) due to the longitudinal heat conduction, which results in a fast propagation of the quench, or with long plugs ($\gg 8$ cm) by reason of the heat capacity, which allows more energy to be dissipated in the plug before overheating. Such a plug length allows a quench detection threshold of 0.2 V and a current decay time constant of about 3 s to keep the hot spot in the plug at about 300 K.

Assuming that the ends of the plug remain at the helium bath temperature, the temperature in the plug does not exceed 20 K because of the longitudinal heat conduction. The resistive voltage reaches about 10 mV. Experimental results showed that the quench propagation continues at the ends of a plug.

5.4 Protection of Busbars

In order to protect the busbar, a reliable quench detection is required (see Section 1.5). The quench can be detected either locally or globally (see Section 8.1.1):

- the local quench detection is based on the installation of voltage taps between the magnets in the busbar. The voltage across two taps is compared with the neighbouring voltage and a quench is detected if the voltage difference exceeds a predefined threshold. This detection scheme would require about 2000 local quench detectors for the busbars of the LHC main magnets. Using the same quench detection scheme for the 600 A busbar cables means about 7500 detectors for the spool piece busbars and about 15500 detectors for all circuits of the lattice corrector magnets (one quench detector for every half cell).

- the global detection measures the current and voltage across the entire cold part of the circuit. In order to detect a quench at any time (i.e. during the current ramp) the global voltage detector computes the inductive voltage as a function of the circuit inductance and the time derivative of the excitation current. The quench is detected when the difference of the measured and expected voltage exceeds a threshold. The use of global detection reduces the number of required quench detectors but requires a higher detection threshold as the noise level can be larger.

  From the experimental results and the simulation studies, it was concluded that a global quench detection scheme is adequate for the protection of the busbars using a voltage threshold of about 1 V for the main busbars and 0.2–0.5 V for the 600 A busbar cables.

5.5   Current Leads

Current leads are the feedthroughs that connect the cold part (at 1.9 or 4.2 K) to the warm part of the circuit (at ambient temperature). They are designed to minimise the heat load on the cryogenic system. In order to reduce the heat conduction, the cross-section of a current lead should be small which increases its resistance per length and the heat generation. Reducing the heat generation by increasing the cross-section leads to a larger heat conduction.

The cross-section of a current lead decreases towards the cold end since the resistivity and the heat generation reduces with decreasing temperature. The evaporated helium in the cold mass is used to cool the current leads with forced gas flow along the lead.

The use of high critical temperature superconductors (HTS) for a certain length of a current lead reduces the heat generation and enables the current lead to be designed with a smaller cross-section with respect to conventional copper current leads (see Fig. 5.11) [32].

The LHC will contain various types of current leads. About 700 different circuits use current leads with a high critical temperature superconducting part: all circuits with main magnets and the 600 A circuits powering the lattice and multipole corrector magnets. The closed orbit corrector magnets are operated at 60 and 120 A and will be powered with conventional copper current leads.

The superconducting current leads are protected with voltage detectors. Three voltage taps are installed at the top, at a midpoint and at the bottom. The power converter is switched off if one of the two voltages exceeds a predefined threshold. The current leads are designed to withstand the current decay when the quench originates in the high temperature superconducting part.
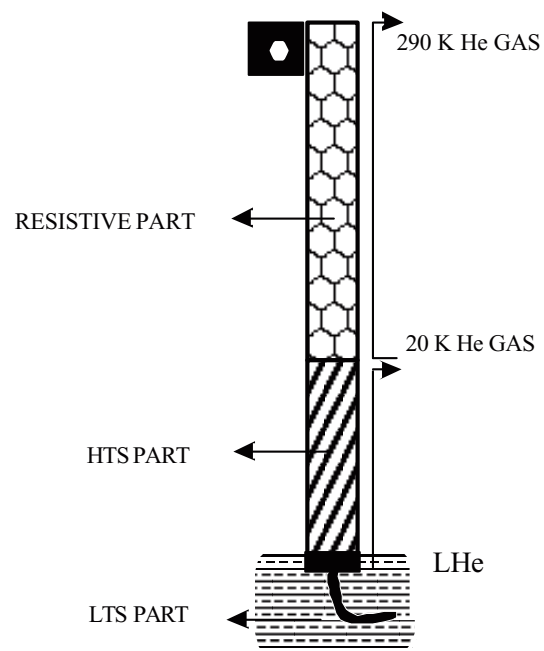
Figure 5.11: *Sketch of a current lead using high critical temperature superconductors (courtesy of A. Ballarino): HTS = high critical temperature superconductor; LTS = low critical temperature superconductor; LHe = liquid helium.*

Chapter 6

Quenching of Corrector Magnets

The LHC corrector magnets are for the correction of field errors in the main magnets (generally in the dipole magnets), and for the control of beam parameters. The corrector magnets are wound with wires made of twisted NbTi filaments inside a copper matrix. The quench propagation is more complicated than for busbars, as the quench propagates longitudinally along the cable and transversely between layers and turns inside the magnet coils. The transverse quench propagation can dominate the resistance growth. The current decay during a quench causes a change in the magnetic field, which induces eddy currents in between the twisted filaments of the superconducting cable. These interfilament coupling currents lead to losses due to the copper matrix between the filaments. The induced heat generation can cause a massive quench that is not thermally connected with the quench origin. The importance of this quench process, known as the magnetic quench back, has been demonstrated during quenches of various prototype magnets.

After presenting the model of the quench process inside corrector magnets, the quench back effect is explained. Experimental results from various prototype magnets are presented and compared with the outcome of finite difference method calculations, which include the modelling of eddy currents during a quench. The results are extrapolated to simulate a quench of a corrector magnet in a circuit with several magnets connected in series. The conclusions for the protection of these magnets are discussed.

6.1   Corrector Magnets for the LHC

The various LHC corrector magnets were introduced in Section 1.3.3. The LHC dipole magnets will be equipped with sextupole (MCS), octopole (MCO) and decapole (MCD) correctors to compensate the strongest higher order field components.

The lattice correctors with different coil designs are:

- the chromaticity sextupoles (MS) and skewed sextupoles (MSS) that have identical coil design.

- the trim quadrupole magnets (MQT) for adjusting the beam tunes and the skewed quadrupole magnets (MQS). The MQS corrector coils are identical to the MQT design.

- the long trim quadrupole magnets (MQTL) for the adjustment of beam parameters. At several locations the MQTL magnets will be operated in series of five magnets per circuit to replace a main insertion quadrupole magnet.

- the arc octopole magnets (MO) for steering beam parameters (Landau damping).

6.1.1 Parameters of the LHC Corrector Magnets

The parameters of the corrector magnets connected in series are given in Table 6.1. The 600 A

Magnet		MCS	MCD	MCO	MS	MQT	MQTL	MO
A_{tot}	[mm^2]	0.689	0.689	0.214	0.689	0.689	0.689	0.689
$r_{Cu/SC}$		1.6	1.6	4	1.6	1.6	1.6	1.6
Magnet length	[m]	0.11	0.066	0.066	0.369	0.32	1.3	0.32
Inductance	[mH]	0.8	0.4	0.4	36	31	120	1.5
Nominal current	[A]	550	550	100	550	550	550	550
Maximum family size		154	77	77	12	8	5	12
Energy/circuit	[kJ]	18.6	4.66	0.15	65.3	37.5	90.8	3.0

Table 6.1: *Parameters of the corrector magnets connected in series.*

corrector magnets are wound with the same cable (A_{tot}=0.689 mm^2). For illustration the cross-section of the MS magnet is shown in Fig 6.1. The powering parameters of the different circuits of
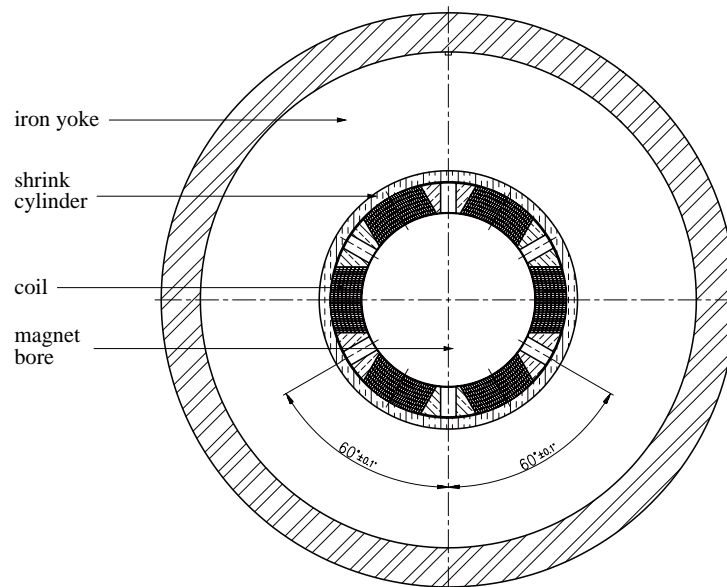
Figure 6.1: *Cross-section of the chromaticity sextupole magnet (MS). The coil is wound with 8 layers consisting of 14 turns each.*

the multipole and lattice corrector magnets are listed in Table 6.2 showing the number of magnets in a circuit, the number of circuits, the stored energy and electrical parameters (inductance L_{tot}, operating current I_0, stored energy E_0, and current decay time constant τ). The current decay time constant τ is computed by the circuit inductance and the resistance of the circuit (warm part at 300 K).

Several types of closed orbit corrector magnets are required for the LHC: the standard dipole corrector (MCB) in the arcs, which is placed next to the chromaticity sextupole magnets (MS); the

Magnet	number of		L_{tot}	I_0	E_{tot}	τ
name	magnets	circuits	[H]	[A]	[kJ]	[s]
MCS	154	16	0.123	550	18.6	14.5
MCD	77	16	0.031	550	4.66	3.6
MCO	77	16	0.031	100	0.15	0.9
MS	12	32	0.432	550	65.3	51.0
MS	10	32	0.360	550	54.5	42.5
MS (MSS)	4	16	0.144	550	21.8	66.0
MQT	8	32	0.248	550	37.5	29.3
MQT	1	64	0.031	550	4.7	15.5
MQT (MQS)	4	8	0.124	550	18.8	57.0
MQT (MQS)	2	16	0.062	550	9.4	31.0
MQTL	5	8	0.600	550	90.8	83.1
MQTL	2	8	0.240	550	36.3	82.8
MQTL	1	56	0.120	550	18.2	60.0
MO	13	16	0.020	550	3.0	10.0
MO	8	16	0.012	550	1.8	6.0

Table 6.2: *Parameters of the lattice and multipole corrector circuits.*

dipole corrector magnets in the insertions (MCBC, MCBR and MCBY); and the dipole correctors in the inner triplet (MCBX) between the strong focusing quadrupole magnets MQX close to the experiments. The dipole corrector magnets are powered individually. Table 6.3 gives their main parameters.

Magnet	Number	Cable parameters		length	L	I_0	E_{tot}	T_{bath}
name	of magnets	A_{tot} [mm^2]	$r_{cu/sc}$	[m]	[H]	[A]	[kJ]	[K]
MCB	752	0.110	4.0	0.65	7.000	60	12.6	1.9
MCBC	156	0.214	4.0	0.84	2.600	120	18.7	1.9
MCBR	16	0.214	4.0	0.84	2.240	74	6.13	4.5
MCBY	80	0.214	4.0	0.84	4.100	120	29.5	4.5
MCBX	48	1.301	1.6	0.50	0.166	600	29.9	1.9

Table 6.3: *Parameters of dipole corrector magnets and their cables.*

As can be seen in Table 6.1 and 6.3 the cross-section of the conductors used to wind corrector magnets is small with respect to the busbar powering these magnets (see Section 5.3). Since the quench propagation velocity changes with the cross-section, the normal conducting zone spreads out faster with respect to a quench in a busbar. The temperature also increases faster.

6.2   Experimental Results

The current versus time is shown for a typical quench of a prototype magnet in Fig. 6.2 (top) (here for a MQTL quadrupole magnet). The current decays within 0.25 s. The lower diagram in Fig. 6.2 shows the start of the current decay with and without filtering. The data smoothing reduces the scatter of ± 20 A to about ± 3 A.
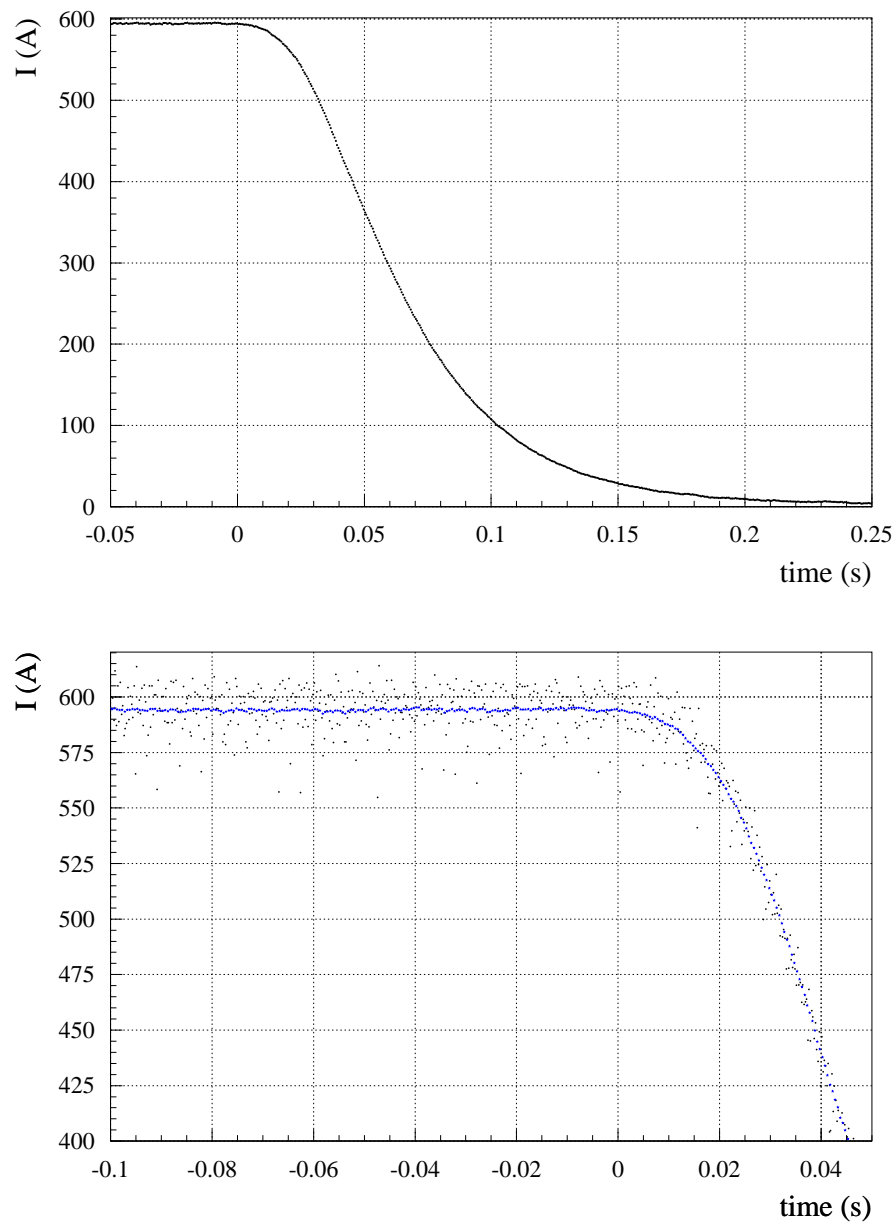
Figure 6.2: *Current measurement during a typical quench in a prototype corrector magnet (here for a MQTL quadrupole magnet): current decay (top); and the effect of filtering the data with the extraction program team_convert (see Section 4.4) (bottom).*

The voltage development during a quench is shown in Fig. 6.3 for a quench in a MS prototype sextupole magnet; a resistive voltage is positive, an inductive voltage negative. The predicted inductive voltage signal per pole is also shown (signal 'ldI/dt'). The data acquisition saturates at about 25 V, which is reached by the first quenching pole (signal 'p2'). At $t = 0$, the quench is detected and the power converter is switched off (short circuited), which induces a noise signal in the voltages. The other pole voltages are purely inductive until about 20 ms after quench detection. The difference between the predicted inductive voltage and the pole voltages after this time indicates a resistive contribution which can be explained with magnetic quench back (see Section 3.4.2).

As the quench propagation from one turn to the next takes about 2–3 ms, a time of about 30–45 ms is required for the transverse quench propagation from one pole to the next. With a longitudinal quench propagation velocities of about 30–40 m/s at nominal current and a magnet length of 0.5 m (prototype length, length for the machine is 0.369 m), the longitudinal quench propagation takes about 12 ms to quench an entire turn. Apart from the pole in which the quench originated, all other poles start quenching within a time interval of 2 ms in the given example, which cannot be explained by longitudinal or transverse quench propagation. Quench back due to a temperature increase by induced eddy currents can explain this quench process. For completeness the current decay curve is shown for the same quench.

Quench Propagation

The longitudinal quench propagation velocity was determined for various prototype magnets (MS, MQT, MQTL) that were instrumented with voltage taps and spot heaters as described in Section 4.1.

An example of the quench propagation velocity measured at 600 A in a MQT magnet is shown in Fig. 6.4.

The longitudinal quench propagation velocity can also be derived from the voltage growth at the start of the quench when the resistivity is independent from the temperature (up to about 20 K) and the RRR value is known. This has been done for the closed orbit corrector MCB and the chromaticity sextupole magnet MS.

The transverse quench propagation velocity was measured in various prototype magnets (MQT, MQTL, MS and MCB) with the help of installed voltage taps between several layers and turns. The time delay Δt_t required to quench an adjacent turn or layer can also be determined from the growth of a pole voltage. When a new turn starts to quench, the slope of the voltage increases. This method was used for the MCS and MQTL prototype magnets. An example is shown in Fig. 6.5 (measured in a MQTL magnet).

The quench propagation can also be obtained indirectly by changing the input parameters for the longitudinal and transverse quench propagation velocity in the QUABER simulation model. When the simulation reproduces the measured quench load for various quench currents, the quench propagation parameters are known. This method was used for the MCO and MCB magnets.

An overview of the experimentally derived longitudinal and transverse quench propagation velocity at various currents is given in Table 6.4.

Protection by a Parallel Resistor

When several magnets are connected in series per circuit, the magnets can be protected with resistors that are mounted parallel to each magnet (see Section 1.5). In case of a quench, the
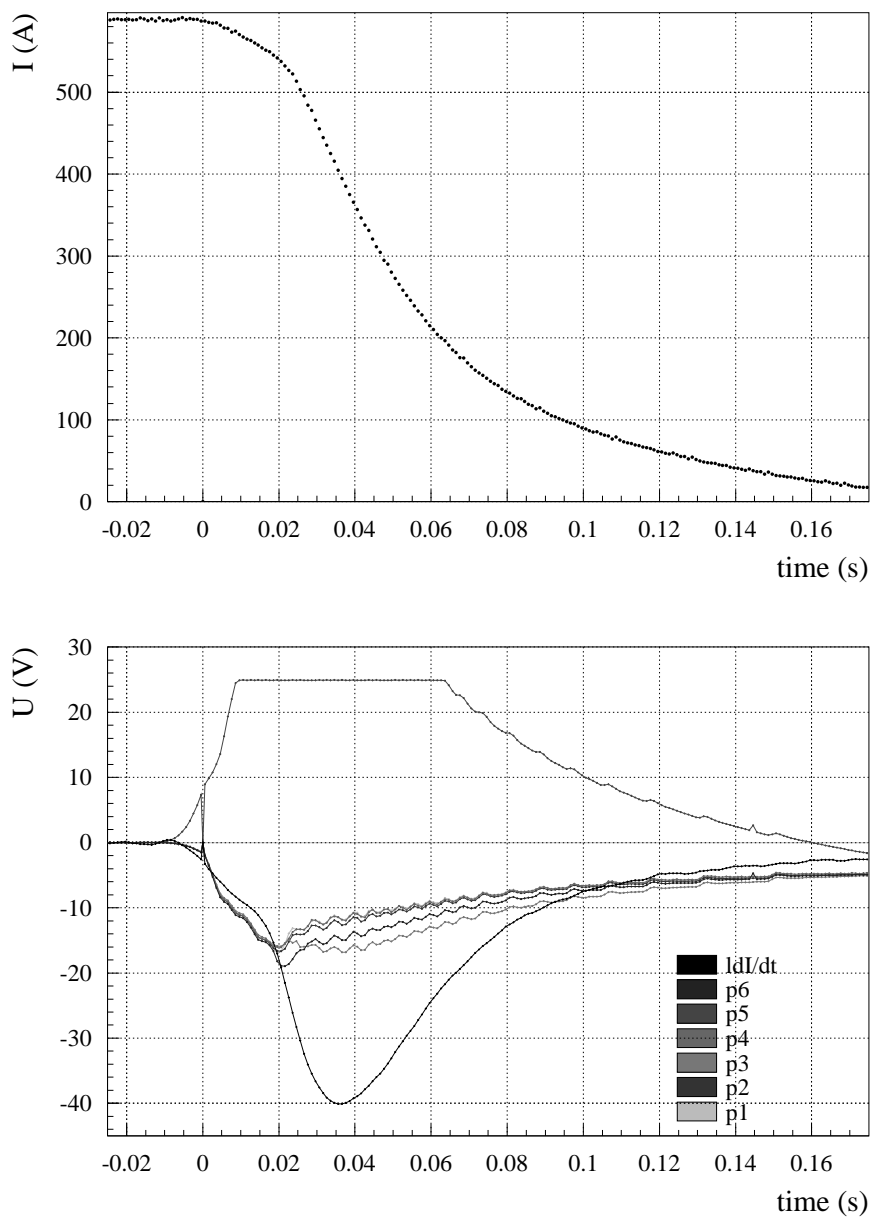
Figure 6.3: *Current decay and pole voltages ('p1–p6') measured during a quench of a MS prototype sextupole magnet (MCSS BC, quench 304). The data acquisition saturates at 25 V which is reached by the first quenching pole (signal 'p2'). The other pole voltages stop being purely inductive and start to quench 20 ms after quench detection within a time interval of 2 ms. This can be explained with magnetic quench back (see Section 3.4.2) but not with longitudinal or transverse quench propagation.*
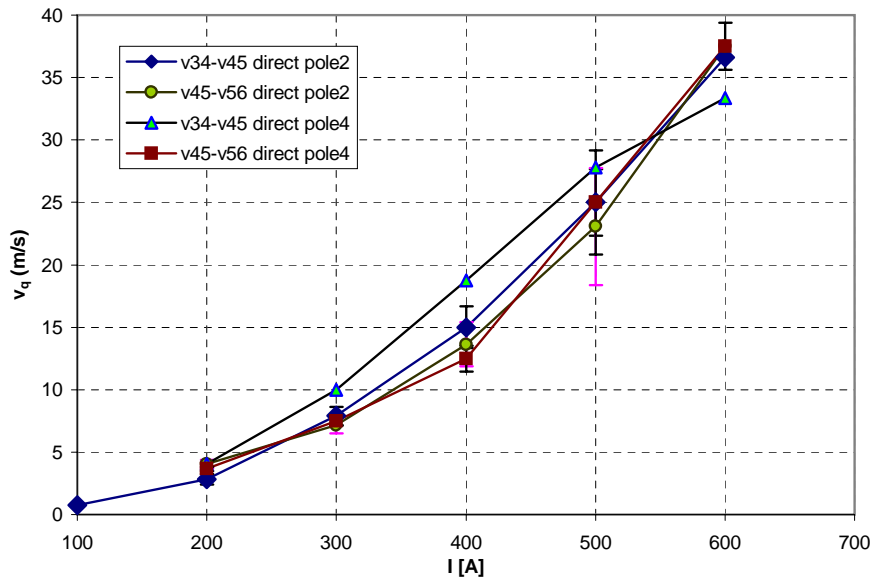
Figure 6.4: *Longitudinal quench propagation velocity determined on a MQT prototype quadrupole magnet. The error bars represent the scatter of the measurements for various quench experiments at the same current.*
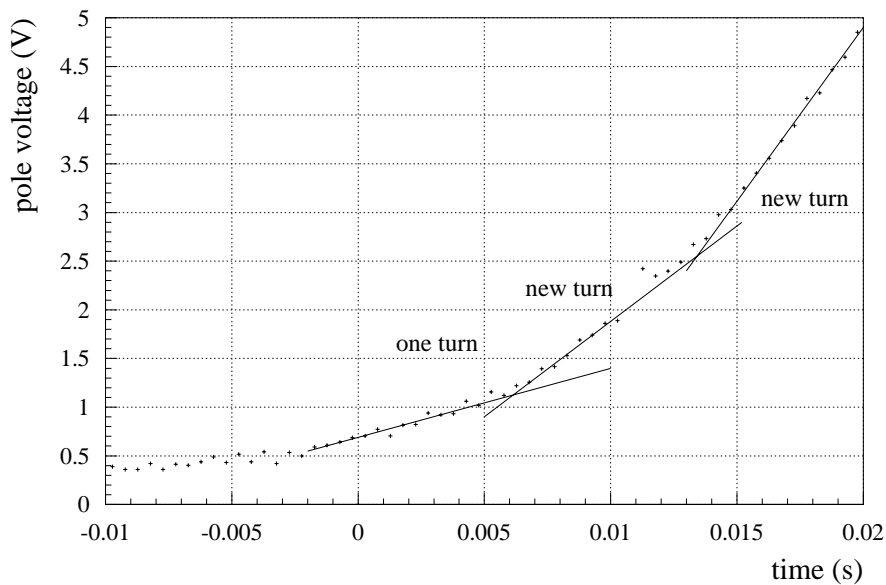
Figure 6.5: *Transverse quench propagation velocity determined with the voltage development in a MQTL prototype quadrupole magnet after a provoked quench at 400 A. The resistivity is assumed to be constant. This means that the slope of the voltage only increases when a new turn starts to quench. In the given example, the turn-to-turn delay is about 7 ms.*

Magnet	I	v_q	Δt_t	evaluation
name	[A]	[m/s]	[ms]	method
MQT	600	30–40	3–4	direct with voltage taps in the coil
MQTL	600	25-35	-	direct with voltage taps in the coil / voltage rise
MS	580	-	2–3	voltage taps in various layers
MCB	55	-	1–2	voltage taps in various layers
MCS	550	25–30	2–3	voltage rise of the pole voltages
MCO	110	30–50	1–2	calibrated simulation for quench load reproduction

Table 6.4: *Results of the evaluated longitudinal (v_q) and transverse (Δt_t) quench propagation in corrector magnets with direct measurements, voltage development analysis and the help of calibrated simulation studies.*

resistance grows inside the magnet and exceeds the value of the parallel resistor. Consequently, the current starts to bypass the quenching magnet and the stored magnetic energy of the other magnets in the series is dissipated into the parallel resistor.

The current distribution of a corrector magnet protected with a parallel resistor of $100\,\text{m}\Omega$ was measured in a MCS magnet. A large inductance was switched in series with the MCS magnet. The load inductance resulted in a slower current decay (I_{tot}) in the circuit. The parallel resistor led to a fast current decay inside the magnet (I_{mag}) and the current started to flow through the parallel resistor (I_{R_p}). An example of the measured current distribution is shown in Fig. 6.6.
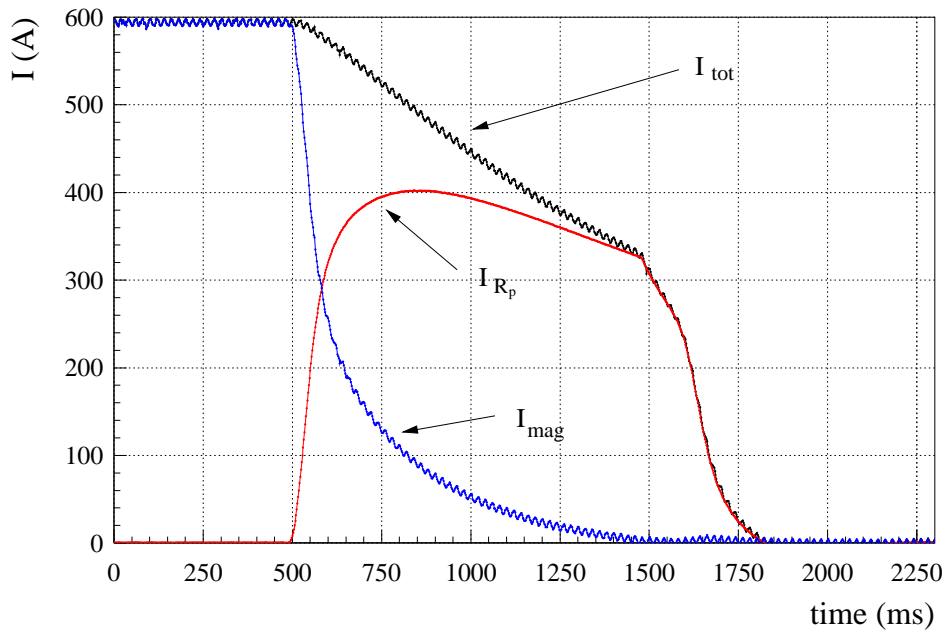
Figure 6.6: *Current distribution after a provoked quench at 600 A in a MCS prototype magnet equipped with a parallel resistor for protection.*

The current decay in the magnet was derived from the measured value of the parallel resistor R_p, the voltage across the magnet and the total current. The voltage across the magnet is identical

to the voltage across the parallel resistor, which is used to compute the current in the magnet and its resistance growth. The value of the parallel resistor R_p is assumed to be constant

$$U_{mag}(t) = L_{mag}\frac{dI_{mag}(t)}{dt} + R_{mag}(t)I_{mag}(t) = R_p I_{R_p}(t) \tag{6.1}$$

$$\Rightarrow I_{R_p}(t) = \frac{U_{mag}(t)}{R_p} \tag{6.2}$$

which gives

$$I_{mag}(t) = I(t) - I_{R_p}(t) = I(t) - \frac{U_{mag}(t)}{R_p} \tag{6.3}$$

$$R_{mag}(t) = \frac{U_{mag}(t) - L_{mag}\frac{dI_{mag}(t)}{dt}}{I_{mag}}$$

$$= \frac{U_{mag}(t) - L_{mag}\frac{d(I(t) - \frac{U_{mag}(t)}{R_p})}{dt}}{I(t) - \frac{U_{mag}(t)}{R_p}} \tag{6.4}$$

As can be seen in Eq. 6.1, a leakage current flows through the parallel resistor when the current changes. This leakage current causes an additional heat load and an offset between the current provided by the power converter and the current flowing through the magnet. This might require a compensation by the power converter control for the precision of the magnetic field (see also Section 6.4). If a parallel resistor is required for protection, a single value is used for one type of magnet in order to simplify the production and installation in the machine.

Magnetic Quench Back

Magnetic quench back that is caused by induced eddy currents during the current decay (see Section 3.4.2) has been observed in many prototype corrector magnets [79], for example in the sextupole magnet MCS, in the quadrupole magnets MQT and MQTL, and the chromaticity sextupole magnet MS. An example for observed magnetic quench back is given in Fig. 6.7 for a training quench at about 1000 A of a MCS magnet. The quench starts in pole 6. At 96 ms the other five poles develop a resistive voltage due to magnetic quench back. The transverse and longitudinal quench propagation can not explain the appearance of a quench in five poles in a time interval of about 1 ms.

6.3   Simulation Studies

Finite difference method calculations were performed with SPQR to predict the longitudinal and transverse quench propagation and to study the quench back effect in corrector magnets. The outcome of SPQR simulations was crosschecked with experimental results presented above and used as input for QUABER simulations. These were carried out to study protection issues for the corrector magnets.
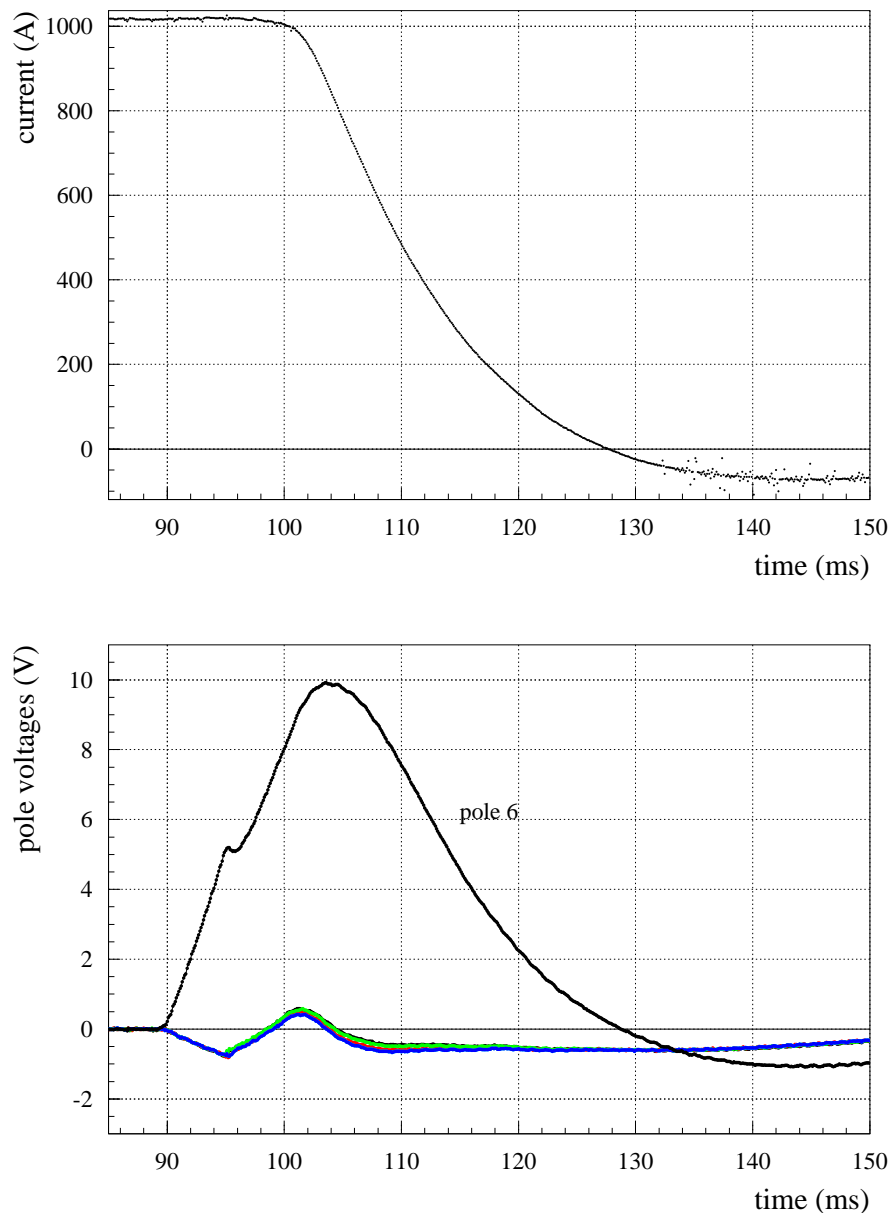
Figure 6.7: *Current decay and pole voltages of a MCS sextupole magnet showing a magnetic quench back: the negative current at the end of the decay is a consequence of the bipolar power converter control that applies a negative voltage for a fast current decay. The slow current control loop causes that the power converter does not stop at zero current but applies a current in opposite direction before going to zero. The quench appears at 90 ms in pole 6. The voltages of the poles 1–5 stop being purely inductive at 96 ms and start to quench. The other five poles quench at the same time which can be understood by quenching due to losses of induced eddy currents, which is called magnetic quench back. Thermal quench propagation can not explain the quenching of five poles at the same time.*

6.3.1 Quench Propagation

Since the evaluation of the temperature profile becomes very time-consuming with an increasing number of finite elements, SPQR could not be used to model the quench process in an entire coil. The simulations were carried out as described before for the busbars to derive the longitudinal quench propagation. An example is shown in Fig. 6.8. In a second step, the simulation was
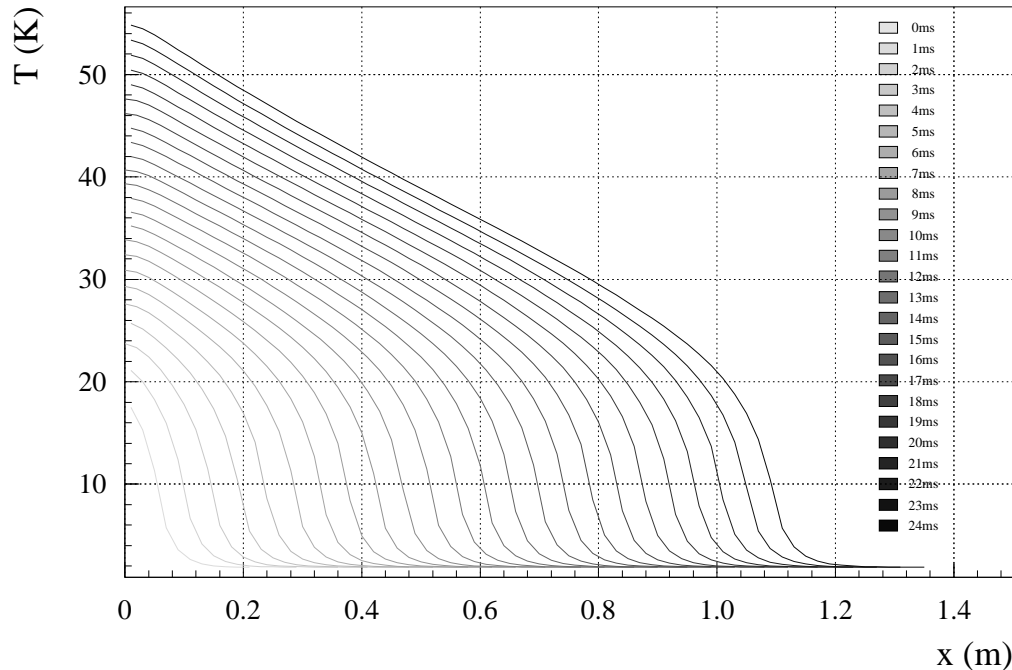
Figure 6.8: *Simulation of the longitudinal quench propagation in a lattice corrector magnet with a quench current at 600 A ($A_{tot} = 0.689\,mm^2$, $r_{cu/sc} = 1.6$, $RRR = 80$). The time between two neighbouring curves is 1 ms.*

repeated with a two-dimensional model including several layers to simulate the quench propagation from one layer to the next. This allowed a crosscheck of the simulation result for the longitudinal quench propagation in the one-dimensional model. The simulation was also carried out with a three-dimensional model (several layers and turns) to obtain the quench propagation from one turn to the next.

The small dimensions of the corrector cable require that the initial timestep must be set in the range of 1–2 ns in the three-dimensional model and that a longitudinal discretisation of 1–5 mm must be used. For the computation of the longitudinal quench propagation with the one-dimensional model, consistent results are obtained with a longitudinal discretisation of up to 1 cm.

The longitudinal quench propagation velocity was simulated to be about 35 m/s at 600 A and an applied magnetic field of 3 tesla. Changing the magnetic field in the range of 2.5–4 tesla leads to a change of the quench propagation velocity of ±5 m/s.

The turn-to-turn delay at 600 A and 3 tesla was simulated to be 3.2 ms which is slightly larger than the experimental result (for an epoxy insulation layer of 120 μm). The result strongly depends on the thickness of the insulation layer between two turns or layers which was assumed to be twice

the thickness of the cable insulation layer. An insulation layer thickness of $100\,\mu$m results in a turn-to-turn delay of 2.8 ms at nominal current.

6.3.2   Magnetic Quench Back

The theoretical description of magnetic quench back was introduced in Section 3.4.2 and experimental evidence was described in Section 6.2.

The current decays after the start of a quench with a time constant of some ten milliseconds in an individually powered corrector magnet. Depending on the magnet and cable parameters, quench back can start as early as 10 ms after a natural quench (see Eq. 3.54). The simulation results for magnetic quench back agree with results from tests with single corrector magnets. The quench back start-time for the MCS magnet was experimentally determined to be 9 ms (for a natural quench at 1000 A and 5 tesla). The simulation results in a quench back start-time of 8 ms. Changing the initial magnetic field by 0.5 tesla affects the simulation outcome by about 1 ms.

The impact of the filament twist pitch of the conductor has been tested experimentally on two MCS (spool piece sextupole magnets). The strength of the induced interfilament coupling currents is proportional to $dB/dt \cdot L_p^{f2}/\rho_{cu} \cdot (1 - \exp(-t/\tau_{if}))$. Using a first order Taylor expansion series for short times gives $(1 - \exp(-t/\tau_{if})) \approx t/\tau_{if}$. Inserting $\tau_{if} \propto L_p^{f2}/\rho_{cu}$ shows that the effect of a different twist pitch and ρ_{cu} cancels for short time scales. Typical values of τ_{if} are about 10 ms, thus the approximation can be used for a quench back starting in that time range.

The cables had twist pitches of 18 mm and 40 mm and RRR values of 130 (for L_p^f=18 mm) and 50 (for L_p^f=40 mm). The quench back started about 2 ms earlier in the magnet with the 40 mm twist pitch cable which is likely to be due to the RRR value with larger resistivity at low temperature. Since $P \propto \rho_{cu}I_{if}^2$ and the effect of a changed twist pitch length cancels on a short timescale, the different quench back start-time is due to the RRR value, which was also confirmed in SPQR simulation studies.

During a current ramp with constant dI/dt the larger L_p^f yields stronger induced coupling currents compromising the field quality. If a quench is followed by a fast current decay, the quench back start-time is very small and a change of the twist pitch from 18 mm to 40 mm does not accelerate the start of magnetic quench back. It was therefore concluded to use the smaller twist pitch length for the series production of the corrector cables.

SPQR simulation studies were carried out to extrapolate experimental results to the LHC circuit with up to 154 magnets powered in series and slower current decays, in order to determine whether magnetic quench back is a reliable mechanism for magnet protection. The simulation outcome is shown in Table 6.5 as a function of the current decay time constant, RRR, and various twist pitches.

For a current decay time constant longer than 0.1 s, magnetic quench back does not start fast enough to be helpful for magnet protection. The current decay in magnets equipped with a parallel resistor can be fast enough to cause magnetic quench back early, which is not needed for protection in this case because of the parallel resistor.

Tests on protype magnets with a larger inductance confirmed that quench back does not occur after a quench in a magnet with a current decay time constant significantly larger than 0.1 s.

Table 6.6 compares the experimental and simulation results for the quench propagation in corrector magnets.

L_p^f [m]	0.001	0.005	0.010	0.050	0.100	0.500	1.000	5.000
RRR=80, τ=0.1 s	-	-	late	yes	yes	late	-	-
RRR=130, τ=0.1 s	-	-	late	yes	yes	late	-	-
RRR=80, τ=0.25 s	-	-	-	late	late	-	-	-
RRR=130, τ=0.25 s	-	-	-	late	-	-	-	-
RRR=80, τ=0.5 s	-	-	-	-	-	-	-	-
RRR=130, τ=0.5 s	-	-	-	-	-	-	-	-

Table 6.5: *Simulation results for the magnetic quench back effect in corrector magnets. Magnetic quench back that starts early enough for protection is marked as 'yes'. Magnetic quench back that appears but too late to be helpful for protection is marked as 'late'. The simulation study was carried out as a function of the changeable cable parameters (L_p^f = 18 mm for the LHC corrector magnets).*

	simulation	experiment
v_q	35 m/s	30–40 m/s
Δt_t	3.2 ms	2–3 ms
quench back start	8 ms	6–9 ms

Table 6.6: *Comparison of quench simulation studies and experimental results at 600 A and a current decay time constant of 70 ms for the standard cable of the lattice corrector magnets in a MCS coil (A_{tot} = 0.689 mm², $r_{cu/sc}$ = 1.6, RRR= 80).*

6.4   Protection of the Corrector Magnet Circuits

A protection similar to the main magnets (with local quench detection and quench heaters, see Sections 1.5 and 7.1) cannot be considered for the corrector magnets, since this would be an over-design, possibly compromising LHC operation reliability [79]. As every active element has a certain failure rate, an active protection system for the corrector magnets would increase the downtime of the machine.

QUABER simulations are performed to simulate a quench in a corrector magnet connected in series and to determine the required protection for the various circuits of corrector magnets in the LHC. The outcome of the SPQR simulation studies and the experimental results of prototype magnets [62, 80, 81] are used as input parameters for the calibration of the QUABER model. The temperature calculations are performed with two different models: a conservative model assuming the quench remains in a single coil (model 1), and a more realistic model assuming the quench can propagate from one coil to the others (model 2). The power converters for the corrector magnet circuits are voltage limited. In order to define a current power source with a voltage limitation of 8.5 V in SABER, a negative current had to be used.

The protection system for the corrector magnet includes quench detection, energy extraction, and possibly the installation of parallel resistors.

The magnetic energy of the circuit can be extracted in two different ways:

- by a dump resistor that is switched into series with mechanical switches (same principle as for the 13 kA circuits). The voltage-to ground-limitation is about 420 V, thus allowing an extraction resistor of up to 700 mΩ.

- by a small resistor that can be switched into series by thyristors when the power converter is switched off. The voltage-to-ground limitation is about 30 V, thus allowing a small extraction resistor of about 50 mΩ.

Lattice Corrector Magnets

The results of the QUABER simulations are given in Table 6.7, which includes the number of magnets connected in series for the corrector circuits and the required protection (value of parallel and extraction resistor). The quench detection parameters are a threshold of 1 V and a quench verification time of 20 ms. The hot spot temperature does not exceed 200–240 K.

Magnet name	Current [A]	Magnets per circuit	Energy extraction	R_{ex} [mΩ]	R_{par} [mΩ]	Reason for energy extraction
MCS	550	154	yes	700	80	protection of magnet and busbar
MCD	550	77	yes	700	-	protection of magnet and busbar
MCO	110	77	no	-	-	
MS	550	12	yes	700	150	protection of magnet and busbar
MS	550	10	yes	700	150	protection of magnet and busbar
MSS	550	4	yes	50	150	protection of busbar
MQT	550	8	yes	700	250	protection of magnet and busbar
MQT	550	1	yes	50	-	protection of busbar
MQS	550	4	yes	50	250	protection of busbar
MQS	550	2	yes	50	-	protection of magnet and busbar
MQTL	550	5	yes	700	200	protection of magnet and busbar
MQTL	550	2	yes	700	200	protection of magnet and busbar
MQTL	550	1	yes	50	-	protection of magnet and busbar
MO	550	13	yes	200	-	protection of magnet
MO	550	8	yes	200	-	protection of magnet

Table 6.7: *Foreseen protection schemes for the LHC corrector magnets. R_{ex} is the required value for the protection of the superconducting elements in the circuit. R_{par} is the required value for the parallel resistor.*

- In order to protect the MCS spool piece corrector magnets, a parallel resistor of 80 mΩ and an energy extraction resistor of 0.7 Ω have to be installed.

- Due to the smaller amount of stored magnetic energy, the MCD spool piece magnets can be protected by a dump resistor of 0.7 Ω without a parallel resistor. The dump resistor has to be switched into series within 90 ms after the quench start.

- The MCO spool magnets are self-protecting when the power converter shuts down after quench detection at a threshold of 8.5 V. An example of the simulation result is shown in Fig. 6.9.

- In order to keep the hot spot temperature within safe limits for the MS magnets (chromaticity sextupoles), a parallel resistor of 150 mΩ or a parallel diode with a turn-on voltage of 1.5 V have to be installed (see Table 6.8). The protection with a parallel diode was abandoned due to technical reasons such as irradiation effects and others.
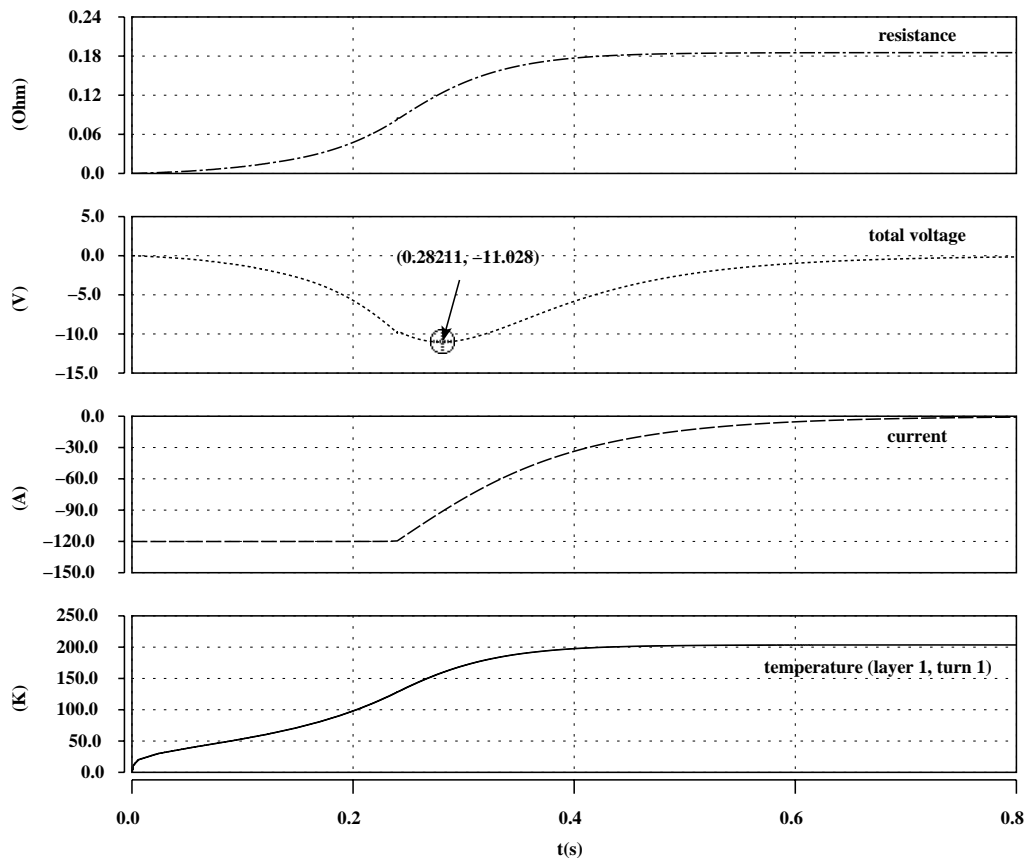
Figure 6.9: *QUABER simulation result of the hot spot temperature for a quench in one of the 77 MCO magnets connected in series showing the current, the voltage across the magnet, the resistance and the adiabatically calculated hot spot temperature as a function of time. In order to simulate a voltage limited power converter, a negative current had to be used for the simulation.*

A energy extraction resistor of $0.7\,\Omega$ is required for the circuits with 10 and 12 magnets connected in series. A parallel resistor of $400\,\mathrm{m}\Omega$ leads to a simulated hot spot temperature of about $300\,\mathrm{K}$ which might be too high. Such a hot spot temperature produces a temperature gradient inside the magnet that can damage the impregnation of the coil. On the contrary, a parallel resistor of $400\,\mathrm{m}\Omega$ would reduce the leakage current and a compensation in the power converter control would not be required.

- A parallel resistor of $250\,\mathrm{m}\Omega$ has to be installed parallel to the magnets for the trim quadrupole circuits with 4 and 8 MQT magnets connected in series. Several dump resistors are required for the different circuit types.

- The long trim quadrupole magnets (MQTL) that are connected in series of 2 and 5 magnets per circuit are protected with a parallel resistor of $200\,\mathrm{m}\Omega$. Different extraction resistors are needed for the various MQTL circuits.

- The arc octopole magnets (MO) can be protected without parallel resistors by using a dump

Resistance [mΩ]	T_{max} Model 1 [K]	T_{max} Model 2 [K]
100	175	160
150	200	180
200	230	205
400	280	235
500	335	250
diode (U_{on}=1.5 V)	180	160

Table 6.8: *Simulated hot spot temperature for the MS magnet connected in series of 12 magnets as a function of various parallel protection resistors and a protection diode with a turn-on voltage of 1.5 V.*

resistor of about 200 mΩ. A simulation result of the current decay, the temperature and voltages curves versus time is shown as an example in Fig. 6.10.

Magnet	MCS	MS	MQT	MQTL
L [mH]	0.8	36	31	120
R_{par} [mΩ]	80	150	250	200
dI/dt [A/s]	10	10	10	10
I_{leak} [A]	0.1	2.4	1.24	6
P_{leak} [mW]	0.8	864	384.4	7200
dI/dt [A/s]	5.2	1.4	2.9	0.5
I_{leak} [A]	0.052	0.336	0.360	0.3
P_{leak} [mW]	0.2	16.9	32.2	18

Table 6.9: *Heat load per magnet due to the parallel resistor for the corrector magnets for a current ramp rate of 10 A/s and the maximum expected current ramp rate of each magnet type that is required for the LHC operation.*

The heat load due to the installation of a parallel resistor was calculated using the maximal current ramp rate of 10 A/s. Apart from the MQTL magnets connected in series of 5 magnets per circuit, the heat load is small with respect to the given limits by the available cryogenic power. The heat load reduces significantly applying the fastest current ramp rates that are expected in the LHC to values of less than 50 mW per magnet (5.2 A/s for the MCS magnet, 2.9 A/s for the MQT, 1.4 A/s for the MS, and 0.5 A/s for the MQTL) [82]. The heat load is given for each magnet type in Table 6.9.

Closed Orbit Correctors

The individually powered closed orbit correctors do not require a special protection system. The maximum temperature evaluated from experiments on prototype magnets is about 150 K (MCB magnets). The power converter for the closed orbit correctors can provide a maximum voltage of 8.5 V. When this voltage is exceeded, the power converter shuts down and the current decays. QUABER simulations demonstrated that 8.5 V is reached after about 150 ms for the MCB magnet (operated at 60 A) and 50–70 ms for the other closed orbit correctors (operated at 110 A).
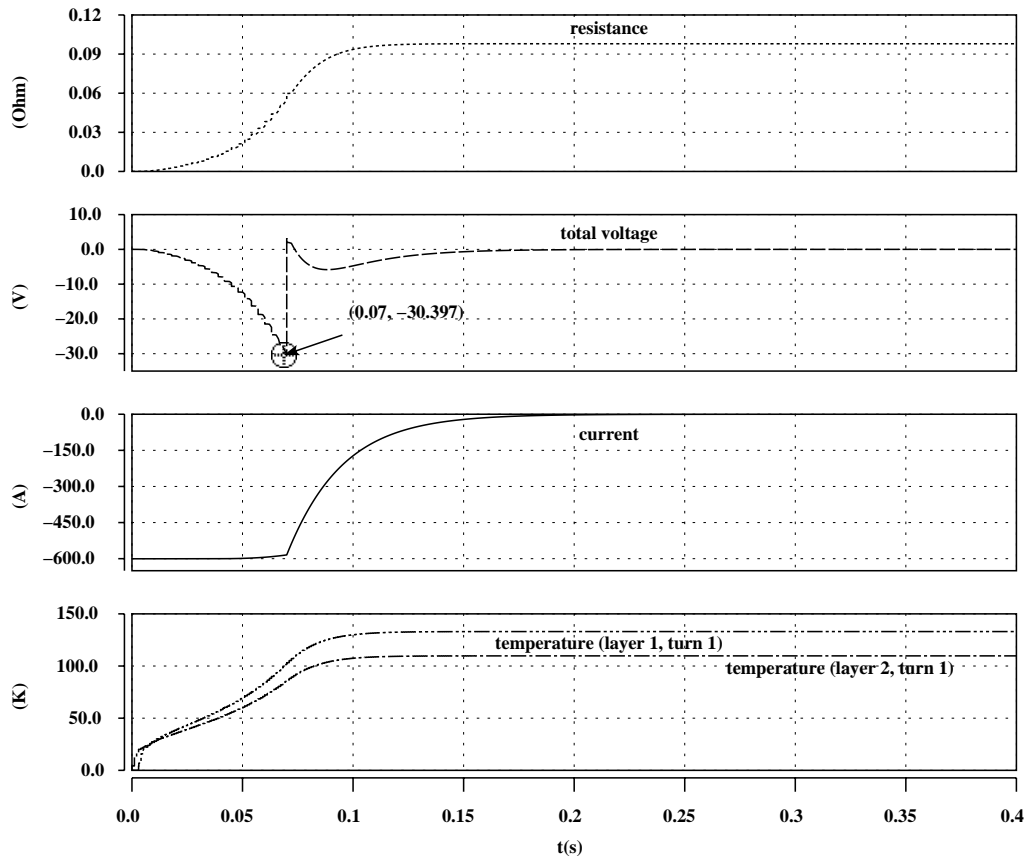
Figure 6.10: *Simulation example of a quenching MO magnet in a circuit of 12 magnets showing the resistance, the voltage, the current and the adiabatically calculated temperature as a function of time. As in Fig. 6.9, an initial negative current is applied to simulate a voltage limited power converter.*

An example of the simulation result is given in Fig. 6.11 for the MCBY dipole corrector magnet operated at 110 A.

> **The additional energy dissipated into the magnet until the voltage limitation of the power converter is reached corresponds to a few percent of the stored magnetic energy and does not significantly increase the hot spot temperature in the magnet. The closed-orbit corrector circuits are therefore self-protecting.**
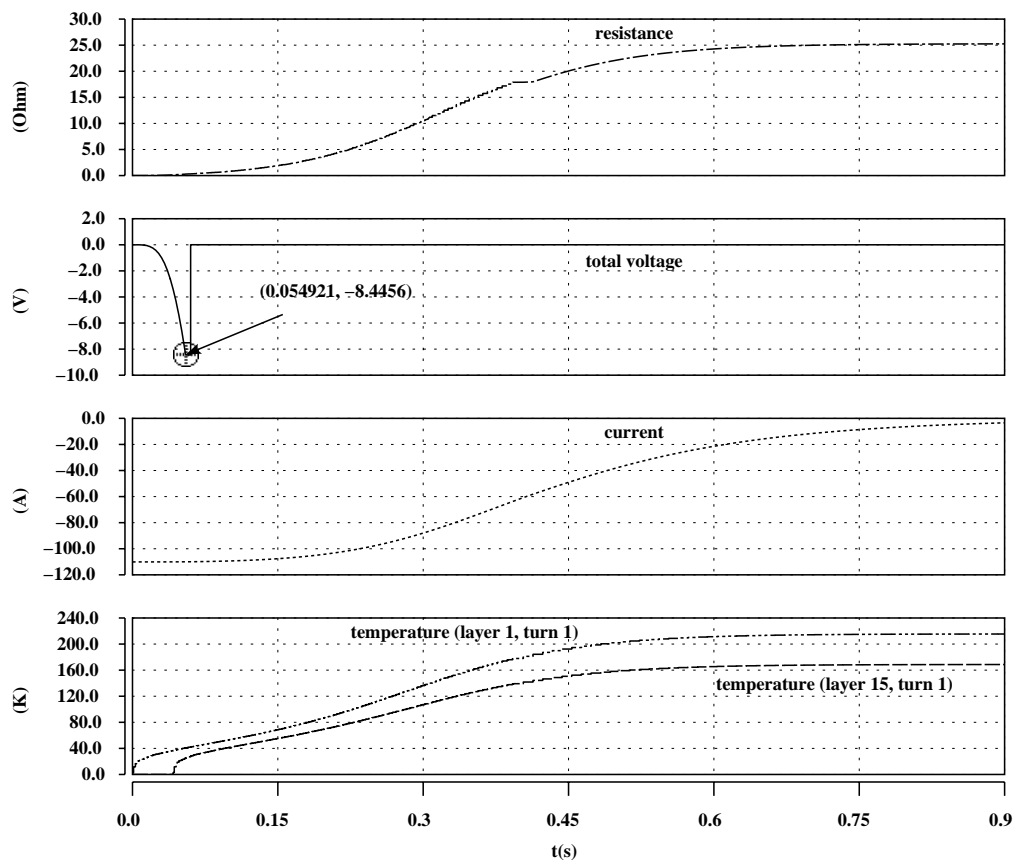
Figure 6.11: *Simulation example of the MCBY magnet showing the resistance, the voltage, the current and the adiabatically calculated temperature as a function of time. As in Fig. 6.9, an initial negative current is applied to simulate a voltage limited power converter.*

Chapter 7

Quench Process of Main Magnets

The main magnets of the LHC are the bending (dipole) and focusing (quadrupole) magnets in the arcs and insertions. These magnets store a significant amount of energy and therefore have to be protected by quench heaters as the natural quench propagation is not sufficient to avoid overheating or excessive voltages. The quench process in the main magnets is the most complex case as the heating of quench heaters has to be included in the model. Since these magnets are made of Rutherford type cables, which consist of different wires (strands), a changing magnetic field induces interfilament and interstrand coupling currents and losses at the contact resistances that can cause magnetic quench back during the current decay after a quench. Tests on prototype magnets have shown the important impact of magnetic quench back during fast current decays.

Quench experiments in the main dipole magnets are analysed with the help of simulation studies. The quench model includes the quench back effect and forced quenching by heaters to compute heater delays, adequate voltage detection thresholds and to simulate the impact of the induced eddy currents. The conclusions of quench experiments performed on prototype main quadrupole magnets for the arcs and the insertions are presented and compared with simulations. The calculations that extrapolate the situation of a quenching main magnet in the LHC machine in order to determine the required protection are outlined.

7.1   LHC Main Magnets

The LHC main magnets are the dipole magnets to deflect the beam and the quadrupole magnets to focus the beam. In total 1232 dipole magnets will be installed in the LHC, 154 of them connected in series in each sector. The apertures of the arc quadrupole magnets will be powered in series of 47 and 51. In the insertions, the apertures of the quadrupoles (MQM and MQY) are either powered individually or in series of two. When the strengths of the strong single aperture focusing quadrupoles at the interaction points (MQX) is changed to collide the beams at nominal energy, the strengths of the twin aperture magnets in the insertions can be individually changed for the compensation of beam parameters (e.g. the transverse tunes). The beam optics in the arc therefore does not change. The protection scheme for the beam separation and recombination dipole magnets (MBR family and MBX) and the strong focusing quadrupole magnets close to the experimental detectors (MQX) is included for completeness. The different LHC main magnets are listed in Table 7.1. The design parameters of the main magnets and their superconducting cables are given in Section 1.3.3. The circuits parameters and protection equipment for the main magnets are summarised in Table 7.2.

Magnet	Meaning	L_{mag} [mH]	l [m]
MB	Main arc dipole	108	14.3
MQ	Main arc quadrupole	2×5.6	3.1
MBRA	Twin aperture (234 mm) separation dipole	50.6	9.45
MBRB	Twin aperture (194 mm) separation dipole	50.6	9.45
MBRC	Twin aperture (188 mm) separation dipole	50.6	9.45
MBRS	Single aperture separation dipole	25.8	9.45
MBX	Single aperture separation dipole	25.8	9.45
MQM	Twin aperture insertion quadrupole	2×15.1	3.4
MQMC	Short twin aperture insertion quadrupole	2×10.7	2.8
MQML	Long twin aperture insertion quadrupole	2×21.3	4.8
MQR	Single aperture insertion quadrupole	15.1	3.4
MQRL	Long single aperture insertion quadrupole	28.0	5.1
MQY	Wide twin aperture insertion quadrupole	2×74.0	3.4
MQXA	4 layer single aperture quadrupole	90.7	6.3
MQXB	2 layer single aperture quadrupole	19.1	5.5

Table 7.1: *The various main magnets for the LHC. The MQXA single aperture magnets are provided by the KEK laboratory, the MQXB by the FNAL laboratory. These magnets are located close to the experiments. Their field gradient is very high to minimise the beam size and to maximise the luminosity.*

Type	$\sum$ of magnets	$\sum$ of circuits	I_{max} [A]	L_{tot} [H]	U_{det} [V]	Δt_{det} [ms]	R_{ex} [mΩ]	Number of DQHTS
MB busbar	154	8	13000	16.5	1	5000	75	-
MB	1232	-	13000	0.108	0.2	10	diode	4
MQ busbar	47/51	16	13000	0.263/0.286	0.5–1.0	1000	6.6/7.7	-
MQ	392	-	13000	2×0.0056	0.2	10	diode	2
6 kA busbar	≤4	180	6000	≤0.15	0.2–1.0	10–20	-	-
MQM+MQMC	2	24	5820	0.026	0.5–1.0	10–20	-	2
MQM	1	4	5820	0.015	0.5–1.0	10–20	-	2
MQM at 4.5 K	2	4	4650	0.030	0.5–1.0	10–20	-	2
MQM at 1.9 K	2	24	5820	0.030	0.5–1.0	10–20	-	2
MQML	1	64	5820	0.021	0.5–1.0	10–20	-	2
MQR	1	8	4650	0.015	0.5–1.0	10–20	-	2
MQRL	1	8	4650	0.028	0.5–1.0	10–20	-	2
MQY	1	16	3900	0.074	0.5–1.0	10–20	-	4
MQY	2	12	3900	0.148	0.5–1.0	10–20	-	4
MQXA	4	8	7000	0.220	0.2–0.5	10–20	-	2
MQXB	2	8	11410	0.038	0.2–0.5	10–20	-	2
MBRA+MBRB	2	2	6000	0.101	0.2–0.5	10–20	-	4
MBRC	1	8	6000	0.050	0.2–0.5	10–20	-	4
MBRS	4	2	6000	0.101	0.2–0.5	10–20	-	2
MBX	1	4	6000	0.026	0.2–0.5	10–20	-	2

Table 7.2: *The various circuits of the LHC main magnets and their protection (see Section 1.5). The number of DQHTS (heater power supplies) is given per magnet. An overview for the corrector circuits can be found in Table 6.7.*

Quench Propagation

The simulation of a quench in main magnets wound with Rutherford cables includes longitudinal and transverse quench propagation, the impact of induced interfilament and interstrand coupling currents, and forced quenching by heaters.

A initial timestep of 0.05–0.1 μs and a longitudinal discretisation smaller than 1 cm has to be used for a stable computation of the temperature profiles with SPQR.

As for the corrector magnets, the one-dimensional model was used first to compare the simulation output for the longitudinal quench propagation with experimental results. This crosschecked model was also used to study the heater performance and the quench impact of induced eddy currents. The three-dimensional model was used to determine the transverse quench propagation velocity.

The longitudinal quench propagation velocity at nominal current of 11.5–11.8 kA of various dipole magnets was measured to be in the range of 15–20 m/s. The transverse propagation (turn-to-turn delay) was determined as Δt_t=10–15 ms. The longitudinal quench propagation is simulated to be 16 m/s and Δt_t simulation yields 12 ms using the constant temperature gradient approximation for the simulation of the heat transfer through the insulation layer (see Section 3.5.2) at nominal current.

7.2   Quench Performance of Short Dipole Magnets

Due to the lengthy production time of 15 m long prototype magnets, the short dipole magnet program was launched. This meant that feedback was faster on experimental data concerning design changes [83]. Short model magnets are built in-house and are cheaper than long prototype magnets built in industry and many questions can be answered with experiments on short dipole magnets. Parallel to tests on single aperture magnets (MBSMS), twin aperture magnets (MBST) are constructed to evaluate the impact of the twin aperture design.

Significant design modifications have been the change from a 5-block to a 6-block coil structure after magnet MBSMS 13 (see Fig. 1.8); collars made of stainless steel and aluminium; and varying cable properties such as the $RRR = 60$–200 and $r_{cu/sc} = 1.84$–1.96. From MBSMS 12 onwards, the outer layer of the magnets was wound with a Rutherford cable containing more helium (4.5 % instead of 3 %).

The last constructed single aperture magnet was MBSMS 23 followed by the assembly of several twin aperture models (MBST 4–MBST 9). The insulation layer material was changed after MBST 6 from the polyimide Kapton[1], to the polyimide Apical[2].

Training

The maximum magnetic field after training is higher for magnets with the 6-block design and those built with stainless steel collars (see Fig. 7.1). Using a Rutherford cable that contains more helium does not have an impact on the training level. Various coil designs have been compared by the ratio of the reached quench current and the nominal current, which is about 1.18 to 1.23 for 6-block magnets, and 1.11 to 1.19 for 5-block magnets with aluminium collars. The higher values of 6-block magnets are due to the improved mechanical design and an increased mechanical stability.

---

[1]Trademark of DuPont Corporation
[2]Trademark of Kanegafuchi Chemical
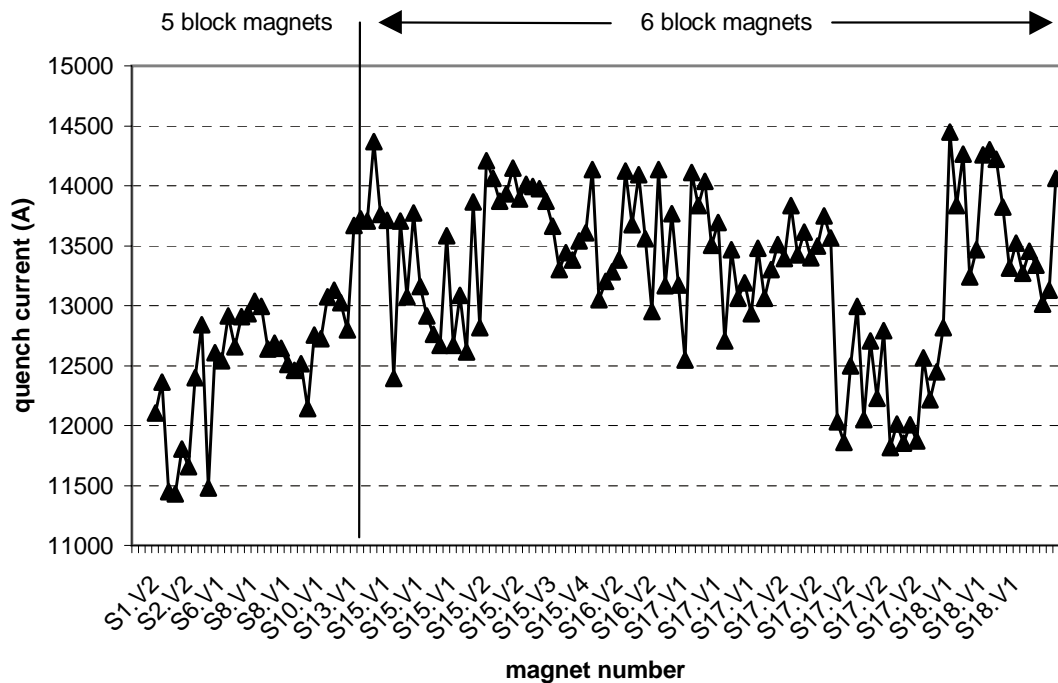
Figure 7.1: *Reached quench currents of different short dipole models (magnets MBSM S1 to MBSM S18) for quenches without energy extraction. Some magnets have been retested after a modification (e.g. recollaring), which is indicated by the number of the magnet version V1, V2, etc.*

When the full energy is deposited in the magnet (no energy extraction), detraining can be observed [84], which means that the quench current decreases with respect to the previous level. This has always been the case when the quench occurs in the outer turn of the outer layer (turn 16, block 2, highest field of the outer layer). The observed detraining is stronger for 6-block magnets because of higher quench currents. In magnets with stainless steel collars detraining is less pronounced.

With respect to short dipole magnets, the 15 m long prototype magnets tested so far reached a maximum field of 9 tesla after several training quenches (2–10 quenches). The quench currents are in average lower by about 500–1000 A with respect to short dipole magnets (corresponds to about 0.7 tesla).

Current Decay

For a reliable machine performance, the magnet should quench close to the critical current to avoid accidental quenches at the operating current. Since a higher quench current increases the quench load, which also increases the hot spot temperature, a more powerful magnet protection system is required. The quench propagation velocity increases with the current, which results in a fast current decay after a quench at a high current as the resistance in the magnet grows faster. 6-block magnets and 5-block magnets with stainless steel collars operate closer to the critical current that leads to a faster current decay compared to 5-block magnets with aluminium collars. The maximum values
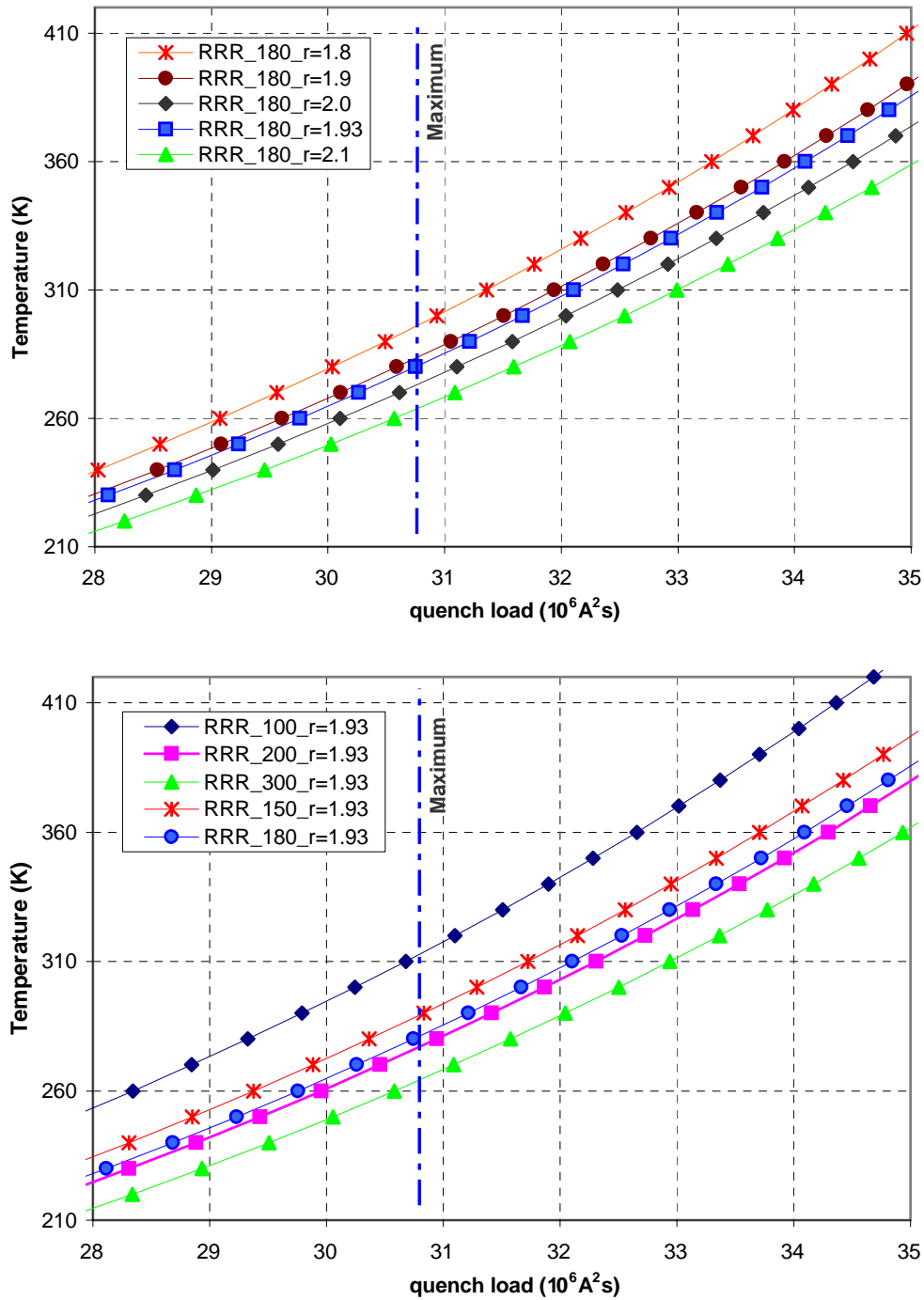
Figure 7.2: *Dependency of the hot spot temperature for a given value of the quench load on $r_{cu/sc}$ (upper plot) and RRR (lower plot) for the Rutherford cable of the outer layer.*

of dI/dt are about 50 kA/s for quenches without energy extraction and 80 kA/s for quenches with energy extraction.

Hot Spot Temperature

The dependence of the hot spot temperature on RRR and $r_{cu/sc}$ for a given value of the quench load (Eq. 3.5) is shown in Fig. 7.2. The low values of RRR =113 and $r_{cu/sc}$ =1.91 in magnet MBSMS 15 with respect to other 6-block magnets explain an increased hot spot temperature.
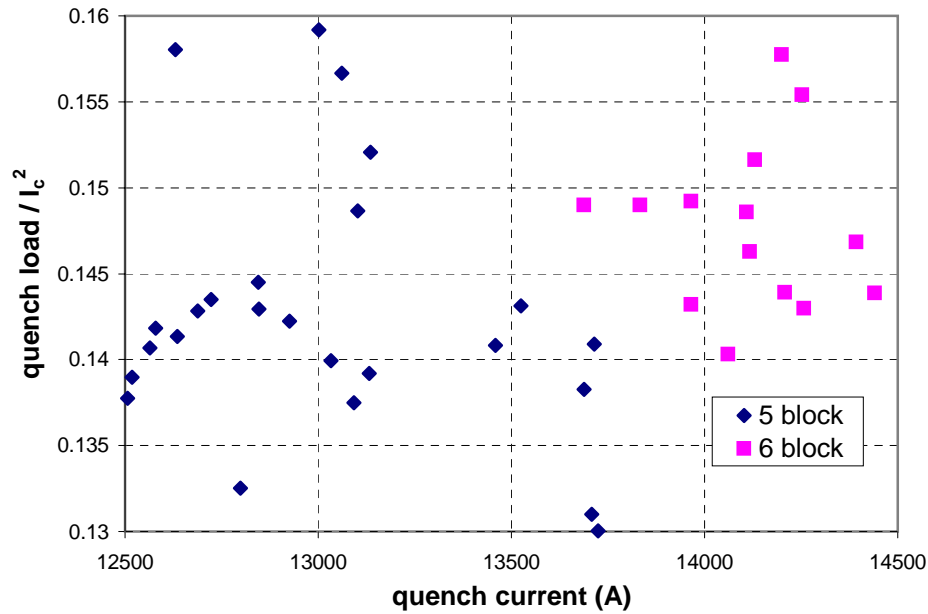
Figure 7.3: *Quench load normalised to the critical current at nominal field squared.*

To compare magnets with different designs, the value of the quench load is normalised to the critical current at nominal field squared

$$\int I^2(t)dt^{norm} \equiv \frac{\int I^2(t)dt}{I^2_{crit}} \tag{7.1}$$

The result is shown in Fig. 7.3 demonstrating that the quench load is dominated by the reached quench current.

Resistance Growth

The voltage across a coil is

$$V_{tot}(t) = R_{tot}(t) \cdot I(t) + L_{tot}(t) \cdot \frac{dI}{dt}(t) \tag{7.2}$$

$$\Leftrightarrow R_{tot}(t) = \frac{V_{tot}(t) - L_{tot} \cdot \frac{dI}{dt}}{I(t)} \tag{7.3}$$
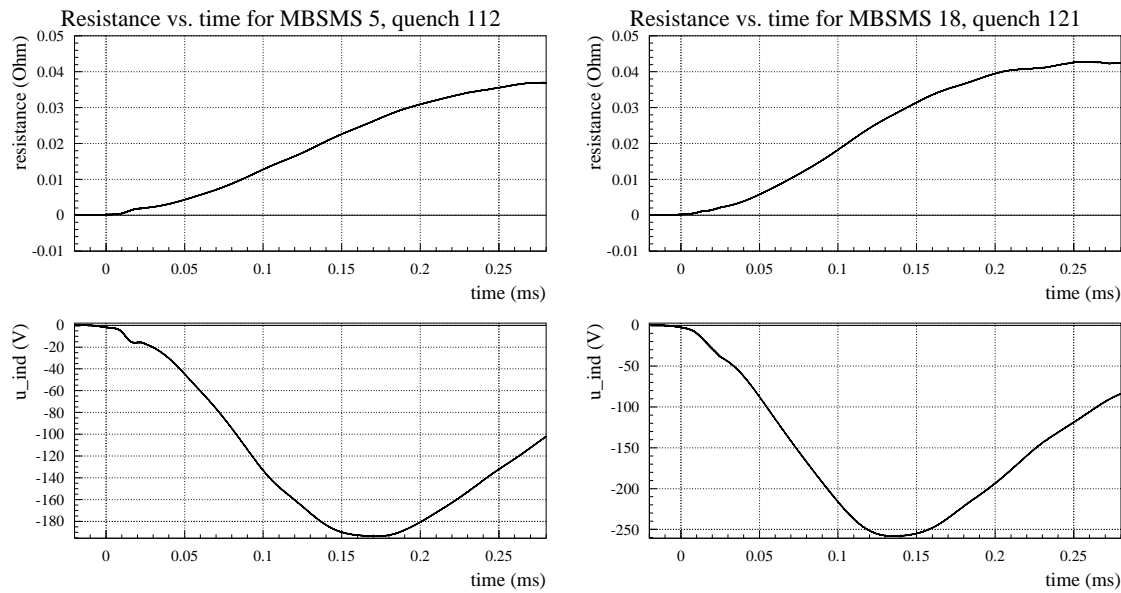
Figure 7.4: *Resistance and inductive voltage versus time for quench 112 MBSMS 5 (left); and quench 121 MBSMS 18 (right).*

$I(t)$ and $V_{tot}(t)$ are measured whereas dI/dt is calculated. L_{tot} is determined by other measurements and considered to be constant in this approximation. Fig. 7.4 shows an example of the resistance and the inductive voltage for two quenches.

The curves of the resistance versus time in Fig. 7.4 are very similar. The calculated inductive voltage becomes higher during the quench of a 6-block magnet because the current decays faster.

The slope of the resistance growth is similar for all analysed quenches and the maximum values at the end of the current decay are in the range of 32–47 mΩ. The spread of the calculated values is due to different cable parameters, quench current, etc. The fastest resistance growth has been observed for MBSMS 13 due to the highest resistivity at low temperature (lowest RRR).

> **The comparison of the current decays, the normalised quench load and the resistance growth showed that the quench process is similar in short dipole magnets of both 5 block and 6 block design.**

7.3   Quench Heater Studies

The heater strip position for the twin aperture dipole magnets is shown in Fig. 7.5 (see Sections 1.5 and 3.5.3). 16 heater strips are installed, two on each side of every pole. The strips located in areas with high magnetic field are called 'high-field heaters' (HF) and 'low-field heaters' (LF) in areas with low magnetic field.

> **The protection scheme with quench heaters is designed to be fully redundant, which requires that the magnet can still be protected if some heaters are not fired because of a failure.**
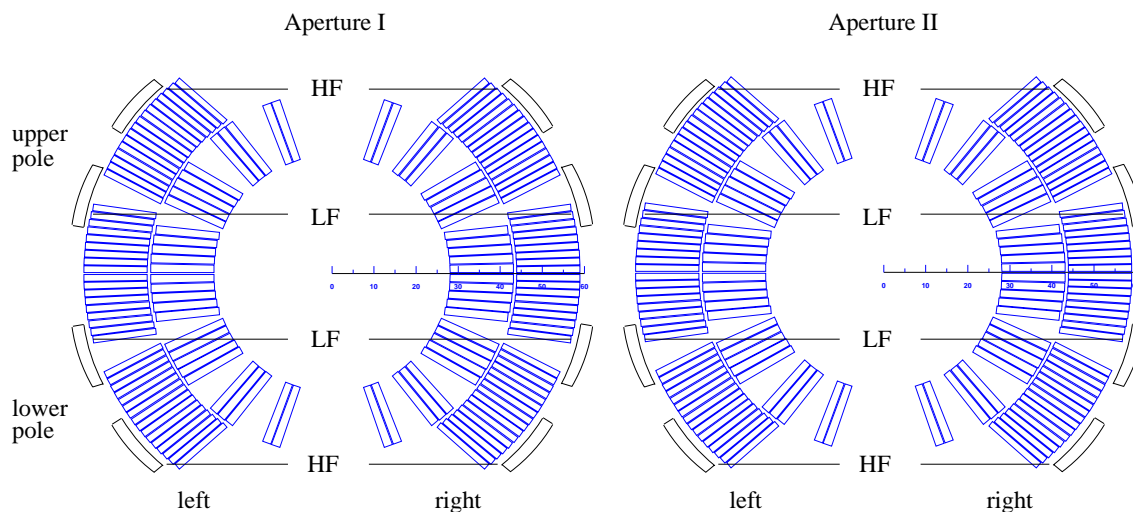
Figure 7.5: *Position of the heater strips in the twin aperture magnet: HF = high-field heaters, LF = low-field heaters.*

The quench heaters strips are 0.025 mm thick and 15.0 mm wide, glued between two layers of polyimide electrical insulation foil of 0.075 mm thickness each (see also Fig. 3.14).

Powering the 15 m long heater strip individually requires the installation of return cables in the magnets, which can be avoided by connecting two heater strips in series. This also halves the number of power supplies required to eight per dipole magnet for the protection by all heaters and to four for the protection by only high-field heaters.

The copper-plating pattern has to be adapted to provide both short heater delays at high current and effectiveness at lower currents. This needs to be studied to guarantee the heater efficiency in the entire magnet operating range. Table 7.3 gives the heater circuit parameters such as the strip resistance, the heater current decay time constant and the adiabatic temperature for heater strips with different copper-plating patterns.

Heater strip design	R at 1.9 K for 15 m long strip	1 strip per channel			2 strips per channel		
		I_{QH_0}	T_{max}	τ_{QH}	I_{QH_0}	T_{max}	τ_{QH}
25-25	12 Ω	58 A	270 K	85 ms	29 A	180 K	170 ms
12-24	8 Ω	88 A	350 K	56 ms	44 A	220 K	112 ms
12-36	6 Ω	117 A	410 K	43 ms	58 A	270 K	85 ms
12-40	5.6 Ω	125 A	420 K	40 ms	62.5 A	280 K	79 ms

Table 7.3: *Quench heater circuit parameters for different heater strip designs and an initial voltage of 700 V. The values are obtained using an average resistance of a 15 m long heater strip between 1.9 and 300 K. The temperature values correspond to adiabatic heating of the strip without heat flux into the Rutherford cable. τ_{QH} is the current decay time constant of the heater circuit (Eq. 3.95).*

The time between firing the quench heaters and the start of a provoked quench is called the quench heater delay Δt_{QH}

$$\Delta t_{QH} = t_{start} - t_{firing} \tag{7.4}$$

The energy dissipated into the heater strip increases with time according to

$$
\begin{aligned}
E_{QH_{max}} &\equiv E_{QH}(t=\infty) = \int\limits_{t_{firing}}^{\infty} P_{QH}(t')dt' \\
&= \frac{1}{2}C_{QH}U(t=0)^2 = \frac{1}{2}C_{QH}R_{QH_0}^2 I_0^2 = \frac{1}{2}R_{QH_0}I_0^2\tau_{QH} \qquad (7.5) \\
E_{QH}(t) &= \int\limits_0^t R_{QH}(t')I_{QH}(t')^2 dt' \\
&\approx R_{QH_0}\int\limits_0^t I_{QH}(t')^2 dt' = E_{QH_{max}}(1-\exp(-\frac{2t}{\tau_{QH}})) \qquad (7.6)
\end{aligned}
$$

These equations are valid for an RC circuit (like the power supply used for the LHC quench heater system; see Section 3.5.3). It is assumed that the resistivity of the heater strip remains constant with temperature, which is a good approximation for stainless steel. With increasing current in the magnet, the energy required from the heater to provoke a quench decreases due to the lower temperature margin.

7.3.1 Short Dipole Magnets

A single aperture dipole magnet is covered by 8 quench heater strips placed on both sides of the upper and lower poles on the two blocks of the outer layer. The two heater strips cover 13 out of 26 turns for one side of one pole in 5-block magnets and 12 out of 25 turns in 6-block magnets.[3]

The hot spot temperature as a function of the number of turns quenched by heaters is calculated with a simple model for an average magnetic field. The results are shown for the 5 and 6-block designs and nominal current in Fig. 7.6.

It is assumed that the magnet is quenched by the heaters 60 ms after the start of the natural quench. Neither the natural quench propagation nor the quench back effect are considered. The length of the quenched zone provoked by heaters gives the resistance that dominates the current decay. The calculation is performed twice for each magnet type: firstly, the quench is provoked in the turns covered by heater strips; then secondly, all turns of the outer layer are quenched after firing the heaters. Quenching 12 (13) is a conservative case whereas quenching 25 (26) turns is an optimistic assumption. If the quench process is dominated by the quench heater system, the calculated current decays represent the boundary curves for the current decay one expects in an experiment. Consequently, the measured current decay would lie between the two curves. The calculated temperature difference between 5 and 6-block magnets for nominal current is between 20 and 30 K. The measured value of the hot spot temperature is about 250–300 K. The difference of the hot spot temperature derived from the measured quench load for 5 and 6-block magnets is up to 30 K. When the calculation is repeated for the same current for both magnet designs, the difference between the hot spot temperatures is less.

Experimental Results

The quench heater delay tests are performed by firing either two high-field heater strips or two low-field heater strips. The high-field heater strip covers block 2 whereas the low-field heater strip

---

[3]For precision it should be noted that the heater strips cover 12.5 rather than 12 turns for the 6-block design.
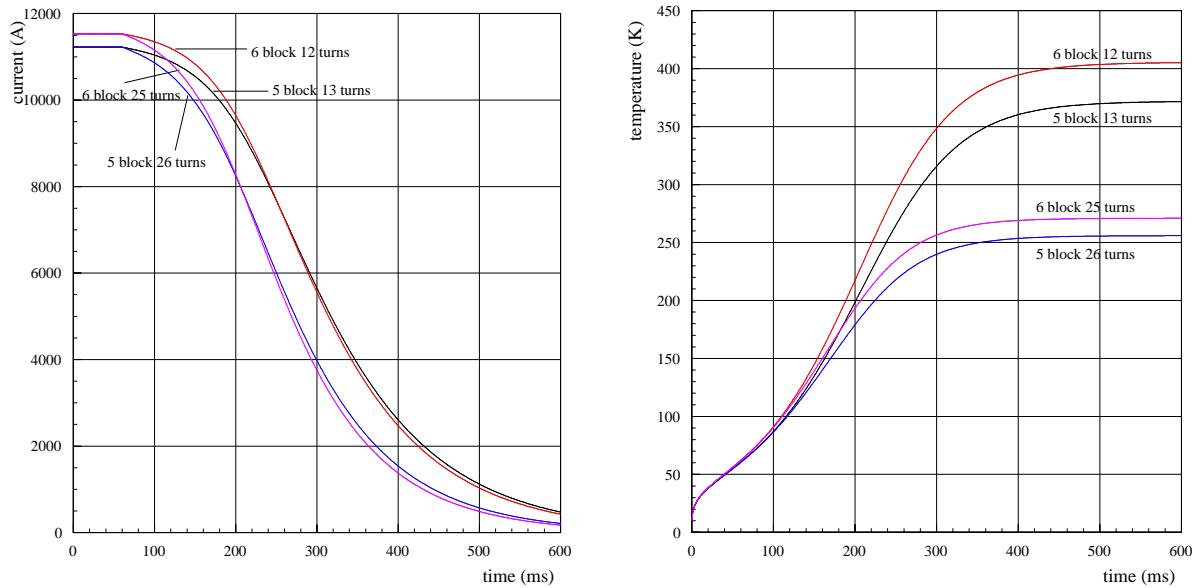
Figure 7.6: *Simulation of the current decay and temperature versus time for 5 and 6-block magnets with a different number of turns quenched by heater strips with a heater delay of 60 ms.*

covers mainly block 1. One heater strip per upper and lower pole on the same side of the coil are fired at the same time.

An example of the voltages of the outer and inner layer and the block voltages for both poles of a quench heater test are shown in Fig. 7.7. The firing of heater strips causes an inductive noise signal at -40 ms and the start of a quench at about -10 ms. 17 ms after detecting the quench, the energy extraction resistor is switched into series, which changes the slope of the voltage signals due to the large voltage across the dump resistor.

The results from the heater delay tests at different currents are summarised in Fig. 7.8 for an initial quench heater current of 50 A and τ_{QH}=56 ms.

In order to study the impact of magnet design changes on the quench heater performance, the data is sorted for 5-block and 6-block magnets, for MBSMS 12 (cable containing more helium) and MBSMS 8 (very high RRR value). The results from several tests at the same magnet current are averaged separately for low and high-field heaters.

High-field heater strips have significantly shorter delays than low-field heater strips at high magnet operating currents ($\Delta t_{QH}^{high} \approx$35 ms; $\Delta t_{QH}^{low} \approx$50 ms). The heater delay for very low magnetic fields should be the same for both heater strips. Within the statistical error the test results confirm this expectation. The measured quench heater delays of 5 and 6-block magnets as well as for magnet MBSMS 8 and MBSMS 12 are similar. This indicates that a change of the RRR or the helium content in the Rutherford cable does not affect the quench heater delays. In order to combine the heater delays for different currents, the experimental results were fitted according to Eq. 7.7

$$\Delta t_{QH}(I_{magnet}) = \Delta t_{QH_0} \exp(-\kappa I_{magnet}) \tag{7.7}$$

with κ being the exponential constant and Δt_{QH_0} being the heater delay at zero current.

The results of the fit for the heater delay at zero current in the magnet, the exponential decay constant and the fit uncertainties are listed in Table 7.4. The fit results show that high-field heaters at I_{mag}=0 A have a longer delay and a larger exponential constant. When the results of all tests are
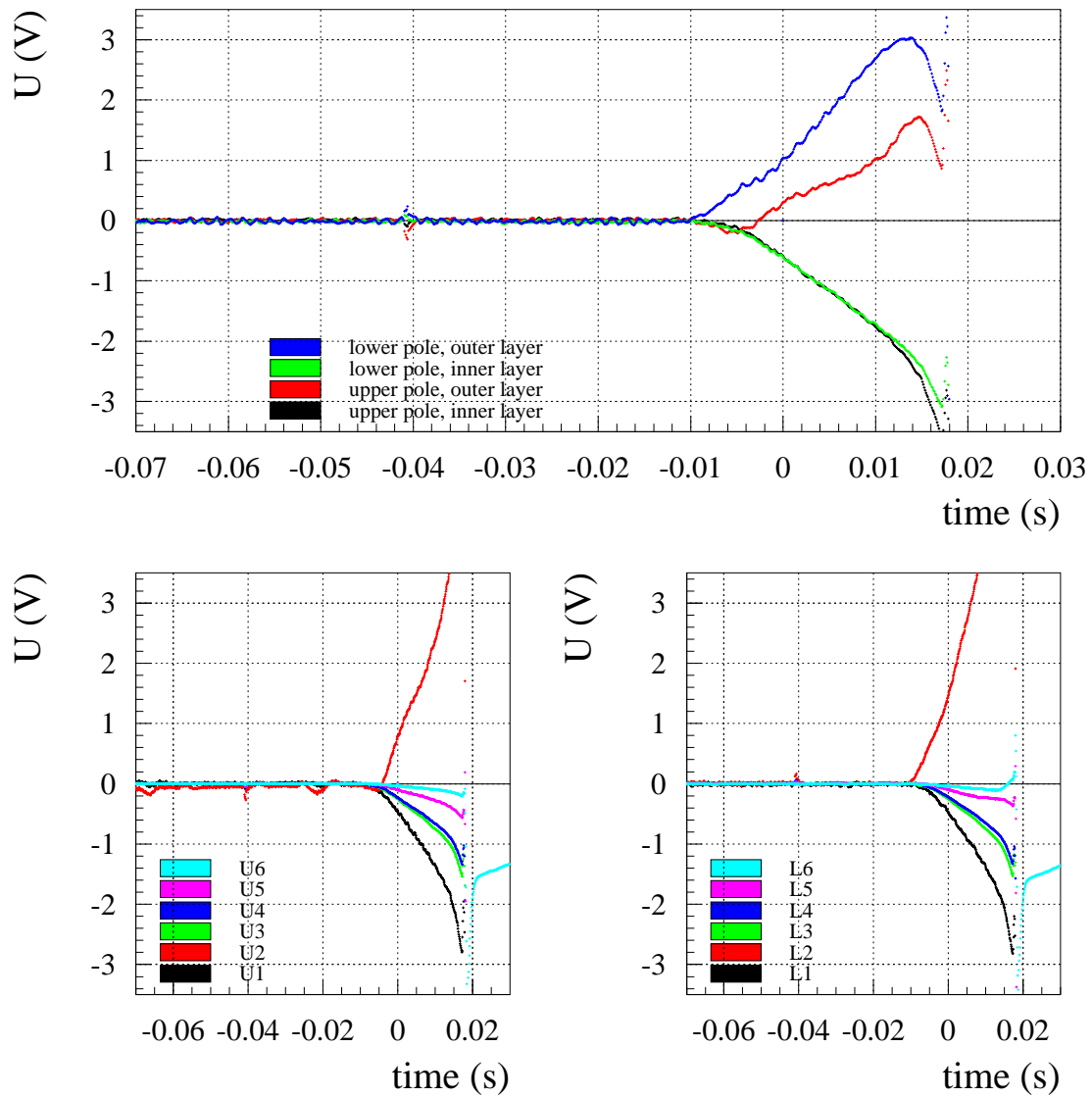
Figure 7.7: *Voltages during a quench heater delay test at $I_{mag} \approx 13\,kA$: L = lower pole, U = upper pole, 1–6 = block voltages of the poles. At t = 0, the quench is detected (t_{det}) and the power converter is switched off which induces a spike in the recorded voltages. At t = 17 ms, the dump resistor for energy extraction is switched in series with the magnet. The propagation of the quench into the inner layer causes a peak in the voltage signals at 15 ms.*
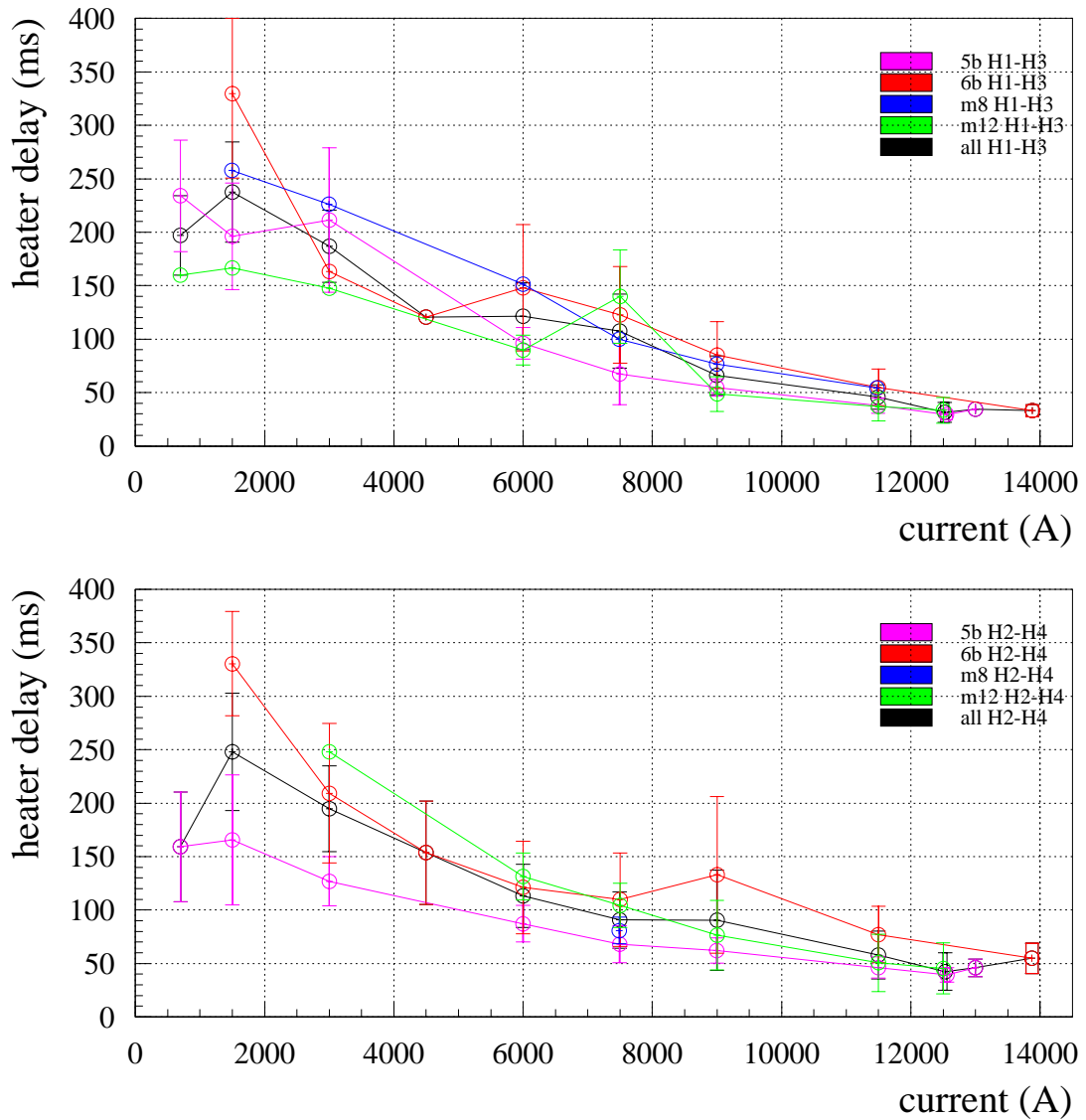
Figure 7.8: *Averaged heater delays for short models as a function of current (top: high-field heater strips; bottom: low-field heater strips). The statistical uncertainties of the average values are plotted as error bars. The data is sorted for 5-block and 6-block magnets, MBSMS 8 (very high $r_{cu/sc}$), MBSMS 12 (new cable containing more helium), and the average heater delays for all magnets.*

Magnet type	Heater strips	Δt_{QH_0} [ms]	$\sigma_{\Delta t_{QH_0}}$ [ms]	κ [A^{-1}]	σ_κ [A^{-1}]
5-blocks	high-field	260	38	$1.67\cdot10^{-4}$	$1.5\cdot10^{-5}$
5-blocks	low-field	175	28	$1.14\cdot10^{-4}$	$1.8\cdot10^{-5}$
6-blocks	high-field	448	104	$1.86\cdot10^{-4}$	$2.2\cdot10^{-5}$
6-blocks	low-field	358	58	$1.42\cdot10^{-4}$	$2.5\cdot10^{-5}$
MBSMS 8	high-field	228	112	$1.10\cdot10^{-4}$	$6.6\cdot10^{-5}$
MBSMS 8	low-field	-	-	-	-
MBSMS 12	high-field	244	92	$1.63\cdot10^{-4}$	$4.6\cdot10^{-5}$
MBSMS 12	low-field	364	170	$1.69\cdot10^{-4}$	$6.2\cdot10^{-5}$
average	high-field	263	31	$1.54\cdot10^{-4}$	$1.2\cdot10^{-5}$
average	low-field	242	36	$1.24\cdot10^{-4}$	$1.6\cdot10^{-5}$
average	all	253	32	$1.37\cdot10^{-4}$	$1.4\cdot10^{-5}$

Table 7.4: *Fit results of the exponential heater delay decrease for different types of short models. The errors indicate the large scatter of the heater delays at low magnet operating currents.*

averaged, the heater delays of low and high-field heaters at zero magnet current are about the same. The larger value of κ for high-field heaters indicates that the delay for those strips is shorter. The quench heater delays of 5-block magnets are shorter than those of 6-block magnets at low magnet operating currents.

7.3.2 Simulation Results

Forced quenching by heaters can be modelled with SPQR (see Section 3.5.3). A simulation study has been performed to optimise the copper-plating pattern and the insulation layer thickness between the heater strip and the coil. The aim has been to minimise the quench heater delays at low and high magnet current to allow connecting two 15 m long heater strips in series (l_h=30 m). The capacitor discharge supply (heater power supply) has a capacitance of 7.05 mF and a maximum voltage of 900 V. Since the lifetime of capacitors increases with decreasing voltage, an operating voltage of 750 V was assumed for the simulation. Two parameters are analysed:

- the 'initial' heater delay, which is defined as the time between firing the heaters and provoking a quench in the conductor covered by a heated part of the heater strip. This delay becomes shorter by increasing the copper-plated length which reduces the heater strip resistance and increases the initial current.

- The 'total' heater delay, which is the time between firing the heaters and having provoked a quench in the entire conductor under the heater strip.

The simulation model was crosschecked by comparing the simulated quench propagation velocity with the experimental results (about 15–20 m/s at nominal current). A typical example of the simulation output is given in Fig. 7.9, which shows the simulated temperature profiles along the cable for various times including the provoked quenching by the non-copper-plated parts of the heater strips.

In order to compare the heater delays for different copper-plating patterns at low current, adiabatic conditions are assumed to exclude the uncertainty in the longterm behaviour of the
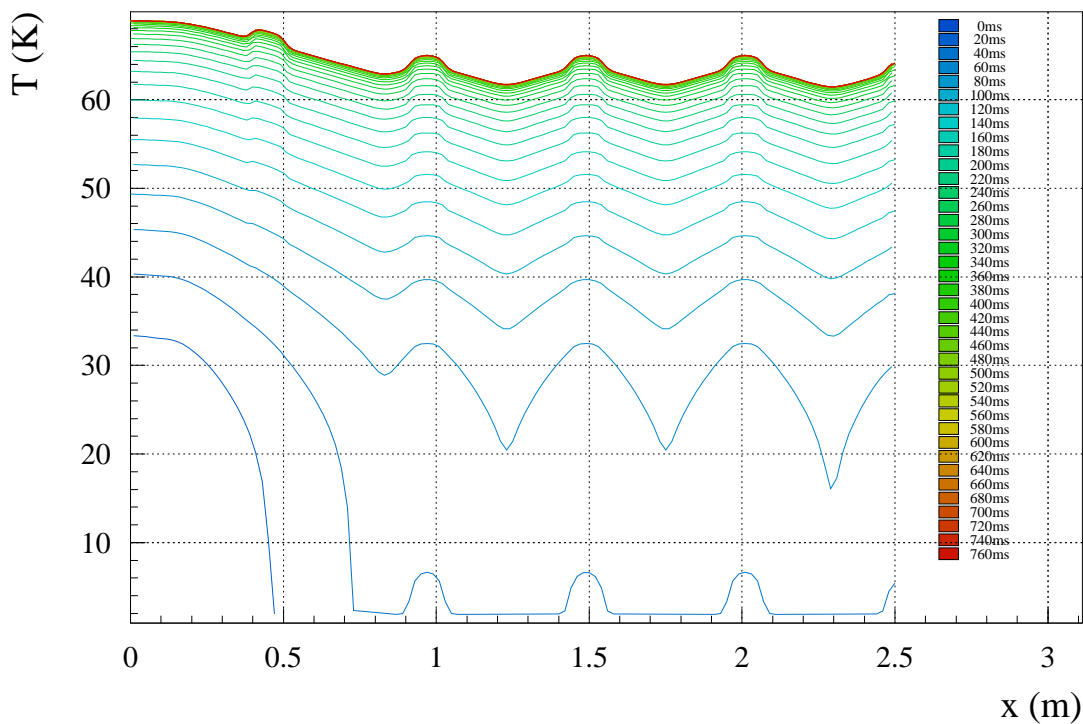
Figure 7.9: *Simulation of the temperature profile along the cable with forced quenching by copper-plated heaters. The time interval between two neighbouring curves is 20 ms. The initial current was 11.8 kA, cable cross-section 19.2 mm², 3% helium content, $r_{cu/sc} = 1.9$, $RRR = 100$, initial time step for the computation 0.05 μs. The heat generation in the heater strips occurs only at the non-copper-plated parts. Consequently, the temperature in the conductor first increases below the non-copper-plated parts (see also Fig. 3.13).*

cooling model by heat transfer into helium. In a second step, the simulations are repeated including the cooling by helium. The results for the dipole magnet operating at injection current of 750 A demonstrated that longer heated parts yield shorter heater delays at low current. This is due to the minimum propagation zone (Eq. 3.11). Assuming that only the minimum quench energy (MQE) is dissipated into the conductor the minimum propagation zone (MPZ) exceeds 20 cm at injection current. The shorter length of the heated part is sufficient as the energy dissipated into the superconducting cable by the heaters is significantly higher than MQE. A heated length of 8 cm gives shortest initial heater delay assuming adiabatic conditions. Including heat transfer into helium, a heated zone of less than 8 cm is not sufficient to provoke a quench at injection current when the initial heater voltage was limited to 900 V. A lower limit of 10 cm for the heated length is given by the twist pitch (L_p^s) of the Rutherford cable.

The results from the simulation for initial and total heater delays at nominal current are summarised in Fig. 7.10. Generally, two heater strips are connected in series except for the heater strip with the copper-plating pattern of 25 cm heated length and 25 cm copper-plated length (25-25), which requires individual powering.

Combining the simulation results at injection and nominal current, a heated length of 10-12 cm and a copper-plating length of 40-50 cm gives the best performance for the entire operational range.
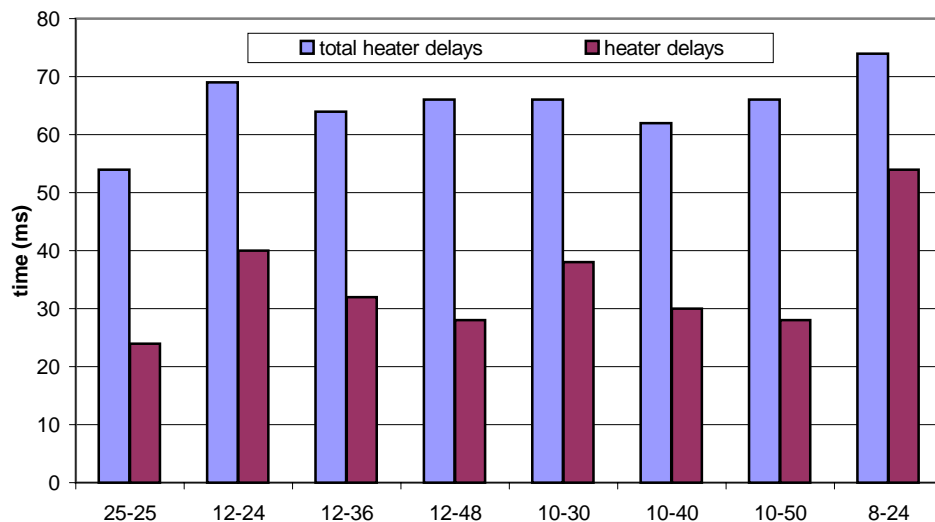
Figure 7.10: *Heater delays simulated with SPQR at nominal current as a function of the copper-plating ratio (heated/non heated lengths in cm) at an initial voltage of 750 V. The optimisation of the copper-plating cycle reduces the total heater delay by about 5 ms.*

7.3.3 Comparison of Simulations and Experimental Results

Copper-Plating

Heater strips with plating patterns (lengths in cm) of 25-25, 12-24, 4-24, 12-36 and 12-40, have been tested in various short dipole magnets to validate the simulation results.
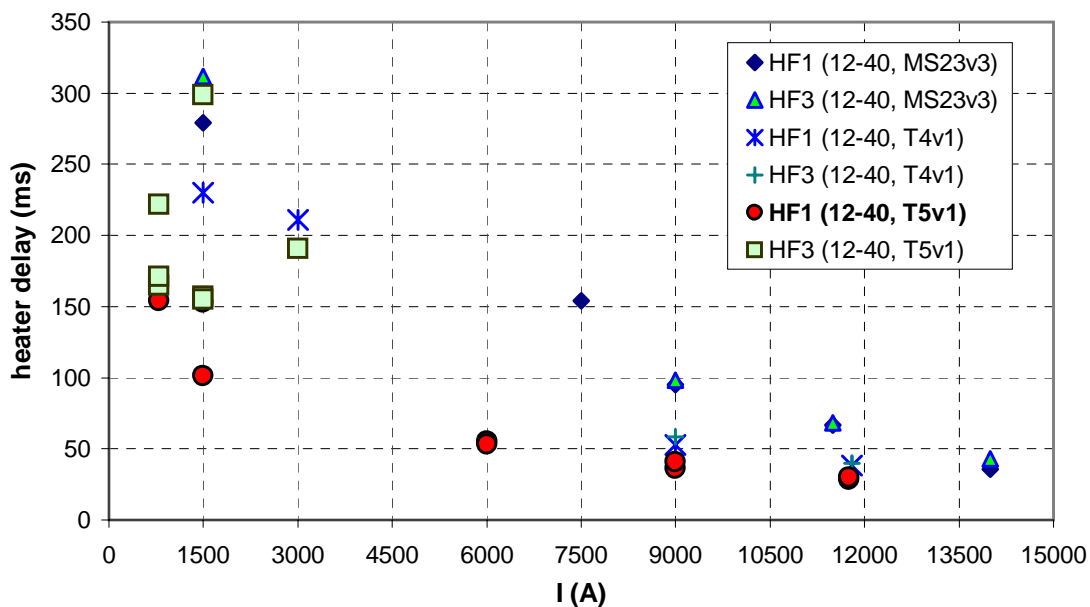
Figure 7.11: *Measured high-field heater delays on the MBSMS 23, MBST 4 and MBST 5 magnets as a function of magnet operating current.*
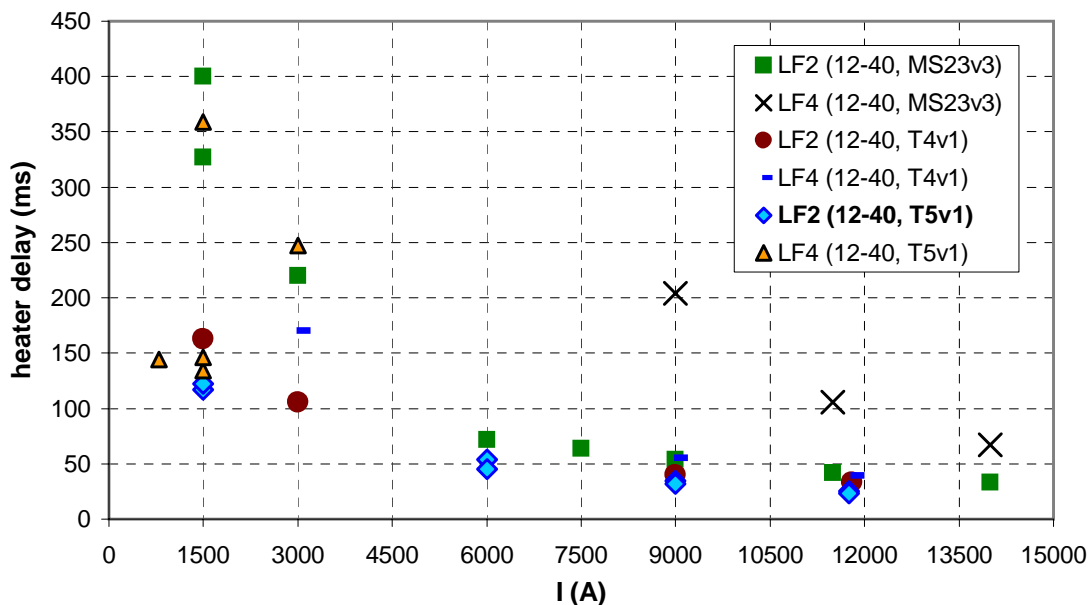
Figure 7.12: *Measured low-field heater delays on the MBSMS 23, MBST 4 and MBST 5 magnets as a function of magnet operating current. The larger low field heater delays of MBSMS 23 with respect to those of MBMST 4 are due to the installed 4-24 heater strips powered with circuit parameters that correspond to the power density of 12-40 heater strips.*

- The magnets MBSMS 23 and MBST 4 were both equipped with 4-24 and 12-36 heater strips. The quench heater performance depends on the power and energy density in the heated part of the strip. Switching an additional resistance in series with the quench heater allows the adjustment of the power density to simulate various copper-plating patterns for 15 m long heater strips.

  A heated part of 4 cm proved to be too short to provoke quenches at magnet operating currents lower than 4.5 kA. The predicted minimum propagation zone at this current level is in the order of 10 cm.

  The measured heater delays are shown as a function of the magnet current in Fig. 7.11 for the high-field heaters and Fig. 7.12 for the low-field heaters with an initial heater voltage of 700 V.

- The twin aperture short dipole magnet MBST 5 was the first magnet equipped with 12-40 heaters. The heater delays of the high-field heaters are about 30 ms at nominal current. Increasing the initial heater voltage to 900 V reduces the heater delays to about 25 ms at nominal current. The shortest heater delays for high-field heaters were obtained with 12-40 heater strips. Using a minimum voltage of 700 V, this type of quench heaters is effective in the entire magnet operating range.

The initial heater delays from simulations and experiments are compared in Table 7.5 for the high-field heaters. The experimental results given in the table are averaged heater delays ascertained from various magnets with a spread of about 5 ms. The test set-up was equivalent to a power supply voltage of 900 V feeding two 15 m long heater strips connected in series. For the strip with a plating pattern of 25-25, a single heater strip was powered with 800 V. The use of 12-40 heater strips connected in pairs gives similar heater delays as the individual powered 25-25 copper-plating pattern.

U_{min} is the minimum heater voltage required to provoke a quench at injection current. A quench heater system that can provoke a quench in the entire magnet operating range is desirable as the minimum current at which heaters are required for the protection does not need to be defined.

| Pattern | P0/A | τ_{QH} | U_{min} | Heater delay [ms] | |
Fe-Cu [cm]	[W/cm^2]	[ms]	[V]	measured	simulation
25-25	50	85	750	30	34
12-24	35	112	900	35	38
12-36	60	85	750	28	30
12-40	70	77	700	25	28
12-48	94	68	700	-	24
10-40	94	68	750	-	26
4-24	112	48	≥900	25	30

Table 7.5: *Comparison of measured and predicted quench heater delays. The simulations were carried out for the HF heaters only. P0/A is the initial power density, and τ the time constant for the heater pulse.*

From the simulation study and experimental results, a copper-plating pattern consisting of 12 cm heated part and 40 cm copper-plated part was chosen. This copper-plating patterns allows a continuous production of the 15 m long quench heaters for the LHC dipoles by industry (since the heater strip length is a multiple of 52 cm).

Maximum Heater Strip Temperature

Further simulations and tests were carried out to investigate the maximum temperature of a heater strip during the current pulse. This temperature, if calculated adiabatically, would reach about 400 K with an operating voltage of 900 V. Considering the heat transfer from the heater strip through the insulation layer into the cable, the simulation predicts a maximum temperature of about 280 K (with nominal insulation thickness). The current and voltage across the heater strip were measured after firing the heater at different magnet operating currents to evaluate the heater strip resistance and the temperature. Although the error of this temperature measurement is rather large due to the scatter of the measured signals, the maximum temperature was found to remain below 300 K (see Fig. 7.13).
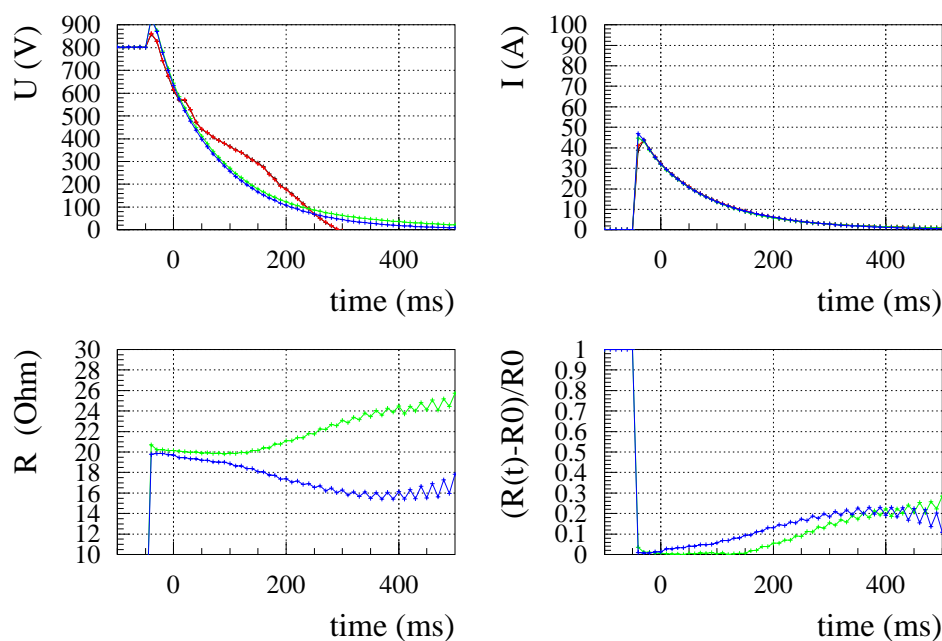
Figure 7.13: *Measured resistance of a heater strip after firing. The upper graphs show the current and the voltage across two heater circuits as a function of time. The lower graph on the left shows the change of the heater resistance (positive and negative slope to better distinguish the two heater circuits). The lower graph on the right shows the relative increase of the resistance for both circuits. As the heater resistance as a function of temperature is known from other experiments, this measurement derives the maximum heater strip temperature.*

Impact of the Insulation Layer Thickness

The simulation studies show an exponential increase in the heater delays as a function of the thickness in the insulation layer (see Fig. 7.14). A strong increase in the heater delays has been seen during tests on a short dipole magnet with an increased insulation layer thickness. For the redundancy of the quench heater system, it is required to protect the magnet with only half of the high-field heaters. Therefore an increase in the insulation layer thickness by a factor of two is not permissible using the same type of polyimide film that is foreseen for the insulation of LHC
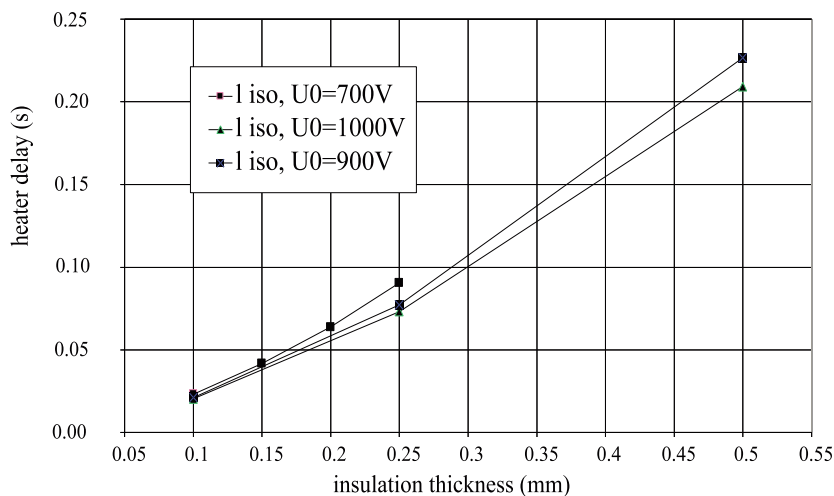
Figure 7.14: *Impact of the insulation layer thickness on the heater delay at nominal magnet operating current of 11.8 kA. The heater delays steeply increase with an increasing thickness of the insulation layer, thus reducing the heater strip performance.*

cables. The change to another insulation material with higher thermal conductivity would allow an increased thickness of the insulation layer.

Starting with MBST 6, the twin aperture magnets have been made with stainless steel collars. The impact on the measured quench heater delays can be seen in Fig. 7.15 (top). The use of stainless steel collars causes a larger scatter of the heater delays depending on their position being in between the two magnet bores or facing outwards. A possible explanation might be a variation of the applied stress over the cross-section.

The insulation material was changed from Kapton to Apical for the coil insulation from MBST 7 onwards. Changing the insulation material does not have a significant impact (Fig. 7.15 bottom). The scatter of the heater delays remains but is likely to be due to the stainless steel collars.

7.3.4   Experiments on 15 m Long Dipole Magnets

The heater delays were also measured on several long prototype magnets. Most of them were equipped with 25-25 heaters. Powering these heaters individually with an initial heater voltage of 800 V yielded heater delays in the range of 30–35 ms at nominal current (MBP2N1). The results for the first long prototype magnet equipped with 12-36 heaters (MBP2O1) and an initial heater voltage of 900 V are about 30 ms for the high-field heaters at nominal current.

During one training quench of a long prototype dipole magnet (MBP2N1 v2) at about 11 kA, the heaters were fired but a spark appeared in the feedthrough of the heater powering cables. The energy of the heater power supply was not dissipated into the heater strips but burnt the instrumentation cables in the feedthrough. The recorded voltages and current decay are shown in Fig. 7.16. Evidence of magnetic quench back has not been observed in the voltage signals. The tests had to be stopped for repairs to the instrumentation cables that were severely damaged in the feedthroughs. This accident showed the robustness of the magnet winding as the magnet could be trained after the repair up to 9 tesla.

The protection with quench heaters for the main dipole magnets has been tested for its redundancy on the first long prototype dipole magnet (15 m long, 6-block coil geometry).
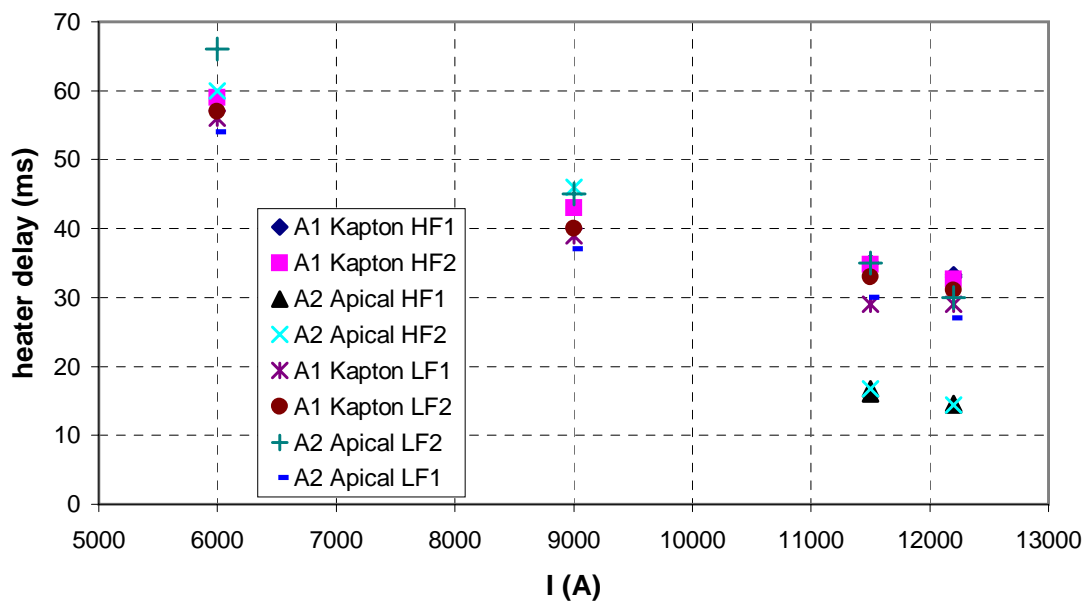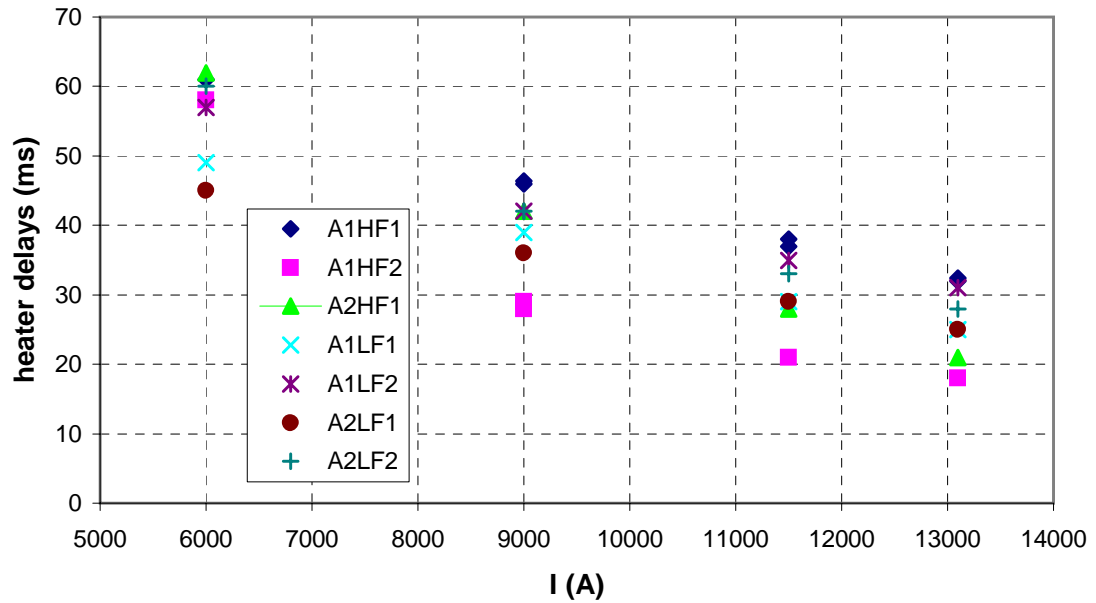
Figure 7.15: *Heater delays in a magnet with stainless steel collars (upper plot) and the effect of the insulation material on the heater delays (lower plot): A1 = aperture 1, A2 = aperture 2, LF = low-field heaters, HF = high-field heaters.*
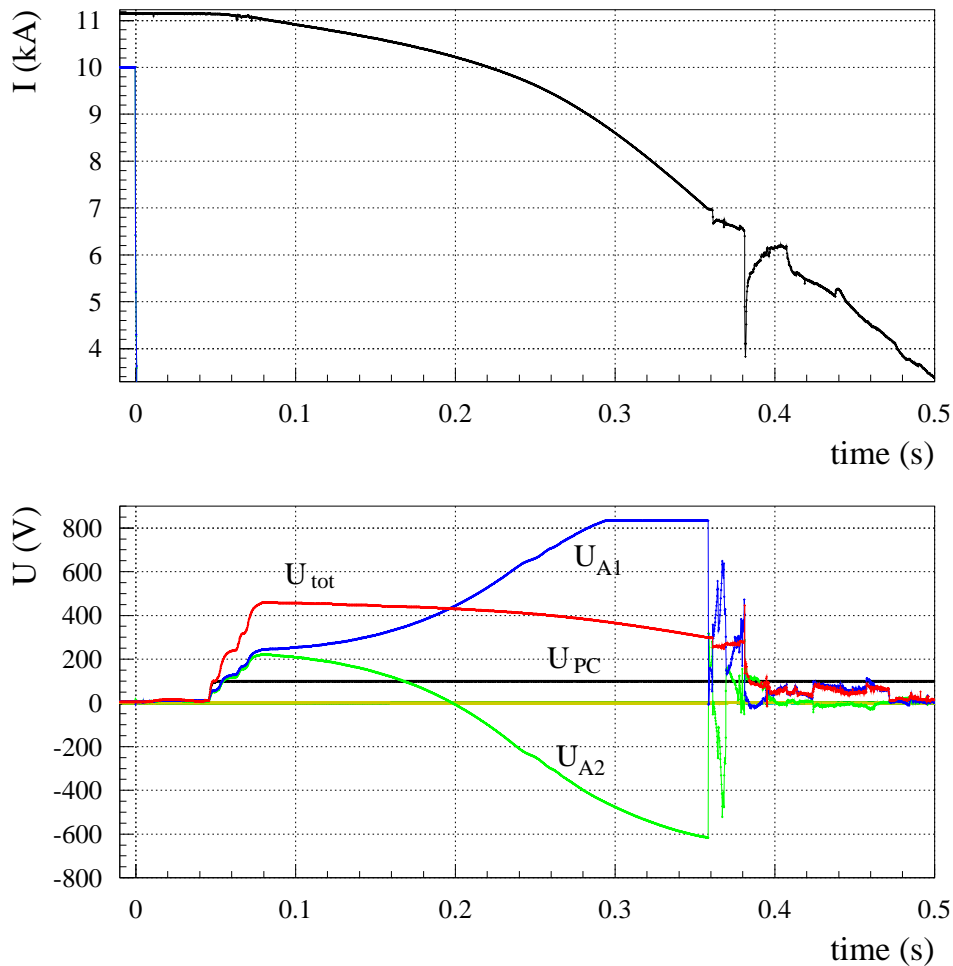
Figure 7.16: *Measurements of the current and pole voltages after a training quench with a failure during the firing of the heaters. The current decays much slower and shows some induced noise at 0.37 s after quench detection. The lower graph shows the voltages across the magnet (U_{tot}), across the apertures (U_{A1}, U_{A2}) and across the power converter (U_{PC}). As can be seen, the instrumentation cables are lost at 0.37 s after quench detection apart from the power converter signal U_{PC}. The analysis of this accident showed that a spark appeared in the connection box (feedthrough for the instrumentation cables from 1.9 K to 300 K). As a consequence, the quench heater energy was not dissipated into the strips and the instrumentation cables burnt in the connection box.*

Redundancy of the protection scheme is an important issue, since about 6000 heater power supplies will be installed in the LHC tunnel. Such supplies will have a certain failure rate, and protection should not be compromised if some fraction is not available. It was concluded that the protection with high-field heaters are fully redundant since powering just half of the high-field heaters safely protects the magnet (see Fig. 7.17). The tests demonstrated that using only two high-field heater strips (one power supply) leads to quench load values of more than $30 \cdot 10^6$ A^{2}s, which is considered to be too large and might cause a degradation of the magnet.
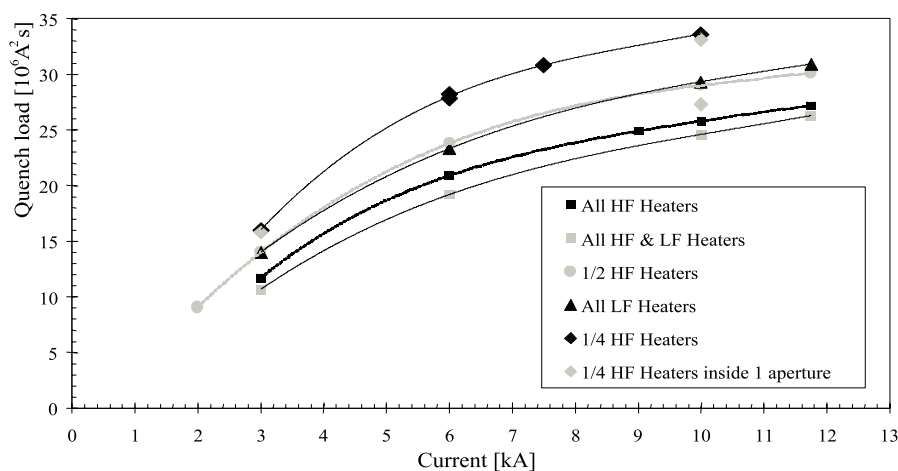
Figure 7.17: *Quench load versus current for different heater protection schemes of the prototype MBP2N1 v2. Note that quenches were provoked by spot heaters. The initial heater power supply voltage was 800 V.*

The protection of the LHC main dipole magnets with high-field heaters alone (4 heater circuits with two 15 m long heater strips connected in series) has the required level of redundancy in view of their operation in the LHC machine conditions [85].

Voltage Development

The voltage signals of heater tests performed on a 15 m long prototype magnet were used to evaluate the maximum voltage-to-ground during a quench (see Fig. 7.18). The voltage-to-ground is shown at various potentials (block voltages of the poles) and the maximum level does not exceed 900 V even for asymmetric firing of heaters (protection of heaters solely on one side per aperture) at nominal current. In the LHC, the energy extraction resistor switched into series will increase the measured voltage by up to 900 V. A maximum voltage-to-ground of about 1.8 kV is expected, which remains below the design limit of 3.1 kV.

7.3.5 Protection Simulations

QUABER simulations were carried out to study the impact of changing quench propagation parameters. The simulation model used a longitudinal quench propagation of 15 m/s, a turn-to-turn delay of 20 ms, and a $RRR = 80$. Assuming the quench detection based on the voltage difference between the two apertures, a threshold of 0.1 V is reached within 14 ms and 0.2 V within 21 ms for a quench starting in a low-field area in the outer layer. The turn-on voltage of the diode is
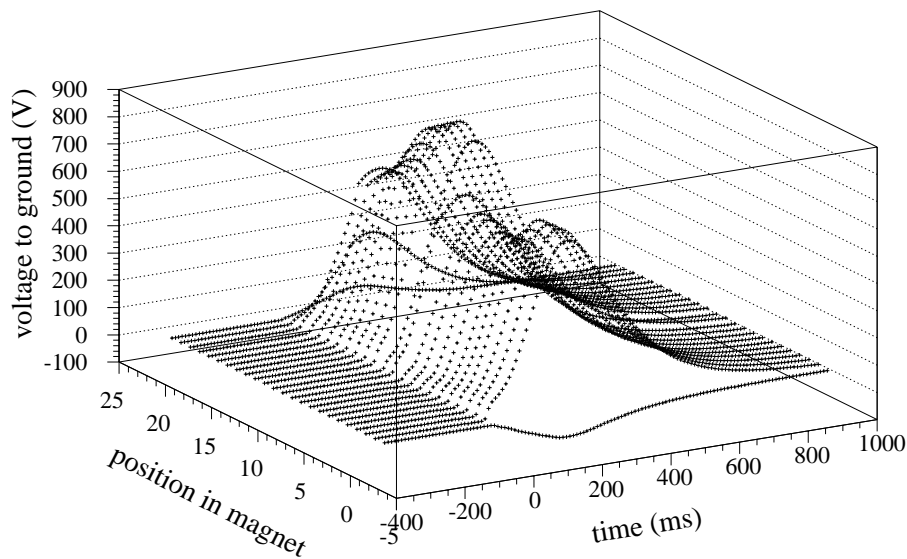
Figure 7.18: *Measured voltage-to-ground at various potentials (pole voltage taps) during a quench with asymmetric heater firing of a 15 m long prototype dipole magnet.*

about 8 V (corresponding to a resistance across the magnet of about $0.7\,\mathrm{m\Omega}$ at nominal current). The quench detection time depends on the operating current as follows: t_{det}=29 ms (9 kA); 85 ms (4.5 kA); 906 ms (0.8 kA) for a detection threshold of 0.2 V.

A quench load of $29\cdot10^6\,\mathrm{A^2s}$ is computed (corresponds to 280–300 K for an applied magnetic field of 4–6 tesla) at nominal current. The magnet is protected by high-field heaters which provoke a quench in the covered turns 40 ms after the quench detection (10 ms for quench validation and 30 ms heater delay). An energy extraction resistor is switched in series 60 ms after quench detection (time for opening switches).

If the turn-to-turn delay is modified by 10 ms, the temperature varies less than 20 K. A change of the longitudinal quench propagation by 10 m/s changes the simulated hot spot temperature by about 5 K. If the heater delays are increased by 5 ms, the hot spot temperature rises by 15 K.

The maximum operating current at which the heaters are not required to protect the magnet under machine conditions (series connection of magnets with cold diodes across them) has been calculated with QUABER to be about 2 kA. The turn-on voltage of the protection diode will still be attained after some time due to natural quench propagation, and a quench load of about $30\cdot10^6\,\mathrm{A^2s}$ would not be exceeded (see also Fig. 7.19). This approach is conservative as it does not take into account either cooling by helium or the fact that the quench process lasts more than a few seconds.

For a quench provoked with a spot heater at 2 kA, a quench load of $22.4\cdot10^6\,\mathrm{s}$ was measured for the dipole prototype magnet MBP2N1 v2 (without a diode mounted parallel to the magnet) after the protection systems have all been switched off. The simulated value of the quench load is higher since the turn-on voltage of the diode (about 8 V) must be reached before the current decay starts.

A scatter of the heater delays in the range of about 10 ms does not lead to unacceptably high voltages between the coil layers or to ground. The simulation study revealed a negligible effect of
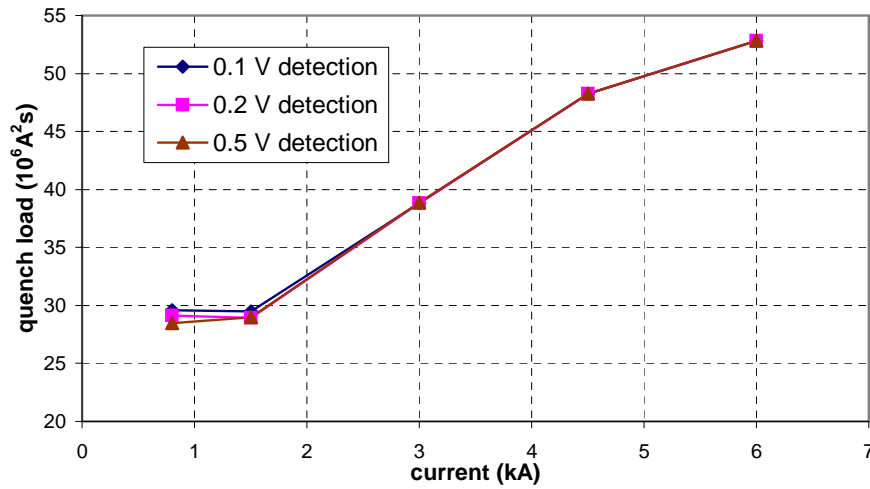
Figure 7.19: *Simulated minimum current at which quench heaters are required for protection.*

the copper-plating pattern on the quench load due to the quench propagation velocities of about 15 to 20 m/s at nominal current.

7.4 Magnetic Quench Back in Dipole Magnets

The analyses of the quench heater performance and the current decay in the short and long dipole magnets indicated that the resistance growth is largely affected by magnetic quench back (see also Section 3.4.2).

7.4.1 Short Dipole Magnets

The current decay causes a change in the magnetic field which induces coupling currents $I_{cc} \propto dB/dt$. Coupling currents generate heat at contact resistances between the strands and in the copper matrix between the twisted filaments of a strand. If the field change is fast enough, the heat generation causes a quench in a large fraction of the magnet (quench back). The quench back is the dominating quench mechanism for short dipole magnets. The quench back start-time t_{QB} is defined as the time between the start of a natural quench and the quench back start-time. The energy E_{QB} deposited at the contact resistance is proportional to the field change

$$E_{QB}(t) = \int_0^t P_{I_{cc}}(t')dt \propto \int \left(\frac{dB}{dt}\right)^2 dt' \tag{7.8}$$

The power loss depends on the direction of the local magnetic field and E_{QB} becomes a function of

$$E_{QB} = E_{QB}\left(I_{mag}(t); \frac{d\vec{B}(\vec{r})}{dt}\right) \tag{7.9}$$

During the current decay, the induced heat generation leads to a temperature increase inside the magnet coils which approach T_c. The critical temperature T_c increases as the magnetic field and the current density decrease. A quench back occurs if the actual temperature exceeds the critical temperature $T(t) > T_c(t)$. This can also be expressed as a condition for the current as $I(t_{QB}) > I_c(t_{QB})$.

The fast current decay starts when the resistive voltage across the magnet becomes too high to be compensated by the power converter. The time derivative of the current reaches values up to 80 kA/s depending on the initial current. In the short dipole magnets the quench back occurs at about 30 ms after the start of the quench. The quench back start-time is the same for both 5-block and 6-block magnets.

An example is given in Fig. 7.20 (upper graph) for the block voltages of a quench in a 6-block magnet. The natural quench starts at -12 ms and exceeds the detection threshold at -10 ms. After a quench validation time interval (see Section 1.5) of 10 ms the quench heaters are fired and the power converter is switched off (at 0 ms). The quench originates inside block 2 of the outer layer of the lower pole. This block is connected with block 6 in the inner layer. The quench propagates along the cable and quenches block 6 and block 5. The voltage signals of the blocks which have not yet been quenched cease following the expected inductive voltage at 18 ms. The signals are then the sum of resistive and inductive voltage contributions. The resistive development cannot come from the fired heaters as their heater delays at high current are about 30-40 ms as explained in Section 7.3.

The resistive development can be seen in the bottom graph of Fig. 7.20, in which the inductive voltages have been subtracted. The resistive growth of the block voltages U_{block} that have not quenched due to quench propagation along the cable are compared to the largest inductive block voltage U_{ind}^{max}. The voltage curves are scaled to the averaged ratio f_{scale} between the original block voltage and the largest inductive block voltage

$$f_{scale} = \frac{\int_{t_0}^{t_{QB}} \frac{U_{block}(t')}{U_{ind}^{max}(t')} dt'}{t_{QB} - t_0} \tag{7.10}$$

$$U_{block}^{new} = \frac{U_{block}}{f_{scale}} \tag{7.11}$$

The magnetic field in block 1 is low and its direction is perpendicular to the cable axis. In block 6 the field is the largest, but the angle between field and cable is small. In areas of high magnetic field, the resistance growth after a quench is expected to be strong due to the magneto-resistance. For the inner layer, the cables in block 3 are perpendicular to the field direction, and the magnetic field is low. The quench back first starts in block 4.

Magnetic quench back depends on the following parameters:

- the contact resistances (R_a, R_c) are determined by the cable design and the manufacturing process. Measurements have shown that the interstrand contact resistances vary by more than an order of magnitude.

- the interfilament coupling currents depend on the copper-parameters and the twist pitch of the filaments inside a strand.

- the amount of helium inside the cable defines the cooling conditions and influences the time dependence.
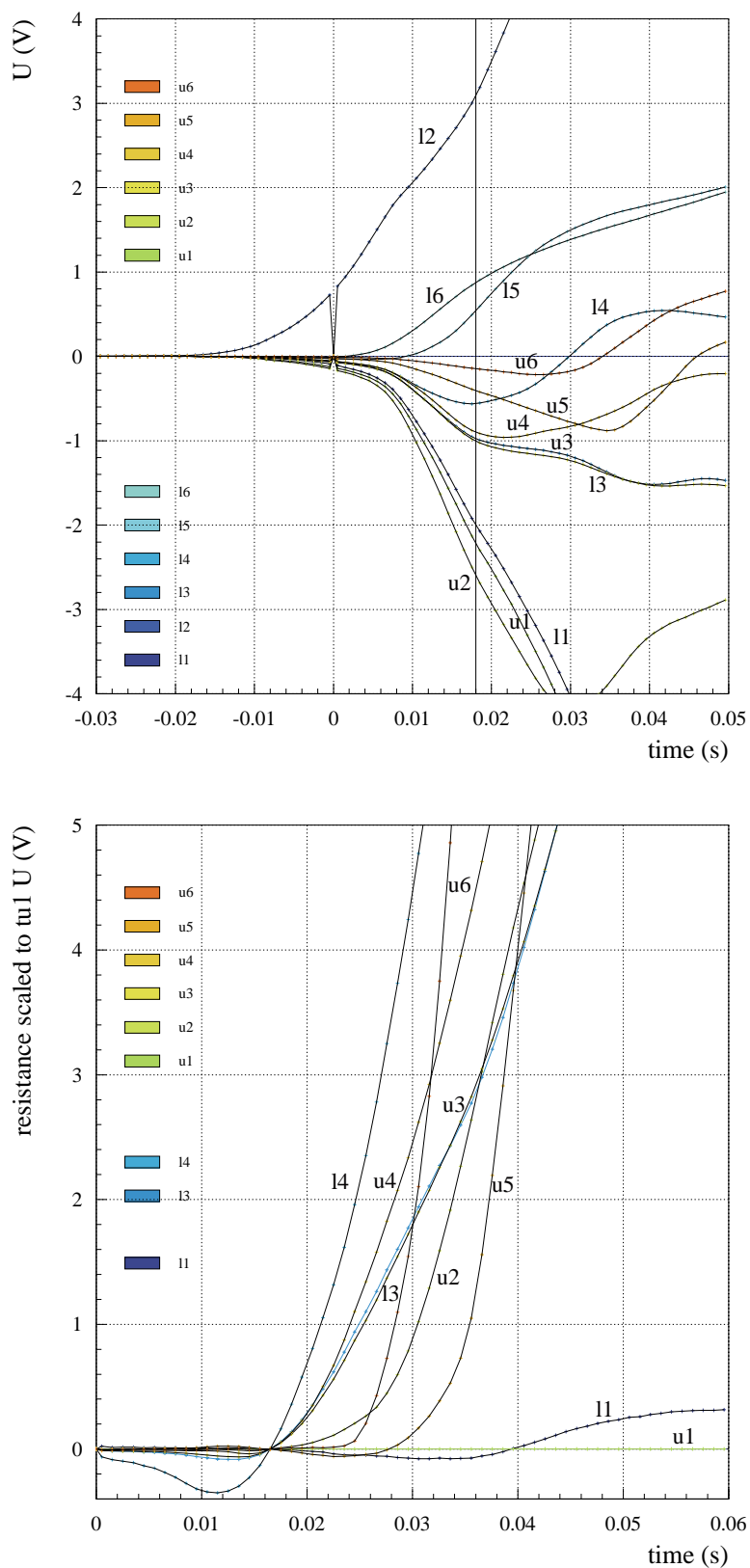
Figure 7.20: *Quench back example: block voltages of a short dipole magnet after a quench (top); the same voltages taking out the inductive voltage (bottom); l = lower pole, u = upper pole, 1–6 = conductor blocks. The noise in the voltages signals at t = 0 ms comes from the power converter that is switched off. The different slopes of the resistive voltages depend on the strength of the induced eddy currents and on the magneto-resistance.*

- assuming a linear relation between the strength of the magnetic field and current, larger values of dB/dt are obtained in high-field areas.

- the induction of coupling currents depends on the angle of the magnetic field direction with respect to the cable. A field perpendicular to the broad side of the cable causes a maximum induction of coupling currents, whose strength is at its minimum when the field is parallel.

- the magneto-resistance is larger for the high-field area increasing the value of the contact resistances between filaments. For a larger value of the contact resistance the coupling currents generate more heat, but the strength of the currents decreases.

- with zero contact resistance between the strands, heat would be generated solely between the filaments inside the strands and in bulk copper. With an infinite contact resistance, interstrand coupling currents would not be induced.

7.4.2 Long Dipole Magnets

When the voltage across the quenching magnet exceeds the turn-on voltage of the protection diode, the current starts to bypass the magnet and decays with a time constant of about 250–300 ms. The decay time is similar to that of short dipole magnets.
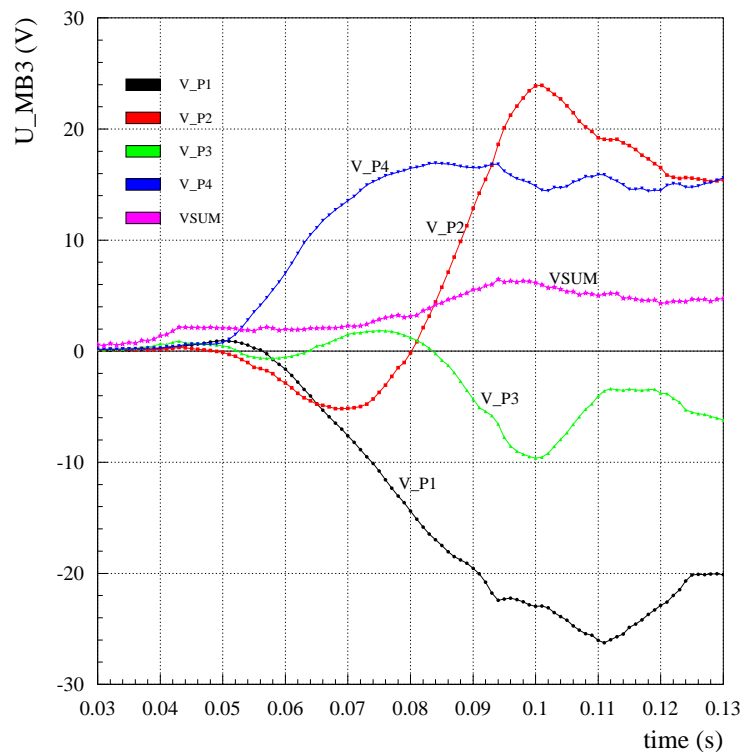
Figure 7.21: *Voltage signals during the quench back experiment on a 10 m long prototype magnet (2/12/98).*

As the analysis of the short dipole magnets showed that the quench back is a powerful mechanism for quench propagation, a test was performed at the LHC Test String I on a 10 m long prototype twin aperture dipole magnet [86]. The three dipole magnets in the string were connected

in series and one of the dipole magnets was equipped with a protection diode parallel to the magnet. For the quench back experiment the heaters were only fired in one aperture at the nominal current of 12.4 kA in the third dipole magnet (MB 3). The recorded voltage curves are shown in Fig. 7.21.

The voltage signals for a quench provoked by firing the heaters in both apertures are given in Fig. 7.22 for comparison. The current through the magnet was not measured and cannot be deduced from the recorded signals.
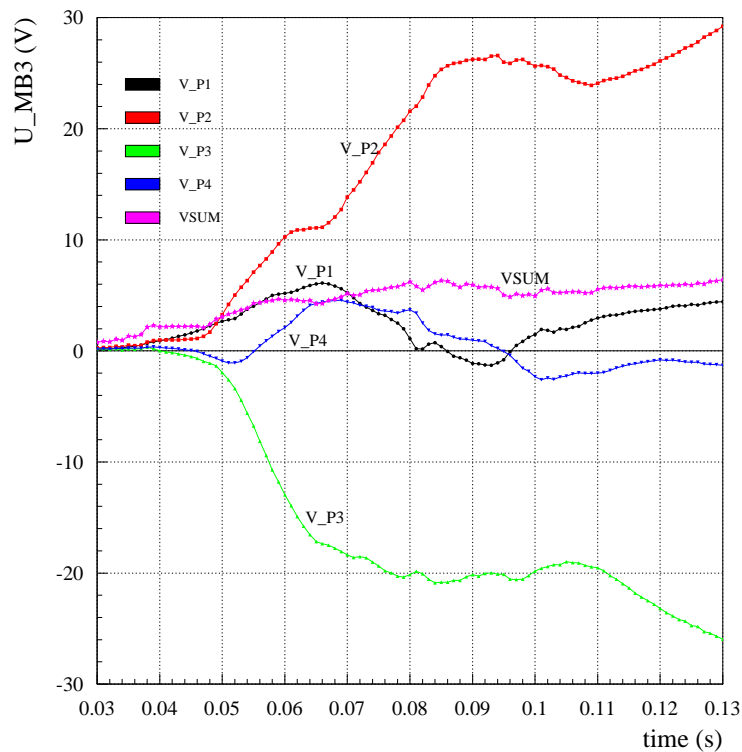
Figure 7.22: *Voltage signals of a quench provoked by firing the quench heaters in both apertures of a 10 m long prototype magnet (24/11/98).*

In Fig. 7.21 the heaters provoke a quench in the aperture with the pole voltages V_{P3} and V_{P4} but not in the other. The quench starts at 0.04 s. At the beginning, all four pole voltages develop a resistive voltage before the voltage signals V_{P1} and V_{P2} become inductive. V_{P4} quenches faster than V_{P3}. The quench back occurs at 0.065 s on V_{P2}. The resistance growth of V_{P2} is strong enough that this signal reaches the highest voltage. The quench back start-time of V_{P1} is between 0.085 and 0.09 s. The behaviour of V_{P1} and V_{P2} at the start of the quench shows that there is a resistive zone although the quench was provoked in the other aperture.

For quenches provoked by firing all heaters, the heaters on pole with the signal V_{P3} are less efficient (see Fig. 7.22). The resistance development of the signals V_{P1} and V_{P2} is faster and causes the inductive voltage to exceed the resistive voltage in V_{P3} and V_{P4}.

The voltages obtained during the quench back experiment are smaller than the voltages of a normal quench ($| U_{max}^{QB} | \approx 35\text{-}40$ V; $| U_{max}^{normal} | \approx 45\text{-}50$ V). The time constant for the current decay after both quenches is the same ($t_{quench} \approx 0.5$ s). The quench back start-time is similar to that of short dipole models ($\tau_{QB}^{string} \approx 25\text{-}50$ ms; $\tau_{QB}^{sh.d.} \approx 30$ ms). The fast current decay magnets is caused by the current sharing between the diode and the magnet in the long dipole magnets after firing of

the heaters and by the switched off power converter in the short dipole magnets. The experiment demonstrated that quench back occurs in long magnets at nominal current. Firing the heaters in just one aperture is sufficient for magnet protection.

> **Magnetic quench back was observed above a current of 6 kA in the 15 m long prototype magnets. Quenches were provoked with spot heaters and various sets of quench heaters were fired. The quench back started earlier when more heaters were fired because of the larger resistance that was provoked. Without provoking a forced quench by heaters, the current decay is too slow to induce significant magnetic quench back.**

An example of the voltages showing the starting quench back is given in Fig. 7.23. At 30 ms all voltage signals have a resistive contribution although the quench heaters were fired only in aperture I (high-field heaters only). Magnetic quench back induces a quench in aperture II. A thermal quench propagation between the two apertures is unlikely, since the propagation along the connecting busbar or heat transfer through helium requires a significantly longer time interval.

7.4.3   Comparison with Simulation Studies

The magnetic field components parallel and perpendicular to the broad side of the cable of the LHC dipole magnet are shown in Fig. 7.24.

A parameter study was carried out to determine the quench back start-time t_{QB} as a function of the time constant for the current decay, values of R_c and R_a, the initial current and various positions in the LHC dipole magnet (see Table 7.6). The current decay was approximated by a Gaussian function with the time decay constant τ.

block	$B_\perp$	$B_\parallel$	$\mid B \mid$	ϕ
	[T]	[T]	[T]	[rad]
1	-0.838	-1.332	1.57	1.01
2	-0.820	-4.058	4.14	1.37
3	-6.006	-0.900	6.07	0.15
4	-5.366	-3.700	6.52	0.60
5	-3.980	-6.254	7.41	1.00
6	-1.820	-7.568	7.78	1.33

Table 7.6: *The average magnetic field in the conductor blocks and the field components parallel and perpendicular to the blocks. The angle is defined such that 0 means a perpendicular field with respect to the broad side of the cable ($\pi/2$ means parallel).*

In some experiments with various short and long prototype dipole magnets the number of heater strips fired was changed, since this affects the resistance growth and therefore the current decay time constant τ. The simulation results for the quench back start-time t_{QB} are in good agreement with the experimental results (see Table 7.7). The table does not include data for the outer layer blocks as quenches are induced there with heaters. The impact of quench back on the magnet protection depends on its start-time. The simulated values for quench back start-times range from 30 ms for $\tau = 0.2$ s to 60 ms for $\tau = 0.3$ s at nominal current and average field in block 3. Firing one heater strip per pole already induces quench back fast enough to avoid magnet degradation. The minimum current at which quench back occurs is computed to be about 5 kA. During the
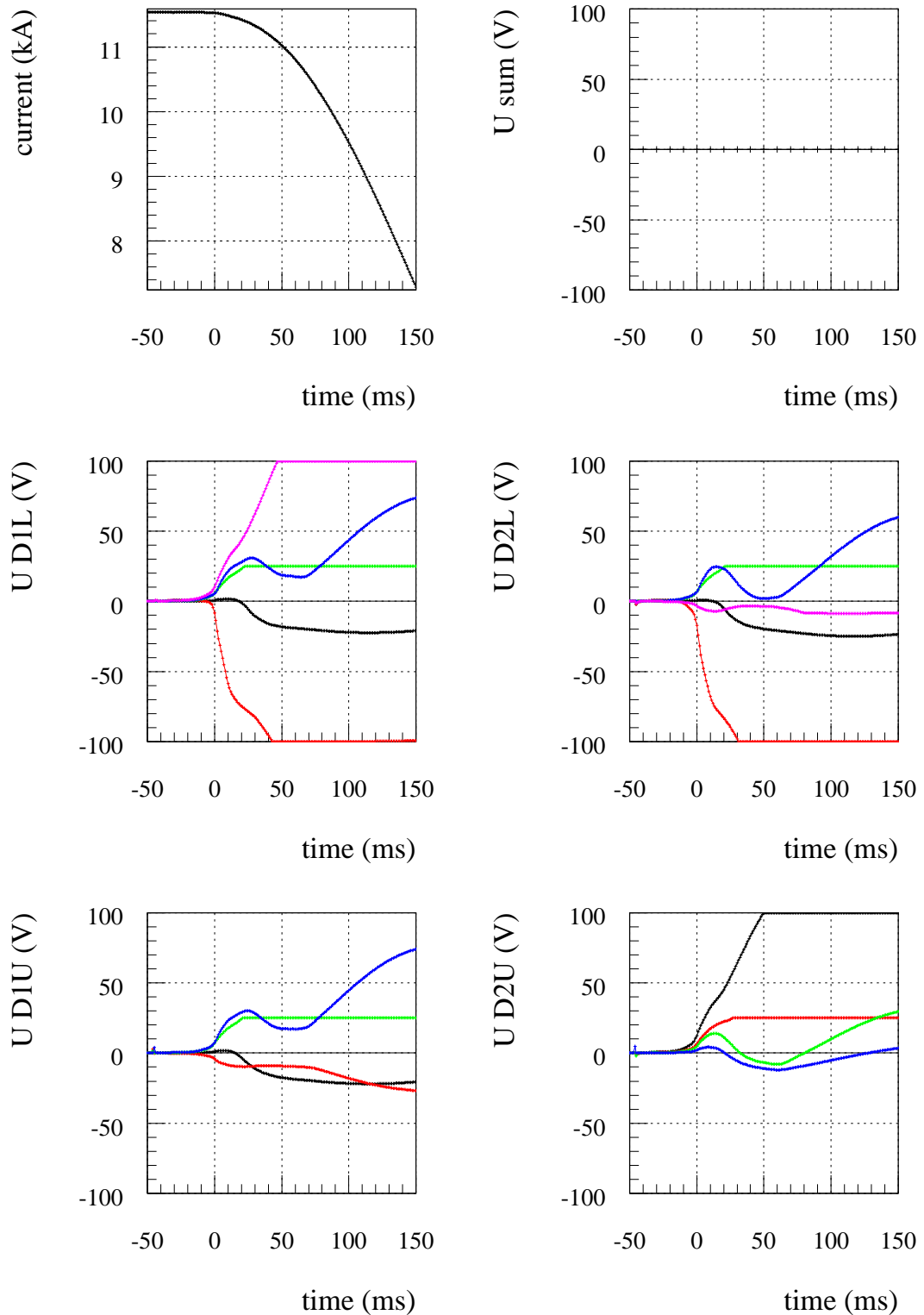
Figure 7.23: *Quench back observed during a spot heater induced quench in a 15 m long prototype magnet. The block voltages are given for every pole (D1, D2 stand for aperture I and II, U for the upper pole, L for the lower pole).*
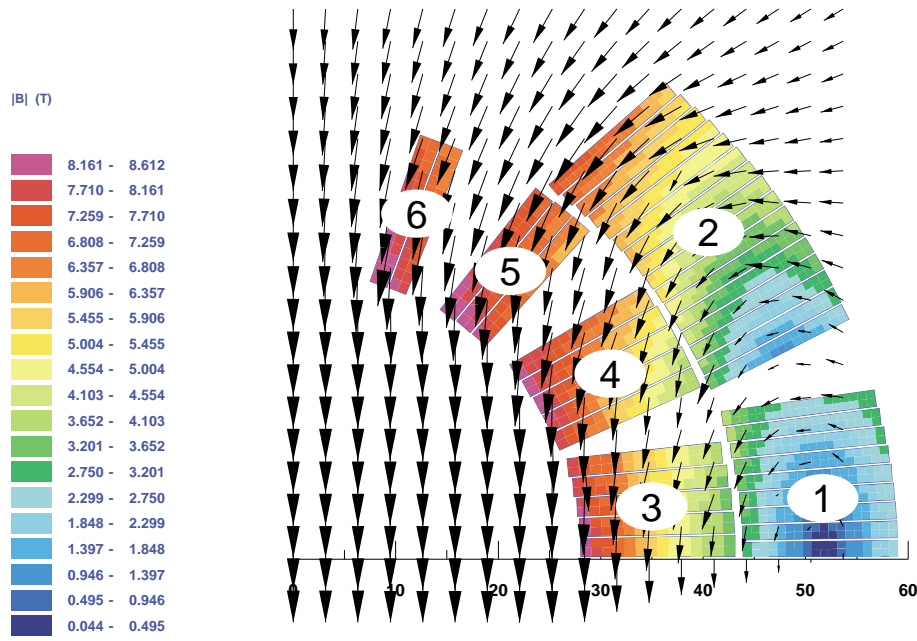
Figure 7.24: *LHC dipole magnet 2D cross-section showing the magnetic field map (calculated at nominal field with ROXIE [9]).*

Quench	Block	I_0 [kA]	τ [ms]	B [T]	angle rad	R_c [$\mu\Omega$]	R_a [$\mu\Omega$]	A_{Cu} [mm^2]	t_{QB}^{sim} [ms]	t_{QB}^{exp} [ms]
1	3	11.7	203	6.07	0.148	20	100	15.4	32	30±6
1	4	11.7	203	6.51	0.603	20	100	15.4	35	35±5
1	5	11.7	203	7.41	1.004	20	100	15.4	39	40±4
1	6	11.7	203	7.78	1.334	20	100	15.4	40	42±3
2	3	11.7	178	6.07	0.148	20	100	15.4	27	25±5
2	4	11.7	178	6.51	0.603	20	100	15.4	30	30±4
2	5	11.7	178	7.41	1.004	20	100	15.4	32	34±3
2	6	11.7	178	7.78	1.334	20	100	15.4	33	36±3
3	3	11.7	276	6.07	0.148	20	100	15.4	49	45±8
3	4	11.7	276	6.51	0.603	20	100	15.4	54	58±6
3	5	11.7	276	7.41	1.004	20	100	15.4	58	60±6
3	6	11.7	276	7.78	1.334	20	100	15.4	60	62±4
4	3	11.7	266	6.07	0.148	20	100	15.4	47	44±8
4	4	11.7	266	6.51	0.603	20	100	15.4	51	54±7
4	5	11.7	266	7.41	1.004	20	100	15.4	56	59±6
4	6	11.7	266	7.78	1.334	20	100	15.4	57	61±4

Table 7.7: *Example of the parameter study for quench back effect in main magnets (with Rutherford type cable) and the comparison of the simulation results with experimental data (quench numbers: 1 = training quench; 2,3,4 quenches provoked with spot heaters; 2 = protection with all HF heaters, 3 = protection with half HF heaters, 4 = protection with all LF heaters). The different values for τ are due to the number of heater strips fired. The quenches have been performed on the 15 m long prototype dipole magnet MBP2N1 v3.*

experiments quench back occurred for quenches at 6 kA whereas at 3 kA no quench back was observed.

Further simulations were carried out to study the influence of R_c and R_a. The results are summarised in Table 7.8. The typical contact resistance values of R_c=20 $\mu\Omega$ and R_a=100–150 $\mu\Omega$

R_a $[\mu\Omega]$	R_c $[\mu\Omega]$	Block	t_{QB}^{sim} [ms]	P_{if} [W/m]	P_{is} [W/m]	Block	t_{QB}^{sim} [ms]	P_{if} [W/m]	P_{is} [W/m]
100	0.10	3	5.05	0.26	0.02	6	40.0	10.3	0.42
100	1.00	3	37.1	12.2	62.5	6	56.5	14.8	9.19
100	10.0	3	46.4	16.4	232	6	57.4	15.4	13.1
100	50.0	3	47.4	18.2	65.4	6	57.4	15.4	3.02
100	100	3	47.6	18.2	34.3	6	57.4	15.4	1.59
1.00	20.0	3	47.0	16.9	432	6	57.4	15.4	23.8
10.0	20.0	3	47.1	17.2	171	6	57.5	15.6	8.77
50.0	20.0	3	47.1	17.3	148	6	57.5	15.6	7.43
200	20.0	3	47.1	17.3	143	6	57.5	15.7	7.18

Table 7.8: *Parameter study of the magnetic quench back effect in main magnets (with Rutherford type cable) with I_{init} = 11.7 kA, τ = 0.26 s and A_{cu} = 15.4 mm^2, values for the magnetic field from Table 7.6, variation of R_c and R_a.*

for the dipole Rutherford cables were taken from ramp rate sensitivity measurements [87]. Assuming these values, the interstrand coupling losses are mainly induced by the field component perpendicular to the broad side of the cable over the contact resistances R_c.

For Block 3 the dominating quench back mechanism is due to induced interstrand coupling currents. For Block 6 the magnetic field is almost parallel to the broad side of the cable, and the interfilament coupling losses P_{if} dominate the magnetic quench back.

When the values for R_c and R_a are increased, the quench back is in general dominated by interfilament coupling currents. For very small values of R_c the model predicts strong induced coupling currents but little power dissipation. Adding these to the excitation current, the critical current could be exceeded.

Although the average magnetic field and its angle with respect to the cable varies from about 1.5 tesla and 90° in Block 1 to about 8 tesla in Block 6 and 5°, the quench back starting time scatters less than 15 ms for the different conductor blocks at nominal current, which is in agreement with experimental results.

Experiments and simulations demonstrate that quench back starts long before the time of maximum dB/dt at about 0.2 s, with dB/dt ≥20 T/s and dI/dt ≥40 kA/s for the inner layer. With such gradient the coupling losses would be about 150±10 W/m for the interfilament losses and 600±100 W/m for the interstrand losses (with R_c =20 $\mu\Omega$ and R_a =100 $\mu\Omega$, the values are given for Block 3 assuming an averaged magnetic field). At the start of the quench back, a typical value of dB/dt is 8 T/s.

If the quench back starting time is small compared to the interstrand coupling current time constant τ_{is}, the following approximation can be made. As the time constant of the interstrand coupling currents (τ_{is}) is about $\tau_{is} \approx 25$ ms for $R_c = 20\,\mu\Omega$, $R_a = 100\,\mu\Omega$ for the inner layer cable and τ_{is} is proportional to $1/R_c$ (Eq. 3.56), one can write

$$1 - \exp(-t/\tau_{is}) \approx t/\tau_{is}; t \ll \tau_{is} \tag{7.12}$$

The interstrand coupling currents are proportional to $L_{p_s}/R_c \cdot (dB/dt)$ (see Eq. 3.57). Using the approximation of Eq. 7.12 the effect of R_c cancels for times smaller than τ_{is}.
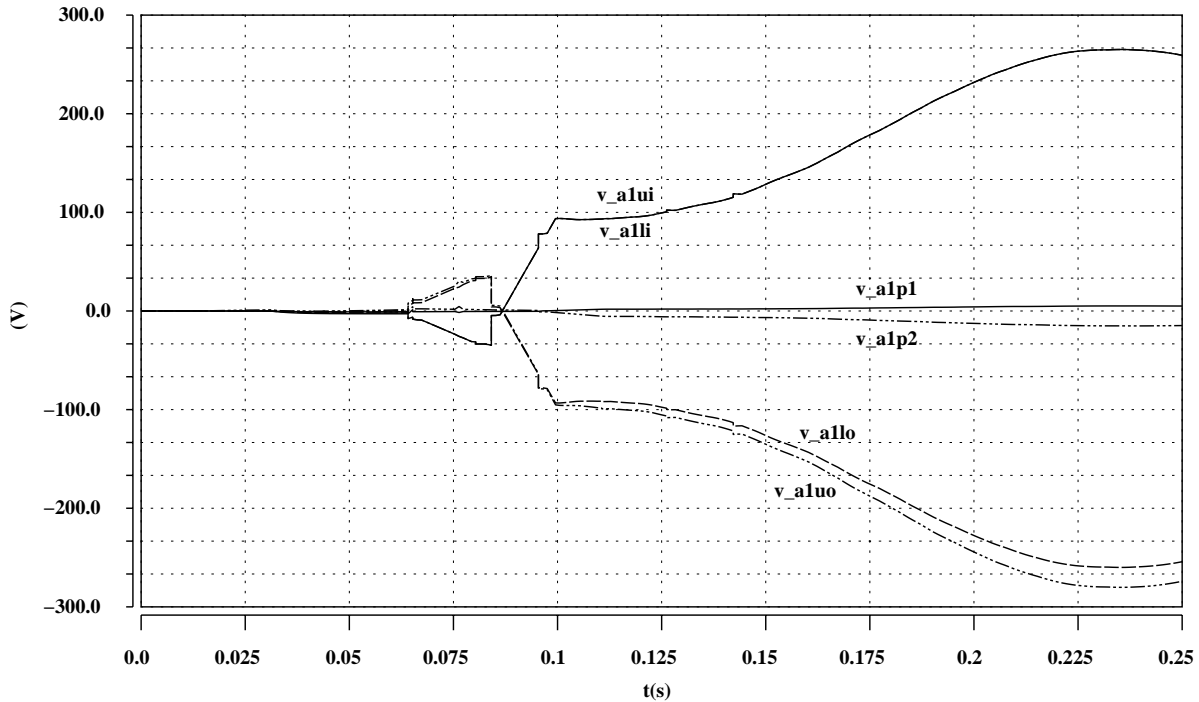
Figure 7.25: *QUABER output of the voltages in a quenching LHC dipole magnet including the simulation of magnetic quench back (voltage signals: v_a1li/lo = aperture 1, lower pole, inner/outer layer; v_a1ui/lo = aperture 1, upper pole, inner/outer layer; v_a1p1/2 = aperture 1, upper/lower pole).*

A QUABER model was calibrated with the output parameters of SPQR simulation studies and experimental results. The QUABER simulation aimed to reproduce the voltage development in a dipole magnet including quench propagation, forced quenching by heaters and magnetic quench back. The start of magnetic quench back is simulated by artificially quenching the inner layer of the magnet at the expected quench back start-time. As an example of the simulation study, Fig. 7.25 shows the voltages during a quench and Fig. 7.26 gives an overview of the temperature, the current decay and the resistance growth. When the heaters become efficient, the block voltages of the poles reach about ±100 V, which is in agreement with measured voltages (see Fig. 7.23). The voltages increase to about ±280 V (measured values ±320 V).
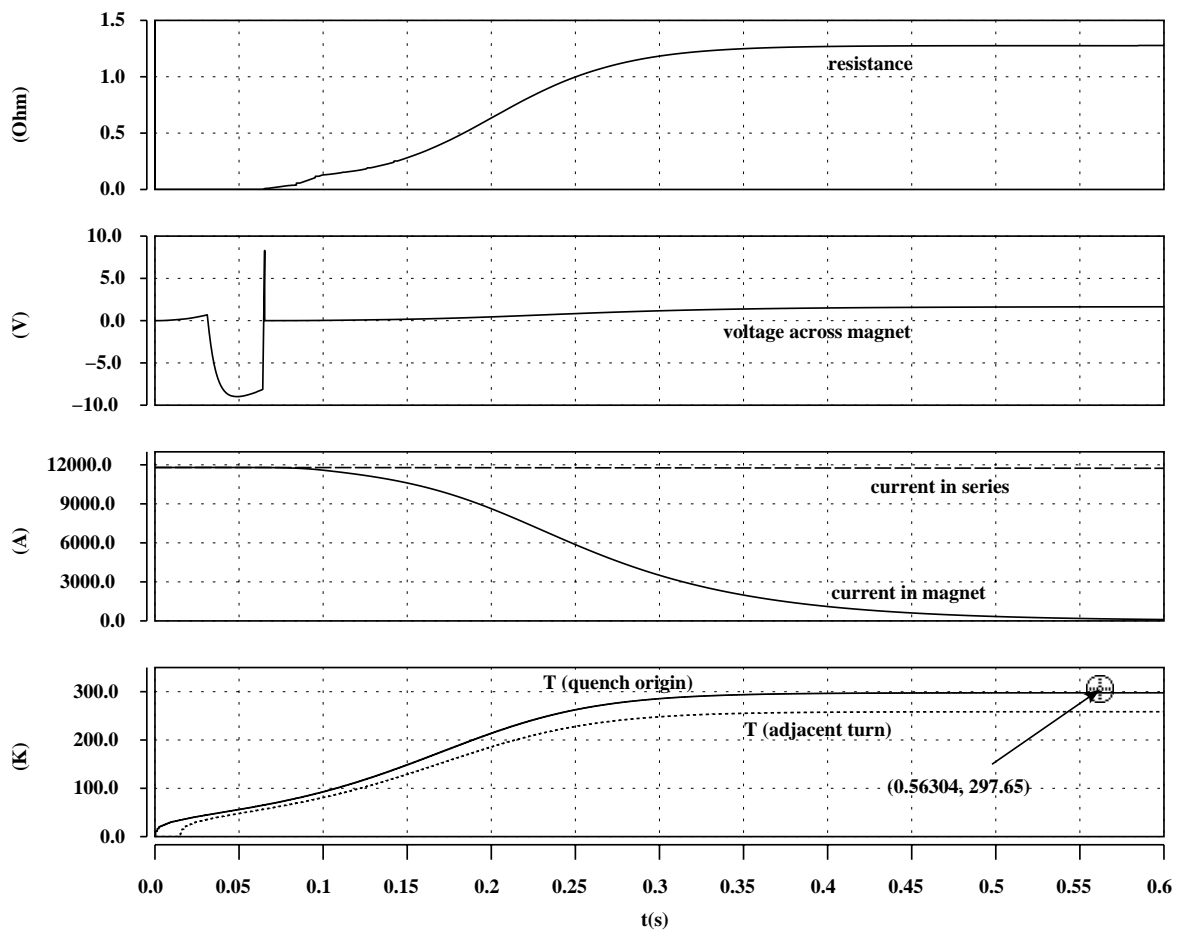
Figure 7.26: *QUABER output of the temperature, the current decay and the resistance growth in a quenching LHC dipole magnet including the simulation of magnetic quench back.*

7.5   Main Quadrupole Magnets

The design operating gradient of the main arc quadrupole magnet is 223 tesla/m at a nominal current of 11.87 kA. This gives a maximum field in the coil of about 6.5 tesla and a higher margin to the critical surface than for the main dipole magnets. The magnetic field for the two-dimensional MQ magnet cross-section is shown in Fig. 7.27. The required current distribution is approximated with a two-layer structure and four conductor blocks with the same cable in both layers (also used for the outer layer of the main dipole magnets). The two full-size prototype magnets mounted in the short straight sections SSS3 and SSS4 reached 13 kA after a few training quenches.
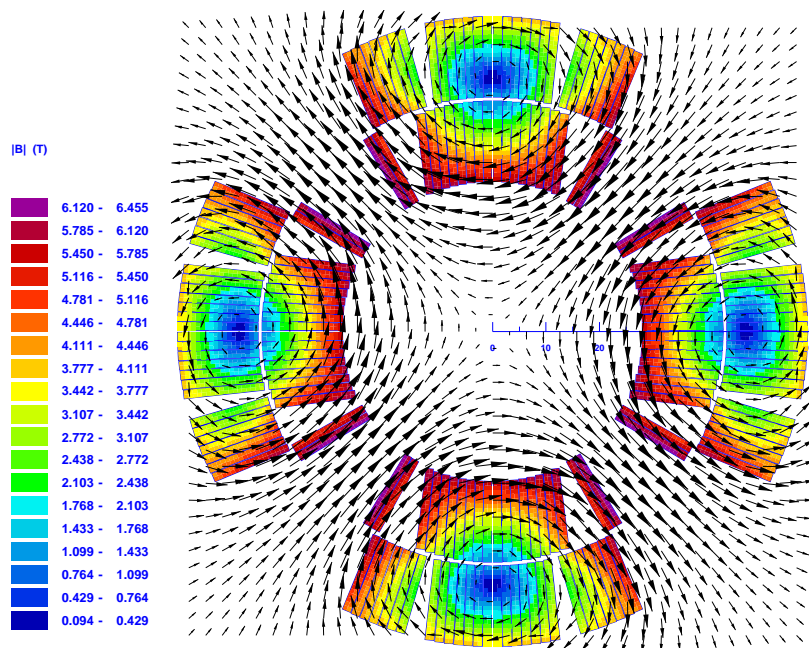
Figure 7.27: *Magnetic field distribution in the main arc quadrupole magnet MQ (field map calculated with ROXIE [9]).*

7.5.1   Protection

Four, 2 times 3 m long heater strips (total length of 24 m) will be connected in series, requiring two heater power supplies per magnet. The copper-plating pattern is adapted to keep the resistance of the heater circuit identical with the one for the dipole magnets, which gives a copper-plating pattern of 12 cm of heated part with 32 cm of copper-plated parts. The other heater strip parameters remain unchanged. The same heater power supplies as for the dipole magnets will be used [85].

The foreseen connection scheme of the quench heater strips is shown in Fig. 7.28. For redundancy each channel is connected with heater strips in both apertures. A quench is detected by a voltage bridge detector as for the main dipole magnets. The difference is that two detectors are installed (one per aperture) which compare the voltage across two poles with the voltage across the other two poles. Two quench detectors are required as the two apertures are connected in different series (focusing and defocusing quadrupole circuits). The current of the apertures can vary slightly,
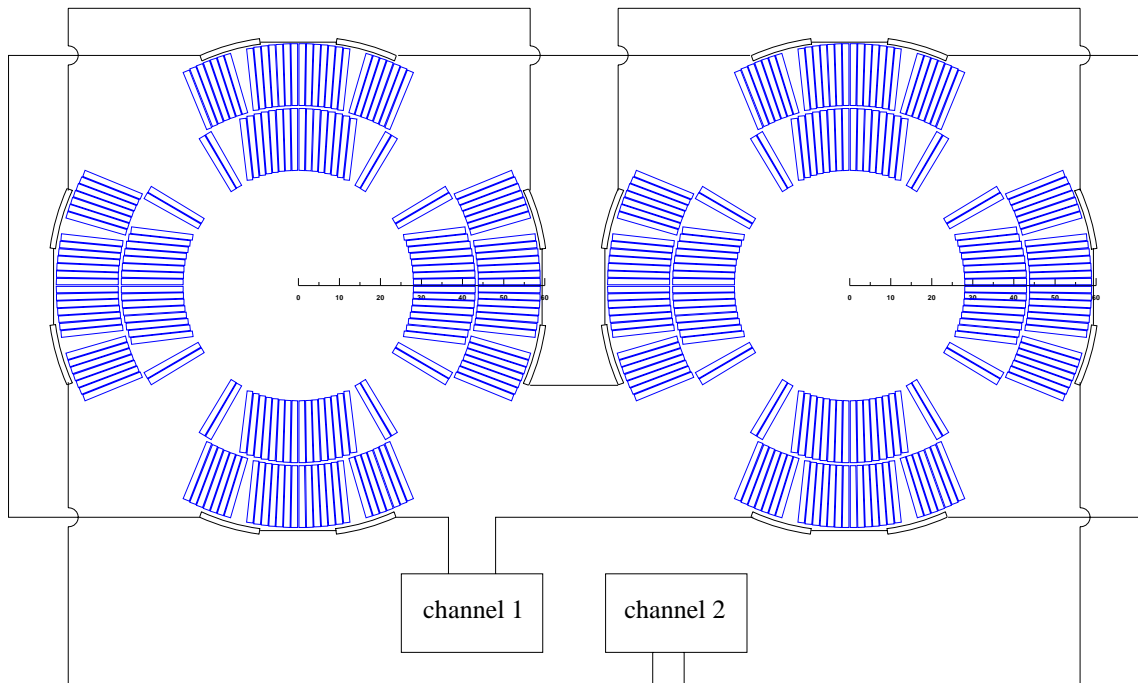
Figure 7.28: *Cross-section of the arc quadrupole magnet (MQ) and the connection scheme of the quench heaters.*

consequently the voltage across the apertures can be different during a fast current discharge. If one bridge detector is installed for both apertures, the difference of the voltages across the apertures might exceed the detection threshold, which would lead to an unwanted firing of the heaters.

7.5.2 Experimental Results

Heater delay tests were performed on SSS3 and are similar to those determined on the main dipole magnets (e.g. about 30 ms at nominal current).

Quench load experiments were also performed on the first full-scale prototype short straight section (SSS3) in slightly different conditions (see Fig. 7.29). The quench load at nominal current reached $29.1 \cdot 10^6$ A^{2}s (corresponds to about 290 K) protecting the magnet with only half the quench heaters.

> **With a tolerated hot spot temperature of about 300 K, the quench heaters for the arc quadrupole magnets are fully redundant as half of the heaters can safely protect the quadrupole magnet.**

7.6 Insertion Quadrupole Magnets

The insertion quadrupole magnets are the twin aperture MQM and MQY magnets and the strong focusing single aperture quadrupole magnets close to the experimental detectors (MQX magnets). The protection issues of the MQX magnets are discussed by Lamm [88] and Burkhardt [89].
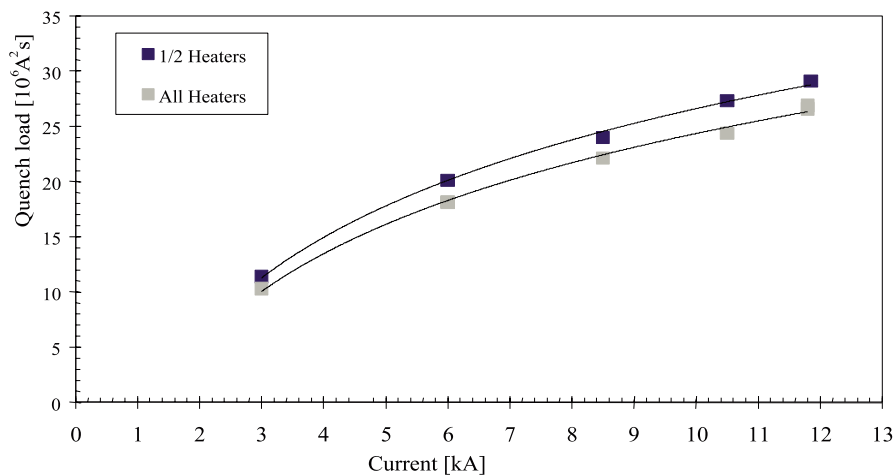
Figure 7.29: *Quench load versus current measured on a prototype arc quadrupole magnet. Note that all quenches were provoked by firing a quench heater strip.*

7.6.1   MQM Magnets

The MQM magnets are the twin aperture focusing quadrupole magnets with a two-layer cross-section located in the insertions and dispersion suppressors (at the beginning of the arcs). The length of the coil varies (2.5-5 m), which requires various copper-plating patterns for the heater strip in order to keep the same resistance of the heater circuits. Four heater strips of twice the magnet length will be connected in series and two heater power supplies will be required per magnet (same connection scheme as for the MQ magnets). Quenches will be detected globally including the protection of the busbar. In case of a quench detection the heaters will be fired. Energy extraction is not foreseen.

Experimental Results

The heater delays were tested on a 1 m long prototype magnet adjusting the power and energy density in the heated part of the strip by switching an external resistor in series. The magnet was equipped with heater strips between the layers and between the coil and the magnet collars. The measured quench heater delays are shown in Fig. 7.30.

> **The quench load was measured as a function of the operating current (see Fig. 7.31) on a prototype magnet. The tests demonstrated that the outer heaters alone can redundantly protect the magnet (300 K corresponds to about $2.8 \cdot 10^6$ A^{2}s).**

Additional tests were performed delaying the heater firing to simulate the quench detection at a threshold level of 0.5–1.0 V (20–25 ms delay). The quench load remained below a critical value [90]. For that reason the series production is foreseen without inner heaters, which simplifies the manufacturing process.

7.6.2   MQY Magnets

The MQY magnets are wide aperture quadrupoles with a four-layer structure. Two sets of heaters are installed between layer 2 and 3 and between layer 4 and the magnet collars. Different cables
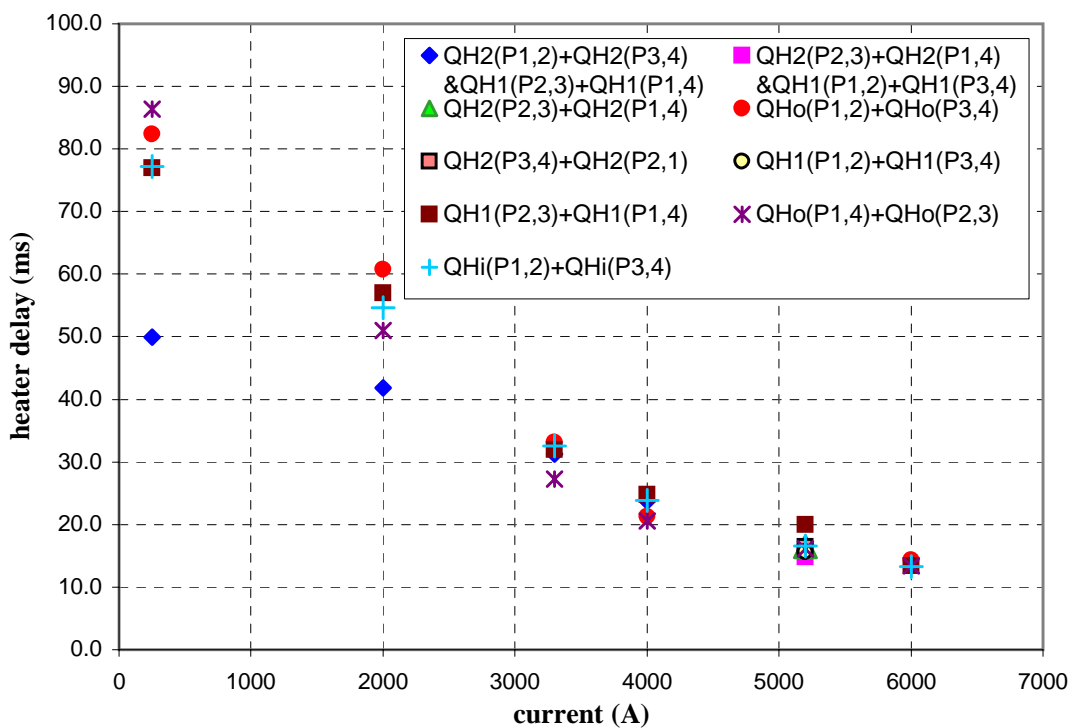
Figure 7.30: *Quench heater delays as a function of magnet current for a MQM prototype magnet (H1 = aperture 1; H2 = aperture 2; o = outer layer heaters; i = inner layer heaters; P(1–4) = poles).*
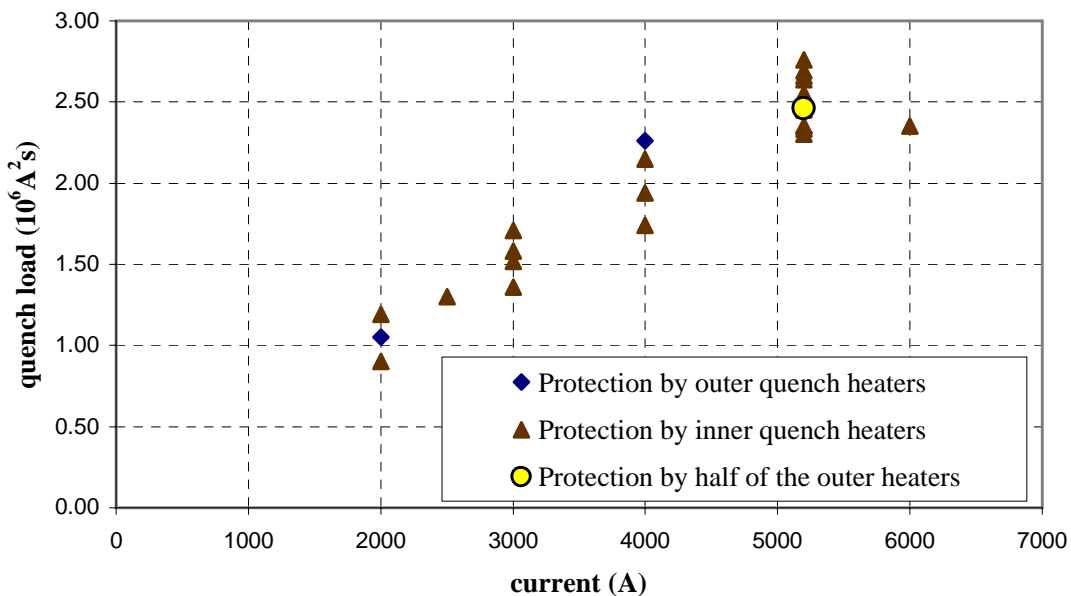
Figure 7.31: *Quench load versus operating current for the MQM prototype magnet. The quenches were provoked by spot heaters.*

are used to wind the two inner and the two outer layers. Since the installation of heater strips between layers is difficult, the protection with outer heaters alone was tested for its redundancy.

Experimental Results

A MQY twin aperture prototype magnet of 1 m length was tested for its quench performance and protection. The series magnets will be about 3.1 m long. Inner and outer quench heaters were installed. Three quenches were provoked by spot heaters. Because of a limited volume for helium recuperation, an energy extraction resistor was switched into series 100 ms and 200 ms after quench detection. Up to 15 % of the stored magnetic energy was extracted. All heaters were fired for the protection after the first provoked quench at nominal current. The magnet was protected solely with internal heaters during the second quench, and only the external heaters were used during the third quench. The quench heater delays were not measured but can be estimated to be about 20 ms (from MQM quench heater tests).

The experimental results have been used to calibrate the simulation model. The longitudinal quench propagation velocity is in the range of 25-30 m/s and the turn-to-turn delay is about 10-15 ms. Clear evidence of magnetic quench back has not been observed.

The experimental data concluded that external heaters on their own can protect the magnet (quench load of $2.2 \cdot 10^6 \, A^2 s$ with an equivalent adiabatic temperature 160 K). The maximum voltage was extrapolated to be around 60 V [91].

Simulation Studies for Protection

Simulation studies are required to scale the experimental results to the quench situation in the LHC. Two apertures in two different magnets of 3.4 m length will be powered in series (prototype length 1.3 m). As for the MQM magnets, a quench detection scheme is foreseen with a voltage threshold in the range of 0.5–1.0 V. The prototype magnet was equipped with specially made quench heaters (17 mm wide). For the series production one aims to use the standard heater strips with a width of 15 mm. The protection scheme has to be fully redundant at ultimate current (4000 A with respect to 3200 A during the prototype testing). An energy extraction facility is not foreseen.

The simulation study showed like the experimental results that induced eddy currents have little impact on the quench process. A resistive voltage of 1 V is reached after about 20 ms which increases the total heater delay with respect to immediate heater firing. This corresponds to an increase of the quench load by $0.4 \cdot 10^6 \, A^2 s$. The 17 mm wide strips take two extra turns to provoke a quench when compared to the standard quench heaters. Therefore, the use of standard heaters reduces the resistance development. The length of the magnet increases the maximum voltage-to-ground.

The simulation model is calibrated with experimental data (total external quench heater delay 60 ms, inner heater delay 70 ms) and includes all blocks of every pole in two full size magnets (two apertures connected in series). The inductance map has been calculated with ROXIE [9]. Various protection schemes were simulated:

- protection with half and all external heaters (total heater delay of 60 ms), assuming quench back and energy extraction (maximum voltage-to-ground 420 V)

- protection with all external heaters without quench back

- protection with all external heaters without quench back or energy extraction

- protection with half and all inner heaters without quench back or energy extraction

The simulation demonstrated that the maximum voltage-to-ground does not exceed a threshold of about 500 V for any protection scheme. A tolerated hot spot temperature of about 300 K excludes the protection with just half of the external heaters even if magnetic quench back would occur and an energy extraction resistor would be switched in series with the magnet. Without quench back and energy extraction, the protection with all external heaters cannot safely protect the magnet. Inner quench heaters of standard size can protect the magnet.

> **The simulation result outlines that the protection with external heaters alone leads to unacceptably high temperatures in the MQY magnets. It has been concluded that internal and external heaters together redundantly protect the MQY magnets (see Fig. 7.32).**

Internal heaters need to be installed in spite of a more complex manufacturing process. This protection scheme requires four heater power supplies for each twin aperture MQY magnet.
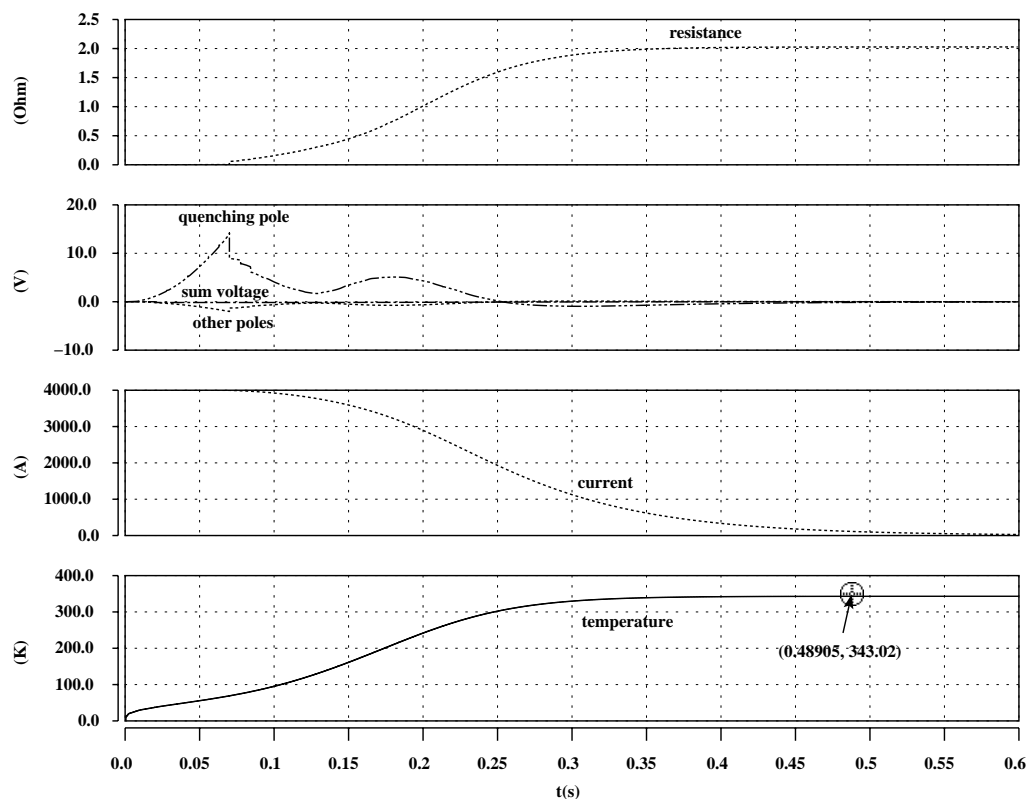
Figure 7.32: *QUABER simulation output for the MQY magnet protected with only half the inner heaters (heaters were fired at the same time). The voltage development of the first quenching pole, the other poles and the voltage sum are shown together with the resistance, the current and the hot spot temperature as a function of time.*

Chapter 8

The LHC Protection System

The stored energy in the superconducting elements of the LHC can cause damage during a quench due to overheating or excessive voltages (see Section 1.5). Therefore a reliable protection system is required to ensure the safety of the superconducting elements and to avoid machine downtime for repair. The functions of the system are to detect a quench in all superconducting circuits and to deal with the stored magnetic energy. Depending on the type of power circuit, different actions have to be taken: quench heaters must be fired; the current has to bypass the quenching magnet via a parallel diode or a resistor; and/or the energy is extracted with the help of a dump resistor that is switched into series.

This chapter introduces the different components for the LHC protection system and summarises the protection schemes foreseen for the numerous superconducting elements and power circuits. The consequences of the performed quench analyses and computations for the LHC protection system are shown. The different quench detection procedures are discussed and expected operation scenarios are presented.

8.1   Protection Elements

Fig. 8.1 gives an overview of the various parts in a typical LHC circuit. The magnet symbolises either a chain of magnets connected by a busbar or an individually powered magnet. The protection elements for the magnet are not included in the drawing. This section lists the equipment required for the protection of the various superconducting elements: the magnets, busbar cables with interconnects, and the current leads. The protection elements for a main magnet connected in series (MB and MQ magnets) are shown in Fig. 8.2.

8.1.1   Quench Detection

Quench detection was already discussed in Section 5.4. Two different approaches are possible: a local quench detection based on a difference voltage exceeding a threshold (bridge detectors); and a global quench detection based on the measurement of the voltage across the cold part of the circuit and its comparison with the computed inductive voltage (global quench detector).

Local Quench Detection

Resistive transitions are detected with floating bridge detectors for each main magnet connected in series. The signal is validated for about 10 ms. The principle is sketched in Fig. 8.3.
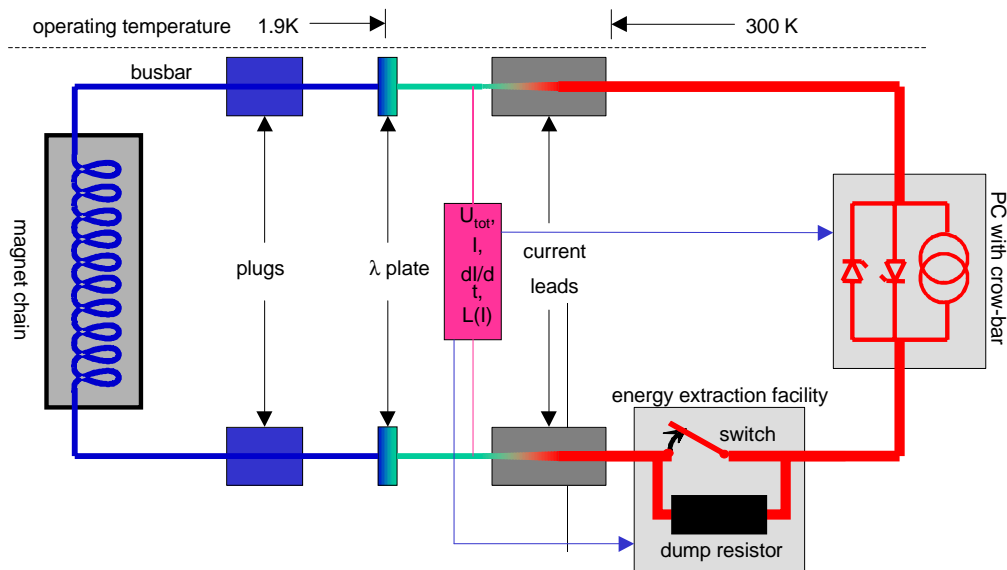
Figure 8.1: *Schematic view of a LHC circuit including a global quench detector (measurement of U_{tot} and I). The protection elements for the magnets (parallel diode or resistor, quench heaters) are not included. When a quench is detected, a power abort signal is sent to the power converter and the dump resistor is switched into series. The protection issues and the quench process have been analysed in the Chapters 5, 6 and 7 for the various superconducting elements.*
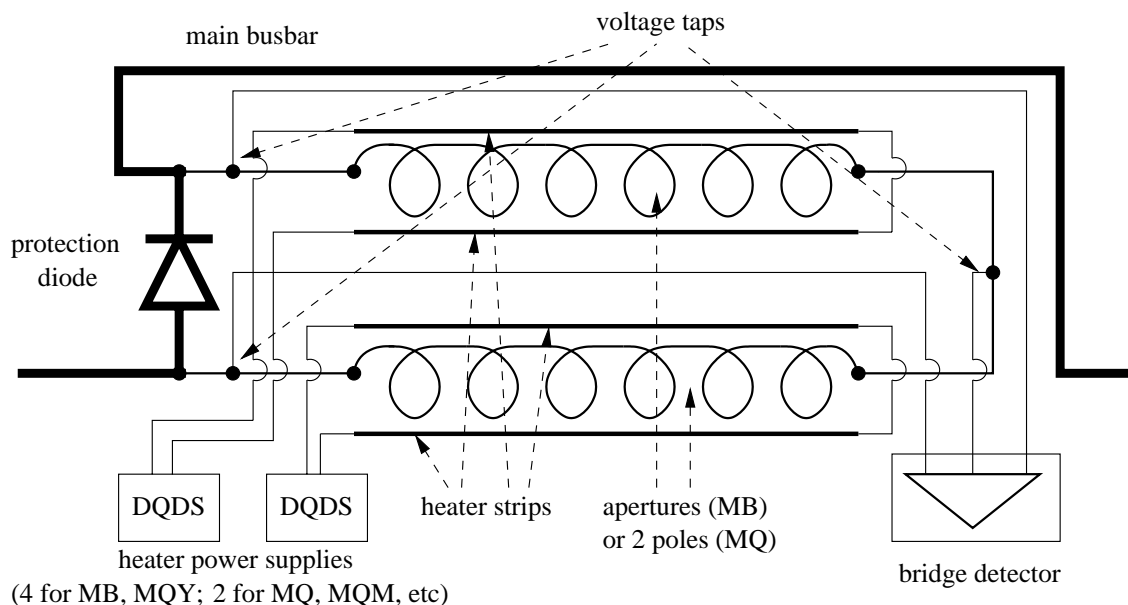
Figure 8.2: *Protection instrumentation for the main magnets. The main dipole and arc quadrupole magnets connected in series are protected by local quench detection (bridge detectors), quench heaters and a diode parallel to the magnet. The insertion quadrupole and injection dipole magnets are protected with a global or a bridge detector (see Fig. 8.1) and quench heaters.*
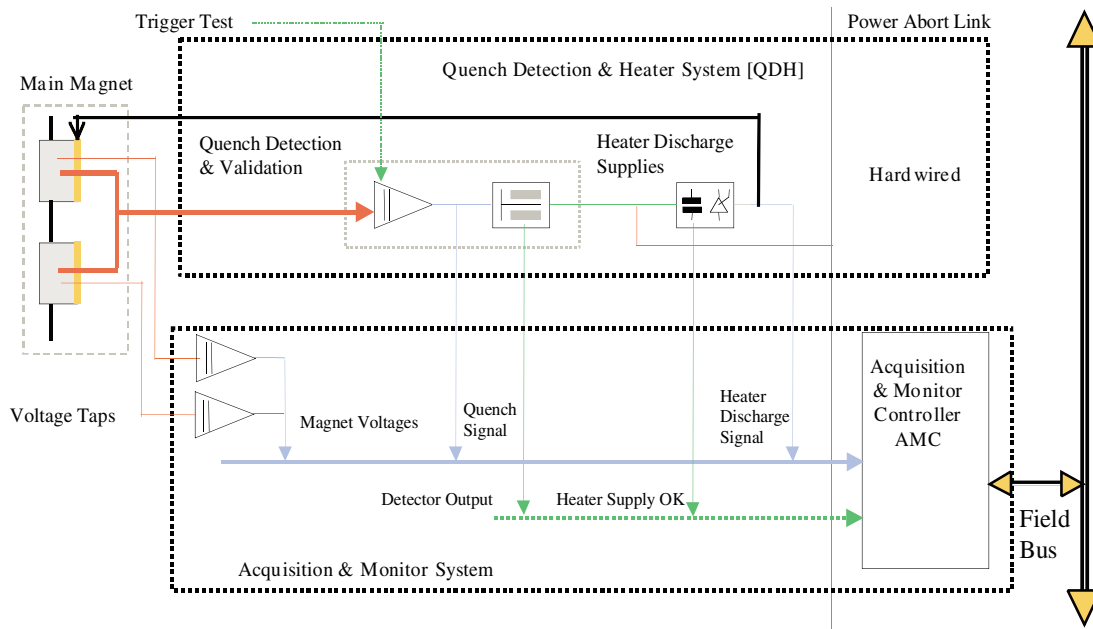
Figure 8.3: *Principle of the quench detection for the main magnets with a local quench detector and data acquisition.*

Global Quench Detector

The global voltage detector measures the current and the voltage across the cold part of the circuit as a function of time. The current signal can either be provided by the power converter or, if needed, it can be measured independently by a hall sensor or DCCT (DC current transformer). An inductance map as a function of current is stored in the detector. From the current measurement the detector calculates the current derivative and computes the expected inductive voltage. If the absolute value of the difference between the expected voltage and the measured voltage exceeds a threshold, a quench is detected.

8.1.2   Magnet Instrumentation

The LHC main magnets will be equipped with voltage taps for the bridge detectors and voltage monitoring (see Section 4.1). Voltage taps are installed in the main dipole magnets at three different points: two taps per busbar connection at the entrance, two at the exit of the magnet, and two at a midpoint between the two layers. The main quadrupole magnets will have voltage taps at the entrance, two at the exit of both apertures, and two between pole 2 and 3 for each aperture (see Fig. 8.2). The installation of two voltage taps at each position is foreseen for redundancy.

All other circuits have voltage taps at the bottom of the current leads. The global quench detector uses these voltage taps to measure the voltage across the cold part of the circuit. Additional voltage taps might be installed once every half or full cell. These would then be used for data acquisition or additional bridge detectors.

The high temperature superconductor current leads are equipped with a voltage tap at three different positions (at the cold and warm ends and at an intermediate point). These current leads will be protected by a voltage threshold detection (see Fig. 8.4).
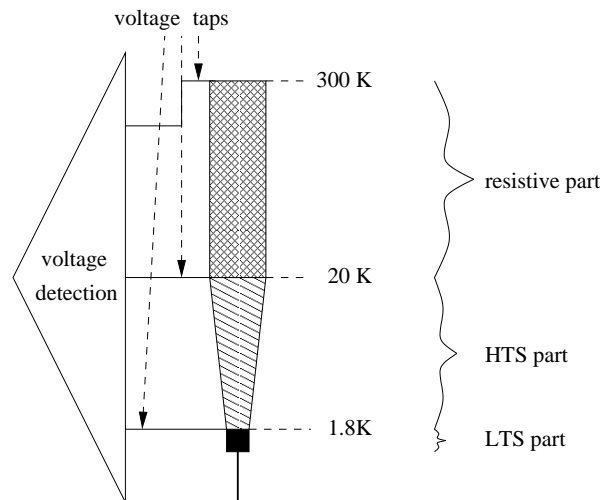
Figure 8.4: *Protection instrumentation for the current leads with a high temperature superconducting (HTS) part.*

8.1.3 Resistors in Parallel

Parallel resistors are required for some lattice corrector magnets connected in series (see Section 6.4). In case of a quench the growing resistance in the quenching magnet exceeds the value of the parallel resistor within a short time interval and the current starts to bypass the quenching magnet flowing through the parallel resistor [79].

8.1.4 Diodes in Parallel

The high-current silicon diodes with a 6–8 V turn-on voltage of the diffusion type will be connected parallel to the superconducting magnets and operate inside the magnet cryostat at a temperature of 1.9 K. The quadrupole diodes must safely withstand an estimated dose of about 400 Gy and neutron flux of about $2.4 \cdot 10^{12}$ n/cm^2 during 20 years of operation. For the dipole diodes a dose of about 60 Gy and a neutron fluency of about $3.0 \cdot 10^{11}$ n/cm^2 has been estimated [92].

One bypass diode will be installed across each twin-aperture dipole magnet. As focusing and defocusing quadrupoles will be powered separately, each single quadrupole aperture requires a diode. The two diodes assembled in one pack are galvanically separated. Each diode package must be able to conduct an ultimate current pulse of 13 kA peak with a nominal decay time constant of about 100 s for the dipole circuit, and about 40 s for the quadrupole circuit. The heat sinks absorb an energy of about 1.5 MJ for a dipole diode; and 0.7 MJ for a quadrupole diode. The diodes have to operate within a temperature range of 1.8 to 450 K, withstand the associated thermal stresses, and continue to operate reliably after several cold-warm cycles. Before installation, all diode packages will be tested at liquid helium temperature. As the differences of the electrical characteristics between 1.9 K and 4.2 K are rather small, most tests will be carried out at 4.2 K. Only a few of the series diode assemblies will be tested at 1.8 K to verify their turn-on characteristics [93].

8.1.5   Quench Heaters

The heaters for the dipole magnets consist of pairs of austenitic stainless steel strips (0.025 ± 0.002 mm thick and 15.0 ± 0.1 mm wide) bonded in between two layers of polyimide electrical insulation foil (see Fig. 3.14). The latter acts as support and insulates the strips against the coils and the collar structure that is at ground potential. The thickness of each insulation foil is 0.075 mm$\pm5\%$. A layer of 0.025 mm of epoxy glue will be clad on the internal face of the polyimide foils for proper bonding to the strips during a warm rolling process. The quench heaters are subsequently creased to match the geometry of the magnet outer coils. They are then equipped with powering leads through soldered connector elements. Once installed in a magnet, the heater strips are strongly compressed between the superconducting coil and the collars (pressures around 50 MPa for the LHC dipoles). Therefore, the austenitic stainless steel strips must have smooth burr-free edges to avoid punching through the electrical insulation foil. The heater strips have a length of about 15 m each, and cover the entire length of each outer coil. The total copper-plating pattern is 52 cm long, alternating 40 cm plated and 12 cm non-plated periods. The copper thickness is 0.004 ± 0.001 mm and its RRR value exceeds 30. The electrical resistance of the strips drops from 1.5 Ω/m at room temperature to about 0.35 Ω/m at 1.9 K. The design of the quench heaters for the quadrupole magnets is similar: their length will be about two times 3 m, and each strip covers two poles. The copper-plating pattern will alternate 12 cm of unplated steel with 32 cm of copper-plated parts [93].

The copper-plating pattern is adjusted for the various insertion magnets protected with quench heaters to keep the same resistance in the heater circuit. This means only one type of a heater power supply is needed for the entire machine. Table 8.1 gives an overview of the various heater strips to be installed in the different main magnets.

Magnet name	length [mm]	pattern l_{Fe} [mm]	pattern l_{Cu} [mm]	width [mm]	strips in series
MB		120	400	15	2
MQ		120	320	15	4·2
MQMC	2486	125	100	21	4·2
MQM	3491	120	170	21	4·2
MQML	4891	140	350	21	4·2
MQR	3491	*100*	*70*	21	2·2
MQRL	4891	*120*	*125*	21	2·2
MQY inner	3508	130	190	21	4·2
MQY outer	3508	100	250	15	4·2
MQXA	6530	115	230	15	2·2
MQXB	5714	120	215	15	2·2
MBRA, B, C	9646	100	400	15	4·2
MBRS, MBX	9646	*100*	*200*	15	2·2

Table 8.1: *The heater strip layouts for the LHC magnets. A list of the various heater protected magnets can be found in Table 7.1. Values given in italics are preliminary.*

8.1.6 Heater Power Supplies

The quench heater power supply determines the amount of energy which is dissipated into the heater strips. Each power supply has a maximum stored energy of 3.5 kJ. The supply is based on the thyristor-triggered discharge of aluminium electrolytic capacitors. It contains a bank with 6 capacitors (4.7 mF/500 V), where two sets of 3 parallel capacitors are connected in series, resulting in a total capacitance of 7.05 mF (see Fig. 8.5). In order to enhance the capacitor lifetime, the foreseen operating voltage is 90 % of the rated voltage. The nominal operating voltage of the capacitors will be U_{nom}=450 V with a mid connection to ground, giving a maximum stored energy of 2.86 kJ [93]. After detection of a quench, a capacitor power supply applies a voltage of 900 V
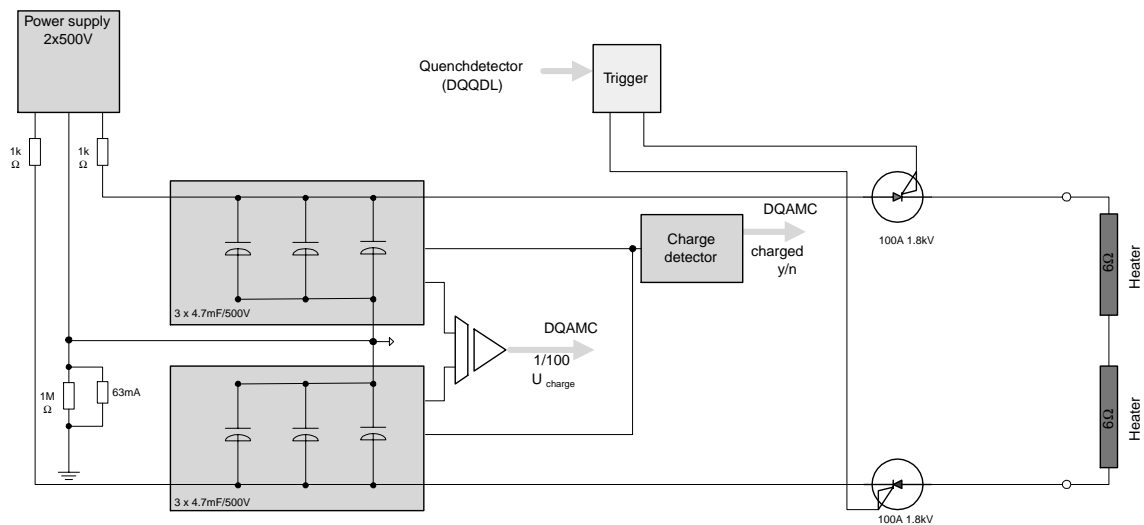
Figure 8.5: *Sketch of the quench heater power supply.*

across the heater strips connected in series, providing a peak current of about 85 A. The time constant of the heater circuit is about 75 ms.

8.1.7 Energy Extraction

For a fast current discharge in the case of a quench, many of the superconducting circuits with magnets connected in series will be equipped with external energy extraction systems that consist of mechanical circuit breakers and energy-absorbing dump resistors. The 1.33 GJ of stored energy in the dipole magnets of each sector will be extracted into two symmetrically placed energy dump facilities, inserted in series with the two half-chains. This configuration limits the maximum voltage to ground to 500 V; it halves the energy deposit in each resistor unit and allows symmetrical grounding of the power circuit (the mid-point of the mid-arc dump resistor). The transfer function analysis of the chains has shown that this grounding concept provides important advantages for ripple, ramping and transient phenomena. The resistance value (75 mΩ each unit) limits the maximum current decay rate to -125 A/s. Four 4.5 kA DC circuit breakers will carry the current, fed from a current-equalising bus-way. Each cluster of breakers consists of eight individual units, with two breakers in series for redundancy. Each breaker has two independent release mechanisms (for slow opening and current impulse for fast release). The dump resistors incorporate a forced air-to-water heat exchanger, as heat dissipation into the tunnel air is inadmissible. A single

extraction system is foreseen for each of the quadrupole chains. The dump resistance values are 7.7 mΩ and 6.6 mΩ, which give a maximum decay rate of -325 A/s. The same breakers as for the dipole magnets are used [93].

600 A energy extraction facilities will be installed for the protection of the corrector magnets and their busbars. The extraction resistor varies in the range of 200–700 mΩ and is adapted to the needs of the individual circuits (see Section 6.4).

8.1.8 Radiation Tolerant Equipment

The equipment installed in the tunnel includes capacitor discharge power supplies for firing the quench heaters, quench detectors, breaker control electronics, data acquisition systems, programmable logic controllers (PLC) and interfaces to field buses. Due to beam losses and interactions with the residual gas in the beam tube, this equipment is exposed to radiation (order of magnitude: 1 to 10 Gy per year) during LHC operation [92]. All these devices are tested under conditions similar to those expected in the LHC in the irradiation test zone in the fixed target North area of the CERN SPS accelerator [93]. The dose rate in this area is about 10 Gy per week corresponding to a fast neutron fluency of some 10^{11} n/cm^2. The zone is equipped with cable connections to a local control allowing for dynamic, on-line measurements of the components and radiation levels.

8.2 Protection Schemes

Each main quadrupole and dipole magnet will have its own protection system that is fully redundant and independent of other magnets. When a quench is detected, the protection will activate the powering of the quench heater strips, shut down all power converters in the sector and open the switches across the dump resistors. For a quench in a busbar, the system will shut down the power converter of the circuit and open the dump switches without firing heaters. The quench detection for the dipole magnets is based on floating bridge detectors. For the main quadrupole magnets, the comparison will be made between two sets of two poles, since the two apertures of the quadrupole magnets are powered separately.

For the protection of the corrector and insertion magnets as well as for all busbars, the voltage at the cold end of the current leads will be measured to detect a quench (global quench detection). Quenches in busbars for main dipole and quadrupole magnets are very unlikely, as they are installed in regions of low magnetic field, protected from direct radiation and highly stabilised with copper. It is sufficient to detect any resistive growth on long stretches, using the global quench detection scheme. If the quench in a busbar is detected late (more than 60 s after a quench) part of the heaters can be fired for a faster current decay. This is an emergency situation that is not included in the normal protection procedure.

Quench Detection Parameters

The requirements quench detection parameters have been finalised. The bridge detectors work at a detection threshold of 0.2 V with a quench verification time interval of 10 ms. The global voltage threshold for the insertion quadrupole and corrector magnets is in the order of 0.5–1.0 V with a quench verification time interval of 10–20 ms.

Due to the high inductance in the dipole circuit, the global voltage detector for the main busbars acts slower at a threshold of 1 V and a verification time in the order of 5 s. The old baseline for the quench detection included bridge detectors comparing two half cells or full cells (i.e. 600 bridge detectors for the three main busbars).

Data Acquisition and Monitoring

The controllers for data acquisition and monitoring (AMC) will monitor the status of the protection system, allow for powering, and acquire data for both on-line and post-mortem analysis (magnet voltages, quench detector signals, signals from the heater power supplies). The AMC units are continuously acquiring the signals and storing them in a circular buffer. When a quench is detected, the acquisition continues during a defined short period of time and then stops. On request the data is sent to the operators allowing a post-mortem analysis of the event. The integrity of the protection system is monitored, for example if heater discharge units are not correctly charged, heater discharge units are not fired, or failures of quench detectors. If a failure is detected, the machine cannot be powered and a message is sent to the operators. Each machine sector will have about 200 AMC systems that are connected via a field bus to an intermediate controller (WAN-PLC). This controller acts as a bridge between the AMC units and the Control Room (see Fig. 8.3). In order to minimise cost and development, it has been decided to use a PLC-like structure. This means that a commercially available system can be used, leaving just the program to be developed at CERN. Each unit will have a data memory exceeding 48 Kbytes, an acquisition cycle of less than 10 ms, and analogue inputs with an accuracy of 10 bits. A field bus will be used for the communication.

Conclusions and Outlook

The analysis of the experimental results and simulation data has shown that analytical models are insufficient to describe the coupled electrodynamic and thermodynamic processes during a quench. Consequently, the application of such analytical models can lead to errors in the design of the magnet or the protection system. If the design of the protection system is too conservative, this could cause additional machine downtime. Using the standard equations of quench propagation could also result in inadequate protection with severe consequences in case of a fault.

The advancements and improvements in the simulation model allow a more precise study of the quench processes in superconducting busbars and magnets, since the impact of the cooling conditions on the hot spot temperature and the influence of induced eddy currents due to a changing magnetic field are integrated. The analyses and simulation studies yielded an improved understanding of the quench propagation, including the quench back effect.

The conclusions were not only used to determine the required busbar dimensions and protection but also to establish adequate detection levels and protection schemes for the all superconducting circuits of the LHC. Other topics addressed the protection of magnets, for example the optimisation of the quench heater strip layout, the heater powering parameters and the values of parallel resistors.

Summary of Results

The quench process was explained as a coupled electrodynamic and thermodynamic process as described in Chapter 3. The simulation model includes the longitudinal and transverse quench propagation, cooling by helium, forced quenching by heaters, and quench impact of induced eddy currents.

The modelling of the heat transfer through the insulation layer allowed the consistent reproduction of experiments performed on busbars and the determination of the required copper stabilisation. The simulation outcome showed that a global quench detection is sufficient for the protection after a busbar quench (see Chapter 5).

The observed magnetic quench back in corrector and main magnets was explained by the modelling of dynamic losses due to induced eddy currents (see Chapters 6 and 7). For the design of a new accelerator with superconducting magnets, the impact of quenching due to induced eddy currents should already be included in the design phase for the magnet production.

The quench heater performance of the main magnets was studied on different short and long prototype magnets. Simulations were carried out to understand the measurements. As a result, the copper-plating pattern was optimised such that two 15 m long heater strips can be connected in series without compromising the quench heater performance (see Chapter 7).

Due to the improvements of the quench heater performance and the understanding of the impact of magnetic quench back, the protection scheme for the main magnets was optimised and simplified. High-field heaters alone can redundantly protect the dipole magnets. The number of

required heater power supplies was therefore reduced from 16 to 4 for the dipole magnets, and from 4 to 2 power supplies for the twin aperture quadrupole magnets (see Chapters 7 and 8).

The protection parameters of the corrector magnets have been finalised. The outcome of the analyses demonstrated that active protection equipment such as quench heaters, diodes or bridge detectors are not needed as it was originally foreseen. This optimises the reliability of the protection system. The magnets that require protection by a parallel resistor and the circuits that need energy extraction were identified. The values of the parallel and extraction resistors were defined (see Chapter 6).

Outlook

The foreseen protection schemes will be validated at the String II setup [74]. Adjustments of the defined voltage thresholds for the local and global quench detection will be possible, if the experience shows that the expected noise level in the signals are different. Quench propagation from one magnet to the next will be studied. The final test of the protection system will be done during the commissioning of the first LHC octant with and without beam injection.

A more detailed model of the helium will be required to study numerically the quench propagation between magnets due to heat transfer in the helium bath.

Appendix A

Numerical Approach

The discretisation used in the simulation model is shown in Fig. A.1. The current flows in the x-direction and the conductor is discretised in $Nelem$ elements of length Dx. When modelling corrector magnets, the discretisation in the y-direction Dy corresponds to the different layers, whereas Dy are the elements along the the broad side of a Rutherford cable for main magnets. The discretisation in z-direction Dz refers to various turns of the coil. The quench heater strips lie in the x-z plane.

The size of the discrete elements in space and time must be carefully adjusted in order to avoid numerical instabilities such as oscillations and diverging temperatures [76, 94]. For that reason the chosen step-width and initial timestep have to be changed for each application so that consistent results are achieved. For a fast program execution, the number of elements should not be too large. Increasing the initial timestep and the variables responsible for the Δt adjustment compromises the precision and reliability.

A.1   Discretisation of the Heat Balance Equation

In the one-dimensional model the cable is discretised in $Nelem$ nodes of Dx length. The timestep Δt is dynamically adjusted by the program depending on the material properties (Δt_{act}). The user sets the initial and minimal timestep with the variable $timestep$ (or Δt^0). The actual time is updated according to $t_{new} = t_{old} + \Delta t_{act}$. In discrete space, the continuous temperature $T(x)$ becomes $T(i_x)$ meaning T at the position $Dx \cdot i_x$. The same notation is used for P and A as a function of x. The time is noted as t although it is a discrete time t_n with a changing time interval between two timesteps. The algorithm for the evaluation of the temperature development contains nested loops

- program initialisation

- time loop with dynamically calculated $timestep = \Delta t_{act}$

- nested loop for temperature evaluation of $Nelem$ elements with length Dx.

The quench energy is calculated from the enthalpy difference between the computed temperature profile and helium bath temperature

$$\dot{q} = Dx \cdot \left(\sum_{i_x} A(i_x)(H(T(i_x)) - H(T_b)) \right) \tag{A.1}$$

discretisation in x,y
taking an average
value for z

x

Dx

Dy

turn

turn

turn

y

dV=DxDyDz

turns

z
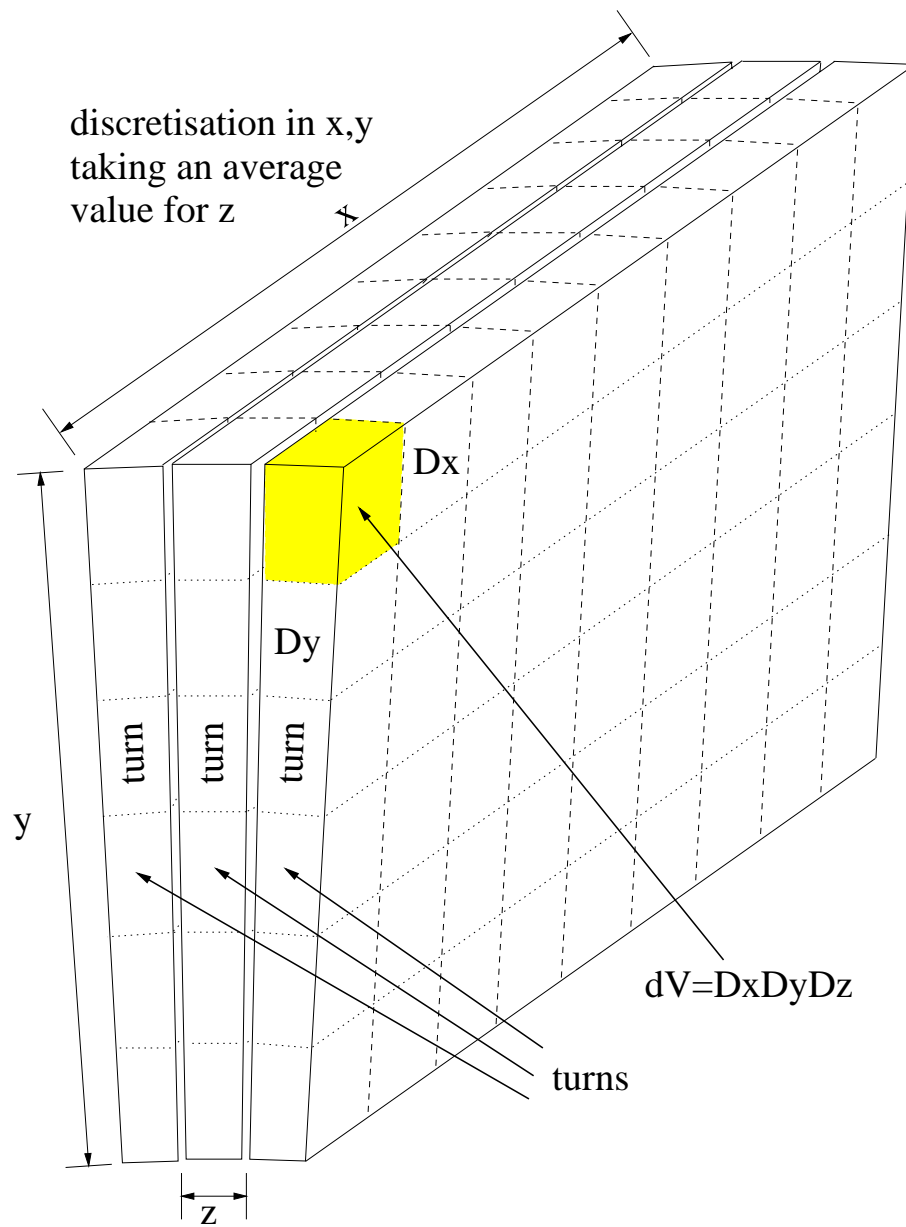
Figure A.1: *Discretisation of the superconducting structure.*

After initialisation, the temperature is evaluated with the discretised one-dimensional heat balance equation (see also Eq. 3.86). The new temperature $T^{new}(i_x, t^{new})$ is given by

$$
\begin{aligned}
T^{new}(i_x, t^{new}) \;=\; & T(i_x, t) + \frac{\Delta t_{act}}{c(T(i_x, t))} \cdot \left[k(T(i_x, t)) \frac{T(i_{x+1}, t) + T(i_{x-1}, t) - 2T(i_x, t)}{(Dx)^2} \right. \\
& \left. - h^{He}(T(i_x, t)) \frac{P(i_x)}{A(i_x)} + \frac{G(T(i_x, t), t)}{A(i_x)} \right]
\end{aligned}
\tag{A.2}
$$

Eq. A.2 is valid only for a constant cross-section A along the conductor, otherwise the derivative dA/dx has to be included.

The terms of Eq. 3.1 are expressed in Eq. A.2 as follows:

- the time derivative of the temperature is $(T^{new} - T)/\Delta t_{act}$.

- the first time derivative of the temperature in x is $(T(i_{x+1}) - T(i_{x-1}))/(2Dx)$. The second time derivative of the temperature in x is given by $(T(i_{x+1}, t) + T(i_{x-1}, t) - 2T(i_x, t))/(Dx)^2$.

- the heat generation is given by $G(T(i_x, t), t)$.

- the values of the material properties ρ, c, k and the heat transfer to liquid helium h^{He} are linearly interpolated from a look-up table that is calculated at the start of the simulation (according to input parameters $B - field$, RRR, $r_{sc/cu}$, etc). The common material parameters are computed as a function of temperature according to the proportions of the materials A_{sc}/A_{tot}, A_{cu}/A_{tot}, and A_{he}/A_{tot}; and are stored in look-up tables with a temperature step width of 0.1 K (see Section A.2).

The temperature evaluation ends when an abort criterion is fulfilled (normally if the time exceeds the end-time: the input parameter $fintime$). The abort criterion can also be a very high temperature (greater than 1000 K) in the cable; a temperature or voltage threshold; zero current; length of normal conducting zone; or a collapsing quench.

The timestep is calculated according to

$$
\Delta t_{act}^{new} = \begin{cases}
\alpha \cdot c(\min(T(i_x, t))) \frac{(Dx)^2}{k(\min(T(i_x, t)))} & \text{if } \Delta t_{act} < \Delta t_{act}^{new} < \Delta t_{control} \cdot \alpha \\
\Delta t^0 & \text{if } \Delta t_{act}^{new} \leq \Delta t^0 \\
\Delta t_{control} \cdot \alpha & \text{if } \Delta t_{act}^{new} < \Delta t_{control} \cdot \alpha
\end{cases}
\tag{A.3}
$$

In order to reduce the required computation time, the number of terms in the heat balance equation can be reduced, when the heat generation vanishes. If the current decayed to zero, the temperature is evaluated with an equation that does not include the ohmic heat generation term.

Heat Transfer through Insulation

Eq. A.2 changes to a system of two differential equations when the cooling model takes heat transfer through the insulation of the material into account

$$
\begin{aligned}
T^{new}(i_x, t^{new}) = \; & T(i_x, t) + \frac{\Delta t_{act}}{c(T(i_x, t))} \cdot \left[k(T(i_x, t)) \frac{T(i_{x+1}, t) + T(i_{x-1}, t) - 2T(i_x, t)}{(Dx)^2} + \right. \\
& \left. k_{iso} \left(\frac{T(i_x, t) + T_{iso}(i_x, t)}{2} \right) \frac{P(i_x)}{A(i_x)} \frac{T_{iso}(i_x, t) - T(i_x, t)}{l_{iso}} + \frac{G(T(i_x, t), t)}{A(i_x)} \right]
\end{aligned}
\tag{A.4}
$$

Eq. A.4 contains the heat conductivity through the insulation material and the temperature on the surface between insulation and helium bath $T_{iso}(i_x, t)$. It is calculated by

$$T_{iso}^{new}(i_x, t^{new}) = T_{iso}(i_x, t) + \frac{\Delta t_{act}}{c_{iso}(T_{iso}(i_x, t))} \cdot \tag{A.5}$$

$$\left[k_{iso}\left(\frac{T(i_x, t) + T_{iso}(i_x, t)}{2}\right) \frac{P(i_x)}{A(i_x)} \frac{T(i_x, t) - T_{iso}(i_x, t)}{l_{iso}} - h^{He}(T(i_x, t))\frac{P(i_x)}{A(i_x)} \right]$$

Due to the iterative temperature evaluation in the conductor, a numerical problem can occur. The temperature dependence of the heat transfer model can cause that more heat is transferred into helium than comes from the conductor through the insulation layer. This would yield a temperature in the insulation layer below T_b, which is an unphysical result corrected by resetting $T_{iso}^{new} = T_b$. The algorithm for the temperature evaluation including heat transfer through an insulation layer is

- program initialisation

- time loop with dynamically calculated $timestep = \Delta t_{act}$

- inside two nested loops:

  - temperature $T(i_x, t)$ evaluation for $Nelem$ elements with length Dx
  - temperature $T_{iso}(i_x, t)$ evaluation for $Nelem$ elements with length Dx.

Using this model and including the helium fraction inside the superconducting structure, the wetted perimeter is no longer a fit parameter that requires a calibration of the simulation model. The remaining uncertainties are due to the amount of helium in the structure that is not precisely known and the heat transfer constants into helium on the surface of the insulation material. The amount of helium might need to be varied to reproduce the measured quench propagation velocity. For insulated cables, the heat transfer from the insulation into the helium bath only plays a role for the longterm evaluation of the hot spot temperature.

Quench Heaters

In order to simulate quenches provoked by quench heaters (see Fig. A.2), the heat balance equation for the quench heater is solved iteratively with the equation for the conductor for every timestep.

$$
\begin{aligned}
T_h^{new}(t^{new}) &= T_h(i_x, t) + \frac{\Delta t_{act}}{c_h(T_h(i_x, t))} \cdot \left[\rho_h(T_h(i_x, t))\frac{I_h(t)^2}{A_h} \right. \\
&\left. - f_h \cdot k_{iso}^h\left(\frac{T_h(i_x, t) + T(i_x, t)}{2}\right) \frac{T_h(i_x, t) - T(i_x, t)}{l_{iso}^h t_h} \right]
\end{aligned}
\tag{A.6}
$$

The heater cross-section A_h is $w_h \cdot t_h$ (heater strip dimensions are width w_h in z direction and thickness t_h in y direction). The time dependence of the current flowing through the heater was described in Eq. 3.97.

Heat transfer from the heater strip into the superconductor occurs solely at the heated parts of the strip. For this reason, the calculation of a single heater strip temperature is sufficient. This reduces the number of elements to be evaluated per timestep and accelerates the simulation run. The approximation simplifies Eq. A.6 to

$$T_h^{new}(t^{new}) = T_h(t) + \frac{\Delta t_{act}}{c_h(T_h(t))} \cdot \left[\rho_h(T_h(t))\frac{I_h(t)^2}{A_h} \right.$$
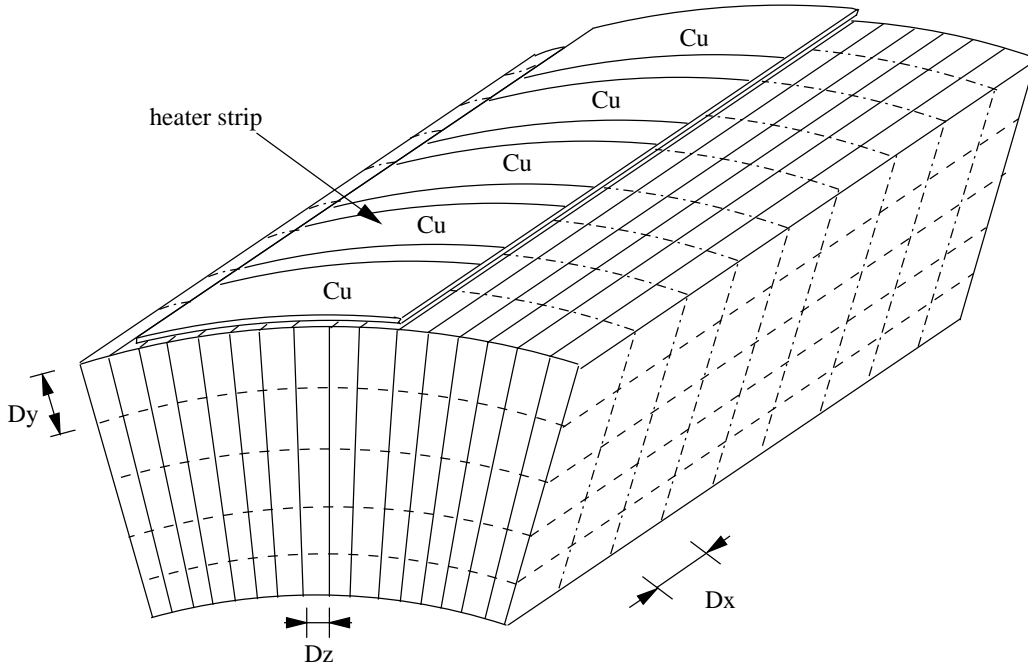
Figure A.2: *Discretisation of the coil geometry including quench heater strips.*

$$-f_h \cdot k_{iso}^h \left(\frac{T_h(t) + T_{u.h.}(t)}{2} \right) \frac{T_h(t) - T(t)}{l_{iso}^h t_h} \right] \tag{A.7}$$

The average temperature in the cable under the heater strip $T_{u.h.}$ is given by

$$
\begin{aligned}
T_{u.h.}(t) &= \frac{1}{N_{cov}} \sum_{i_x=i_0}^{N_{elem}} T(i_x, t) \cdot c_{i_x} \tag{A.8} \\
N_{cov} &= \sum_{i_x=i_0}^{N_{elem}} c_{i_x} \\
c_{i_x} &= \begin{cases} 1 & \text{if element } i_x \text{ is under a heated part of the heater strip} \\ 0 & \text{if element } i_x \text{ is under a non-heated part of the heater strip} \end{cases}
\end{aligned}
$$

The integer c_{i_x} determines whether an element i_x is located under a heated part of the quench heater strip or not. The first i_0 elements are not used for the evaluation of $T_{u.h.}(t)$ in order to avoid an error due to the expanding normal-conducting zone. The temperature in the normal-conducting zone would increase $T_{u.h.}(t)$. The use of an averaged temperature disregards the heat conduction inside the superconducting cable that reduces the temperatures at the ends of the heated elements. Although this effect is rather small, the program can also evaluate the temperatures according to Eq. A.6 when a higher precision is needed.

Eq. A.7 changes to Eq. A.9 when heat transfer into the magnet collars is included.

$$
\begin{aligned}
T_h^{new}(t^{new}) &= T_h(t) + \frac{\Delta t_{act}}{c_h(T_h(t))} \cdot \left[\rho_h(T_h(t)) \frac{I_h(t)^2}{A_h} \, k_{iso}^h \left(\frac{T_h(t) + T_{u.h.}(t)}{2} \right) \frac{T_h(t) - T(t)}{l_{iso}^h t_h} \right. \\
&\left. -k_{iso}^h \left(\frac{T_h(t) + T_b}{2} \right) \frac{T_h(t) - T_b}{l_{iron} t_h} \right] \tag{A.9}
\end{aligned}
$$

The temperature in the the superconducting cable including heat transfer from heaters is evaluated as

$$
\begin{aligned}
T^{new}(i_x, t^{new}) &= T(i_x, t) + \frac{\Delta t_{act}}{c(T(i_x, t))} \cdot \left[\frac{G(T(i_x, t), t)}{A(i_x)} - h^{He}(T(i_x, t)) \frac{P(i_x)}{A(i_x)} \right. \\
&+ \left(k(T(i_x, t)) \frac{T(i_{x+1}, t) + T(i_{x-1}, t) - 2T(i_x, t)}{(Dx)^2} \right) + \\
&\left. g(i_x) k_{iso}^h \left(\frac{T(i_x, t) + T_h(t)}{2} \right) \frac{T_h(t) - T(i_x, t)}{l_{iso}^h Dy} \right]
\end{aligned} \tag{A.10}
$$

Eq. A.10 changes to Eq. A.11 if the cooling model includes heat transfer through the insulation

$$
\begin{aligned}
T^{new}(i_x, t^{new}) &= T(i_x, t) + \frac{\Delta t_{act}}{c(T(i_x, t))} \cdot \left[\frac{G(T(i_x, t), t)}{A(i_x)} \right. \\
&+ k_{iso} \left(\frac{T(i_x, t) + T_{iso}(i_x, t)}{2} \right) \frac{T_{iso}(i_x, t) - T(i_x, t)}{l_{iso} Dy} \\
&+ \left(k(T(i_x, t)) \frac{T(i_{x+1}, t) + T(i_{x-1}, t) - 2T(i_x, t)}{(Dx)^2} \right) + \\
&\left. g(i_x) k_{iso}^h \left(\frac{T(i_x, t) + T_h(t)}{2} \right) \frac{T_h(t) - T(i_x, t)}{l_{iso}^h Dy} \right]
\end{aligned} \tag{A.11}
$$

The algorithm for the temperature evaluation of the superconducting structure including heat transfer from a quench heater strip can be summarised as follows

- program initialisation

- time loop with dynamically calculated $timestep = \Delta t_{act}$

- nested loops:

    - temperature evaluation of $T_h(t)$ or $T_h(i_x, t)$ for $Nelem$ elements

    - temperature evaluation of $T(i_x, t)$ for $Nelem$ elements using

        * direct heat transfer into helium or
        * heat transfer through the insulation material including the temperature evaluation of $T_{iso}(i_x, t)$ for $Nelem$ elements.

Two-dimensional Finite Difference Method

The numerical approach assumes a Rutherford cable with discretisation along the conductor and its broad side. The temperature $T_h(i_x, t)$ in the heater at i_x is evaluated including the heat transfer to the first element in the superconducting cable $i_y = 0$ with temperature $T(i_x, 0, t)$ (see Eq. 3.96)

$$
\begin{aligned}
T_h^{new}(i_x, t^{new}) &= T_h(i_x, t) + \frac{\Delta t_{act}}{c_h(T_h(i_x, t))} \cdot \left[\rho_h(T_h(i_x, t)) \frac{I_h(t)^2}{A_h} \right. \\
&\left. - f_h \cdot k_{iso}^h \left(\frac{T_h(i_x, t) + T(i_x, 0, t)}{2} \right) \frac{T_h(i_x, t) - T(i_x, 0, t)}{l_{iso}^h t_h} \right]
\end{aligned} \tag{A.12}
$$

The discretised two-dimensional heat balance equation including heat transfer from quench heaters is

$$
\begin{aligned}
T^{new}(i_x, i_y, t^{new}) = {} & T(i_x, i_y, t) + \frac{\Delta t_{act}}{c(T(i_x, i_y, t))} \cdot \left[\frac{G(T(i_x, i_y, t), t)}{A(i_x)} - h^{He}(T(i_x, i_y, t)) \frac{P(i_x)}{A(i_x)} \right. \\
& + \left(k(T(i_x, i_y, t)) \frac{T(i_{x+1}, i_y, t) + T(i_{x-1}, i_y, t) - 2T(i_x, i_y, t)}{(Dx)^2} + \right. \\
& \left. \frac{T(i_x, i_{y+1}, t) + T(i_x, i_{y-1}, t) - 2T(i_x, i_y, t)}{Dy^2} \right) + \\
& \left. g(i_x, i_y) k^h_{iso} \left(\frac{T_h(i_x, t) + T(i_x, 0, t)}{2} \right) \frac{T_h(i_x, t) - T(i_x, 0, t)}{l^h_{iso} Dy} \right]
\end{aligned}
\tag{A.13}
$$

Eq. A.13 includes two terms for the heat conduction inside the superconducting cable along x and y. The other terms are identical to those of Eq. A.2. The $g(i_x, i_y)$ is the discrete version of $g(x, y)$ defined in Section 3.5.4.

Three-dimensional Finite Difference Method

The modelling of the quench propagation between turns of a Rutherford cable requires the approximation of the three-dimensional heat balance equation in order to simulate the quench process in a coil. The model is similar to the two-dimensional approach. It includes an additional term for the heat transfer between two adjacent turns (via the insulation thickness l^t_{iso} with heat conductivity k^t_{iso}). The heat conduction in z-direction inside the superconducting cable is neglected because the width of a turn is an order of magnitude less than its height (typically 1–2 mm with respect to about 15 mm). The discretised three-dimensional heat balance equation for the main magnets is

$$
\begin{aligned}
T^{new} \quad & (i_x, i_y, i_z, t^{new}) = T(i_x, i_y, i_z, t) + \frac{\Delta t_{act}}{c(T(i_x, i_y, i_z, t))} \cdot \left[\frac{G(T(i_x, i_y, i_z, t), t)}{A(i_x)} + \right. \\
& \left(k(T(i_x, i_y, i_z, t)) \frac{T(i_{x+1}, i_y, i_z, t) + T(i_{x-1}, i_y, i_z, t) - 2T(i_x, i_y, i_z, t)}{(Dx)^2} \right. \\
& \left. + \frac{T(i_x, i_{y+1}, i_z, t) + T(i_x, i_{y-1}, i_z, t) - 2T(i_x, i_y, i_z, t)}{Dy^2} \right) + \\
& k^t_{iso}(T(i_x, i_y, i_z, t)) \frac{T(i_x, i_y, i_{z+1}, t) + T(i_x, i_y, i_{z-1}, t) - 2T(i_x, i_y, i_z, t)}{l^t_{iso} Dz} - \\
& g(i_x, i_y, i_z) k^h_{iso} \left(\frac{T(i_x, i_y, i_z, t) + T_h(i_x, t)}{2} \right) \frac{T_h(i_x, t) - T(i_x, i_y, i_z, t)}{l^h_{iso} Dy} + \\
& \left. h^{He}(T(i_x, i_y, i_z, t)) \frac{P(i_x)}{A(i_x)} \right]
\end{aligned}
\tag{A.14}
$$

with $A(i_x) \equiv A = Dy \cdot Dz$. Eq. A.14 needs to be changed to include cooling by heat transfer through insulation. The function $g(i_x, i_y, i_z)$ is the three-dimensional version of $g(i_x, i_y)$ in the two-dimensional model. To study forced quenching, the heat balance equation of the heater strip Eq. A.12 has to be solved in addition to Eq. A.14.

The three-dimensional model for the corrector magnets takes into account that heat transfer into the helium bath only takes place at the boundary elements (edges of the coil) since the coils are fully impregnated with epoxy.

The heat balance equation becomes

$$
\frac{dj_x}{dx} \quad + \quad \frac{j_y^- - j_y^+}{dy} + \frac{j_z^- - j_z^+}{dz} + \frac{\rho \cdot I^2}{A^2} = \frac{du}{dt}
$$

$$
j_y^- \quad = \quad \frac{K(T_{i-1}) - K(T_i)}{dy}
$$

$$
j_y^+ \quad = \quad \frac{K(T_i) - K(T_{i+1})}{dy}
$$

$$
j_z^- \quad = \quad \frac{K(T_{i-1}) - K(T_i)}{dz}
$$

$$
j_z^+ \quad = \quad \frac{K(T_i) - K(T_{i+1})}{dz}
$$

$$
K(T) \quad = \quad \int k_{ins}(T\prime)\, dT\prime \tag{A.15}
$$

j^- is the inner flux and j^+ the output flux in a turn. The evaluation is made using a steady state approximation

$$
j \quad = \quad k(T) \cdot \frac{dT}{dx} = const_x
$$

$$
\int_{x_1}^{x_2} j\,dx \quad = \quad \int_{x_1}^{x_2} k(T(x)) \cdot \frac{dT}{dx} dx
$$

For elements at the conductor boundary, the heat transfer into helium through the insulation layer is evaluated using the matrix model, which is presented next.
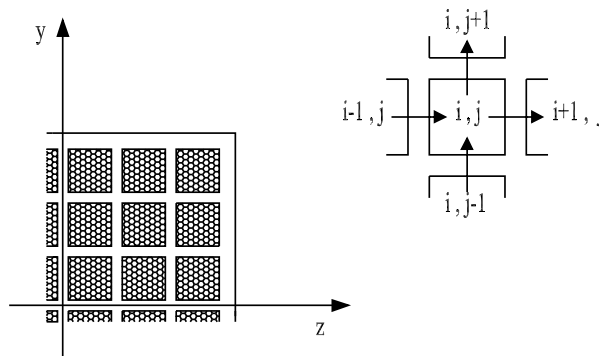
Figure A.3: *Three-dimensional model for corrector magnets.*

Matrix Model

As pointed out in Section 3.5.2, the precise modelling of the heat flux through the insulation layer requires a radial discretisation. This is needed if the insulation layer thickness is of the same

order of magnitude as the conductor diameter. Assuming radial symmetry, the discretisation of the insulation layer adds another dimension to evaluate the temperature (N longitudinal elements for the conductor and M radial insulation layer elements per longitudinal element of the conductor). In order to reduce the number of heat balance equations that need to be solved for each timestep, the heat flux as a function of radial position and the time derivative of the temperature dT/dt is evaluated before the quench computation for a given width and material of the insulation layer. The first radial element is heated with different rates of dT/dt. The heat flux through the different elements is then evaluated with the boundary condition of the heat transfer model into the helium bath at the last element. The results are stored in a matrix which is read at the beginning of the quench computation and linearly interpolated to obtain the actual heat flux out of the conductor element

$$
\begin{aligned}
T_i^{New} &= T_i + \frac{\Delta t}{C_{ins} \cdot \Delta^2} \cdot \left[\frac{T_{i+1} - T_{i-1}}{4} \left(\frac{2 k_{ins}(T_i)}{i + i_0} + \right.\right. \\
&\qquad \left.\left. k_{ins}(T_i) - k_{ins}(T_{i-1}) \right) + k_{ins}(T_i)(T_{i+1} + T_{i-1} - 2T_i) \right] \\
i_0 &= \frac{R(0)}{\Delta r}
\end{aligned}
\tag{A.16}
$$

Feedthrough Calculations

The insulation with epoxy is used for the busbar feedthroughs between two neighbouring cells to stop helium flow from one cell to the next (known as plugs). Due to these cryogenic sectors, it is possible to warm up just a few cells of the machine and to leave the rest at 1.9 K. Two matrix files are calculated (one for the epoxy insulation and one for the polyimide film), in order to simulate the quench propagation through a feedthrough. Fig. A.4 sketches a busbar geometry that requires the modelling of heat through two different insulation materials for the quench simulation.
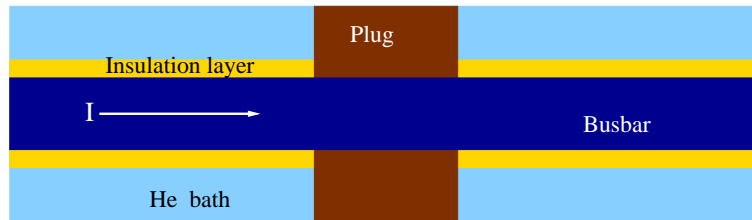
Figure A.4: *Busbar geometry with a plug to stop helium flow.*

Eddy Currents

Following the description of induced eddy currents in Section 3.4.2, the external magnetic field as a function of current is

$$
B(I(t)) = a + b \cdot I(t); \qquad \frac{dB}{dt} = \frac{B(t_{i-1}) - B(t_i)}{timestep}
\tag{A.17}
$$

The resistivity is evaluated as $\rho \equiv \rho(B(I(t)), RRR, T(t))$ for each element and timestep. The geometry parameters are specified at the program start. The required input parameters for the eddy current calculation are: the filament diameter d_fil, filament and strand twist pitch Lp_fil and Lp_strand, the number of cable layers and strands N_strand, the angle in between the cable axis (width) and the magnetic field, the constants a and b for evaluating the field as a function of the current. The main loop of the temperature evaluation calls functions that calculate the strength of the induced eddy currents and their time constants. The contribution of the dynamic losses is added to the heat generation to evaluate the temperature increase in a generalised function $G(B(x, I(t)), I(t), T(x, t), \rho(B(x, I(t)), RRR, T(x, t)))$.

A.2 Temperature Dependence of the Material Parameters

Measured material properties at various temperatures are stored in look-up tables in temperature steps of 0.1 K: the heat conductivity; the resistivity; the heat capacity for copper, niobium-titanium [30] and stainless steel [95]; the insulation material (polyimide films and epoxy) [42, 95, 96], and the heat transfer coefficient [42, 43].

The material properties for the homogeneous cable are calculated as

$$c = \frac{r_{cu/sc}}{1 + r_{cu/sc}} c_{cu} + \frac{r_{cu/sc}}{1 + r_{cu/sc}} c_{sc} \tag{A.18}$$

$$k = \frac{r_{cu/sc}}{1 + r_{cu/sc}} k_{cu} + \frac{r_{cu/sc}}{1 + r_{cu/sc}} k_{sc} \tag{A.19}$$

$$\rho = \frac{1 + r_{cu/sc}}{r_{cu/sc}} \rho_{cu} \tag{A.20}$$

The resistivity of copper as a function of the applied magnetic field, temperature and RRR value is given by

$$\rho_{cu}(RRR, T, B) = (1 + r)\rho_{cu}(RRR, T, B = 0)$$

$$\rho_{cu}(RRR, T, B = 0) = \rho_0 + \rho_i + \rho_{i0}$$

$$\rho_0 = \frac{15.53 \cdot 10^{-9}}{RRR}$$

$$\rho_i = \frac{1.171 \cdot 10^{-17} \cdot T^{4.49}}{1 + 4.498 \cdot 10^{-7} \cdot T^{3.35} \exp(-(50/T)^{6.428})}$$

$$\rho_{i0} = 0.4531 \frac{\rho_0 \rho_i}{\rho_0 + \rho_i}$$

$$\log r = -2.662 + 0.3168 \log s + 0.6229(\log s)^2 - 0.1839(\log s)^3 + 0.01827(\log s)^4$$

$$s = \frac{15.53 \cdot 10^{-9} \cdot B}{\rho_{cu}(RRR, T, B = 0)} \tag{A.21}$$

The copper thermal conductivity is computed according to the Wiedemann-Franz law, assuming that the Lorentz constant L is independent of the magnetic field

$$k_{cu}(RRR, T, B) = \frac{2.44 \cdot 10^{-8} \cdot T}{\rho_{cu}(RRR, T, B)} \tag{A.22}$$

The niobium-titanium thermal conductivity is assumed to be independent of the magnetic field and computed as a function of temperature

$$k_{NbTi}(T) = 7.5 \cdot 10^{-3} \cdot T^{1.85} \tag{A.23}$$

As for the cable parameters, the heat capacity, resistivity of stainless steel (type Al304); the thermal conductivity and capacity of the polyimide insulation are read from a look-up table and linearly interpolated. The heat transfer into liquid helium can be calculated with various heat transfer models in steps of 0.1 K that are listed below

$$h_1^{He}(T(x,t),t) = \begin{cases} 0 & \text{if } T(x,t) \le T_b \vee t - t(T > T_{f.boil}) > t_{f.boil} \\ 180 \left[\frac{W}{m^2 K^4}\right] \cdot (T(x,t)^4 - T_b^4) & \text{if } T(x,t) \le T_{f.boil} \\ 100 \left[\frac{W}{m^2 K}\right] \cdot (T(x,t) - T_b) & \text{if } T(x,t) > T_{f.boil} \wedge t - t(T > T_{f.boil}) < t_{f.boil} \end{cases}$$

$$h_2^{He}(T(x,t),t) = \begin{cases} 0 & \text{if } T(x,t) \le T_b \vee t - t(T > T_{f.boil}) > t_{f.boil} \\ 180 \left[\frac{W}{m^2 K^4}\right] \cdot (T(x,t)^4 - T_b^4) & \text{if } T(x,t) \le T_{f.boil} \\ 1000 \left[\frac{W}{m^2}\right] & \text{if } T(x,t) > T_{f.boil} \wedge t - t(T > T_{f.boil}) < t_{f.boil} \end{cases}$$

$$h_3^{He}(T(x,t),t) = \begin{cases} 0 & \text{if } T(x,t) \le T_b \\ 180 \cdot (T(x,t)^4 - T_b^4) & \text{if } T(x,t) \le T_{n.boil} \\ 100000 \left[\frac{W}{m^2}\right] & \text{if } T_{f.boil} > T(x,t) > T_{n.boil} \\ 100 \cdot (T(x,t) - T_b) & \text{if } T(x,t) > T_{f.boil} \wedge t - t(T > T_{n.boil}) < t_{f.boil} \\ 1000 & \text{if } t - t(T > T_{f.boil}) > t_{f.boil} \end{cases} \tag{A.24}$$

$$h_4^{He}(T(x,t),t) = 670 \left[\frac{W}{m^2 K}\right] \cdot (T(x,t) - T_b) \tag{A.25}$$

A.3   Numerical Limitations

The precision of the simulation result depends on the setup of the model and on the discretisation of the finite difference elements.

The temperature map might be wrong if the length of Dx, Dy, Dz is set too long (problem of setting the mesh) due to the linear evaluation and interpolation of the temperature and material properties. A diverging temperature or temperature oscillations are possible if the timestep is too big. This occurs for example if the temperature jumps over several Kelvin in an element that becomes normal conducting within Δt.

The implemented numerical approach is known as the explicit method. It compromises the risk of a numerical instability with fast evaluation and simple extension of the model. The implicit method is stable since the new temperature is evaluated iteratively by a matrix inversion, but requires many more calculation steps with respect to the explicit method [76, 94]. The additional computation time can be reduced by increasing the timestep but the explicit method remains faster. The risk of a numerical instability in the explicit method is avoided by reducing the sizes of the discrete elements in space and time until the program output stabilises. The application of the explicit method approach is appropriate due to the available computing power. An empirical optimisation of the discretisation in space yields $Dx \approx \sqrt{A_{tot}}$.

The timestep is calculated as a function of material parameters for the present temperature profile (see Eq. A.3)

$$\Delta t = \alpha \frac{c(\min(T(x,y,z)))\min(Dx, Dy, Dz)^2}{k(\min(T(x,y,z)))} \tag{A.26}$$

where α is an input parameter to steer the timestep evaluation (normally 0.1 K). The initial timestep can also be set as a program input parameter and used for the entire computation. In Eq. A.26 the calculation of Δt is proportional to the length of the finite difference element squared. As the precision of the temperature evaluation relies on how fine the finite difference element mesh is set up, the timestep must be reduced accordingly. For example, if the simulation includes heat transfer to helium for the cable of the LHC dipole magnets, Dx may not be set longer than 1 cm. This requires an initial timestep Δt of about 0.1–1 μs. The other limiting factor for the precision is the longterm modelling of the heat transfer into helium (simulation of temperature evaluation several seconds after a quench starts).

The implicit method was programmed to crosscheck the outcome of the explicit approach for the one-dimensional quench propagation without transverse cooling. The comparison gave the same quench propagation velocity and a difference of the hot spot temperature by less than 2 % when the discretisation in space and time was adjusted in the explicit method as described above [75].

Comparison with Analytical Models

In order to test if the numerical model is correctly calculating the heat conduction along the cable, the code has been compared with an analytical model.

The temperature profile $T(x,t)$ for a thin one-dimensional conductor that receives an initial heat Q at $x=0$ for $t=0$ can be analytically calculated as follows

$$T(x,t) = T_0 + \frac{Q}{c\sqrt{\pi 4 D_w t}} \exp\left(-\frac{x^2}{4 D_w t}\right) \tag{A.27}$$

with $t \geq 0$ and $D_w = k/c$. In order to verify the consistency of the numerical code, averaged material constants are used for the analytical approach (Eq. A.27) and for the simulation. The error of the numerical results depends on the mesh dimensions (the initial timestep and the space discretisation).

Another crosscheck is the evaluation of the dissipated energy using the enthalpy and its comparison with the electrical energy. Without heat transfer to liquid helium, both values are identical. Including heat transfer, the difference of both values corresponds to the energy which is taken by the helium bath. The electrical energy is

$$E(t) = \int_0^t R(t')I(t')^2 dt'$$

$$E(t_n) = \sum_{i=0}^n R(t_i)I(t_i)^2 \Delta t_i \tag{A.28}$$

The resistance $R(t_i)$ is given by

$$R(t_i) = 2 \sum_{j=0}^{Nelem} \frac{\rho(T_j(t_i))Dx}{A} \qquad \text{or for the three-dimensional model}$$

$$R(t_i) \;=\; 2 \sum_{j=0}^{Nelem} \sum_{k=0}^{Nyelem} \sum_{l=0}^{Nzelem} \frac{\rho(T(j,k,l)(t_i))Dx}{Dy \cdot Nyelem \cdot Dz} \tag{A.29}$$

The energy obtained with the enthalpy is

$$E(t) \;=\; (H(t) - H(t_0))V$$

$$E(t_n) \;=\; \sum_{j=0}^{Nelem} (H(T_j(t_n)) - H(T_j(t_0)))V_j \qquad \text{respectively}$$

$$E(t_n) \;=\; 2 \sum_{j=0}^{Nelem} \sum_{k=0}^{Nyelem} \sum_{l=0}^{Nzelem} (H(T(j,k,l,t_n)) - H(T(j,k,l,t_0)))DxDyDz \tag{A.30}$$

where V is the total volume, $V_j{=}Dx \cdot A$. This test showed that the endpoints can be assumed as extrema (no heat flux) of the temperature profile.

Calibration of Heat Transfer through the Insulation Layer

When the superconductor is replaced by the insulation layer, the program evaluates the heat transfer through the insulation layer, which can be used to study the assumption of a linear temperature gradient in the insulation layer (see Section 3.5.2). If the temperature difference between the
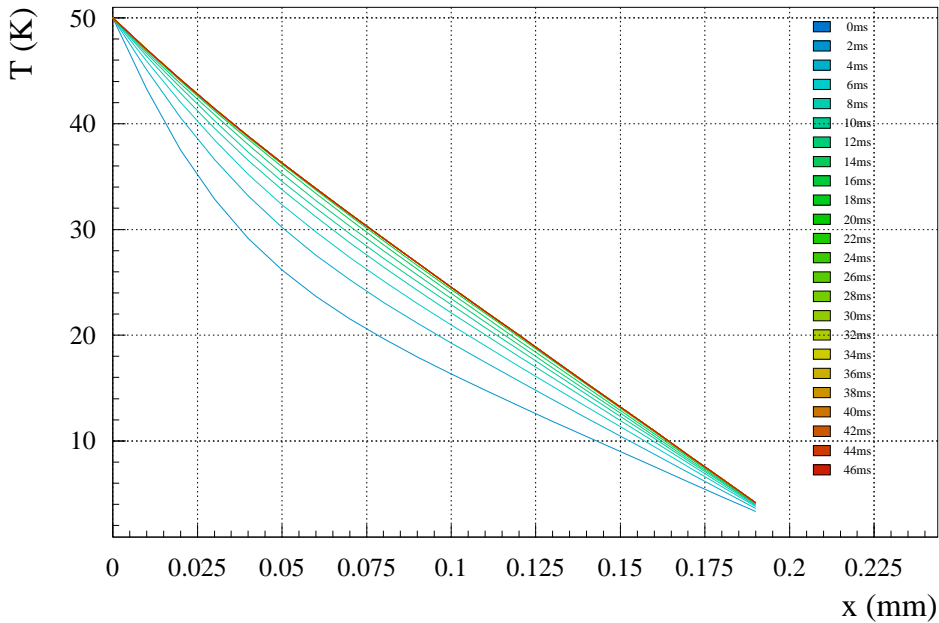
Figure A.5: *Test of the heat transfer model through a thin insulation layer.*

surfaces of a 200 μm thick insulation layer is 50 K, the temperature gradient reaches a linear profile in less than 50 ms (see Fig. A.5).

This test proves that the discretisation of the insulation layer (applying the matrix model) is required if the insulation thickness is comparable with the dimension of the conductor as for the 600 A busbar cable (see Fig. A.6).
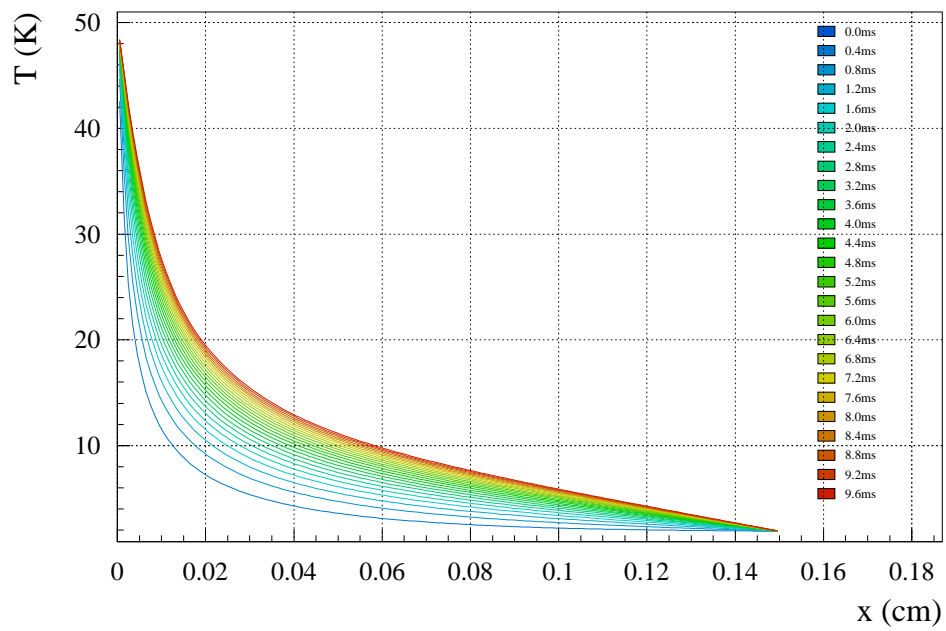
Figure A.6: *Test of the heat transfer model through a thick insulation layer.*

Bibliography

[1] The LHC study group. LHC the Large Hadron Collider - Conceptual Design. *CERN/AC/95-05*, October 1995. Vol. II.

[2] O. Brüning. Accelerator physics at the LHC. *Summer Student Lectures, CERN*, 1999.

[3] R. Schmidt. Accelerator physics and technology of the LHC. *CERN Yellow Report 99-01*, 1998.

[4] F. Gianotti. Physics at the LHC. *Summer Student Lectures, CERN*, 1999.

[5] C. Caso et al. The Higgs Boson. *The European Physical Journal C3*, 1998.

[6] U. Amaldi et al. Consistency checks of GUT's with LEP data. *CERN-PPE/91-190*, 1991.

[7] P. Schmüser. Superconductivity. *CERN CAS School on Superconductivity*, 1995.

[8] Wolff Mess, Schmüser. Superconducting accelerator magnets. *World Scientific Publishing Co. Pte. Ltd.*, 1996.

[9] S. Russenschuck et al. ROXIE routine for the optimisation of magnet x-sections, inverse field calculations and coil end design. *CERN Yellow Report 99-01*, 1998.

[10] S. Claudet et al. Specification of the refrigeration units for the LHC. *Proceedings of ICEC 18, Bombay, India*, 2000.

[11] M. N. Wilson. Superconducting magnets. *Oxford Science Publications*, 1983.

[12] H. K. Onnes. 1908.

[13] H. K. Onnes. *Akad. van Wetenschappen (Amsterdam)*, 1911.

[14] W. Meissner and R Ochsenfeld. *Naturwissenschaften*, 1933.

[15] F. London and H. London. *Z. Phys.*, 1935.

[16] Cooper Bardeen and Schrieffer. *Phys. Rev.*, 1957.

[17] V. L. Ginzburg and L. D. Landau. *Sov. Phys. USSR*, 1950.

[18] L. P. Gorkov. *Sov. Phys. JETP*, 1960.

[19] B. D. Josephson. *Phys. Rev. Lett*, 1962.

[20] Bednorz and Müller. Possible high T_c superconductivity in the Ba-La-Cu-O system. *Zeitschrift für Physic B*, 1986.

[21] W. Buckel. Supraleitung. *VCH Verlagsgesellschaft*, 1990.

[22] D. R. Tilley and J. Tilley. Superfluidity and superconductivity. *Institute of Physics Publishing Ltd*, 1990.

[23] M. N. Wilson. Superconducting materials for magnets. *CERN CAS School on Superconductivity*, 1995.

[24] Y. Aharonov and D. Bohm. *Phys. Rev.*, 1955.

[25] U. Essmann and H. Träuble. *Phys. Lett*, 1971.

[26] A. A. Abrikosov. *Sov. Phys. JETP*, 1957.

[27] A. Kuijper et al. *Diploma Thesis, University of Twente*, 1999.

[28] Y.B. Kim et al. *Phys. Rev*, 1965.

[29] P. W. Anderson. *Phys. Rev. Lett*, 1962.

[30] A. Devred et al. Influence of eddy currents in superconducting particle accelerator magnets using rutherford-type cables. *CERN 96-03*, 1996.

[31] Larbalestier and Lee. Prospects for the use of high temperature superconductors in high field accelerator magnets. *Proceedings of PAC 1999*, 1999.

[32] A. Ballarino. Application of high temperature superconductors to accelerators. *Proceedings of EPAC 2000, Vienna, Austria*, 2000.

[33] A. Devred. Superconductor development in europe. *Proceedings of the Workshop on VLHC Magnets, FNAL*, 2000.

[34] A. F. Greene. Recent status of superconductors for accelerator magnets. *Proceedings of the Workshop on AC-Superconductivity, KEK*, 1992.

[35] R. Perin. Field, forces and mechanics of superconducting magnets. *CERN CAS School on Superconductivity*, 1995.

[36] Ph. Lebrun. Superfluid helium as a technical coolant. *Proceedings of the 15th UIT*, 1997.

[37] Arp and Hust. Hepak. *Computer code supplied by CRYODATA*.

[38] W. F. Vinen. Superfluidity. *CERN CAS School on Superconductivity*, 1995.

[39] O. Penrose and L. Onsager. *Phys. Rev.*, 1956.

[40] L. D. Landau. *J. Phys. USSR*, 1947.

[41] R. P. Fenman. *Progress in Low Temperature Physics*, 1955.

[42] P. Bauer. Stability of superconducting strands for accelerator magnets. *PhD Thesis, Technische Universität Wien*, 1998.

[43] S. W. v. Sciver. Forced flow he II cooling for superconducting magnets - design considerations. *Cryogenics 38*, 1998.

[44] S. S. Kutateladze. *Statistical Science and Technical Publications*, 1952.

[45] C. Schmidt. Review of steady-state and transient heat transfer in pool boiling helium I. *Stability of Superconductors*, 1981.

[46] L. Dresner. Stability of superconductors. *Plenum Publishing Corporation*, 1995.

[47] Z. Stekly et al. Stability of superconductors. *IEEE Trans. 12*, 1965.

[48] B.J. Maddock et al. Stability of superconductors. *Cryogenics 9*, 1969.

[49] L. Dresner. On the connection between normal zone voltage and hot spot temperature in uncooled magnets. *Cryogenics 34*, 1994.

[50] B. Turck. About the propagation velocity in superconducting composites. *Cryogenics 20*, 1980.

[51] R. Herzog et al. The superconducting busbar cable powering the auxiliary magnets of the LHC. *Proceedings of IEC 1999, Montreal, Canada*, 1999.

[52] D. Hagedorn and F. Rodriguez-Mateos. Modelling of the quenching processes in complex superconducting magnet systems. *IEEE Trans. Magn. 28*, 1992.

[53] F. Sonnemann and R. Schmidt. Quench simulations of LHC accelerator magnets and busbars. *Cryogenics 40, CHATS 2000 Proceedings*, 2000.

[54] F. Sonnemann et al. Quench process and protection of LHC dipole magnets. *LHC Project Note 184*, 1999.

[55] T. Ogitsu. Influence of cable eddy currents on the magnetic field of superconducting particle accelerator magnets. *SSCL-N848*, 1994.

[56] G.H. Morgan. Theoretical behaviour of twisted multicore superconducting wires in a time varying uniform magnetic field. *J.Appl.Phys. 41*, 1970.

[57] E.M.J. Niessen. Continuum electromagnetics of composite superconductors. *PhD Thesis, University of Twente*, 1993.

[58] A. P. Verweij. Electrodynamics of superconducting cables in accelerator magnets. *PhD Thesis, Twente University*, 1995.

[59] D. Hagedorn. Studies on the quenching process with inductive coupling in the MBS dipole. *CERN/EA/Note 1975/78-6*, 1975.

[60] A. P. Verweij. Modelling boundary-induced coupling currents in Rutherford-type cables. *Proceedings of Applied Superconductivity Conference, Pittsburgh, USA*, 1997.

[61] A. P. Verweij et al. Boundary-induced coupling currents in a 1.3m Rutherford-type cable due to a locally applied field change. *Proceedings of Applied Superconductivity Conference, Pittsburgh, USA*, 1997.

[62] R. Schmidt et al. Quench studies for the lhc corrector magnet MSBH. *LHC Project Note 28*, 1995.

[63] F. Rodriguez-Mateos et al. Thermo-hydraulic quench propagation at the LHC superconducting magnet string. *Proceedings of ICEC 17, Bournemouth, United Kingdom*, 1998.

[64] M.A. Green. Quench back in thin superconducting solenoid magnets. *Cryogenics 24*, 1984.

[65] M.A. Green. The role of quench back in quench protection of a superconducting solenoid. *Cryogenics 24*, 1984.

[66] G.H. Morgan. Eddy currents in flat metal-filled superconducting braids. *J. Appl. Phys 44*, 1973.

[67] K. Takeuchi et al. Interfilament coupling loss for protection of superconducting multicoil magnets. *Cryogenics 38*, 1998.

[68] Bronstein and Semendjanjew. Taschenbuch der Mathematik. *Teubner, P. 116f.*, 1981.

[69] W. B. Bloem. Transient heat transfer to supercritical helium at low temperatures. *Netherlands Energy Research Foundation*, 1986.

[70] K. Hama et al. Film boiling on a horizontal cylinder in saturated and subcooled helium II. *Cryogenics 38*, 1998.

[71] F. Rodriguez-Mateos et al. Quench heater experiments on the LHC main magnets. *Proceedings of EPAC 2000, Vienna, Austria*, 2000.

[72] S. Jongeleen et al. Quench localisation and current redistribution after quench in superocnducting dipole magnets wound with Rutherford-type cables. *Proceedings of ASC Pittsburgh, USA; LHC Project Report 59*, 1996.

[73] L. Coull et al. Quench propagation tests on the LHC superconducting magnet string. *LHC Project Report 70*, 1996.

[74] F. Bordry et al. The LHC magnet string programme: status and future plans. *Proceedings of PAC 99, New York, USA*, 1999.

[75] M. Calvi. Quench simulations for LHC busbars. *Diploma Thesis, University of Turin*, 2000.

[76] A. Bejan. Heat transfer. *John Wiley & Sons, Inc.*, 1993.

[77] J.L. Perinet-Maquet et al. Measurement of superconducting busbars models for the LHC main dipole. *Proceedings of MT16 1999*, 1999.

[78] F. Sonnemann et al. Modelling of the quench process for the optimisation of the design and protection of superconducting busbars for the lhc. *Proceedings of ICEC 18, Bombay, India*, 2000.

[79] R. Schmidt et al. Protection of the superconducting corrector magnets of the LHC. *Proceedings of EPAC 2000, Vienna, Austria*, 2000.

[80] F. Sonnemann et al. Passive protection by a parallel resistor for corrector magnets connected in large electical series. *MTA-IN-98-054*, 1998.

[81] F. Sonnemann et al. Quench propagation experiments of the MQT quadrupole. *MTA-IN-99-099*, 1999.

[82] O. Brüning and F. Sonnemann. Maximum current ramp speed, required accuracies and protection for the corrector circuits. *LHC Project Note in preparation*, 2000.

[83] N. Andreev et al. State of the short dipole model program for the LHC. *LHC Report 223, Proceedings of EPAC 98, Stockholm, Sweden*, 1998.

[84] A. Siemko. Detraining in LHC short dipole magnets. *private communication*, 1998.

[85] F. Rodriguez-Mateos et al. Quench heater experiments on the LHC main superconduting magnets. *Proceedings of EPAC 2000, Vienna, Austria*, 2000.

[86] J. Casas-Cubillos et al. Experiments and cycling at the LHC prototype half-cell. *LHC Project Report 110, Proceedings of PAC 97 Vancouver, Canada*, 1997.

[87] Z. Ang et al. Measurement of ac loss and magnetic field during ramp in the LHC model dipole. *IEEE Trans. Appl. Supercond. 9*, 1999.

[88] M. Lamm et al. Quench protection of the LHC inner triplet quadrupoles built at fermilab. *ASC 2000 Proceedings*, 2000.

[89] E. Burkhardt et al. Quench protection heater studies for the KEK low-beta quadrupoles for the LHC. *ASC 2000 Proceedings*, 2000.

[90] R. Ostojic et al. Performance of the 1 m model of the MQM twin aperture quadrupole for the LHC insertions. *ASC 2000 Proceedings*, 2000.

[91] G. Kirby et al. Performance of the 1 m model of the MQY twin aperture quadrupole for the LHC insertions. *ASC 2000 Proceedings*, 2000.

[92] R.Rausch and M.Tavlet. *CERN-TIS-TE/IR/98-11, Proceedings of PAC 99, New York, USA*, 1999.

[93] F. Sonnemann et al. The protection system for the superconducting elements of the LHC at CERN. *Proceedings of PAC 99, New York, USA*, 1999.

[94] Nonino Comini, Del Giudice. Finite element analysis in heat transfer. *Taylor & Francis, Series in Computational and Physical Processes in Mechanics and Thermal Sciences*, 1994.

[95] Dieter Hagedorn. Material properties measured at CERN. *private communciation*.

[96] Arp and Hust. Cryo-Pac. *Computer code supplied by CRYODATA*.

List of Figures

List of Tables

Acknowledgements

Lebenslauf

Name	<u>Florian</u> Johannes Daniel Sonnemann
Geburt	19.09.1974 in Braunschweig
Familienstand	verheiratet
August 1981	Einschulung in die Comeniusgrundschule in Braunschweig
Juni 1993	Abitur am Pelizaeus-Gymnasium in Paderborn
Oktober 1993	Beginn des Studiums der Physik an der RWTH Aachen
September 1995	Vordiplom in Physik
Mai 1997	Diplomarbeit am III. Physikalischem Institut A bei Prof. Dr. M. Tonutti Technischer Student am europäischen Forschungslabor CERN in Genf in der SL-Division
July 1998	Diplom in Physik
seit August 1998	Doctoral Student am europäischen Forschungslabor CERN in Genf in der LHC-Division